PhD Thesis

Submitted for the degree of Doctor of Philosophy from UNIVERSITÉ POLYTECHNIQUE HAUTS-DE-FRANCE, INSA HAUTS-DE-FRANCE, and UNIVERSITY OF MONS, Faculty of Science

Subject: Materials Engineering

Presented and defended by **Muthusundar KUMAR** on **09/10/2025, Maubeuge**

Investigating the Cold Sintering Process of Bioactive Materials

Doctoral school: Doctoral School Polytechnic Hauts-de-France (ED PHF n°635)

Research unit: Laboratory of Ceramic Materials and Mathematics (CERAMATHS) & Laboratory of Polymeric and Composite Materials (SMPC)

JURY

BRAEM Annabel, Professor, KU Leuven, Reviewer

BRAM Martin, Professor, Forschungszentrum Jülich, Reviewer

LOCS Janis, Professor, Riga Technical University, Jury President

BERMEJO Raúl, Professor, Montanuniversität Leoben, Examiner

LERICHE Anne, Professor, UPHF, Director

RAQUEZ Jean-Marie, Professor, UMONS, Co-director

MINCHEVA Rosica, Doctor, UMONS, Co-supervisor

LASGORCEIX Marie, Doctor, UPHF, Co-supervisor

BEN ACHOUR Mohamed Aymen, Doctor, UPHF, Co-supervisor, Guest

GONON Maurice François, Professor, UMONS, Guest

HOCQUET Stéphane, Doctor, Belgian Ceramic Research Centre, Guest

Thèse de doctorat

Pour obtenir le grade de Docteur de l'UNIVERSITÉ POLYTECHNIQUE HAUTS-DE-FRANCE et de l'INSA HAUTS-DE-France et UNIVERSITÉ de Mons, Faculté des Sciences

Discipline: Génie des matériaux

Présentée et soutenue par **Muthusundar KUMAR** Le **09/10/2025, Maubeuge**

Étude du processus de frittage à froid de matériaux bioactifs

École doctorale: École Doctorale Polytechnique Hauts-de-France (ED PHF n°635)

Unité de recherche: Laboratoire de Matériaux Céramiques et de Mathématiques (CERAMATHS) et Service des Matériaux Polymères et Composites (SMPC)

Membres du jury

BRAEM Annabel, Professor, KU Leuven, Rapportrice

BRAM Martin, Professor, Forschungszentrum Jülich, Rapporteur

LOCS Janis, Professor, Riga Technical University, Président du jury

BERMEJO Raúl, Professor, Montanuniversität Leoben, Examinateur

LERICHE Anne, Professor, UPHF, Directrice de thèse

RAQUEZ Jean-Marie, Professor, UMONS, Co-Directeur de thèse

MINCHEVA Rosica, Doctor, UMONS, Co-encadrant

LASGORCEIX Marie, Doctor, UPHF, Co-encadrant

BEN ACHOUR Mohamed Aymen, Doctor, UPHF, Co-encadrant, Invité

GONON Maurice François, Professor, UMONS, Invité

HOCQUET Stéphane, Doctor, Belgian Ceramic Research Centre, Invité

Acknowledgements

I owe my deepest thanks to my thesis directors, Prof. Anne Leriche (UPHF) and Prof. Jean-Marie Raquez (UMONS), for their consistent guidance, timely discussions, and for creating numerous opportunities and collaborations that advanced my research and personal development. I am especially grateful to them for welcoming me into their research groups, for their trust, and for enabling a cross-disciplinary and cross-cultural research path. A special mention to Prof. Philippe Dubois, Rector, UMONS, and Prof. Christian Courtois, Director, Ceramaths (UPHF).

Special thanks to my supervisors and co-supervisors, Dr. Mohamed Ben Achour, Dr. Marie Lasgorceix, and Dr. Rosica Mincheva, whose guidance and comments were invaluable throughout my thesis journey. I further thank Prof. Clive A. Randall, Prof. Maurice François Gonon, and Dr. Stéphane Hocquet for serving as external examiners during my annual thesis reviews and for their insightful questions and constructive recommendations.

I gratefully acknowledge the Belgian Ceramic Research Centre (BCRC) for generously sharing instrumentation facilities, especially FIB-SEM, dilatometry, and μ-XRF. I also thank Materia Nova for access to cryo-milling, melt-flow index measurements, Raman spectroscopy, and rheological testing.

I deeply acknowledge Dr. Russell Maier for his collaboration and for hosting me at the National Institute of Standards and Technology (NIST), USA, which provided the opportunity and facilities to conduct in-situ cold-sintering research. I also thank Dr. Anthony Kotula for invaluable help with in-situ Raman measurements. The NIST experience greatly strengthened this thesis and broadened the direction of my cold-sintering research. I also express my gratitude to the Journal of the European Ceramic Society (JECS) Trust Mobility Grant and the Franeau Mobility Grant, which funded my research visit to NIST (USA).

I warmly thank the technical staff and fellow researchers, past and present, at Ceramaths (UPHF) and SMPC (UMONS), for their collegial spirit, generosity in sharing resources, and for fostering a stimulating research environment. Special thanks to Benoit Jorgowski, Dr.

Florian Jean, and Mr Gerard Moreau (Ceramaths, UPHF) for their technical assistance with SEM imaging and training on other instruments. I am also grateful to Dr. Noémie Hergue and Dr. Samira Benali (SMPC, UMONS), and to Mr Philippe Reco and Ms Caroline Delecluse (Ceramaths, UPHF), who consistently ensured I had access to the necessary equipment and training.

As this was my first move from India to Belgium in 2022, I was fortunate to have Ms Nathalie Vanderest's (SMPC, UMONS) support, which made the relocation smooth. I am grateful for her patient help with the paperwork and administrative formalities at UMONS. I'm also extending gratitude to Ms Carole Draux (Ceramaths, UPHF) for her assistance with paperwork and administrative procedures at UPHF.

Special mention to my former mentors, Dr Anantha Kumar and Mr Peer Mohamed at the CSIR–National Institute for Interdisciplinary Science and Technology (CSIR-NIIST), India, whose mentorship provided the fundamental grounding in ceramics, materials science, and characterization that underpins this thesis. Their steady encouragement and guidance enabled me to reach this milestone and pursue a PhD.

A sincere thanks to all my friends: Jaseem, Bashi, Vimal, Unni, Deepesh, Abirami, Ashwathy, Prasanna, Ajay, Mohan, Vikas, Nagaraj, Balla Murugesh, Sivaramakrishna, Prasad, and Alvero, whose friendship and encouragement sustained me throughout my career development.

Finally, I remain indebted to my family for their unwavering love, encouragement, support, and innumerable sacrifices that have sustained me at every stage and shaped my path.

Abstract

The cold sintering process (CSP) is a non-conventional sintering technique that densifies ceramic materials using a transient liquid phase under applied pressure, typically at low temperatures (<300 °C). This processing window enables co-sintering of ceramic-polymer phases and offers unique advantages over conventional high-temperature sintering, which can compromise material integrity and degrade functional performances.

Bioactive materials play a pivotal role in clinical orthopedic applications because they stimulate the biological events that mediate bone repair and regeneration. This thesis investigates CSP of three distinct bioactive material systems: hydroxyapatite (HA), ternary bioglass (BG, SiO_2–CaO–P_2O_5), and hydroxyapatite-polylactide composite (HA-PLA). The key role of transient liquids, their chemistry, and the associated pressure-solution creep pathway in enabling low-temperature densification was studied. Phosphoric acid was found to be an effective transient liquid for densifying HA to ~90 % and BG to ~89 % under 360 MPa at 200 °C. In both cases, 2 M phosphoric acid drives pressure-solution creep via incongruent dissolution-reprecipitation-recrystallization pathways. In CSP of the HA-PLA composite, consolidation is governed by the HA-to-PLA ratio and the thermal-induced flowability of PLA, as assessed by comparing unplasticized and plasticized PLA.

Finally, the temperature-dependent dynamics of densification in HA, BG, and consolidation in HA-PLA composite were established through in-situ monitoring and in-situ Raman analysis in collaboration with the National Institute of Standards and Technology (NIST), USA. Overall, this thesis provides a fundamental understanding of transient liquid chemistry and the underlying sintering mechanism governing CSP of bioactive ceramics and composite systems, guiding future efforts to advance the technology readiness level (TRL) of CSP for the fabrication of synthetic grafts.

Résumé

Le processus de frittage à froid (CSP) est une technique de frittage non conventionnelle qui densifie les matériaux céramiques à l'aide d'une phase liquide transitoire sous pression appliquée, généralement à basse température (<300 °C). Cette fenêtre de traitement permet le co-frittage des phases céramique-polymère et offre des avantages uniques par rapport au frittage conventionnel à haute température, qui peut compromettre l'intégrité des matériaux et dégrader leurs performances fonctionnelles.

Les matériaux bioactifs jouent un rôle essentiel dans les applications orthopédiques cliniques, car ils stimulent les processus biologiques qui interviennent dans la réparation et la régénération osseuses. Cette thèse étudie le CSP de trois systèmes de matériaux bioactifs distincts : l'hydroxyapatite (HA), le bioverre ternaire (BG, SiO_2–CaO–P_2O_5) et le composite hydroxyapatite-Acide polylactique (HA-PLA). Le rôle clé des liquides transitoires, leur chimie et la voie de fluage sous pression-solution associée permettant une densification à basse température ont été étudiés. L'acide phosphorique s'est avéré être un liquide transitoire efficace pour densifier l'HA à environ 90 % et le BG à environ 89 % sous 360 MPa à 200 °C. Dans les deux cas, l'acide phosphorique 2 M entraîne un fluage sous pression-solution via des voies de dissolution-reprécipitation-recristallisation incongruentes. Dans le CSP du composite HA-PLA, la consolidation est régie par le rapport HA/PLA et la fluidité thermique du PLA, évaluée en comparant le PLA non plastifié et plastifié.

Enfin, la dynamique dépendante de la température de la densification dans le HA/BG et de la consolidation dans le composite HA-PLA a été établie grâce à un test in-situ et à une analyse Raman in-situ en collaboration avec le NIST, aux États-Unis. Dans l'ensemble, cette thèse fournit une compréhension fondamentale de la chimie liquide transitoire et du mécanisme de frittage sous-jacent qui régit le CSP des céramiques bioactives et des systèmes composites, guidant les efforts futurs visant à faire progresser le niveau de maturité technologique (TRL) du CSP pour la fabrication de greffons synthétiques.

Table of Contents

Acknowledgements **5**

Abstract **7**

Résumé **9**

List of Figures **15**

List of Tables **21**

Chapter 1 General Introduction **23**

1.1 Background 23

1.2 Context and Motivation 26

1.3 Thesis Outline 27

Chapter 2 State-of-the-Art **29**

2.1 Bone Tissue and Need for Bioactive Materials 29

2.1.1 Structure and Function of Bone 29

2.1.2 Bone Healing and Challenges 30

2.1.3 Need for Synthetic Bone Grafts 32

2.2 Bioactive Materials and Fabrication Challenges 34

2.2.1 Synthetic Biomaterials for Bone Regeneration 34

2.2.2 Hydroxyapatite Bioceramic 37

2.2.3 Ternary Bioglass 37

2.2.4 Hydroxyapatite-Polylactic acid Composite 39

2.2.5 HA-PLA Composite Fabrication Challenges 41

2.3 Sintering Pathways for Bioactive Materials 43

2.3.1 Conventional Sintering and Its Science 43

2.3.2 Non-Conventional Sintering Techniques 47

2.3.3 Low-Temperature Sintering Techniques 48

2.4 The Cold Sintering Process 50

2.4.1 CSP Protocol 51

2.4.2 CSP Mechanism 51

2.4.3 CSP Parameters 54
2.4.4 In-Situ CSP Monitoring 57
2.5 Progress in CSP of Bioactive Materials 60
2.5.1 Bioceramic Materials 60
2.5.2 Ceramic-Polymer Composite Materials 62
2.6 Research Gap 65
2.7 Thesis Objectives 67
Chapter 3 Materials and Methods 69
3.1 Materials and Preparation Methods 69
3.1.1 Hydroxyapatite Powder 69
3.1.2 Ternary Bioglass Powder 69
3.1.3 HA-PLA Composite Powder 70
3.2 CSP Methodology 72
3.2.1 HA and BG Powders 72
3.2.2 HA-PLA Composite powder 73
3.3 Conventional Sintering of HA and BG 73
3.4 Characterizations 74
3.4.1 Relative Density Measurements 74
3.4.2 Particle Size Distribution Analysis 75
3.4.3 Specific Surface Area Analysis 75
3.4.4 Phase Measurements 75
3.4.5 Morphology and Microstructure Analysis 76
3.4.6 Chemical Analysis 76
3.4.7 Thermal Analysis 77
3.4.8 In-Situ CSP Analysis 77
3.4.9 Mechanical Testing 79
Chapter 4 Cold Sintering Process Framework for Hydroxyapatite 81
4.1 Context 81
4.2 HA Powder Characteristics 82

4.3 HA Cold Sintering Process 84
4.4 HA Cold Sintering Process 86
4.4.1 Density Evolution vs Liquid Phase Chemistry 86
4.4.2 Microstructure and Mechanical Property 89
4.4.3 Phase and Chemical characteristics 91
4.4.3 Influence of Physical Properties in CSP 94
4.5 HA In-Situ CSP Investigation 98
4.6 HA CSP Mechanism 102
4.7 Conclusions 104
Chapter 5 Cold Sintering Process Framework for Ternary Bioglass 107
5.1 Context 107
5.2 BG Powder Characteristics 109
5.3 BG Conventional Sintering 110
5.4 BG Cold Sintering Process 112
5.4.1 Density Evolution vs Liquid Phase Chemistry 112
5.4.2 Phase and Chemical characteristics 114
5.4.3 Microstructure and Mechanical Property 116
5.5 CSP of HA-BG 118
5.6 BG In-Situ CSP Investigation 122
5.7 Conclusions 126
Chapter 6 Cold Sintering Process Framework for HA-PLA Composite 129
6.1 Context 129
6.2 Consolidation vs HA-to-PLA Ratio 131
6.2.1 Density Evolution 131
6.2.2 Microstructure 133
6.3 Plasticization Effect on Composite Consolidation 135
6.4 HA Consolidation in the Composite Matrix 137
6.5 Phase Composition and Thermal Behavior 138
6.6 Composite Mechanical Property 141
6.7 HA-PLA In-Situ CSP Investigation 143
6.8 Conclusions 147

Chapter 7 General Conclusions and Future Work 149

Appendix 153

Appendix A: Supplementary Materials 153

Appendix B: Scientific Dissemination 157

Bibliography 159

List of Figures

Figure 2.1 The chemical composition and multi-scale structure of natural bone 29

Figure 2.2 Illustration of a typical fracture healing process, biological events, and cellular activities at different phases 31

Figure 2.3 General mechanism of apatite formation on the surface of bioactive glass 38

Figure 2.4 Ternary solid-liquid-pore diagram illustrating the different types of sintering that fall under the conventional sintering technique 44

Figure 2.5 Schematic illustration of the fundamental phenomenon that occurs during the conventional high-temperature sintering 45

Figure 2.6 Schematic illustration of mass transport mechanisms contributing to the densification of green compact during high-temperature sintering 46

Figure 2.7 (a) Article count published per year from 2016 to 2024, and (b) breakdown of article counts by material or topic category (up to 2024) published under the framework of the cold sintering process 50

Figure 2.8 Schematic illustration of (a) cold sintering process protocol, (b and c) the mechanism driving density evolution during CSP of ceramic densification 52

Figure 2.9 Schematic representation of the key parameters influencing final densification in the cold sintering process 55

Figure 2.10 a) Schematic representation of the experimental die setup and b) temperature and pressure profile. Electrical measurements are performed during the sintering dwell time 58

Figure 2.11 Schematic of the sample mounted in a thin transparent quartz capillary CSP setup for in-situ X-ray scattering measurements during CSP 59

Figure 2.12 In-Situ observation of CSP of ZnO: represented by the thresholded images of ZnO/acetic acid powder compact being densified at 150 MPa, heated to a temperature of 150 °C at 5 °C/min 60

Figure 2.13 Microstructure of fractured surfaces of the cold sintered chitosan-HA with composites with mass ratios (a) 0/10, (b) 1/9, (c) 3/7, (d) 5/5, (e) 7/3, and (f) 10/0 (CSP parameters: 100°C, 600 MPa, and 20 min) 63

Figure 3.1 Schematic illustration of the HA-PLA composite powder preparation 71

Figure 3.2 Schematic illustration of the CSP protocol and setup involved in the densification of HA or BG powders 72

Figure 3.3 schematic diagram (left), and digital image of the cold sintering setup (right) used for in-situ observations..... 78

Figure 4.1 Particle morphology of the commercial hydroxyapatite powders (HAp201 & HAp202) visualized by SEM 83

Figure 4.2 (a) Microstructure from SEM, (b) dilatometry curve (dashed lines represent the first derivative of the corresponding linear shrinkage curve), and (c) X-ray diffraction patterns of conventionally sintered commercial hydroxyapatite powders (HAp201 & HAp202) 84

Figure 4.3 (a) Relative density values obtained for densified HA corresponding to liquid solutions and their concentrations in CSP. Comparison of linear shrinkage profile obtained during the CSP under 360 MPa at 200 °C (b) without liquids, with water, 2 M AcOH and H_3PO_4 solution, (c) with different concentrations of AcOH solution, and (d) with H_3PO_4 solution 87

Figure 4.4 SEM microstructure images (fractured surface) of HAp202 powder cold sintered at 200 °C (a) without using liquids, (b) with H_2O, (c) with 2 M AcOH solution, and (d) with 2 M H_3PO_4 solution 89

Figure 4.5 (a) X-ray diffraction patterns of cold sintered HAp202 powder with H_2O, ([0.5 & 2 M]) AcOH & H_3PO_4 solution, (b) Thermogram of cold sintered HAp202 powder using H_2O, [2 M] AcOH & H_3PO_4 solutions. FTIR patterns plotted (c) between wavenumber range 4000 to 1250 cm^{-1}, and (d) between wavenumber range 1250 to 530 cm^{-1} 92

Figure 4.6 (a) Lattice parameters along the a & c-axis, and (b) Ca/P ratio values for the HAp202 powder and its cold sintered samples with H_2O, 2 M AcOH, and 2 M H_3PO_4 ... 94

Figure 4.7 Volumetric shrinkage profile of cold-sintered HAp202_600 and HAp202_900 powders under 360 MPa at 200 °C using 2 M H_3PO_4 96

Figure 4.8 (a & b) Comparative XRD patterns for the HAp202 calcined powders (600 & 900 °C) and cold sintered calcined HA powders at 200 °C using 2 M H_3PO_4 solution, respectively. Microstructure of cold sintered (c) HAp202_600 powder and (d) HAp202_900 powder 97

Figure 4.9 Relative linear shrinkage profile measured from the relative changes in the sample length during the CSP of HA without liquid, with H_2O, and with 2 M H_3PO_4. (Inset) Corresponding in-situ sample image frames of particular temperature intervals 99

Figure 4.10 (a) Overall in-situ Raman spectra acquired every 60 s during CSP of HA with 2 M H_3PO_4 (T = 200 °C). At this acquisition rate, each spectrum during the heating ramp corresponds to ~5 °C; spectra were also recorded during the isothermal holding (10 min) and cooling cycle (to 50 °C). (b) Selected spectra at specific temperatures spanning the heating and cooling stages. (c) Relative intensity of the HPO_4^{2-} bands normalized to the main PO_4^{3-} band (962 cm^{-1}). The dashed line in the inset indicates the temperature segments; each data point corresponds to a spectrum shown in panel (a) 100

Figure 4.11 XRD patterns of (a) HA powder (HAp202), (b and c) HA powder mixed with 2 M H_3PO_4 solution before and after heating treatment, respectively. The heat treatment was carried out in powder form at 200 °C (5 °C/min, 10 min isothermal holding) 102

Figure 4.12 Schematic illustration of the densification mechanism that occurs during the cold sintering of HA 103

Figure 4.13 Schematic illustrations of (a) HA crystal structure and (b-c) two models of ion substitution and formation of H-bonding in HA during CSP (since Ca^{2+} ions are not involved in ion substitution and formation of H-bonding, they are not shown in diagrams (b) and (c)) 104

Figure 5.1 (a) SEM morphology, (b) XRD pattern, (c) particle aggregate size distribution, and (d) thermogram of the sol-gel derived 50S BG powder 110

Figure 5.2 (left) SEM microstructure image and (right) X-ray diffraction patterns of conventionally sintered 50S BG at 1000 °C 111

Figure 5.3 (a) Comparison of total volume shrinkage profile (displacement vs time) obtained during the CSP of BG under 360MPa at 200 °C using different transient liquids and (b) the calculated average relative density values of the densified 50S BG corresponding to transient liquids 113

Figure 5.4 (a) XRD patterns and (b) FTIR spectrum (wavenumber 1830-520 cm^{-1} with inset image (wavenumber 4000-2400 cm^{-1})) of the 50S BG after CSP with different transient liquids 114

Figure 5.5 SEM microstructure images (fractured surface) of the cold sintered 50S BG at 200 °C/ 360 MPa (a) without liquid, (b) with H_2O, (c) with 2 M NaOH solution, and (d) with 2 M H_3PO_4 solution 117

Figure 5.6 SEM microstructure images (fractured surface) of the HA+10BG sample cold sintered (a_{1-3}) without transient liquid and (b_{1-3}) with 2 M H_3PO_4 solution 120

Figure 5.7 XRD patterns of the cold sintered HA+10BG composite samples without transient liquid and with 2 M H_2PO_4 solution 121

Figure 5.8 Relative linear shrinkage profile measured from the relative changes in the sample length during the CSP of BG without liquid, with H_2O, and with 2 M H_3PO_4. (Inset) Corresponding in-situ sample image frames of particular temperature intervals 123

Figure 5.9 (a) Overall in-situ Raman spectra acquired every 60 s during CSP of BG with 2 M H_3PO_4 (200 °C/250 MPa). At this acquisition rate, each spectrum during the heating ramp corresponds to ~5 °C; spectra were also recorded during the isothermal holding (10 min) and cooling cycle (to 50 °C). (b) Selected spectra at specific temperatures spanning the heating and cooling stages. (c) Temperature-dependent relative intensity of the HPO_4^{2-}), and PO_4^{3-} bands. The dashed line in the inset indicates the temperature intervals; each data point corresponds to a spectrum shown in panel (a) 124

Figure 5.10 XRD patterns of (a) HA powder (HAp202), (b and c) HA powder mixed with 2 M H_3PO_4 solution before and after heating treatment, respectively. The heat treatment was carried out in powder form at 200 ºC (5 ºC/min, 10 min isothermal holding) 126

Figure 6.1 (a) Relative density values of the compacted and cold sintered samples, and (b) volume shrinkage profile recorded in terms of total displacement versus time during the cold sintering of the composite under 360 MPa 132

Figure 6.2 Cold sintered composites microstructure (polished surface); (a_1&a_2) 80:20 fraction captured in SE mode at magnification 110Kx / 150Kx, (b_1-d_1) and (b_2-d_2) correspond to 70:30, 60:40, and 50:50 fractions captured in BSE mode at magnification 2Kx and in SE mode at 150Kx magnification, respectively 133

Figure 6.3 FIB cross-sectioned SEM micrographs of (a_1 & a_2) 80:20 captured at a magnification of 3Kx / 100Kx, and (b_1 & b_2) 70:30 fraction captured at a magnification of 5Kx / 50Kx 134

Figure 6.4 (a) DSC thermograms of the TBC plasticized PLA, (b) volume shrinkage profile of the compact recorded in terms of total displacement versus time during the cold sintering of the composite made with plasticized PLA under 360 MPa, and (c) Relative density values of cold sintered composites made with plasticized PLA 136

Figure 6.5 (a_1&a_2) Microstructure of the cold sintered composite (polished surface); HA:20TBC/PLA 80:20 fraction captured in SE mode at magnification of 110Kx & 150Kx 137

Figure 6.6 (a) Microstructure of the HA matrix after extracting the PLA from cold sintered HA: PLA 80:20 and (b) HA:20TBC/PLA 80:20 composite. The SEM images were captured in SE mode at a magnification of 150Kx 138

Figure 6.7 (a) DSC thermogram, (b) XRD patterns, and (c and d) FTIR plot of the HA:PLA 80:20 composite made with unplasticized and 20TBC-plasticized PLA 139

Figure 6.8 (a) DSC thermogram, (b) XRD patterns, and (c and d) FTIR plot of the HA:PLA 70:30, 60:40, 50:50 composites made with unplasticized PLA 141

Figure 6.9 (a) Stiffness/hardness values for cold sintered composites made with unplasticized PLA and (b) 80:20 composite made with TBC-plasticized PLA 142

Figure 6.10 Relative linear shrinkage profile measured from the relative changes in the sample length during the CSP of HA:PLA (80:20 wt.%) composite without liquid. (Inset) Corresponding in-situ sample image frames of particular temperature intervals 143

Figure 6.11 (a) Overall in-situ Raman spectra acquired every 60 s during CSP of HAPLA (80:20 wt.%) composite without liquid (T = 200 ºC). At this acquisition rate, each spectrum during the heating ramp corresponds to ~5 ºC; spectra were also recorded during the isothermal hold (10 min) and cooling cycle (to 40 ºC). (b) Selected spectra (only PLA bands) at specific temperatures spanning the heating and cooling stages 144

Figure 6.12 Temperature-dependent relative intensity changes of PLA and HA bands. The dashed line in the inset indicates the temperature intervals; each data point corresponds to a spectrum shown in Fig. 6.10 (a) 146

List of Tables

Table 2.1 Definitions of relevant properties for bone graft materials 33

Table 2.2 Widely studied synthetic bioactive materials and their key properties..... 35

Table 2.3 summarizes the fabrication techniques used to develop HA-PLA composites, along with their corresponding HA content and achieved elastic modulus values..... 41

Table 2.4 List of non-conventional sintering techniques, including brief descriptions, sintering variables explored, and the resulting characteristics of HA ceramics 49

Table 2.5 Summary of the selected functional materials densified using CSP, along with the parameters tested, and the densification outcome 56

Table 2.6 Summary of the reported bioactive materials densified using CSP 61

Table 2.7 Summary of the bioactive ceramic-polymer composite materials consolidated via CSP, along with the reported parameters and consolidation outcome 64

Table 4.1 Physical properties of commercial HA powders (HAp201 & HAp202) 83

Table 4.2 Comparison of mechanical properties of conventionally-sintered and cold sintered HAp202 samples 91

Table 4.3 Physical properties of the calcined HAp202 powders (600 & 900 °C)..... 95

Table 5.1 Comparison of physical/mechanical properties of BG samples after CSP . 118

Table 5.2 Comparison of physical/mechanical properties of cold sintered HA-BG and HA samples 119

Table 6.1. DSC parameters of PLA and TBC plasticized PLA 135

Chapter 1: General Introduction

1.1 Background

Bioactive materials play a pivotal role in clinical orthopedic applications due to their ability to facilitate bone regeneration by supporting cell adhesion, proliferation, and differentiation [1-4]. Indeed, the natural bone possesses a remarkable regenerative capacity, allowing most fractures to heal without complications when treated appropriately. However, critical-size defects such as severe fractures with infections or trauma-induced segmental bone loss surpass the bones' inherent regenerative potential [4-9]. These problems are even more challenging in older individuals with limited regenerative potential, often leading to further complications [3, 8, 9].

In such challenging scenarios, it becomes essential to develop safe and reliable bone substitute graft materials that are available in sufficient quantities and capable of supporting the regeneration of bone defects [7-12]. Traditional clinical orthopedic treatments often rely on materials like autologous/allogenic bone grafts, which are considered the gold standard because of their excellent biological properties, including biocompatibility, bioactivity, osteoconductivity, osteoinductivity, and bioresorbability. However, these options have significant restrictions, such as the limited volume of bone that can be safely harvested and the risk of donor-site complications, including immune rejection [11-15]. These drawbacks have fueled the interest in the development of synthetic bone grafts as a promising alternative solution.

Over the past few decades, significant advancements in materials science, nanotechnology, and processing techniques have greatly expanded the design space for nanosized bioactive to biodegradable materials, including bioceramics, bioglass, and biopolymers, which all offer highly customizable biological properties. The optimal performance of these materials is largely determined by their chemical composition and intrinsic characteristics [8, 10, 16, 17]. Developing synthetic bone grafts with ideal biological and mechanical properties suitable for critical-sized bone defects remains a dynamic area of research [8, 10, 17-19]. Although bioactive materials possess relevant

biological properties, their ultimate performance is critically influenced by the processing and manufacturing methods employed, whether in the form of ceramic-based grafts or ceramic-polymer composites.

Among the various bioactive materials being explored for the development of ceramic-based grafts, hydroxyapatite (HA) and bioglass have been considered as promising candidates. Nano hydroxyapatite ($Ca_{10}(PO_4)_6(OH)_2$) (HA), in particular, has garnered extensive attention due to its excellent bioactivity, osteoconductivity, and chemical similarity to the mineral component of human bone, making it a widely studied bioactive ceramic in bone regeneration and tissue engineering applications [8, 20-23]. In parallel, bioglass, especially ternary silica-based (SiO_2-CaO-P_2O_5) sol-gel derived systems, has received significant interest for its distinctive characteristics. This includes a high dissolution rate that facilitates rapid bonding with bone through the formation of a hydroxycarbonate apatite layer, thanks to its amorphous nature, and the flexibility to tailor its composition for specific clinical needs, as well as controllability over the rate of bonding with bone tissues [24-28].

Traditionally, both HA and bioglass are consolidated via high-temperature sintering (≥1200 °C) to effectively enhance their mechanical strength. This often alters crystallinity, induces uncontrolled grain growth, crystallization of bioglass, and secondary phase formation or decomposition, which negatively affects their biological activities [29-33]. Despite the drawbacks associated with conventional high-temperature sintering, the intrinsic brittleness of HA or bioglass further limits their use as standalone materials in load-bearing applications [7-10]. This limitation has prioritized developing composite-based graft materials as a more viable and effective alternative, which is logically inspired by natural bone; a nanocomposite primarily composed of collagen (organic phase) and apatite crystals (inorganic phase) [8-10]. Thus, creating synthetic grafts that integrate both ceramic and polymer phases holds significant promise for treating critically sized bone defects. These composites not only support bone ingrowth but also enable the gradual resorption and replacement of the implant by newly formed bone tissue [6-8].

Designing a composite graft material that mimics the structural and mechanical complexity of bone remains a significant challenge, particularly in achieving a synergistic integration between the stiffness of the ceramic phase and the toughness, flexibility, and

bioresorbability of the polymer matrix. Synthetic polymers are frequently explored as potential organic matrices due to their chemical versatility, which allows for highly tunable degradation rates and mechanical properties [8,9, 34-36]. Hydroxyapatite (HA), owing to its superior mechanical properties compared to bioglass, is commonly employed as the inorganic filler in composite-based graft development. However, the full potential of HA's stiffness is rarely realized, as it is typically incorporated in limited volume fractions within polymer matrices [36-39].

Among synthetic polymers, poly(L-lactic acid) (PLA) is particularly appealing for bone regeneration applications due to its biodegradability, adjustable thermal properties, and FDA-approved status as a semi-crystalline polyester [35-39]. Numerous studies have concentrated on developing HA-PLA composite graft materials through various fabrication techniques such as chemical cross-linking, solvent casting, injection molding, and 3D printing [34-37]. These methods have facilitated the creation of composites that mimic the hierarchical structure of natural bone. However, only modest advancements have been made in achieving mechanical properties that are satisfactory and align with those of natural bones. Ongoing challenges include limited ceramic loading, poor dispersion, and weak interfacial bonding between the polymer and ceramic phases [38-42]. Furthermore, current processing techniques are not sufficiently effective in consolidating the HA phase within the PLA matrix, which is crucial for attaining the desired mechanical strength.

HA generally requires high-temperature sintering to improve its mechanical integrity. However, the HA-PLA composite fabrication techniques operate at temperatures near the melting point of PLA (~180 ℃). This notable temperature mismatch renders co-sintering HA with PLA impractical. Consequently, conventional high-temperature sintering methods cannot maintain material integrity and preserve the functional properties of bioactive ceramics.

Recognizing these limitations has sparked interest in innovative low-temperature sintering technologies as promising alternatives for processing the bioactive materials. These approaches aim to retain the intrinsic properties of the bioactive components while enabling effective consolidation at temperatures compatible with polymer matrices. Within this framework, the present thesis explores the potential and

fundamentals of a novel low-temperature sintering technique known as the cold sintering process (CSP), which offers a viable pathway for processing bioactive materials.

1.2 Context and Motivation

The cold sintering process, an emerging low-temperature sintering technique, has recently garnered attention for its ability to consolidate ceramic materials at significantly lower temperatures, typically below 300 °C, under the application of pressure [43-47]. This capability presents new opportunities for co-sintering ceramic-polymer phases with high ceramic fraction [46-50]. Thus, CSP offers a transformative solution to the challenges associated with high-temperature sintering techniques, while preserving the functional properties and materials integrity [49,48, 51-55].

CSP is straightforward to implement on a standard laboratory scale and has been successfully applied to various materials, including dielectric ceramics/composites, solid-state batteries and electrolytes, and flexible electro-ceramic devices [57-60]. However, limited research has explored the fundamentals of the cold sintering process in processing bioactive ceramics and composite systems. To expand the application of cold sintering technology in synthetic grafts for bone regeneration, several fundamental research gaps must be addressed, including optimizing processing parameters, understanding the underlying mechanisms, and evaluating the material properties.

Within the EUNICE alliance, under the auspices of the University of Mons and the Polytechnic University of Hauts-de-France, this thesis aims to strengthen collaborative research on the 'cold sintering process of bioactive materials'. The outcomes are expected to contribute to the persisting fundamental research gap in cold sintering of bioactive materials, offering insights that could support advancing the CSP for designing synthetic implants.

1.3 Thesis Outline

This thesis is structured as follows:

- **Chapter 2: State-of-the-art** - provides a comprehensive introduction to bone biology and a review of current bioactive materials relevant to bone regeneration. The various fabrication methods employed in the development of these materials are examined, with particular emphasis on their limitations and associated challenges. Subsequently, the chapter explores sintering science, emerging low-temperature techniques with a special focus on the cold sintering process and its application to bioactive materials processing.
- **Chapter 3: Materials and Methods** - Outlines the experimental procedures and setup used for the cold sintering process. It presents the in-situ experimental setup employed for in-situ observations and characterizations during cold sintering. Then, the materials used and characterization techniques applied to evaluate the cold-sintered samples are detailed.
- **Chapter 4-6: Results and Discussion** - Details the findings on the evaluation of cold-sintered hydroxyapatite ceramics, ternary silica-bioglass system, and HA-PLA composites. It includes an in-depth analysis of the cold sintering mechanism, the influence of various processing parameters on densification, and the resulting physical/mechanical properties of the materials. Furthermore, the underlying dynamics of the CSP mechanisms are examined with in-situ observations and in-situ Raman analysis, providing insights into the underlying densification behavior during the process.
- **Chapter 7: Conclusions and Future Work** - Summarizes the key contributions of the research and outlines potential directions for future studies.

By addressing the challenges associated with traditional sintering methods and harnessing the potential of cold sintering, this thesis will pave the foundation for innovative material solutions in the bioactive materials domain.

Chapter 2: State-of-the-art

2.1 Bone Tissue and Need for Bioactive Materials

2.1.1 Structure and Function of Bone

Understanding the intricate structure and composition of bone tissue is crucial for a better understanding of its biology and for selecting and developing materials to support bone regenerative applications. Bone tissue is a rigid, dynamic, and vascularized structure that provides structural support, enables movement, and protects vital organs [61-66]. These extraordinary functions are rooted in its hierarchical architecture and complex composition, as illustrated in Fig. 2.1.

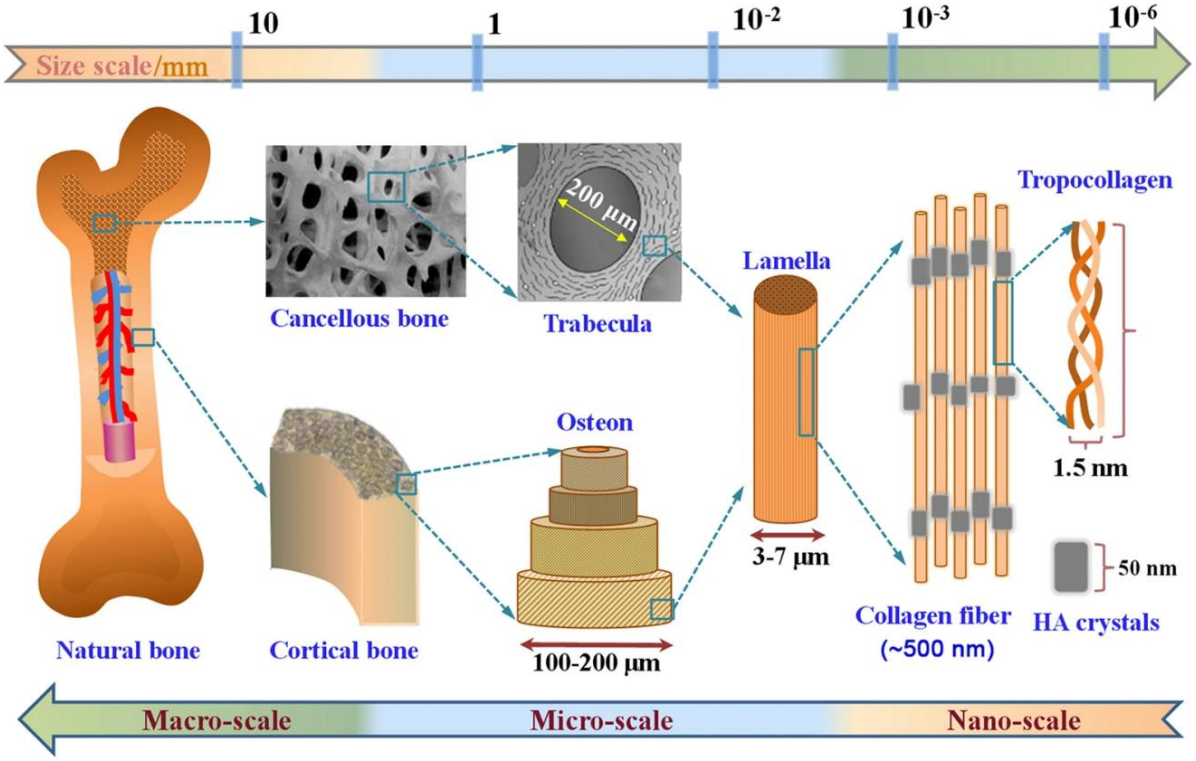

Figure 2.1 *The chemical composition and multi-scale structure of natural bone [66].*

In terms of composition, natural bone is a composite material comprising organic and inorganic phases. The organic phase, accounting for 10-25 wt.%, primarily consists of type I collagen, which imparts toughness to the bone. The inorganic phase constitutes approximately 60-70 wt.% and is predominantly composed of non-stoichiometric nano hydroxyapatite crystals ($Ca_{10}(PO_4)_6(OH)_2$) substituted with various ions, including sodium

(Na^+), potassium (K^+), magnesium (Mg^{2+}), fluoride (F^-), chlorine (Cl^-), carbonate (CO_3^{2-}), and trace elements such as silicon (Si), strontium (Sr), iron (Fe), zinc (Zn), and copper (Cu). The bone apatite has a Ca/P ratio between 1.5 and 2, depending on bone site and substitutions [64-67].

At the macro level, structurally, natural bone exhibits a multi-scale organization and can be divided into cortical bone and cancellous bone. Cortical bone, located on the surface, constitutes 80 wt.% of the total skeletal mass. It is dense and strong, with a low porosity of 5-10 %, providing the strength required for load-bearing and mechanical stability. Its compressive strength, fracture toughness, and elastic modulus of cortical bone range from 100-200 MPa, 2-12 $MPa \cdot m^{1/2}$, and 7-30 GPa, respectively [67-70]. In contrast, cancellous bone, also known as trabecular or spongy bone, is found within the interior of bones. It is characterized by an interconnected network of lamellar trabeculae, which house hematopoietic cells, adipose tissue, and blood vessels. Although cancellous bone comprises only 20 wt.% of skeletal mass, its high porosity (50-90 %) supports vital metabolic functions like calcium exchange and bone marrow storage. The compressive strength, fracture toughness, and elastic modulus of cancellous bone are within 2-12 MPa, 0.1-0.8 $MPa \cdot m^{1/2}$, and 0.2-0.5 GPa, respectively [67, 70-73].

Fundamentally, bone is a hierarchically organized composite material, with mineralized collagen fibrils serving as its primary building blocks. At the nanoscale, the reinforcement of plate-like HA crystals, approximately 50×25×3 nm in size, within the collagen matrix provides hardness and compressive strength. However, the exact spatial and molecular organization of collagen and mineral phases at the nanoscopic level remains incompletely characterized, reflecting the inherent complexity of bone tissue [72-75].

2.1.2 Bone Healing and Challenges

Bone, with its unique multi-scale hierarchical structure, undergoes continuous remodeling throughout life, driven by mechanical and hormonal stimuli [10, 74, 75]. The bone remodeling process endows bone with an intrinsic capacity for regeneration, enabling it to heal effectively when injured or fractured. Fig. 2.2 illustrates the biological events and remodeling activities during bone fracture healing. This dynamic process is highly complex and involves the coordinated activity of multiple cell types. Osteocytes,

the primary mechano-sensors within the bone, aid in detecting mechanical signals and orchestrating the activity of regulatory factors such as osteoblasts and osteoclasts. Osteoblasts are responsible for bone formation, synthesizing and mineralizing new bone matrix, while osteoclasts mediate bone resorption by breaking down old or damaged bone tissue [76-81]. Bone lining cells, which cover inactive bone surfaces, appear to participate in the transition between resorption and formation, contributing to the seamless integration of these processes and maintaining skeletal integrity [77-81].

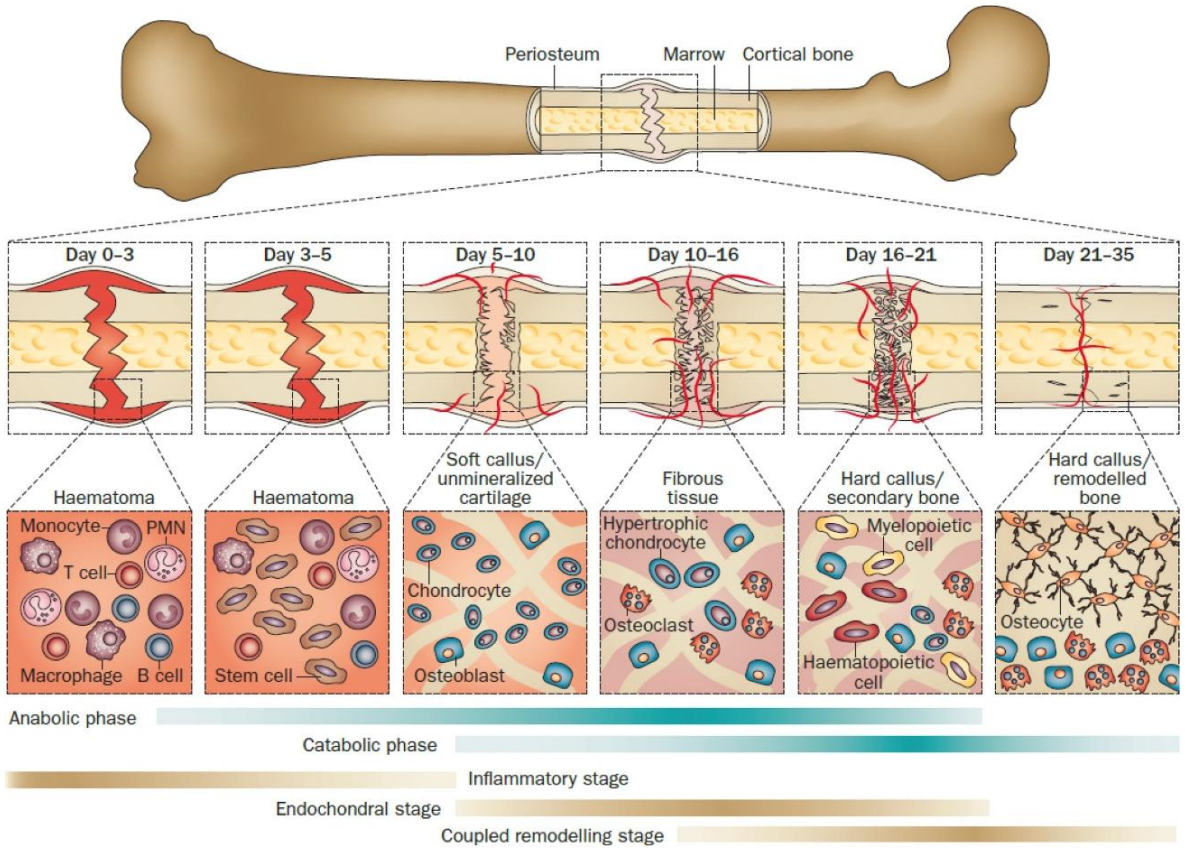

Figure 2.2 *Illustration of a typical fracture healing process, biological events, and cellular activities at different phases [11].*

Bone fractures with a gap of less than 0.1 mm undergo successful healing through continuous ossification and subsequent Haversian remodeling, with the absence of cartilaginous or connective tissue. When the fracture edges are less than twice the diameter of the bone, healing occurs via a well-coordinated sequence of biological events. This process involves blood clotting, bone induction and conduction, engaging various cell types and intricate intracellular and extracellular molecular signaling

pathways [80-82]. Together, these mechanisms drive skeletal repair and restore the bone's structural integrity and functional capacity.

Despite the bone's intrinsic healing capacity, certain conditions can significantly impair its natural ability to regenerate. It includes critical-sized segmental fractures (those exceeding 2 to 2.5 times the diameter of the affected bone), congenital deformities, tumors, and age-related decline in regenerative potential [6, 81, 82]. Addressing such non-union defects often requires external stimulation through medical interventions designed to promote the healing process artificially. In such scenarios, bone grafts serve as essential therapeutic solutions, providing structural support and promoting tissue regeneration [6, 12-13]. These approaches present substantial challenges, including prolonged treatment durations, high postoperative care costs, and significant surgical, socioeconomic, and research hurdles [8-10, 15, 83]. Therefore, developing effective and affordable solutions for these cases remains a critical priority in regenerative medicine and orthopedic research. A key focus lies in creating bone grafts that are not only available in large volumes but also possess the essential properties of biocompatibility, biodegradability, and sufficient mechanical strength to support successful integration and functional recovery [7-9, 13-14].

2.1.3 Need for Synthetic Bone Grafts

Bone grafting, being a conventional orthopedic surgical procedure, utilizes natural bone graft materials, such as autografts, allografts, and xenografts, which are primarily valued for their combined mechanical support and biological properties [7-9, 84]. The key characteristics of bone grafting materials are summarized in Table 2.1.

Autologous bone grafts are harvested from one anatomical site and transplanted to another within the same individual. Due to their excellent biological properties (as detailed in Table 2.1), autogenous bone is considered the 'gold standard' for repairing bone defects. However, autografts have notable drawbacks related to the harvesting process, including donor site complications, increased operative time, potential donor site infections, and a limited volume of available material [10, 15, 84, 85]. To address these limitations, allogeneic bone grafts have been developed. These grafts are bone tissue harvested from one individual and transplanted into a genetically different

individual of the same species. Allografts have proven effective in clinical practice, particularly for patients with poor healing potential, established nonunion, or extensive comminution following fractures. Despite their advantages, allografts also have limitations, including insufficient supply, ethical concerns, and immunogenicity. Notably, the risk of immunological rejection can delay healing and increase the likelihood of infections or disease transmission [10, 15, 84-86]. The use of xenografts: bone grafts derived from animals, particularly bovine sources, has also been explored due to their structural similarity to human bone. However, xenografts face significant challenges, including potential pathogenicity and ethical considerations, which have limited their clinical adoption [87-89].

Table 2.1 *Definitions of relevant properties for bone graft materials.*

Key properties	Definition
Biocompatibility	The ability to perform with an appropriate host response in a specific situation [90, 91].
Bioactivity	The ability to form a direct chemical bond with bone, and thus a uniquely strong biomaterial interface [92].
Osteointegration	The ability to anchor with the formation of bony tissue around the implant at the bone-implant interface [93, 16].
Osteoconduction	The ability to support the attachment of bone cells and allow their migration and ingrowth within the graft [93, 16].
Osteoinduction	The ability to induce bone formation by influencing the differentiation of stem cells into bone-forming cells [93, 16].
Biodegradability	The ability to gradually vanish and leave space for new tissue growth without hindering the regeneration process [7, 94].
Mechanical performance	The ability to offer an optimal balance of stiffness and strength that supports cellular growth, withstands tractional forces, and adapts to changes in the surrounding tissue environment [7, 95].

The serious shortage of natural bone grafts, along with the increasing demands of an aging population, has spurred the need for synthetic bone graft materials. Additionally, the global market has witnessed rising interest in synthetic bone grafts, with a projected

compound annual growth rate (CAGR) of 6.5 % from 2024 to 2034. Currently, Europe commands 29 %, while the United States and Asian markets comprise 60 % of the market share [96]. Efforts are progressing to develop innovative bioactive materials and fabrication techniques to supplement the growing demand for bone regeneration solutions driven by a growing global population.

2.2 Bioactive Materials and Fabrication Challenges

2.2.1 Synthetic Biomaterials for Bone Regeneration

Synthetic biomaterials have revolutionized bone regenerative medicine by offering scalable, customizable solutions that significantly improve patient outcomes [7-11]. These materials have evolved through three consecutive generations, with each generation reflecting targeted improvements in properties and functionalities essential for bone regeneration [7, 8]. The 1st generation biomaterials (Titanium alloys, alumina, zirconia, polyether ether ketone (PEEK)) are bioinert and designed to offer only mechanical support. The 2nd generation biomaterials (bioglass, calcium phosphates) are biologically responsive, encompassing bioactive, osteoconductive, and biodegradable properties. The 3rd generation biomaterials are enriched versions of 2nd generation biomaterials with bioinstructive elements, such as cells and growth factors, capable of 'instructing' the biological healing process [7, 97, 98].

From a materials science perspective, synthetic bioactive materials, such as bioceramics, bioglass, and biopolymers, are commonly studied for the development of synthetic bone grafts [7-11]. Currently, a broad spectrum of those synthetic bioactive nanomaterial options (as detailed in Table 2.2) has been extensively researched for developing synthetic grafts due to their intrinsic biological properties, such as biocompatibility, bioactivity, osteoconductivity, and bioresorbability [8-11, 97-99]. These properties allow them to mimic the natural bone healing process by facilitating cell adhesion, proliferation, and differentiation mechanisms.

Table 2.2 *Widely studied synthetic bioactive materials and their key properties.*

Biomaterials		**Properties**
Bioceramics	Hydroxyapatite	Bioactive, osteoconductive, osteoinductive, high mechanical strength, & slow resorption [102, 103].
	β-Tricalcium phosphate	Bioactive, osteoconductive, osteoinductive, good mechanical strength, & moderate resorption [102,103].
	Amorphous calcium phosphate	Bioactive, osteoconductive, osteoinductive, low mechanical strength, & fast resorption [102, 104].
	Biphasic calcium phosphate	Bioactive, osteoconductive, osteoinductive, good mechanical strength, & moderate resorption [105, 106].
Bioglass	Silicate based	Bioactive, osteoconductive, osteoinductive, high mechanical strength, & rapid degradation [24, 107, 108].
	Borate based	Bioactive, osteoconductive, osteoinductive, good mechanical strength, & rapid degradation [107, 110].
	Phosphate based	Bioactive, osteoconductive, osteoinductive, low mechanical strength, & fast degradation [107, 110].
Biopolymers	Polylactic acid	Good biocompatibility, tunable biodegradability, & high mechanical strength [34-36].
	Polyglycolic acid	Good biocompatibility, high biodegradability, & high mechanical strength [101, 111].
	Polylactic-co-glycolic acid	Good biocompatibility, high biodegradability, & tunable mechanical strength [101, 112, 113].
	Polycaprolactone	Good biocompatibility, slow biodegradability, & good mechanical strength [101, 114].

Given the composite and hierarchical structural features of natural bone, current research focuses on replicating its nanostructured mineralized matrix by engineering ceramic-polymer composites. Such composites combine the strength and stiffness of ceramics with the flexibility and biodegradability of polymers, enabling synergistic performance [99-101]. Notably, designing composites with high ceramic content, mirroring the mineral fraction of natural bone, remains a key strategy for balancing mechanical strength with desirable biological behavior [13-15].

Despite advances in bioactive materials, achieving the optimal biological performance and mechanical properties of native bone remains challenging, largely due to limitations in current fabrication technologies. Effective bone substitutes must offer balanced stiffness and strength to support cellular growth, withstand physiological loads, and integrate with the surrounding tissue environment [17-19]. Research at the intersection of nanotechnology, materials science, and fabrication methods has expanded substantially over recent decades and remains active, with the goal of producing synthetic grafts with optimized biological and mechanical performance [8, 100, 101]. This thesis focuses on nano-hydroxyapatite ceramics, bioglass, and hydroxyapatite–polylactic acid composites as promising candidates for bone regeneration. The following sections discuss the key properties, advantages, limitations, and fabrication challenges of these bioactive materials.

2.2.2 Hydroxyapatite Bioceramics

Hydroxyapatite ($Ca_{10}(PO_4)_6(OH)_2$) is the most commonly encountered bioceramic, owing to its high biocompatibility, bioactivity, osteoconductivity, and osteoinductivity [102, 103]. Stoichiometric synthetic HA has a hexagonal crystal structure with a Ca/P ratio of 1.67. Interestingly, its chemistry and composition are identical to the mineralized phase of natural bone, and the apatite formation on its surface also has a similar composition to natural bone, promoting strong bonding with bone tissue. However, HA's high Ca/P ratio and crystallinity make it very stable under physiological conditions, slowing its degradation and resorption rate. Although HA exhibits good mechanical strength, studies report that delayed resorption can reduce its initial mechanical properties after implantation over several months [11, 21].

Advancements in nanocrystalline hydroxyapatite (HA) have partially addressed the aforementioned drawbacks, as its larger surface-to-volume ratio enhances the resorption rate. Nano-HA also exhibits significantly more grain boundaries than its micro counterpart. These grain boundaries introduce unique surface characteristics, including distinct topography, surface energy, roughness, and wettability, which can substantially influence cell behavior [11, 22, 23]. However, the fabrication of nano-HA through traditional high-temperature sintering (>1000 °C) presents challenges in controlling grain size, crystallinity, and physicochemical properties [29, 30].

Sintering is required to achieve the densification as well as to improve the mechanical properties of HA implants. For instance, depending on sintering temperatures between 1000 and 1300 °C, HA can reach flexural (three-point bending) strength of ~40-150 MPa and compressive strengths of ~100-180 MPa [115-117]. However, higher temperatures typically increase crystallinity, drive uncontrolled grain growth, and promote secondary phase formation or decomposition, all of which can diminish biological performance [29, 30]. Multiple studies show that density, hardness, and flexural strength increase as the sintering temperature rises from ~900 to 1300 °C in air; above ~1300 °C, HA tends to decompose into tricalcium phosphate and tetracalcium phosphate [29, 115-118]. The increase in hardness values with respect to temperature attributed to the increase in the crystallinity of HA [115-118]. In addition, the intrinsic brittleness of HA sintered at high temperatures limits its standalone use as an implantable material at load-bearing sites [29, 115-117].

2.2.3 Ternary Bioglass

Bioglass represents a distinct class of bioactive materials primarily composed of silica (SiO_2), sodium oxide (Na_2O), calcium oxide (CaO), and phosphorus pentoxide (P_2O_5). Owing to their amorphous structure, bioglasses rapidly form a hydroxycarbonate apatite (HCA) layer on the surface, enabling chemical bonding with bone. They are particularly notable for their unique ability to integrate with both hard and soft tissues in the human body [25-28, 108]. The general mechanism of HCA layer formation on the bioglass surface is illustrated in Fig. 2.3.

Since their introduction by L. Hench et al. in 1969, bioglasses have been synthesized in various compositions using multiple fabrication techniques, drawing substantial interest, especially in bone tissue engineering and regeneration [24]. The most commonly utilized bioglasses in clinical settings are Bioglass® 45S5 (46.1 mol% SiO_2, 24.4 mol% Na_2O, 26.9 mol% CaO, and 2.6 mol% P_2O_5) and S53P4 (53.8 mol% SiO_2, 21.8 mol% CaO, 22.7 mol% Na_2O, and 1.7 mol% P_2O_5), both silicate-based compositions typically produced via melt-quenching [119,120]. These formulations contain relatively high concentrations of Na_2O, which act as fluxing agents, facilitating early crystallization during high-temperature sintering (>600 °C). However, this early crystallization reduces the rate of ion release, consequently slowing the HCA layer formation by a factor of three to four [25, 32, 33].

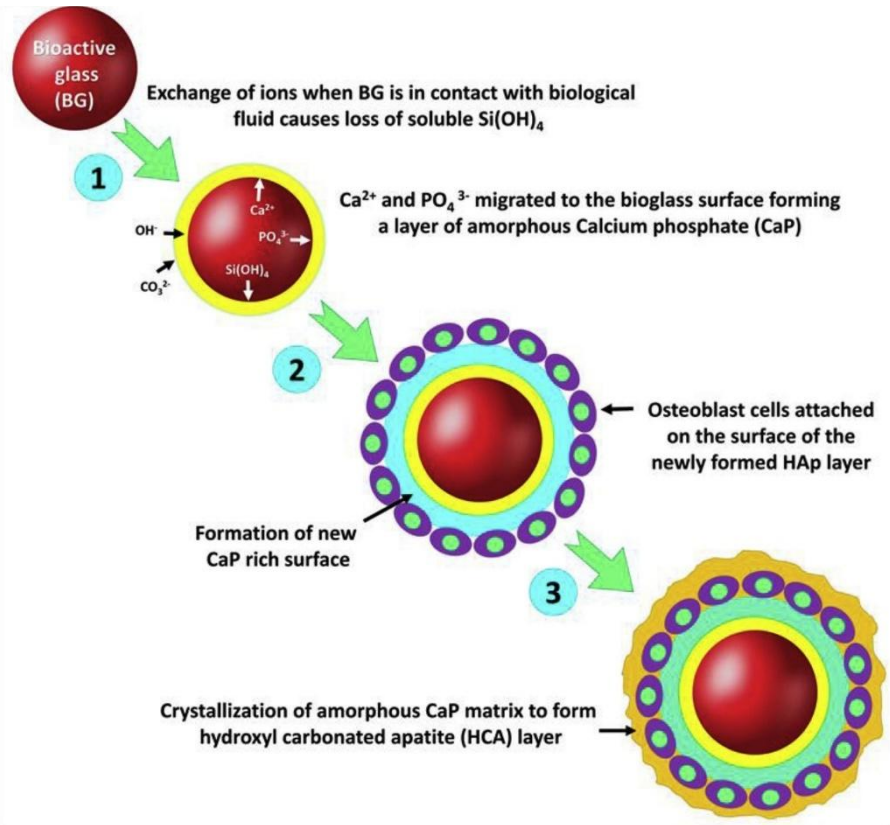

Figure 2.3 *General mechanism of apatite formation on the surface of bioactive glass [117].*

The ternary SiO_2-CaO-P_2O_5 glass system is another attractive alternative to traditional melt-derived bioglasses [19]. These compositions offer enhanced processing flexibility, improved thermal stability, and broader compositional tunability. Unlike 45S5-type bioglasses, ternary systems typically exclude alkali oxides, resulting in higher network

connectivity and greater resistance to devitrification. The first ternary bioglass, with a silica content ranging from 50 to 95 mol%, was developed by Li et al. in 1991 via the sol-gel method [25]. This technique provides several advantages over melt-quenching, including lower processing temperatures, high chemical purity, a broad alkali-free compositional range, and reduced processing steps and time. In contrast to melt-quenching, sol-gel synthesis does not require additional steps such as grinding, fritting, polishing, or sieving [25]. However, ternary systems also present certain limitations; especially, the bioactivity and sinterability of sol-gel-derived ternary bioglasses are highly composition-dependent. Research suggests that an optimal composition, typically around 50-55 mol% SiO_2, 40-45 mol% CaO, and 4-5 mol% P_2O_5, strikes a balance between glass-forming ability and biological performance [25-28].

Besides their exceptional bone-bonding capabilities, the fabrication of implants from both melt- and sol-gel-derived glasses typically requires high-temperature sintering (>600 °C) to achieve sufficient densification [32, 33]. Conversely, high sintering temperatures accelerate crystallization (devitrification), which negatively impacts bioactivity, rendering bioglasses unsuitable for load-bearing applications.

2.2.4 Hydroxyapatite-Polylactic acid (HA-PLA) Composite

Composite strategies offer a promising approach to overcoming the limitations of individual biomaterials by combining their advantageous properties [7-9, 99]. In particular, ceramic–polymer composites are highly attractive for bone tissue engineering, especially treating critical-sized bone defects, as they can function as temporary scaffolds that support new bone formation and gradually degrade in vivo, thus eliminating the need for a second surgical procedure to remove the implant [99, 121-123]. Among bioceramics, HA is one of the most widely studied due to its excellent biocompatibility, bioactivity, and chemical similarity to the mineral component of natural bone. When combined with a suitable polymer matrix, HA can help produce composites that not only mimic the composition and hierarchical structure of bone but also exhibit improved mechanical and biological properties [124-126].

One of the key challenges in developing such composites lies in selecting an appropriate polymer matrix that complements HA. The ideal polymer should offer mechanical

flexibility, ease of processing, and a controllable biodegradation profile while supporting HA's bioactivity. In recent decades, synthetic polymers have gained substantial attention for this purpose, thanks to their tunable chemical structure, reproducibility, and regulatory approval. Compared to natural polymers such as chitosan and collagen, synthetic alternatives also offer more predictable degradation behavior and are more amenable to large-scale production [99, 127, 128].

Polylactic acid (PLA), a synthetic aliphatic polyester derived from renewable plant resources, is particularly notable in this context. Furthermore, PLA's eco-friendly production from renewable, non-toxic feedstocks like sugarcane and corn starch enhances its suitability for human body applications. It is also classified as "generally recognized as safe" (GRAS) by the FDA [34-42, 99]. The biomedical utility of PLA depends not only on its molecular weight but more critically on its isomeric composition: poly(L-lactic acid) (PLLA), poly(D-lactic acid) (PDLA), and poly(D,L-lactic acid) (PDLLA). PLA with low D-content (<2 %) is semi-crystalline, exhibiting a melting temperature (T_m) of approximately 175 °C and a glass transition temperature (T_g) of 55-60 °C. In contrast, high D-content PLA (>20 %) is amorphous with a similar T_g but lacks a distinct melting point [34, 35,129].

Mechanically, semi-crystalline PLA offers superior performance, with a Young's modulus of ~3 GPa and tensile strength ranging from 50-70 MPa. Amorphous PLA, by comparison, has a lower Young's modulus (~1-2.1 GPa) and tensile strength (20-50 MPa) [34, 35, 130, 131]. These differences influence their degradation behavior: semi-crystalline PLA typically loses mechanical strength after about six months and fully degrades over several months to two years, whereas amorphous PLA degrades more rapidly, often within a year, and loses structural integrity much sooner. Consequently, semi-crystalline PLA is generally preferred for load-bearing or structurally demanding bone regeneration applications [132-134].

Despite these advantages, semicrystalline PLA exhibits several limitations, including brittle fracture behavior, lack of bioactivity/osteoconductivity, and an often unpredictable degradation rate [132-134]. To address these issues, the incorporation of HA into PLA matrices has been widely explored. HA enhances the bioactivity, stiffness, and

osteoconductivity of the composite, while PLA contributes flexibility, degradability, and processability. The resulting HA-PLA composites aim to harness the strengths of both constituents while mitigating their individual shortcomings.

Extensive research has focused on optimizing the fabrication techniques, mechanical performance, and degradation profiles of HA-PLA composites to enhance their suitability for the treatment of critical-sized bone defects. The following section will examine the primary challenges associated with designing and developing these composite systems.

2.2.5 HA-PLA Composite Fabrication Challenges

Over the past few decades, various combined fabrication approaches have been employed to prepare HA-PLA composites, as summarized in Table 2.3. Among these techniques, all except hot-pressing have enabled the fabrication of polymer-ceramic composites using PLA as the matrix and HA as particulate or fibrous fillers [116, 135-149]. While these composites exhibit excellent biological behavior and favorable *in vitro* degradation, their mechanical properties are at least one order of magnitude lower than those of cortical bones. Consequently, these composites are more suitable for healing soft bone or cancellous bone defects rather than addressing critical-sized bone defects.

Table 2.3 *Summary of the fabrication techniques used to develop HA-PLA composites, along with their corresponding HA content and achieved elastic modulus values.*

Fabrication method	HA content	Mechanical properties achieved	Ref
Solvent casting/evaporation	10-50 wt.%	Elastic modulus = 0.1-0.9 ± 0.5 GPa	[135-137]
Solvent blending & melt compounding	5-20 wt.%	Elastic modulus <0.2 ± 0.5GPa	[138-140]
Extrusion & injection molding	10-40 wt.%	Elastic modulus = 0.8-5.0 ± 0.5 GPa	[141-145]
Solvent blending & Hot molding or compaction	10-80 wt.%	Elastic modulus = 4.0-11.0 ± 0.5 GPa	[38, 146-149]

Additive manufacturing (3-D printing)	5-50 wt.%	Elastic modulus = 2.0-5.0 ± 0.5 GPa	[116, 150-152]

The primary reasons for the low mechanical strength of HA-PLA composites arise from several fabrication challenges, including the HA content, achieving good dispersion/distribution of HA particles within the PLA matrix, and the interfacial bonding between HA and PLA [37-41]. These are crucial for enhancing the composite's mechanical and biological properties. Typically, when a lower proportion of nano-HA particles is mixed into the PLA matrix, the nanoparticles tend to aggregate, causing uneven dispersion and agglomeration issues. Studies have shown that incorporating HA by more than 75 % greatly improved the mechanical modulus of the composite. Meanwhile, increasing HA content adversely affects the rheology or flowability of the mix, complicating the processability or printability, particularly in additive manufacturing or injection molding methods [39, 40, 42, 150-152].

Additionally, the inherent hydrophilicity of HA and the hydrophobicity of PLA result in poor interfacial affinity, further hindering the uniform distribution of HA in the PLA matrix. This challenge has been addressed through surface modification techniques, where the HA surface is treated with suitable organic molecules as surfactants, plasticizers, or grafted with polymers via plasma treatment [154-158]. The most commonly studied plasticizers include lactic acid oligomers, glycerol esters, citrate oligomers, dicarboxylic ester derivatives, polyethylene glycol, etc. [154-158]. Interestingly, these modifications have been reported to improve the interfacial bonding between HA and PLA, resulting in up to a 20 % increase in the final mechanical properties of the composites [128, 129].

Secondarily, the manufacturing process itself affects the mechanical characteristics, as the processing variables significantly influence the composite's microstructure, homogeneity, and porosity. For instance, composites fabricated through hot-pressing or compaction exhibit lower porosity than those made via injection molding. In the hot-pressing technique, applied pressure aids dense packing of HA particles within the PLA matrix, promoting a more homogeneous microstructure [38-40, 148, 149].

Although the hot-pressing method allows for the fabrication of HA-PLA composites with up to 80 wt.% HA loading, the resulting elastic modulus only meets the lower limit of cortical bone [39, 40, 148, 149]. Nevertheless, the superior elastic modulus observed in hot-pressed composites, compared to those produced by other techniques (as shown in Table 2.3), is attributed to the mechanical interlocking between HA particles and the PLA matrix. Bulk HA achieves an elastic modulus between 80-130 GPa through the consolidation of HA particles via high-temperature sintering (>1000 °C) [29, 30]. In contrast, hot-pressing and other composite processing techniques are conducted at temperatures between 180 and 200 °C, making the consolidation of HA particles within the PLA matrix unfeasible or ineffective. This presents a significant limitation in achieving mechanical strength comparable to that of cortical bone.

Moreover, the temperature difference between HA and PLA makes it impractical to co-sinter both using conventional sintering methods employed for HA densification. To address this challenge, alternative strategies, such as low-temperature sintering techniques, must be explored to enhance the fabrication of HA-PLA composites with mechanical properties comparable to cortical bone. Such methods can also reduce the drawbacks associated with traditional high-temperature sintering of HA ceramics (as discussed in Section 2.2.3).

2.3 Sintering Pathways for Bioactive Materials

This section elaborates on the fundamental principles of sintering and presents a roadmap of non-conventional and low-temperature methods for processing bioactive materials.

2.3.1 Conventional Sintering and Its Science

Sintering is an irreversible thermodynamic process that consolidates loosely bound particles or powder materials into a dense solid artifact. Historically, sintering is one of the oldest material processing techniques, with origins traceable to the firing of ceramics in prehistoric times [159-166]. As such, sintering is a critical step in ceramic manufacturing and materials processing, with the primary goal of achieving the desired mechanical strength of the final product through densification. The conventional sintering techniques are generally pressure-less sintering and are categorized into four

types depending on the volume fraction of solid, liquid, and pore in the green compact, as illustrated in Fig. 2.4.

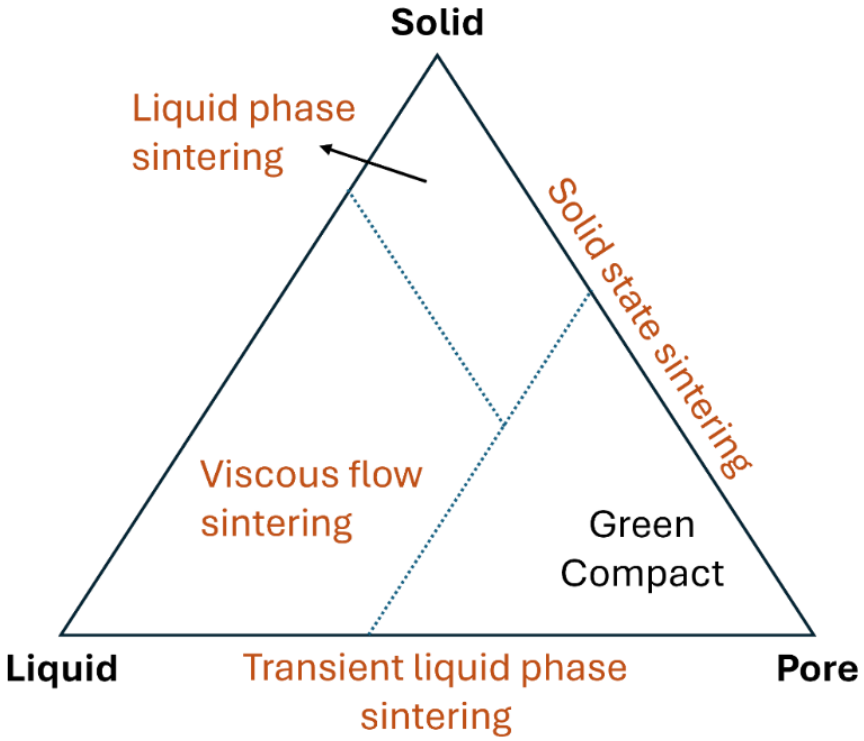

Figure 2.4 *Ternary solid-liquid-pore diagram illustrating the different types of sintering that fall under the conventional sintering technique [163, 164].*

Each sintering type follows distinct diffusion mechanisms and densification behaviors, which significantly influence the microstructure and properties of the final material [159-166]. The theoretical and experimental foundations of sintering were established in the early 20th century, with solid-state sintering emerging as the most extensively studied and widely applied method across various industries. Solid-state sintering occurs entirely within the solid phase, with densification taking place through particle bonding in the presence of pores. In contrast, liquid-phase sintering involves the presence of a minor liquid phase (typically less than 20 % by volume), which enhances mass transport and promotes densification. When the liquid content exceeds approximately 20 %, the process is referred to as viscous flow sintering, where the material behaves as a grain-liquid suspension. In this regime, densification occurs primarily through viscous flow, enabling densification without significant grain shape change. Transient liquid-phase sintering represents a hybrid mechanism, incorporating features of both solid-state and

liquid-phase sintering. In this case, the liquid phase is temporary; it is eliminated during sintering either by evaporation or by reacting to form new solid phases. This temporary liquid phase aids initial particle rearrangement and bonding but does not remain in the final microstructure [161-165].

Sintering is governed by two concurrent and often competing mechanisms: densification and coarsening, which is driven by the reduction in surface or interfacial energy, as described by Equation 2.1. These competing effects are illustrated in Fig. 2.5. Densification is associated with volume shrinkage and increased neck growth between particles, driven by boundary migration. In contrast, coarsening (or Ostwald ripening) results in the growth of larger grains at the expense of smaller ones, increasing particle size while often inhibiting further densification [162-166].

$$\Delta(\gamma A) = (\Delta\gamma)A + \gamma\,(\Delta A) \qquad (2.1)$$

Here, γA represents the total interfacial energy of the powder compact, γ is the specific surface energy, and A is the total surface area. In the equation, $\Delta\gamma$ denotes a change in interfacial energy, which drives densification, while ΔA reflects a change in interfacial area due to grain coarsening.

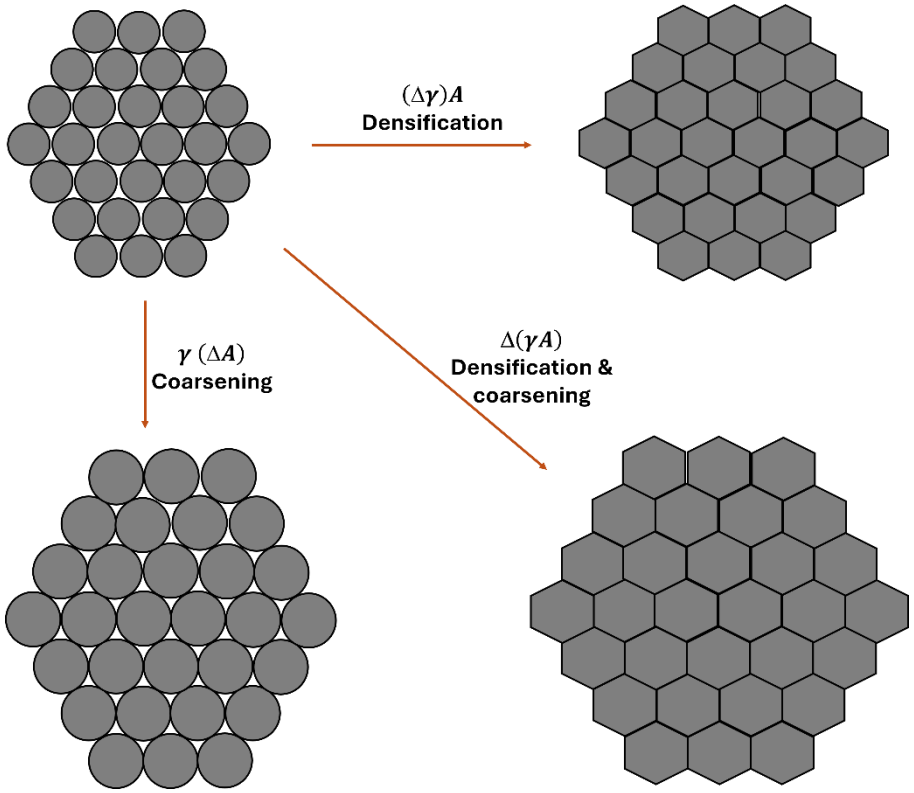

Figure 2.5 *Schematic illustration of the fundamental phenomenon that occurs during the conventional high-temperature sintering [159, 164].*

During sintering, the decrease in surface/interfacial energy drives matter transport via several mechanisms, illustrated in Fig. 2.6. This enables the consolidation of discrete particles into a dense solid via densification or coarsening (Fig. 2.5). In powder compacts, mass transport proceeds via six distinct diffusion-based mechanisms (Fig. 2.6) that are broadly categorized into two types based on their contribution to shrinkage: (i) densifying mechanisms and (ii) non-densifying mechanisms [159-166].

Non-densifying mechanisms, including surface diffusion, lattice diffusion from particle surfaces to neck regions, and vapor transport, contribute primarily to neck growth and microstructural evolution but do not lead to a reduction in pore volume. Conversely, densifying mechanisms such as plastic deformation, grain boundary diffusion, and lattice diffusion from grain boundaries to pores are responsible for actual densification, promoting shrinkage and pore elimination [159-166].

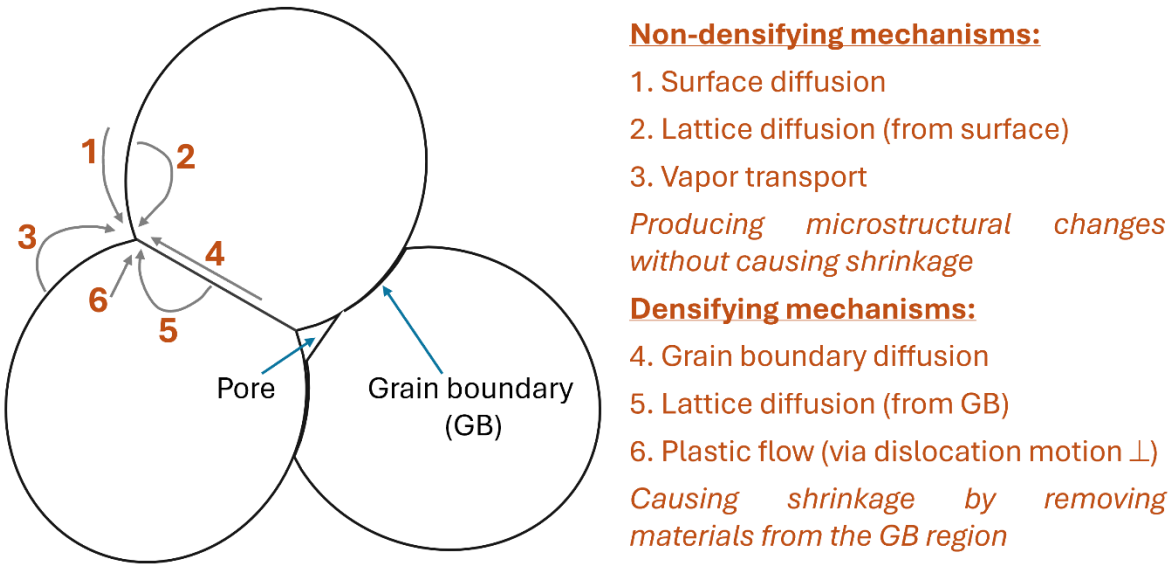

Figure 2.6 *Schematic illustration of mass transport mechanisms contributing to the densification of green compact during high-temperature sintering [166].*

Based on these mechanisms, the solid-state sintering of a green powder compact progresses through three sequential stages:

1. The Initial stage – rapid neck formation between adjacent particles, accompanied by a substantial decrease in surface area (up to 50 %) due to enhanced mass transport via diffusion, vapor transport, plastic flow, or viscous flow. For compacts with an initial relative density of ~0.50-0.60, this stage typically produces ~3-5 % linear shrinkage, increasing the relative density to ~0.65, provided densifying mechanisms predominate.

2. In the intermediate stage, as sintering progresses, pores evolve toward equilibrium shapes under surface and interfacial tensions. Densification proceeds primarily through pore shrinkage. This stage contributes the most to overall densification and eliminates open porosity; by its end, the relative density typically approaches ~0.90.

3. At the final stage, the residual porosity becomes isolated within grains. Densification slows considerably, and grain growth or coarsening becomes dominant. Continued mass transport further reduces pore size while increasing grain size, allowing the compact to reach its theoretical density.

This three-stage sintering model provides a practical framework for understanding the evolution of microstructure and properties in ceramic systems, including bioceramics during thermal processing [159-166].

2.3.2 Non-Conventional Sintering Techniques

The development of non-conventional sintering routes over the past century has laid the groundwork for the emergence of modern low-temperature sintering methods, which offer enhanced energy efficiency, faster processing times, and the ability to consolidate materials with tailored microstructures [167]. Key non-conventional techniques include spark plasma sintering (SPS), microwave sintering (MWS), and flash sintering (FS). These methods leverage external stimuli, such as electromagnetic radiation, electric current, or mechanical pressure, to activate diffusion mechanisms and promote densification at significantly reduced temperatures and time scales.

Spark plasma sintering has historical roots dating back to 1906, with industrial-scale development in the 1960s [167-169]. Microwave sintering emerged in the mid-1940s and achieved wider commercial adoption in the late 1990s [170, 171]. Flash sintering, developed around 2010, with industrial pilot-scale manufacturing demonstrated in 2012

[172, 173]. These techniques offer several advantages over conventional sintering, including reduced grain growth, restricted chemical degradation, enhanced control over microstructure, and significantly lower energy consumption. Table 2.4 summarizes the significance of these non-conventional sintering methods in consolidating bioactive ceramics, hydroxyapatite (HA), with finer grain sizes in a shorter time than traditional solid-state sintering. However, most of these techniques still operate at temperatures higher than 800 °C, which is still too high for the development of composites by co-consolidating polymers and ceramics. Additionally, these techniques demand a specialized experimental setup, unlike the simple furnace used in conventional pressureless sintering. This brings later research advancements that have shifted towards low-temperature sintering methods.

2.3.2 Low-Temperature Sintering Technique

The low-temperature sintering techniques, such as CSP, HHP, and cool-SPS, bring a paradigm shift in sintering to address the challenges associated with the use of high temperatures. These approaches provide a viable platform for densifying bioactive materials at <300 °C, encompassing not only ceramic but also polymer-ceramic composites [183-192]. These techniques provided a platform for low-temperature (<300 °C) densification of bioactive material systems, not only ceramics but also ceramic-polymer composite systems. HHP was introduced by N. Yamasaki and K. Yanagisawa in 1984, which enables the densification of materials in a closed, high-pressure hydrothermal environment [185-187]. The cool-SPS was still the same as SPS but operated at low temperatures under mechanical pressure [183, 184]. CSP, innovated by Randall and coworkers in 2016, relies on mechanical pressure and transient liquid for materials densification at low temperatures [43, 44].

Overall, the advancements in sintering techniques, from conventional to non-conventional to low-temperature sintering, open enormous opportunities to explore the development of synthetic grafts out of bioactive materials. Among the low-temperature sintering techniques, HHP has been demonstrated to be effective for ceramics-based systems rather than ceramic-polymer systems. In contrast, the cool-SPS and CSP are promising for consolidating bioactive ceramics as well as ceramic-polymer composites. Comparatively, both the HHP and cool-SPS required specialized sintering setups, while

CSP consists of a simple experimental setup. Moreover, CSP has a strong theoretical and general mechanistic background, particularly for simple oxide systems and mineral salts [193-196].

Table 2.4 *List of non-conventional sintering techniques, including brief descriptions, sintering variables explored, and the resulting characteristics of HA ceramics.*

Pressureless sintering techniques	
Flash sintering (FS) – apply a high d.c. electric current while heating the sample to its critical sintering temperature. The joule heating and Frenkel pair nucleation induced by the electric field promote rapid densification.	∗ T = 950-1150 °C, electric field 600-150 V/cm, time <5 min. ∗ RD 94-95 %, Avg grain size 100 to 300 nm [174, 175].
Microwave sintering (MWS) – utilizes microwave energy to heat materials (via dielectric heating) for densification.	∗ T = 1100-1300 °C, time 5-30 min. ∗ RD 65-99 %, Avg grain size 0.3 to 3.3 μm [176-178].
Pressure-assisted sintering techniques	
Spark plasma sintering (SPS) - utilizes uniaxial pressure and pulsed direct electric current (DC). The Joule heating effect from DC accelerates grain diffusion and promotes rapid densification.	∗ T = 850-1200 °C, P 30-200 MPa, time 5-10 min. ∗ RD 78-99 %, Avg grain size 100 nm to 6 μm [179-182].
Cool Spark Plasma Sintering (cool-SPS) – same as SPS but employs T <300 °C without using any liquids for densification.	∗ T = 25-150 °C, P 60-120 MPa, time 5-10 min. ∗ RD 52-93 %, Avg grain size <100 nm [183, 184].
Hydrothermal hot pressing (HHP) – utilizes hydrothermal pressure in a liquid-phase environment (closed system) to enable densification at a lower temperature through a dissolution-precipitation mechanism.	∗ T = 100-300 °C, P 30-200 MPa, time 2-6 h. ∗ RD 90-98 %, Avg grain size <100 nm [185-187].
Cold sintering process (CSP) – densification is aided by applied mechanical pressure, in the	∗ T = 25-300 °C, P 200-600 MPa, time 0-120 min.

presence of a transient liquid at a lower temperature, driven by dissolution-precipitation mechanism.	* RD 60-98 %, Avg grain size <100 nm [51-56, 188-192].

2.4 The Cold Sintering Process

The cold sintering process is a non-conventional sintering technique developed by Randal et al, as a novel approach for consolidating ceramics at low temperatures (<300 °C) with the application of applied pressure and transient liquids. Thus, CSP offers a paradigm shift by enabling ceramic densification at significantly lower temperatures as well as providing a platform for co-sintering ceramics and polymers, or metals [44-50].

CSP equipment is typically custom-built and commonly consists of a metallic die, heating jacket, uniaxial automated hydraulic or mechanical press, thermocouple, and necessary controller units or sensors to regulate heating and monitor volume changes (shrinkage) during CSP. Owing to its simple laboratory-scale experimental setup, CSP has been demonstrated to densify dense pellets and multilayered structures of semiconductors, dielectrics, battery materials (including solid electrolytes and cathodic/anodic materials), and biomaterials (Fig. 2.7(a & b)) [44-50]. To date, ~150 different materials, including ceramics, ceramic-ceramic, ceramic-polymer, ceramic-glass, and ceramic-metal composites, have been processed via CSP. Thus, CSP is considered a promising technique, offering advantages in terms of materials integrity, microstructure control, and densification at reduced temperature, time, energy, and cost.

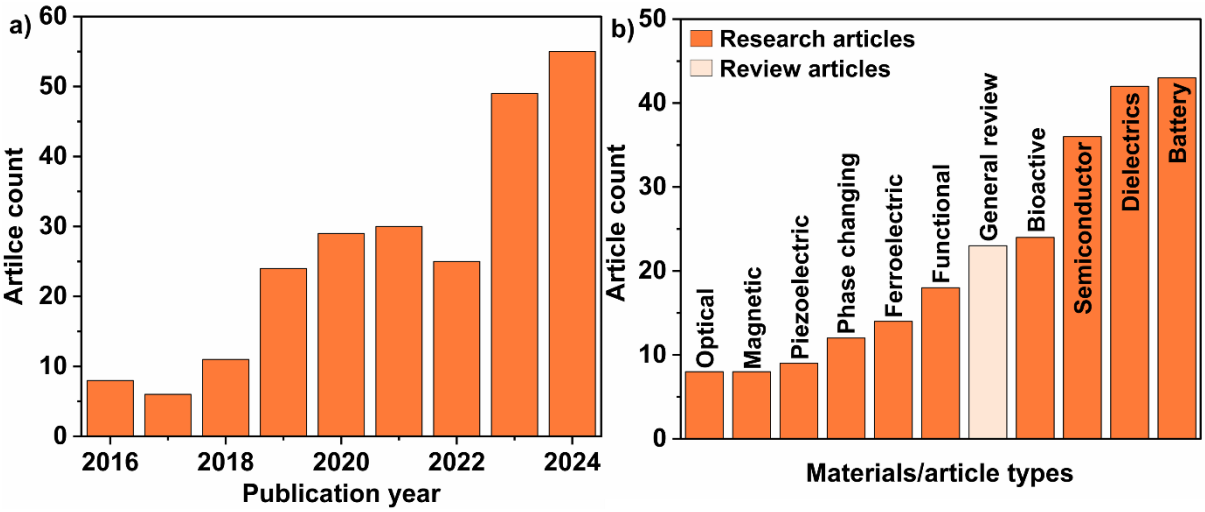

Figure 2.7 *(a) Article count published per year from 2016 to 2024, and (b) breakdown of article counts by material or topic category (up to 2024) published under the framework of the cold sintering process. Counts are based on searches on Scopus, PubMed, and Google Scholar.*

Novel aspects of CSP, as demonstrated by several reported studies include i) simple instrumental setup and straightforward implementation at a standard laboratory scale; ii) evaporation of the liquid solution during densification, requiring a processing temperature typically above the solvent's boiling point but below 300 °C; ii) potential at controlling the microstructure at grain boundary level; iii) able to control the grain growth unlike in high-temperature sintering; iv) low-temperature application provide a flexible strategy for co-consolidating a wide range of thermoplastic polymers with high volume fraction of ceramics, which is not feasible with existing composite processing techniques mentioned in section 2.2.4 [44-50].

2.4.1 CSP Protocol

A typical CSP protocol, illustrated in Fig. 2.8(a), begins with wetting the ceramic powders with a suitable transient liquid capable of partially dissolving the particle surface. The choice of transient liquid includes water, acidic or alkaline solutions, and salt precursor solutions, which depend on the ceramics' solubility and chemistry [193-196]. The moistened powder is then placed into a metallic die and subjected to compaction at room temperature by applying several hundred MPa of pressure (<600 MPa) for a few minutes (10-15 min). While maintaining the targeted pressure, the moistened ceramic powder is consolidated by applying a few hundred degrees Celsius of heat (<300 °C) at a controlled heating rate (1-20 °C/min, depending on the material type). The temperature is held for a certain duration (10-60 min) to allow evaporation of transient liquid through the die-piston gap. Finally, the consolidated samples were recovered after cooling the die to ambient temperature.

2.4.2 CSP Mechanism

The mechanism of CSP differs from the conventional solid-state sintering mechanism discussed in section 2.3.1. To date, CSP has no fully established mechanism; rather, the phenomenological and theoretical descriptions have largely been developed based on

several studies using ZnO as a model system [193-203]. Unlike conventional sintering, the mass transport in CSP is primarily driven by 'pressure-solution creep'. This fundamental mechanistic driving force in CSP closely resembles the geological phenomenon known as pressure-solution creep, which is observed in rock deformation. Pressure solution creep is a chemo-mechanical process involving dissolution-precipitation driven by chemical potential gradients, where solid material in the presence of liquid and applied stress undergoes dissolution in the high-stress region, followed by mass transfer in the fluid phase and precipitates in the low-stress region [195, 204-206]. This phenomenon is also referred to as 'dissolution precipitation creep'.

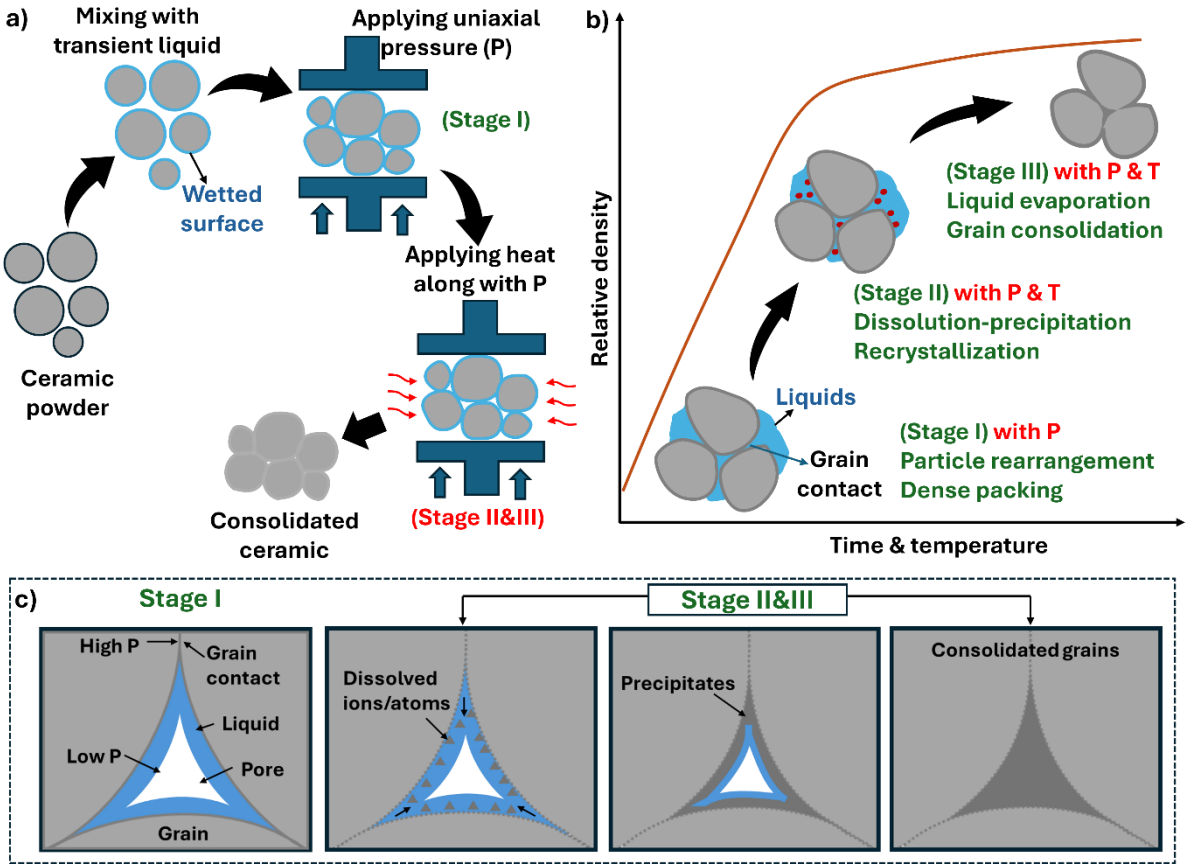

Figure 2.8 *Schematic illustration of (a) cold sintering process protocol, (b and c) the mechanism driving density evolution during CSP of ceramic densification [193, 197].*

In CSP, ceramic densification proceeds in three consecutive stages, as illustrated in Fig. 2.8(b & c). In the first stage, particles undergo rearrangement during compaction, forming a dense packing structure with increased grain (particle-particle) contacts, which contributes to removing a certain amount of porosity. The second and third stages occur

concurrently during the heating process. At this stage, the atom clusters or ions dissolve at grain contacts and precipitate onto the grain surface. This process is driven by a chemical potential gradient between highly stressed particle contact regions and less stressed pore or surface, which provides the thermodynamic driving force for dissolution at contacts, transport of solute through an intergranular solution path, and precipitation at free surfaces or less stressed sites. This collectively refers to pressure-solution creep, the chemical potential differences at the stressed grain contact region and free pore wall (Fig. 2.8(c)) can be given by relation 2.2,

$$\Delta\mu = \mu_\sigma - \mu_p \approx \left(F_\sigma - F_p\right) + \left(\sigma_n - P_f\right)\Omega \qquad (2.2)$$

Here, μ_σ & μ_p represent the mean chemical potential of the solid at the grain contact area and the free pore area, respectively. σ_n denoted the normal compressive stress, while F_σ & F_p represent the Helmholtz free energy at the stressed (grain contact) and local area (pore), respectively. P_f refers to pore liquid pressure and Ω is the molar volume of the solid. If $\Delta\mu > 0$, material will be redistributed by diffusive mass transfer from the contacts to the pore regions, through the intergranular solution phase, thereby driving densification. In the case of $\Delta\mu < 0$, transport from the pores into the contacts will cement the contact regions via a chemical bonding process [194, 196].

The kinetics of CSP under the non-equilibrium thermodynamic condition (refers to temperature gradient during heating ramp) follow a sequence: dissolution at grain contacts, diffusion through the liquid phase along the grain boundaries towards pore surfaces, and precipitation-crystallization at those surfaces. However, it is still debatable whether the precipitation, recrystallization steps are the rate-limiting steps and control the final porosity changes leading to densification. The dissolution process must continue until the saturation point, after which the liquid starts to evaporate at a temperature just above the boiling point of the aqueous solution. Subsequently, the precipitated ions and clusters begin recrystallization at the grain interface, contributing to closure of remaining pores and ceramic densification. During the recrystallization of precipitated species, grain coarsening phenomena are driven by two mechanisms: Ostwald ripening and coalescence, which were found to occur. This was mainly reported in ZnO, which occurs either during recrystallization or shortly after the initial stages of

dissolution. The key difference between coalescence and Ostwald ripening is that, in coalescence, small particles or grains combine to form a larger grain, whereas, in Ostwald ripening, small particles dissolve in a solution and then reprecipitate to form larger particles or grains [193-198].

Despite the CSP being recognized as a pressure-driven, liquid-mediated dissolution–precipitation process, the exact mass-transfer pathways and several fundamental aspects of the densification mechanism remain debated, particularly regarding the influence of solubility of ceramic surfaces, the dissolution-precipitation pathways, and their influence on the grain growth mechanism and their kinetics. Also, no clear mechanism has been established for the CSP of hybrid systems, such as ceramic-ceramic or ceramic-polymers.

2.4.3 CSP Parameters

In geological settings, pressure solution creep occurs very slowly, typically at strain rates below 10-12 s^{-1}, and takes several thousand years to achieve significant strain [195, 204, 205]. In contrast, within the context of CSP, this mechanism operates much more rapidly with the application of high pressure, elevated temperatures, and transient liquid phases [195]. Therefore, CSP effectiveness is strongly dependent on several interconnected parameters, including applied pressure, temperature, and transient liquid chemistry. Moreover, utilizing fine or nanoscale powders considerably enhances the dissolution-precipitation kinetics through the Gibbs–Thomson effect, emphasizing the critical role of powder size in CSP [193-196]. Figure 2.9 illustrates some of those influential parameters in CSP. Table 2.6 highlights selected examples of CSP studied across ceramic and salt systems, showing how liquid phase chemistry and other processing parameters control the extent of densification at low temperature.

Selecting a suitable transient liquid is critical in CSP and is guided based on the powder's physicochemical characteristics, such as specific surface area, crystal structure, chemical composition, chemistry of interaction between the liquid phase and surface, and particle size [193-200]. For instance, in CSP of ZnO, the transient liquids, such as acetic acid and formic acid solutions, are significantly effective than water or citric acid solutions. This correlates with the congruent solubility of ZnO under acidic conditions is

more than at basic or neutral pH, which facilitates dissolution–precipitation mechanisms central to CSP. Moreover, the solution's ionic strength significantly impacts ZnO solubility, with higher ionic strength promoting enhanced dissolution and improved densification [199-203]. In contrast, $BaTiO_3$ ceramics have negligible solubility in water or acid medium; hence, it is cold-sintered with incongruently soluble, inorganic additives or eutectic alkali fluxes, which act as transient liquid or molten phases, enabling particle rearrangement and densification through interfacial diffusion mechanisms rather than dissolution–reprecipitation [207-209]. For SiO_2, alkaline solutions are more effective: at pH >10, silica undergoes incongruent dissolution to form soluble silicate species that drive dissolution–precipitation [211-213]. Many inorganic salts are congruently soluble in water; accordingly, water is an ideal solvent for $KHPO_4$ and $NaNO_2$ systems [57].

Beyond the transient liquid, processing parameters, such as pressure, temperature, and holding time, significantly influence densification. Across the examples in Table 2.5, higher applied pressure consistently enhances densification, irrespective of the liquids tested. Higher pressure improves grain-grain contact and, together with the transient liquid, promotes localized dissolution and subsequent mass transport across grain boundaries, thereby accelerating densification [193-196].

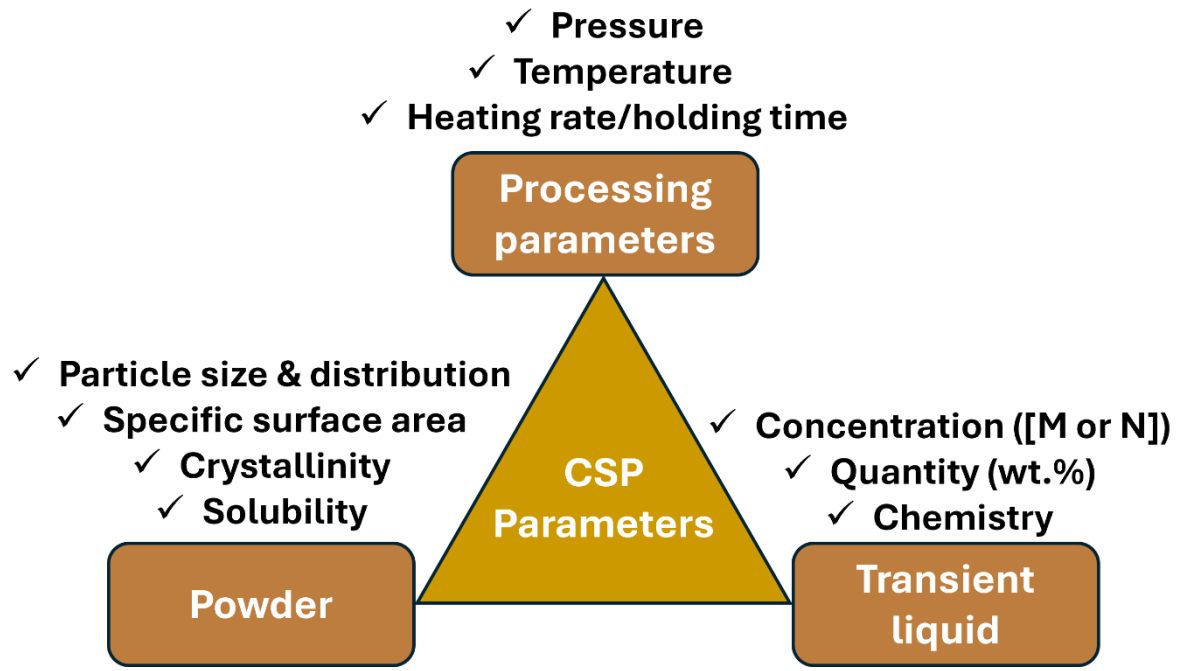

Figure 2.9 *Schematic representation of the key parameters influencing final densification in the cold sintering process [193, 196].*

Table 2.5 *Summary of the selected functional materials densified using CSP, along with the parameters tested, and the densification outcome.*

Material	Transient liquid phase	Processing parameter (P/ T/ HR/ HT) *	Relative density	Ref.
ZnO	20 wt.% of H_2O	77 MPa/ 238 °C/ 5 °C.min^{-1}/ 1 h	<70 %	[197-203]
	1-6-3.2 wt.% of H_2O	100-150 MPa/ 50-300 °C/ 5 °C.min^{-1}/ 5 min	87-93 %	
	4- 35 wt.% of 0.1-2 M AcOH	150-300 MPa/ 25-350 °C/ 2-5 °C.min^{-1}/ 5-480 min	75-99 %	
	Formic acid	335 MPa/ 125-250 °C/ 5 °C.min^{-1}/ 60 min	65-98 %	
	Citric acid	335 MPa/ 125-250 °C/ 5 °C.min^{-1}/ 60 min	62-83 %	
$BaTiO_3$	10 wt.% of $Ba(OH)_2.8H_2O$	350 MPa/ 150-225 °C/ 1-15 h	77-95%	[196, 209]
	10 wt.% of $Ba(OH)_2$	350 MPa/ 150-225 °C/ 1-15 h	<70 %	
	10 wt.% of $Sr(OH)_2.8H_2O$	350 MPa/ 225-270 °C/ 1hr	91-92 %	
	3-6 wt.% (1:1 M) KOH-NaOH	520 MPa/ 300 °C/ 20 °C.min^{-1}/ 12 h	92-99 %	
	10 wt.% of H_2O	350 MPa/ 100-150 °C/ 1 h	<60 %	
	25 wt.% 0.1mol/L $Ba(OH)_2/TiO_2$ (1.2:1 mol) suspension	430 MPa/ 180 °C/ 9 °C.min^{-1}/ 1-180 min	80-95 %	
$KHPO_4$	7 wt.% of H_2O	350 MPa/ 120 °C/ 9 °C.min^{-1}/ 1-180 min	98-99 %	[57]
$NaNO_2$	7 wt.% of H_2O	350 MPa/ 120 °C/ 9 °C.min^{-1}/ 1-180 min	94-98 %	[57]
Yittria stabilized ZrO_2 (3Y-TZP)	30 wt.% of H_2O	350 MPa/ 180 °C/ 9 °C.min^{-1}/ 30-180 min	85-95 %	[210]

SiO_2 (amorphous)	60 wt.% of 2 M NaOH or KOH, or LiOH	200-600 MPa/ 200 °C/ 15 min	80-90, 75-94, 72-92 %	[211-213]
	20 wt.% of 5M NaOH	430 MPa/ 270 °C/ 20 °C.min^{-1}/ 15 min	98 %	
	20 wt.% of TEOS	430 MPa/ 270 °C/ 20 °C.min^{-1}/ 15 min	74 %	
* **P – Pressure, T – Temperature, HR – Heating Rate, HT – Holding time**				

Considering the holding time, materials (ceramics or salts) that are highly soluble in the selected liquid generally require shorter holds (~5-15 min) to achieve substantial densification. In many cases, the applied temperature is typically at least 50-80 °C above the boiling point of the transient liquid, and the isothermal holding time lasts from a few minutes to several hours. As CSP follows the pressure-solution creep mechanism, where densification occurs via stress-enhanced dissolution at grain contacts, followed by diffusion and reprecipitation. Under these conditions, once the solvent reaches the boiling temperature or evaporates, further dissolution stops, or recrystallization occurs, and extended holding times may not be necessary. Therefore, in ceramics such as SiO_2 and inorganic systems like $KHPO_4$ and $NaNO_2$, maximum densification has been achieved with shorter holding times using appropriate solvents and high pressures [57, 211-213].

Overall, transient-liquid chemistry, processing parameters, and powder characteristics are tightly interrelated in determining both the extent of densification and the operative cold-sintering mechanisms (dissolution-precipitation trend). Although CSP has now been applied to a wide range of ceramic systems, the operative mechanism of CSP varies concerning the material type and transient liquid chemistry. Moreover, identifying the key parameters that control consolidation in ceramic-polymer systems continues to be an active and debated area of research.

2.4.4 In-Situ CSP Monitoring

Pressure-solution creep is the proposed densification mechanism in CSP of ceramics. Numerous studies combining ex-situ characterization with molecular dynamics simulations, using ZnO and $BaTiO_3$ as model systems, have provided compelling

evidence for this mechanism [193-195]. To date, the reported CSP investigations have utilized opaque dies to identify the CSP parameters that influence densification and have combined ex-situ characterization techniques to account for the underlying dissolution-precipitation events. These findings consistently support the pressure-solution creep mechanism in CSP. To enable real-time observation of the progression of densification mechanisms, ongoing research and development on in-situ characterization strategies (Fig. 2.10, 2.11) provided a powerful toolkit for monitoring the dynamics of chemical interactions, grain-boundary changes, onset/offset of dissolution, precipitation, and recrystallization steps during CSP [214-218].

Beauvoir et al developed a modified CSP experimental setup shown in Fig. 2.10 for in-situ electrochemical impedance spectroscopy. By tracking impedance during CSP of ZnO with acetic acid as the transient liquid, they resolved GB formation and dynamics at the solid–liquid interface, capturing both thermodynamic and kinetic signatures. Their results supported a three-stage densification pathway: Stage I-wetting and ZnO dissolution (no grain boundary formation); Stage II-grain boundary nucleation via a precipitated Zn–acetate interphase with anisotropic growth; and Stage III-water removal, recrystallization, and GB consolidation [214].

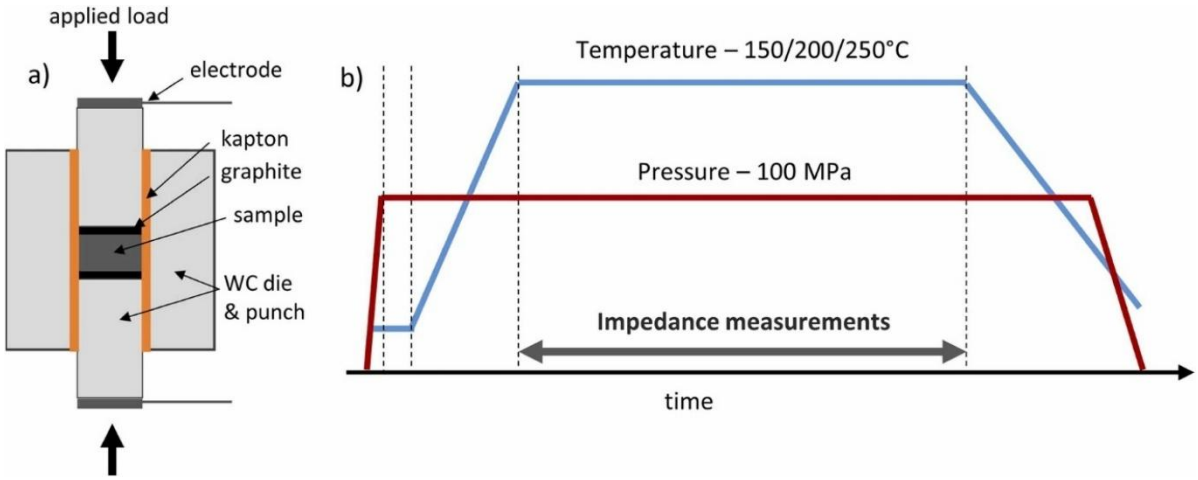

Figure 2.10 *a) Schematic representation of the experimental die setup and b) temperature and pressure profile. Electrical measurements are performed during the sintering dwell time [214].*

Allen and Maier et al devised a custom-built instrumented CSP stage with transparent capillary dies that enable in-situ characterizations, as shown in Fig. 2.11 [216]. Using

synchrotron-based ultra-small- and small-angle X-ray scattering (USAXS/SAXS) along with simultaneous wide-angle X-ray scattering (WAXS), they tracked the real-time changes in grain roughness, transient phases, pore-volume changes, caused by the dissolution-precipitation events in CSP of ZnO and $KHPO_4$ as model systems [213-215].

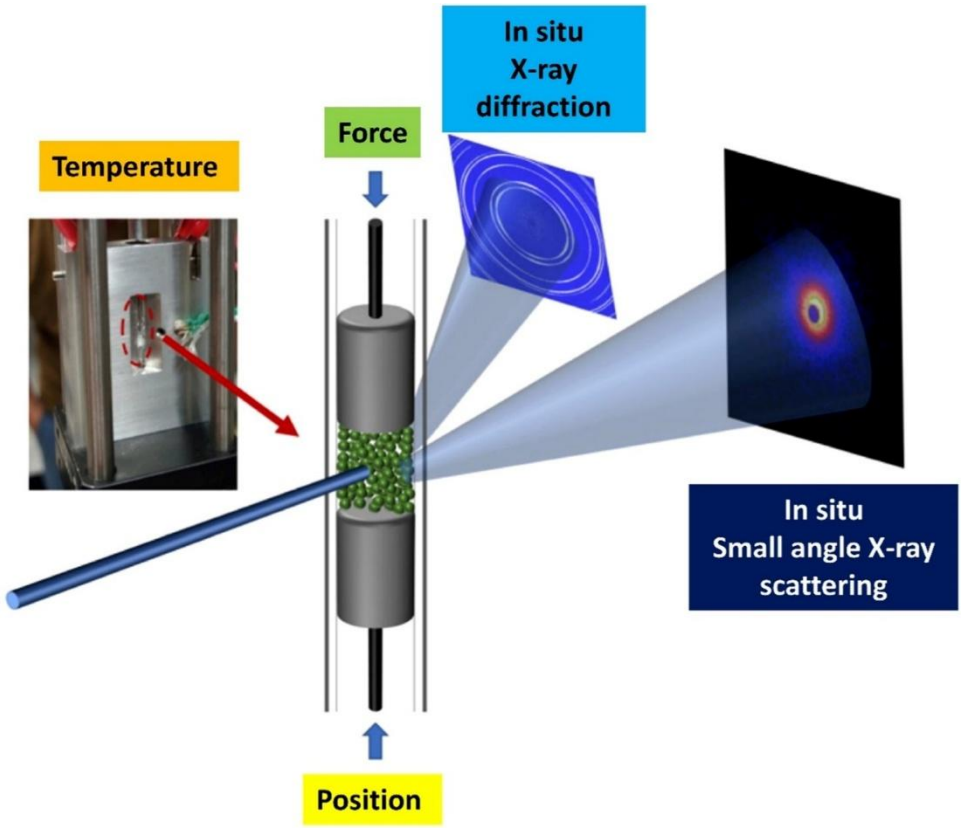

Figure 2.11 *Schematic of the sample mounted in a thin transparent quartz capillary CSP setup for* in-situ *X-ray scattering measurements during CSP [215].*

During CSP of ZnO with acetic acid as a transient liquid, the in-situ x-ray scattering data resolves three CSP stages; (I) early compaction with initially smooth particle surfaces and the onset of dissolution; (II) increases in grain roughness and total surface area driven by dissolution and precipitation of a hydrous zinc-acetate transient phase; and (III) declining pore volume and surface smoothing as necks form, recrystallization proceeds, and ZnO grains grow, leaving residual porosity at triple junctions [215-218]. In another work, Maier monitored densification kinetics CSP of ZnO with acetic acid, in real time using in-situ optical imaging to track sample shrinkage and the onset and timescale of excess-solvent expulsion/evaporation (Fig. 2.12) [218].

Overall, recent advances in in-situ characterization provided a foundation for state-of-the-art CSP metrology. Yet densification mechanisms and mass-transport kinetics remain complex and system-dependent. Consequently, deploying advanced in-situ methods spanning microscopy and analytical spectroscopy across diverse material systems is essential to resolve transient solvent transport, reaction pathways, microstructural evolution, and interfacial reconstruction.

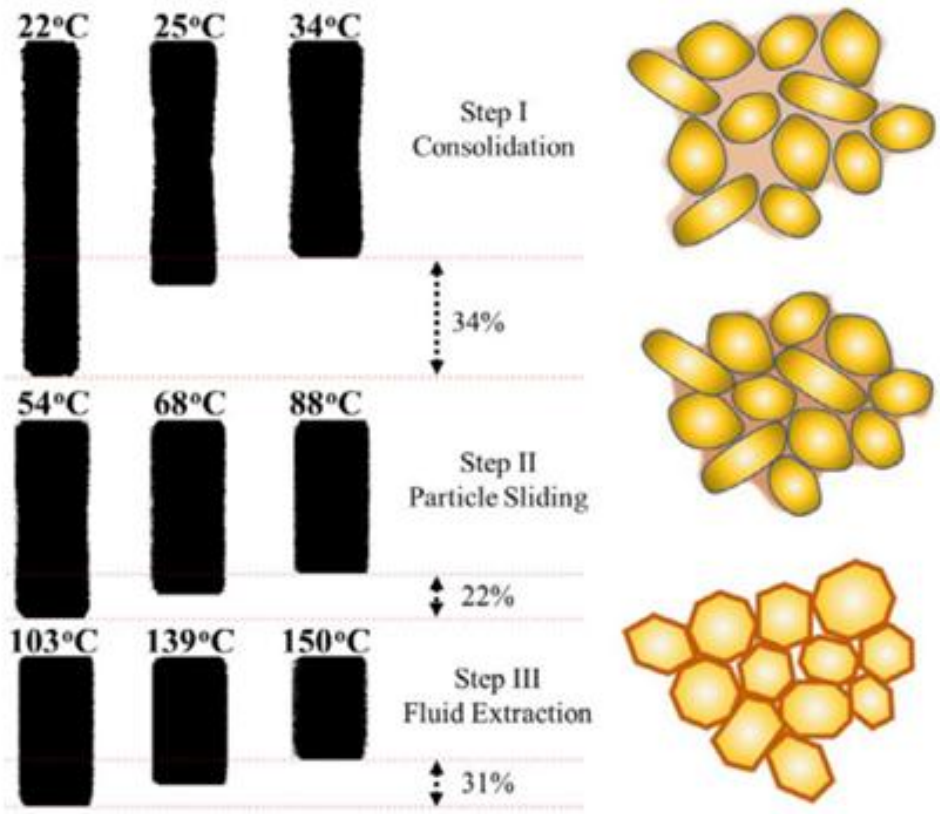

Figure 2.12 In-Situ observation of CSP of ZnO: represented by the thresholded images of ZnO/acetic acid powder compact being densified at 150 MPa, heated to a temperature of 150 °C at 5 °C/min [218].

2.5 Progress in CSP of Bioactive Materials

2.5.1 CSP of Bioceramics

Within the framework of CSP, several studies have demonstrated the densification of different bioactive calcium phosphate ceramic materials, such as hydroxyapatite (HA), β-tricalcium phosphate (TCP), bioglass, amorphous calcium phosphate, dicalcium phosphate dihydrate (DCPD), and dicalcium phosphate anhydrate (DCPA), at

temperatures less than 300 °C [51-57, 188-192, 219-226]. The CSP parameters and densification outcome, along with the bioactive ceramic materials systems studied, are summarized in Table 2.6.

Table 2.6 *Summary of the reported bioactive materials densified using CSP.*

Material	Relative density / transient liquid tested	Processing parameter (P/T/HR/HT) *	Ref.
7 wt.% Iodate-HA (wet precipitated)	96.8 % / without liquid	500 MPa/ 200 °C/ 10 min	[51]
HA (wet-precipitated 20 nm)	≤92 % / 10 wt.% H_2O or 14M NH_4OH or 1M AcOH	500 MPa/ 150 °C/ 10 °C.min^{-1}/ 15 min	[52]
HA (commercial 20-40 nm, <100 nm, 30 μm)	≤72 % / 10 wt.% H_2O or 14M NH_4OH or 1M AcOH		
HA (wet precipitated 20 nm)	70-91 % / without liquid	200-650 MPa/ 100-250 °C/ 10 °C.min^{-1}/ 15 min	[52]
HA (wet precipitated)	60-97 % / without liquid	100-500 MPa/ 50-300 °C/ 0-60 min	[53]
HA (by ball milling $CaHPO_4.2H_2O$ + $Ca(OH)_2$)	72-90 % / without liquid	100-600 MPa/ 150 °C/ 60 min	[55]
	85-90 % / without liquid	500 MPa/ 150 °C/ 0-120 min	
β-TCP (solid-state synthesized)	63 % / 10 wt.% H_2O	166 MPa/ 200 °C/ 4 °C.min^{-1}/ 60 min	[219]
Bioglass (45S5) (flame spray pyrolysis route)	95 % / 80 wt.% H_2O	250 MPa/ 100 °C/ 60 min	[220]
DCPD (wet-precipitated)	78-91 % / without liquid	500 MPa/ 100-250 °C/ 20 °C.min^{-1}/ 15 min	[221]
	86-96 % / 15 wt.% H_2O		
DCPA (wet-precipitated)	76-82 % / without liquid	500 MPa/ 100-250 °C/ 20 °C.min^{-1}/ 15 min	[221]
	84-92 % / 15 wt.% H_2O		
ACP (wet chemical modification of commercial HA)	80-90 % / without liquid	500 MPa/ 20-150 °C/ 5 °C.min^{-1}/ 30 min	[192]
	≤81 % / 20 wt.% H_2O		
HA (mussel shell derived via mechanochemical synthesis)	66 % / without liquid	300 MPa/ 200 °C/ 15 min	[54]
	≤ 75 % /20 wt.% 0.1M AcOH or H_3PO_4		
	74-77 % / 10-30 wt.% 0.1M EDTA		

HA (mussel shell derived via dissolution-precipitation synthesis)	65-92 % / without liquid	250-1500 MPa/ 20 °C/ 10 min	[222]
* **P – Pressure, T – Temperature, HR – Heating Rate, HT – Holding time**			

Across the reported studies, nanometric bioceramics powders are successfully densified to more than 90 % under certain optimized conditions in a shorter time (1-2 h). Interestingly, the microstructure of these densified bioactive ceramics consists of nanosized grains (Fig. 2.13(a)), and phase purity remains unaltered after CSP. However, the mechanical properties are reported to be inferior to those of conventionally sintered samples; cold-sintered HA typically attains an elastic modulus of 23-55 GPa, compared with 80-120 GPa of conventionally sintered HA [188, 220]. The underlying causes for the inferior mechanical properties have not yet been systematically examined.

Hassan et al studies showed that CSP of iodate-substituted HA at 200 °C successfully densified without the volatilization of iodates, which likely shows its suitability for temperature-sensitive ion-substituted bioactive ceramic systems [51, 54]. In addition, a few works highlighted the broader applicability of CSP to densify diverse bioactive ceramic composite formulations such as HA-DCPD, β-TCP-BG, and HA-SiO_2 [55, 188-190, 219, 221].

2.5.2 Bioactive Ceramic-Polymer Composites

An additional noteworthy advantage of CSP is its capability for co-sintering ceramic-polymer composites, offering a more straightforward approach compared to other composite processing techniques discussed in Section 2.2.5. Unlike conventional methods, CSP enables the consolidation of composites with high ceramic content, rather than using ceramics as filler in polymer-ceramic composites. In the context of developing bioactive ceramic-polymer composites (Table 2.7), CSP has been successfully employed to co-sinter the dense composite of HA-chitosan, HA-PLA, HA-polyetheretherketone (HA-PEEK), and bioglass-PLA [220, 222-226].

An example of HA-chitosan composite with a different ceramic-to-polymer mass ratio co-sintered using CSP is shown in Fig. 2.13. Nevertheless, the reported cold-sintered composites exhibit a densely packed, nano-grained ceramic phase that is well bonded to the polymer matrix; the mechanical properties were found to be close to those of

human cortical bone [223]. However, the micro-mechanisms governing the variations in mechanical performance as a function of ceramic content and polymer type remain unclear. For instance, Guo et al reported that the HA-chitosan composite cold sintered at 100 °C under 600 MPa with HA:chitosan mass ratios of 80:20, 70:30, and 50:50 exhibited compressive strength of approximately 75, 130, and 120 MPa, respectively [223]. Similarly, Hu et al reported a value for the HA-PLA composite cold sintered at 80 °C under 500 MPa with the same mass achieved compressive strength of around 48, 80, and 60 MPa, respectively [224]. In both studies, the 70:30 mass ratio yielded optimal mechanical performance, yet the underlying phenomena that control this optimum remain to be elucidated.

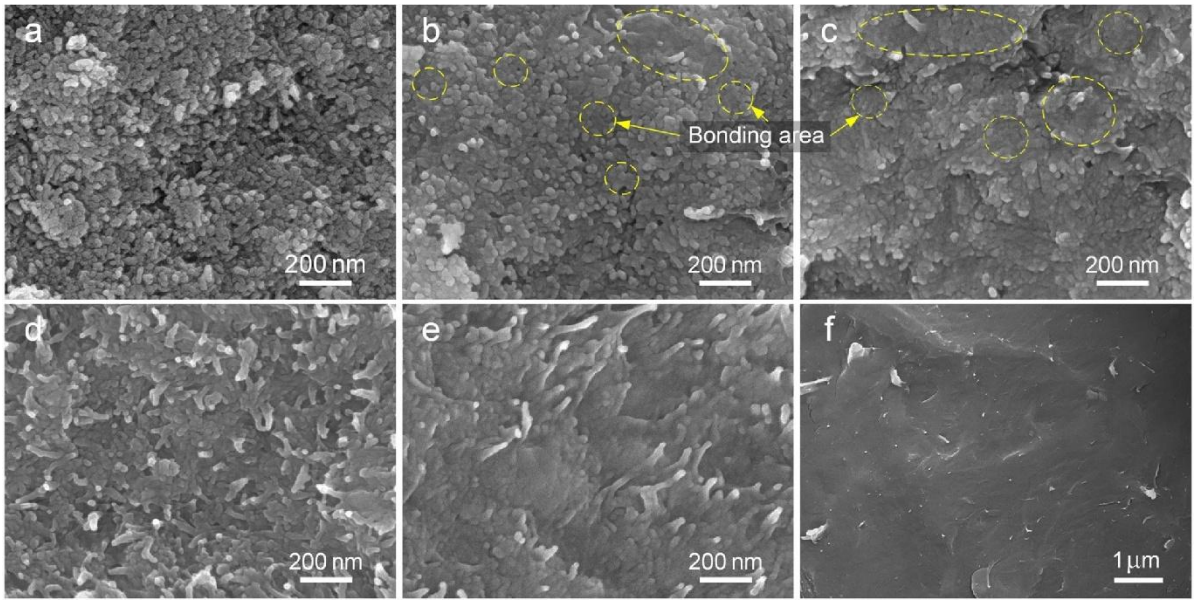

Figure 2.13 *Microstructure of fractured surfaces of the cold sintered chitosan-HA with composites with mass ratios (a) 0/10, (b) 1/9, (c) 3/7, (d) 5/5, (e) 7/3, and (f) 10/0 (CSP parameters: 100°C, 600 MPa, and 20 min) [223].*

Aside from the above discrepancies, CSP has also demonstrated the successful consolidation of in-situ drug-loaded functionalized composites, including doxorubicin-loaded HA-PLA composite and strontium ranelate (SrRAN) loaded HA-chitosan, under certain optimized conditions [223, 224]. Such drug-loaded cold-sintered dense composites show cumulative drug release of 95 % in 24 h in HA-PLA composites, whereas the SrRAN drug-loaded HA-chitosan composite was able to sustain the SrRAN release for more than 15 days, depending on the tested medium [224, 225]. The reported

works on cold sintering of bioactive composites present a promising initial step in CSP toward the development of multifunctional composite grafts with sustained drug delivery. Further research on careful optimization of CSP parameters, in-depth understanding of the co-sintering mechanism, and mechanical properties together will guide the applicability of CSP for developing robust synthetic grafts for bone regenerative applications.

Table 2.7 *Summary of the bioactive ceramic-polymer composite materials consolidated via CSP, along with the reported parameters and consolidation outcome.*

Material	Transient liquid phase	Processing parameter (P/T/HR/HT)	Relative density	Ref.
HA-chitosan (10/0, 9/1, 8/2, 7/3, 5/5, 3/7, 0/10 mass ratio)	No liquid	600 MPa/ 100 °C/ 20 min	77, 87, 88, 91, 92, 95, 95 %	[223]
HA-chitosan (7/3 mass ratio)	No liquid	600 MPa/ 50-150 °C/ 20 min	83-92 %	[223]
		600 MPa/ 100 °C/ 5-90 min	89-91 %	
		200-600 MPa/ 100 °C/ 20 min	74-91 %	
HA-PLA (drug-loaded) (10/0, 9/1, 8/2, 7/3, 6/4, 5/5 mass ratio)	No liquid	500 MPa/ 80 °C/ 30 min	82, 85, 88, 88.5, 92, 92.5 %	[224]
HA-PLA (drug-loaded) (8/2 mass ratio)	No liquid	500 MPa/ 60 or 80 or 100 or 120 °C/ 30 min	82.5, 86.5, 86.5, 78 %	[224]
		500 MPa/ 80 °C/ 20-60 min	82-88 %	
		100-700 MPa/ 80 °C/ 30 min	87-88 %	
HA-chitosan (0, 2, 5, 10 wt.%)	No liquid	1000 MPa/ 20 °C/ 10 min	91, 90, 91.5, 92 %	[222]
HA-chitosan (10 wt.%)	No liquid	250-1500 MPa/ 20 °C/ 10 min	64-98 %	[225]
HA-PEEK (10/0, 80/20, 70/30, 60/40 mass ratio)	12 wt.% 1.5M AcOH	500 MPa/ 300 °C/ 60 min	99, 95, 93, 88, 86 %	[226]
Bioglass (BG)-PLA (10/0, 7.5/2.5, 7/3, 5/5, 4/6, 2/8, 2.5/7.5, 0/10 mass ratio)	80 wt.% H_2O equivalent to BG	250 MPa/ 100 °C/ 60 min	NA	[220]
* **P – Pressure, T – Temperature, HR – Heating Rate, HT – Holding time**				

2.6 Research Gap

Based on the necessity for synthetic bone grafts and challenges in graft fabrication, particularly in treating specific bone defects, CSP is considered a promising approach. As discussed in Section 2.4, the pressure–solution creep framework underlying CSP is reasonably supported both theoretically and experimentally for systems such as ZnO, $BaTiO_3$, and KH_2PO_4, including studies augmented by in-situ characterization tools [193, 199-203, 214-218]. Concerning bioactive materials systems, limited research (see Fig. 2.6(b)) has been conducted and remains elusive, particularly regarding powder characteristics, the transient liquid phase, and dissolution pathways.

As summarized in Table 2.6, HA is the most extensively studied bioactive material within CSP contexts, where the wet-precipitated nano-HA achieves significant densification (≥90 %) under high pressure (>500 MPa) without using any transient liquid [51-55, 192]. In contrast, commercially sourced nanometric HA powders densified poorly (<70 %) under similar conditions, and still, the densification is ineffective even when transient liquids like acetic acid or ammonium hydroxide are employed. It has been proposed that the lattice-bound water ions in co-precipitated HA powders facilitate densification through hydrogen bonding between HA particles, deviating substantially from the classical dissolution–precipitation mechanisms observed in CSP of other functional ceramics [52]. Among various transient liquids investigated, EDTA solutions proved more effective than acetic acid or phosphoric acid, achieving densities up to 82 % at an applied pressure of 600 MPa [52]. This outcome reveals inconsistencies when comparing relative densities obtained with EDTA and without any liquid, suggesting a complexity in densification mechanisms that remain insufficiently understood [54].

Intrinsically, HA has low solubility in water, identifying transient liquids that are compatible with dissolution-reprecipitation-driven CSP, appropriate densification mechanisms, and chemical pathways during CSP for HA are critical. Addressing this gap

is foundational to understanding the effect of transient liquids on the physical, chemical, and mechanical properties of densified HA.

CSP has not yet broadly encompassed various bioactive materials, particularly bioglass systems. Given that CSP primarily depends on pressure-assisted dissolution-precipitation phenomena, the chemical composition of bioglasses significantly influences their reactivity with different transient liquids. Notably, studies on CSP of 45S5 bioglass reported the use of up to 80 wt.% water, far exceeding amounts typically employed for ceramics or salts [220]. Such substantial liquid use raises critical questions regarding its role in effectively densifying bioglass at relatively lower pressures (250 MPa). Furthermore, literature lacks a comprehensive investigation into optimal transient liquids, whether they promote any crystallization, and the dissolution-precipitation mechanisms pertinent to bioglass systems.

To date, only a few bioactive ceramic-polymer composites within CSP have been examined (Table 2.7). Remarkably, these composites have been cold sintered without transient liquids, with increasing polymer content reaching densities exceeding 95 % under high pressures. Logically, not all polymer systems are compatible with water or other transient liquids, such as acids or alkalis. However, this trend is contradicted in cold-sintered HA-PEEK composites using acetic acid, where densities decreased with increasing polymer amounts [226]. Additionally, clear information is lacking for cold-sintered Bioglass-PLA composites using water, as PLA is susceptible to hydrolytic degradation or incompatible [220].

Co-sintering polymer phases with ceramics likely hinders direct ceramic-ceramic contact during compaction, casting uncertainty on whether pressure-solution creep significantly contributes to consolidation in these composites. Instead, reports insist that the pressure-assisted particle rearrangement and polymer-induced plastic deformation, promoting mechanical interlocking and hydrogen bonding between ceramic and polymer phases, appear to be the dominant mechanisms. Thus, a comprehensive understanding of CSP consolidation mechanisms in ceramic-polymer composites remains necessary, particularly regarding to interrelated effects of applied pressure, transient liquids, temperature, and ceramic-to-polymer ratios on the final consolidation. Systematically elucidating these mechanisms would significantly

contribute to rationalizing the distinctions between CSP and conventional hot pressing, guiding the optimization of mechanical properties, and advancing the practical application of CSP in bioactive composite graft development.

2.7 Thesis Objectives

Based on the identified research gaps, this thesis aims to develop a fundamental understanding of the cold sintering process for bioactive materials (HA, BG, and HA-PLA composite) densification that underpins the processing parameters, especially transient liquid chemistry, understanding the underlying sintering mechanisms, and their effects on physical/chemical and mechanical properties.

The main objectives are,

1. To define and optimize a suitable transient liquid chemistry and how it influences chemical, physical, and mechanical properties of the bioactive ceramics.
2. To investigate the role of ceramic-to-polymer ratio, fluidity of PLA concerning the consolidation mechanism, as well as integration between HA and PLA.
3. To study and establish the key dissolution-precipitation mechanism during CSP based on the in-situ Raman characterization.

Chapter 3: Materials and Methods

This chapter describes the materials, preparation routes, and experimental procedures used to investigate the cold sintering process of bioactive systems. It first outlines the CSP protocol, processing parameters, and equipment configuration, followed by a conventional sintering protocol for comparison with CSP. Subsequent sections detail the characterization methods, including their measurement protocols and data-collection procedures. Finally, the in-situ CSP setup, protocol followed for real-time monitoring, and in-situ Raman spectroscopy were detailed.

3.1 Materials and Preparation Methods

3.1.1 Hydroxyapatite Powder

Hydroxyapatite powders (HA), with the commercial trade name: nanoXIM.HAp201 & nanoXIM.HAp202 (CAS 12167-74-7) were purchased from Fluidinova S.A. and is hereafter referred to as HAp201 and HAp202. According to the supplier, both grades consist of aggregated nano HA particles, having similar specific surface areas of ~ 100 m^2/g, and different particle aggregate size distributions (D_{50} = 2.5 µm (HAp201) and D_{50} = 5.0 µm (HAp202)). Detailed physicochemical properties and characterization are provided in Section 4.2 (Chapter 4).

3.1.2 Bioglass Powder

The sol-gel-derived 50S ternary bioglass powder (BG) with a composition of 50 % SiO_2, 45 % CaO, and 5 % P_2O_5 was supplied by the University of Rennes (Institute of Chemical Sciences (ISCR-UMR 6226)). The 50S is designated to indicate the mol% of SiO_2 in the BG powder composition. For the sake of convenience, this 50S ternary bioglass powder will be referred to as BG powder.

The powder was prepared via the sol-gel synthesis method according to the protocol described in a thesis by Nicola Rocton [227]. Tetraethyl orthosilicate (TEOS) ($Si(OC_2H_5)_4$) (99 %, Merck), sodium trimetaphosphate (STMP) ($Na_3P_3O_9$) (95 %, Alfa Aesar), and calcium nitrate tetrahydrate ($Ca(NO_3)_2.4H_2O$) (98 %, Fluka) were used as silicon,

phosphorus, and calcium sources, respectively. The emulsion-based sol–gel procedure used cyclohexane (100 %, VWR) as the oil phase and a combination of Triton X-100® (99 %, Alfa Aesar) and octanol (99 %, Alfa Aesar) as surfactants. Emulsion A was prepared by dissolution in a 2.5 M aqueous ammonia solution, under magnetic stirring, of appropriate amounts of TEOS and STMP. This mixture was kept under strong agitation for 1 h to allow the TEOS hydrolysis. Emulsion B is an aqueous solution of an appropriate amount of $Ca(NO_3)_2.4H_2O$. The emulsions A and B were subsequently mixed at a constant and vigorous speed for 1 h to mix the reagents contained in the aqueous reactors of the emulsions. The mixed emulsions were then left to rest for a maturation (polymerization) time of less than 1 h. After maturation, a white gel is collected by centrifugation and washed several times with ethanol to remove most of the surfactants. It is then dried overnight at 100 °C in an oven. The resulting white powder is calcined in air at 620 °C for 4 h in a muffle furnace and subsequently homogenized by ball milling using ethanol as milling medium. The fine glass powder (particle size distribution indicated in Chapter 5) was collected after centrifugation, washing with ethanol, and drying in an oven at 80 °C.

3.1.3 HA-PLA Composite Powder

Polylactic acid ($(C_3H_4O_2)_n$) with the trade name Ingeo biopolymer PLA 6201D having number-average molar mass (M_n) = 1,16,200 g/mol, dispersity (Đ = 2) (obtained by Size Exclusion Chromatography (SEC) calibrated with polystyrene (PS) standard in $CHCl_3$, D-isomer <2 % according to the supplier), was procured in granule form (between 0.3 to 0.5 mm) from NatureWorks LLC (USA). The solvent chloroform ($CHCl_3$) (CAS 67-66-3) from Chemlab analytical and the plasticizer tributyl citrate ($C_{18}H_{32}O_7$) (CAS 77-94-1) (MW = 360.44 g/mol) from Sigma Aldrich were used as received.

HA/PLA composite powders at different mass fractions of HA/PLA (50/50, 60/40, 70/30, 80/20 wt.%) were prepared via the solvent evaporation method. The schematic illustration of the process involved in the HA/PLA composite powder preparation is detailed in Fig. 3.1. Initially, the PLA was dissolved in chloroform at room temperature in a closed container under continuous magnetic stirring (350 rpm/min). Then, the required amount of HA powder (HAp202) was dispersed into the PLA solution under stirring for 3 h. Following this, the container was left open overnight to allow a slow solvent evaporation under mild stirring conditions (250 rpm/min). The resulting composite solid

mass was dried in a hot air oven at 80 °C for 6 h. The HA:PLA 80:20 wt.% powder was obtained in soft powder form without any lumps, while the other samples consisted of solid chunks. The soft texture of the HA:PLA 80:20 wt.% powder is explained by SEM observations in comparison with 70:30 wt.% powder (Fig. S4, Appendix-A).

The solid composite lumps were subsequently cryo-milled using a Retsch vibro mill with a ball-to-mass ratio of 30:1. The milling was carried out at a frequency of 30 Hz for 9 min, divided into three cycles of 3 min each, with auto precooling to liquid N_2 temperature before each cycle. The prepared composite powders were named based on their compositions: HA:PLA 50:50, 60:40, 70:30, and 80:20.

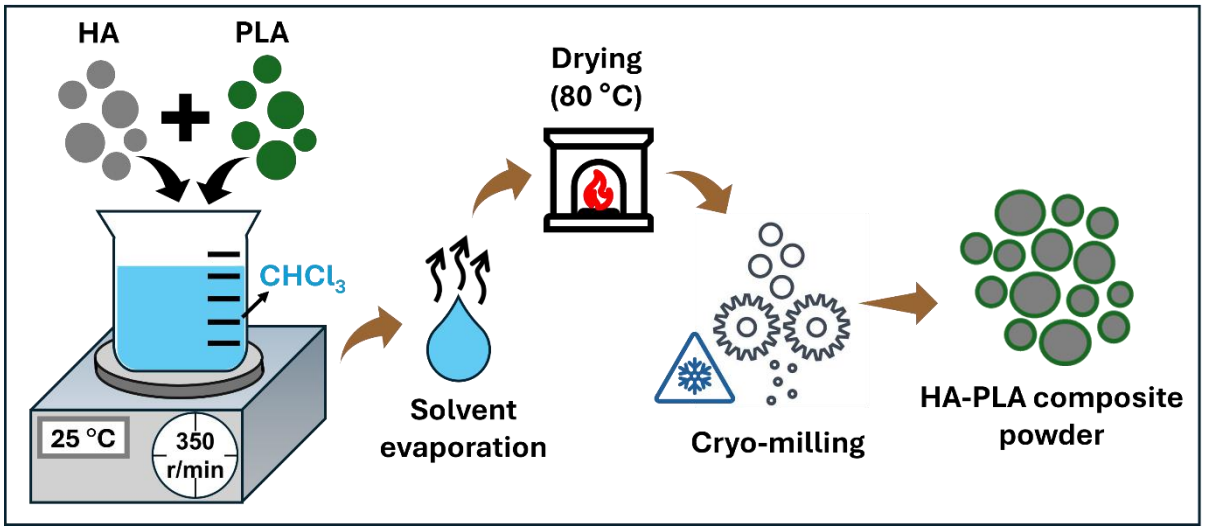

Figure 3.1 *Schematic illustration of the HA-PLA composite powder preparation.*

To assess the effect of PLA fluidity, the PLA was plasticized with tributyl citrate (TBC) at concentrations of 5, 10, and 20 wt.% using a DSM micro compounder (15cc chamber with a vertical twin-screw configuration). The PLA was loaded into the preheated chamber at 190 °C, with the screw speed set to 30 rpm during feeding, and 100 rpm during mixing for 3 min. The required amount of TBC was then added, and the mixture was compounded for 5 min. The extruded plasticized PLA was collected and allowed to solidify at room temperature. Subsequently, the HA:PLA 80:20 wt.% composite powder was prepared using plasticized PLA according to the protocol described in Fig. 3.2. The resulting composite powders were designated as HA:5TBC/PLA, HA:10TBC/PLA, and HA:20TBC/PLA, corresponding to the different TBC concentrations.

3.2 Cold Sintering Process Methodology

3.2.1 HA & BG Powders

The typical CSP protocol and experimental setup employed to study the densification of HA powders are illustrated in Fig. 3.2. Initially, 1.0 g of HA powders was wetted with 10 wt.% of transient liquid by manual mixing using a mortar and pestle. The chosen transient liquids include water, aqueous solution of acetic acid (CH_3COOH, CAS 67-64-1, Carlo Erba Reagents), and phosphoric acid (H_3PO_4 85 wt.% in H_2O, CAS 7664-38-2, AppliChem PanReac) of different molar concentrations ([0.5, 1, or 2 M]). Subsequently, the moistened powders were then transferred into a cylindrical steel die (∅ = 13 mm). The powders were insulated from direct contact with the piston surface using a Kapton polyimide sheet to avoid contamination. A heating jacket was fitted around the die, and a thermocouple was connected laterally to regulate the heating rate.

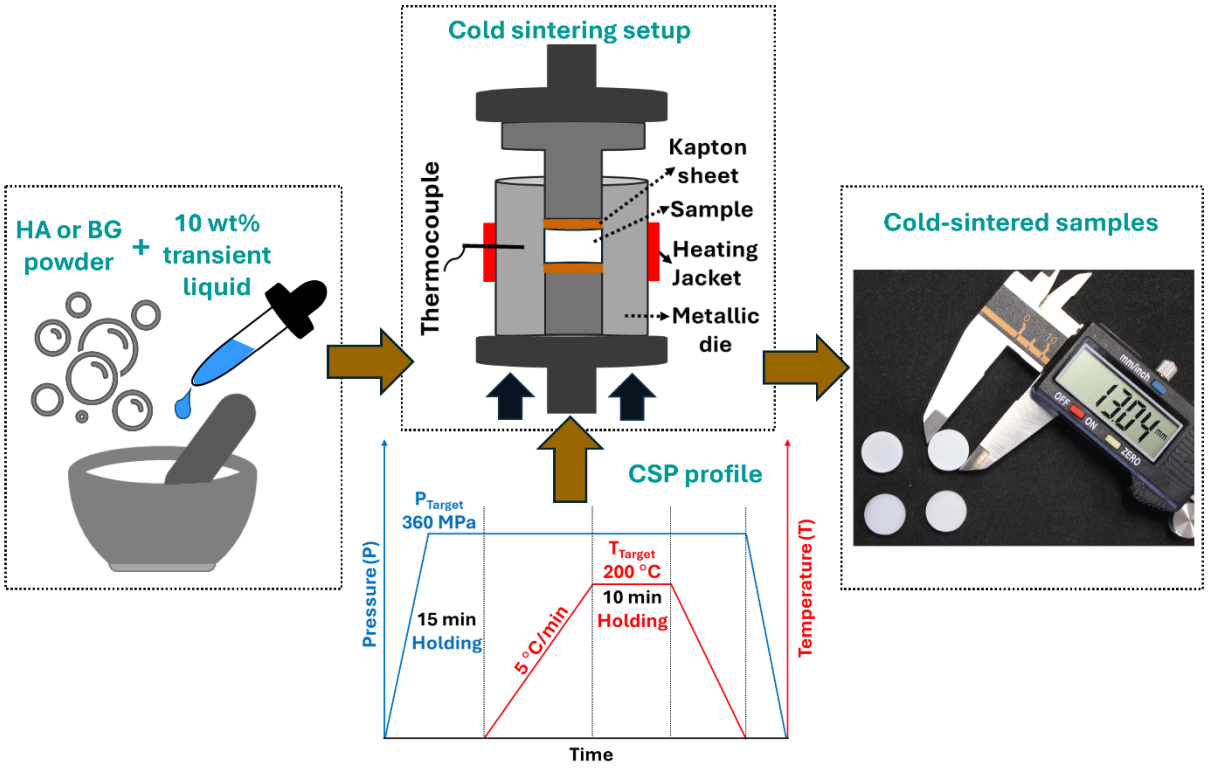

Figure 3.2 *Schematic illustration of the CSP protocol and setup involved in the densification of HA or BG powders.*

The CSP started at room temperature, where the moistened powder was subjected to uniaxial compression using a mechanical testing machine in compression mode (Zwick

Roell model Retroline 1185 with a 100 kN load cell). The powder was compressed at a rate of 7 kN/min until reaching the target pressure of 360 MPa, which was maintained for 15 min. Eventually, the sample was heated up to 200 °C (5 °C/min) and held for 10 min. After cooling to nearly 60 °C, the applied pressure was released, and then the densified samples were ejected from the die. In this way, the cold sintering experiment was done without the addition of any liquids for comparison purposes.

Similarly, cold sintering of 50S BG powders was carried out using water, 2 M solutions of sodium hydroxide (NaOH, CAS 1310-73-2, Merck), and phosphoric acid (H_3PO_4 85 wt.% in H_2O, CAS 7664-38-2, AppliChem PanReac) as transient liquids. The same CSP experimental setup (Fig. 3.2), protocol, and parameters (200 °C, 360 MPa, 10 min holding time) tested for CSP of HA were applied. For comparison, the cold sintering experiment was done without the addition of any liquids.

3.2.2 HA-PLA Composite Powder

The cold sintering setup illustrated in Fig. 3.2 was used to consolidate the HA/PLA composite powders, with a modification that a 1mm thick polyimide pellet replaced the Kapton polyimide sheet, to prevent the PLA from adhering to the die surface. Similar CSP protocol and parameters tested for CSP of HA without liquid (Section 3.2.1) were applied for consolidating 1.0 g of HA/PLA powders without the use of any liquids.

3.3 Conventional Sintering of HA and BG

The conventional sintering of HA powders (HAp201 & HAp202) was carried out for comparison with the cold sintering process. Approximately 1.0 g of powder was uniaxially compacted at ~ 147 MPa using a hydraulic press into a cylindrical pellet (∅ = 13 mm) and then sintered in a programmable Nabertherm high-temperature furnace. The HA powders were heated 5 °C/min to 1200 °C and held isothermally for 2 h.

Similarly, ~1.0 g of sol-gel-derived 50S BG powder was pressed into cylindrical pellets (∅ = 13 mm) and sintered at 1000 °C with a heating rate of 5 °C/min and isothermal holding of 2 h.

3.4 Characterizations

3.4.1 Relative Density Measurements

For the cold-sintered /conventionally sintered HA or BG samples, the apparent density was first determined by hydrostatic weighing according to Archimedes' principle, using water as the immersion medium. Before measurements, samples were dried overnight at 110 °C. For each experiment, a minimum of three samples were tested, and the average value was used in calculating the relative density, as specified in equation 3.1.

$$\rho_r = \frac{m_{air} \times \rho_l}{m_{liq/air} - m_{liq/liq}} \times \frac{100}{\rho_T} \qquad (3.1)$$

where m_{air} stands for the mass of the dry sample in air, $m_{liq/air}$ represents the mass of the water-immersed sample weighed in air, $m_{liq/liq}$ represents the mass of the water-immersed sample weighed in water, and ρ_l & ρ_T is the density of the immersion medium & true density of HA or BG powder, respectively.

The true density values of HA or BG powders were measured with a Helium pycnometer Accypyc III (Micromeritics, USA) after drying the powders overnight at 110 °C. The instrument was calibrated using a 10 cm^3 standard volume cup having and measurements were performed three times while refilling each time, and the average values were used for relative density calculations in equation 2.

For the cold-sintered HA-PLA samples, the bulk density was determined from mass and geometric dimensions and used to calculate the relative density using relation (3.2). At least three samples of each composition were considered.

$$R = 4m / (\pi d^2 h \rho) \times 100 \qquad (3.2)$$

where R is the relative density, m is the mass, d is the diameter, h is the thickness, and ρ is the theoretical density.

The theoretical density of the composite powders was calculated based on the rule of mixtures, using relation (3.3).

$$\rho = \frac{m}{\left(m_{HA}/\rho_{HA} + m_{PLA}/\rho_{PLA}\right)} \qquad (3.3)$$

where m_{HA} and m_{PLA} represent the masses of HA and PLA in the composite, while ρ_{HA} and ρ_{PLA} represent the theoretical density of HA and PLA, respectively. The measured true density of HA/BG powder (He-Pycnometry) and 1.24 g/cm^3 for PLA (provided by the supplier) were used in the calculations.

3.4.2 Particle Size Distribution Analysis

The particle size distribution of the HA or BG powders was quantified with the laser particle sizer method, using a Malvern Mastersizer 3000 particle size analyzer. Before the analysis, the powders were dried overnight at 110 °C. The powders were dispersed at a concentration of 10 wt.% in 100 mL of deionized water and ultrasonicated for 10 minutes to create a uniform suspension. At least three repetitive analyses were performed, and average values were reported.

3.4.3 Specific Surface Area Analysis

The specific surface area (SSA) of the HA or BG powders and cold-sintered samples was measured via the Brunauer-Emmett-Teller (BET) adsorption method, employing the Micromeritics TriStar II instrument. Before the BET analysis, the powders underwent a 12 h degassing process at 200 °C. Similarly, for the cold-sintered samples, the pellets were fragmented into micron-sized chunks before analysis. Between 0.6 and 1.0 g of each sample was loaded for measurement, and SSA values were calculated from nitrogen adsorption isotherms according to the BET theory.

3.4.4 Phase Analysis

The phase composition and purity of HA, BG, HA-PLA powders, as well as the cold-sintered and conventionally sintered samples, were characterized by powder X-ray diffraction analysis. The diffraction pattern was recorded in the 2θ angle range from 10 to 60°, with a scan step size of 0.013°, utilizing the Panalytical X'Pert Pro diffractometer equipped with Cu Kα (λ_{Cu} = 1.542 Å) radiation at 40 kV and 40 mA. For both cold-sintered and conventionally sintered samples, the diffractograms were measured in pellet form using a multi-purpose stage. Phase identification was carried out by comparison with reference patterns from the International Centre for Diffraction Data (ICDD) database.

3.4.5 Morphology and Microstructure Analysis

The morphological and microstructural assessments of the HA or BG powders, as well as the cold-sintered and conventionally sintered samples, were conducted using a Hitachi SU5000 scanning electron microscope (SEM) at an accelerated voltage of 15 or 20 kV. Cold-sintered samples were fractured and sputter-coated with a platinum layer (a few nm thick) prior to SEM imaging. The conventionally sintered samples were first polished (sequentially up to 2400 grit size SiC paper) and thermal annealed at 1100 °C (5 °C/min for 10 min), and SEM observations were carried out after metallization by sputter-coating with platinum.

For the cold sintered HA-PLA samples, the microstructure, including cross-section observation, was examined using a GAIA 3 TESCAN field emission scanning electron microscope (FE-SEM) equipped with a Ga-focused ion beam (COBRA column) to prepare the cross-sections of the specimens. The samples were polished (sequentially up to 4000-grit-sized SiC paper), sputter-coated with platinum, and SEM visualization was performed at an accelerated voltage of 10 or 15 kV to see the microstructure. The FIB cross-section area was visualized at an accelerated voltage of 10 kV. The SEM cross-section analysis was carried out at the Belgian Ceramic Research Centre (BCRC), Mons, Belgium.

3.4.6 Chemical Analysis

The chemical structure of HA or BG or HA-PLA powder before and after cold sintering with different transient liquids was assessed by Fourier-transform infrared spectroscopy (FTIR) using a Bruker IFS 66V/S spectrometer (ATR-FTIR mode) from 4000 to 530 cm^{-1} wavenumber range in transmittance mode with a resolution of 4 cm^{-1}.

For HA samples, the Ca/P ratio before and after cold sintering was determined employing a micro XGT-9000 (Horiba Scientific) X-ray fluorescence spectrometer at an accelerated voltage of 50 kV with a spot size of 100 µm. Before XRF analysis, the HA powder was pelleted by pressing under 2 MPa pressure, and the cold-sintered samples were analyzed as fabricated. For each sample, chemical composition was quantified from five different spots under vacuum, and the average values were presented. The XRF was carried out at the Belgian Ceramic Research Centre (BCRC), Mons, Belgium.

3.4.7 Thermal Analysis

Thermogravimetric analysis (TGA) of HA or BG, or HA-PLA powders, before and after cold sintering was carried out using a TGA Q500 (TA Instruments) at a heating rate of 10 °C/min, ranging from room temperature to 800 °C under a nitrogen atmosphere. Before performing the analysis, the samples were dried in an oven at 100 °C for 6 h, and 11-12 mg of the sample quantity was used.

The thermal behavior of the PLA, plasticized PLA, and the cold-sintered HA-PLA composites was analyzed using the TA Q2000 (TA Instruments) differential scanning calorimeter. Approximately 8-9 mg of each sample was used for experiments under a nitrogen atmosphere (50 mL/min). The experiments were conducted over a temperature range of -80 °C to 200 °C, including an initial heating cycle to 200 °C, followed by cooling to -80 °C, and then a second heating cycle to 200 °C, all at a heating/cooling rate of 10 °C/min. The glass transition temperature (T_g), crystallization temperature (T_c), and melting temperature (T_m) of the PLA and composites were determined from the second heating curve.

3.4.8 In-Situ CSP Analysis

To perform in-situ observations, a miniature version of the CSP setup developed at the Materials and Measurements Laboratory - National Institute of Standards and Technology (NIST, USA) was used [212-216]. A schematic illustration and photograph of the cold sintering stage are shown in Fig. 3.3. Borosilicate transparent capillary tubes with an outer diameter of 3 mm and an inner diameter of 1 mm were used as dies for uniaxial compression. Precision M2 steel pins ($\varnothing = 0.943$ mm) were used to press the powder. The primary components of the stage include a linear actuator, an aluminum heating block, two 60 W cartridge heaters, a K-type thermocouple, and a 20 kgf load cell. The entire setup is controlled using Arduino* software - Arduino IDE(Integrated Development Environment), which is a free source application that helps control the CSP stage, viz., heating, and pressure loading/unloading.

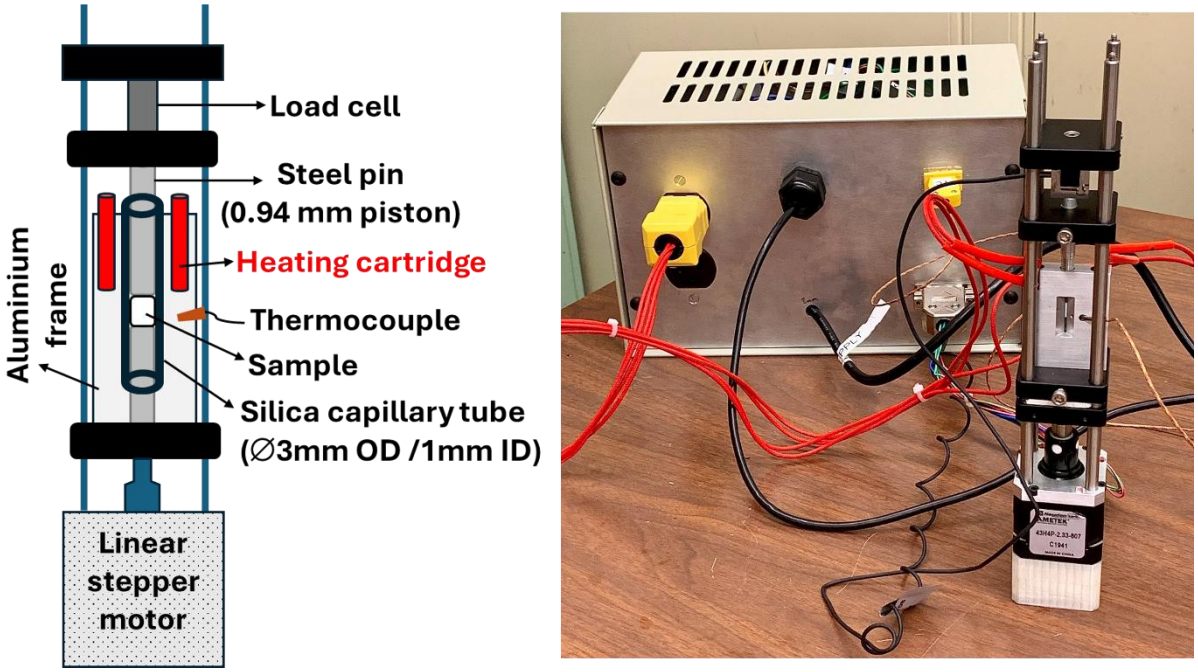

Figure 3.3 *schematic diagram (left), and digital image of the cold sintering setup (right) used for in-situ observations [216].*

Cold sintering of the HA or BG or HA-PLA with optimized transient liquid was carried out by applying a pressure of 250 MPa at 200 °C, with a heating rate of 5 °C/min. During cold sintering, the shrinkage behavior of the samples was monitored through in-situ images recorded every 5 s using a FLIR camera equipped with a photo lens. These images were processed to track the progression of cold sintering by evaluating the linear shrinkage of the samples. The analysis was performed using a MATLAB algorithm (multithresh), which applies Otsu's criterion in a search-based optimization to determine image threshold levels.

The mechano-chemical effects on densification during CSP were evaluated using in-situ time-gated Raman spectroscopy. The cold sintering stage was horizontally integrated with a Raman microscope (Thermo Scientific), where a 1× objective lens was aligned to focus on the sample. Raman analysis was performed using a PicoRaman M3 probe (Timegate Instruments) with a 532 nm laser operating at 20 mW power. The typical laser spot size at the sample focal point was approximately 5 µm.

3.4.9 Mechanical Testing

The elastic modulus and hardness of the cold-sintered samples were evaluated by microindentation analysis using a Zwick Roell (ZHU 0.2) micro-hardness tester equipped with a Vickers diamond indenter. Indentations were made after polishing the sample surface (up to 2400 grit), with a load of 20 N applied for 13 s at a constant displacement rate of 20 N/min during the loading-unloading cycle. The reduced elastic modulus was calculated from the unloading load-displacement data using the Oliver-Pharr method [228]. 10 random indentations were made on each sample, and two samples were tested for each composition. The average values of the elastic modulus and Vickers hardness are presented.

Chapter 4: Cold Sintering Process Framework for Hydroxyapatite

4.1 Context

Hydroxyapatite (HA), owing to its chemical and structural resemblance to natural bone minerals, along with its key attributes such as bioactivity, biocompatibility, and osteoconductivity, makes it a widely preferred material for bone regenerative applications [20-23]. In particular, the significance of nano HA ceramics and the drawbacks associated with their fabrication into synthetic bone graft through conventional sintering techniques were briefly outlined in section 2.2.2. In which the high temperature (>1000 ℃) application has an adverse impact on the biological properties of HA [29, 30, 117].

Therefore, the cold sintering process is considered a viable alternative low-temperature sintering technique to address the challenges associated with high-temperature sintering. Conceptually, in CSP, the ceramic densification is understood to be driven by pressure solution creep (as discussed in section 2.4), where the dissolution/precipitation steps are key in controlling the mechanisms as well as final densification in the presence of transient liquids at low temperatures (<300 ℃) and pressures up to ≤ 600 MPa [43-47]. However, the literature provides evidence of successful densification of freshly precipitated HA powders, achieving relative densities of up to 97 % without the use of any liquids, at a temperature of 150-200 ℃ under high pressures (≧500 MPa) [51-56]. These observations deviate substantially from the classical dissolution-precipitation mechanisms observed in CSP of other functional ceramics.

A hypothesis has been drawn based on the dissolution behaviour of HA ceramics in water, acids, and buffer media, which has been extensively documented by several reports [229, 230]. It is shown that the HA dissolution is known to be faster in acidic pH through the incongruent dissolution mechanism (equation 4.1) than in neutral or alkaline pH, which leads to the formation of thermodynamically metastable clusters, like Posner cluster or amorphous calcium phosphate (ACP) at the crystal surface [229-231].

$$Ca_{10}(PO_4)_6(OH)_2 \overset{H^+}{\Leftrightarrow} Ca_{10-x}(HPO_4)_x(PO_4)_{6-x}(OH)_{2-x} + xCa^{2+}aq + xHPO_4^{2-}aq \quad (4.1)$$

Although the dissolution experiments have been conducted in solutions with low solid content, it is essential to note that dissolution kinetics and mechanisms are influenced by critical factors, including pK_a, nature, and concentration of ions [228, 229]. Correlating the context of CSP with the dissolution behavior of HA, it is apparent that the densification behavior of HA relative to the liquid phase chemistry and ionic concentration of liquid phases, regardless of pressure or temperature in CSP, remains poorly understood.

This chapter examines the role of liquid phase chemistry in cold sintering of HA ceramics under a moderate pressure of 360 MPa using acetic acid (a weakly ionizable organic solvent), phosphoric acid (a strongly ionizable inorganic solvent), and water (an auto-ionizable amphoteric solvent) as transient liquids. Additionally, the influence of physical parameters of the HA powder and the ionic concentration of the chosen liquids on the densification and microstructure evolution during the CSP is also investigated. Finally, the progress of densification and the dynamics of dissolution-precipitation-recrystallization (pressure-solution creep) events were analyzed by deploying a custom-built transparent CSP setup and in-situ time-gated Raman analysis to describe the underlying CSP mechanism.

4.2 HA Powder Characteristics

Fig. 4.1 demonstrates that the commercial HA powders (HAp201 & HAp202) consist of fine micron-sized loosely aggregated nano HA particles having random morphology. The presence of nano-sized crystals was further confirmed by the broader diffraction peaks from the XRD patterns reported in Fig. 4.5(a). Comparatively, HAp201 powder consists of finer micron-aggregate particles than HAp202 powder (Table 4.1). More or less, both HA powders have comparable physical properties like specific surface area, true density, and crystallite size (Table 4.1).

Table 4.1. *Physical properties of commercial HA powders (HAp201 & HAp202).*

HA powders	BET SSA (m^2/g)	Tap density (g/ml)	True density (g/cm^3)	Particle aggregate size distribution (µm)			Crystallite size (nm)
				D_{10}	D_{50}	D_{90}	
HAp201	98.02	0.57	2.93	1.67	2.82	5.25	32 ± 2
HAp202	97.75	0.80	2.96	1.82	5.71	16.21	32 ± 2

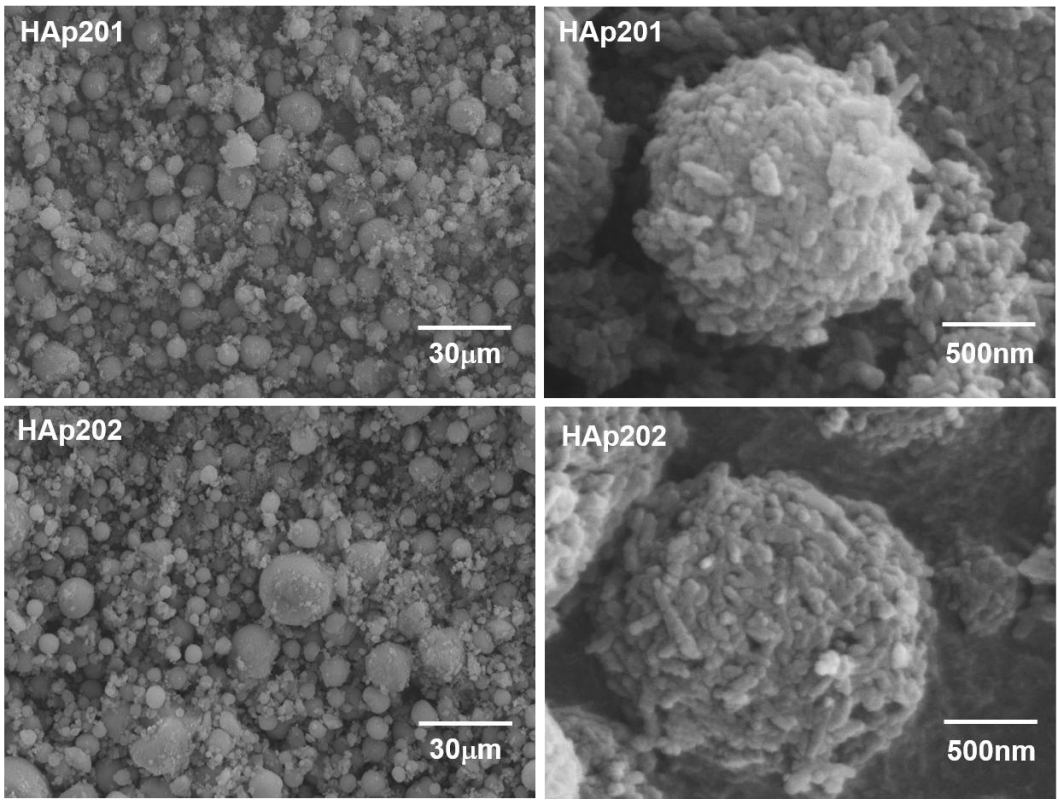

Figure 4.1 *Particle morphology of the commercial hydroxyapatite powders (HAp201 & HAp202) visualized by SEM.*

The observed particle aggregation is attributed to the powder preparation process. At Fluidinova, the aqueous suspension of HA nanoparticles is first produced via controlled wet precipitation using a novel static NETmix reactor [232]. This suspension is then spray-dried at approximately 180 °C into spherically aggregated particles to control the flowability as well as maximize the specific surface area of the powders. The TGA analysis (see Fig. 4.5(b)) confirmed that no polymer additives were added during the spray drying

process, but an observed 6.9 % mass loss up to 650 °C, attributed to the removal of adsorbed/interstitial water molecules and type-b carbonates.

4.3 HA Conventional Sintering

The HA powders were subjected to conventional sintering to evaluate the impact of high-temperature application. First, the optimal sintering temperature was deduced from the linear shrinkage profile (Fig. 4.2(b)), which was obtained by the dilatometric measurements carried out at a heating rate of 5 °C/min up to 1300 °C (BCRC, Belgium).

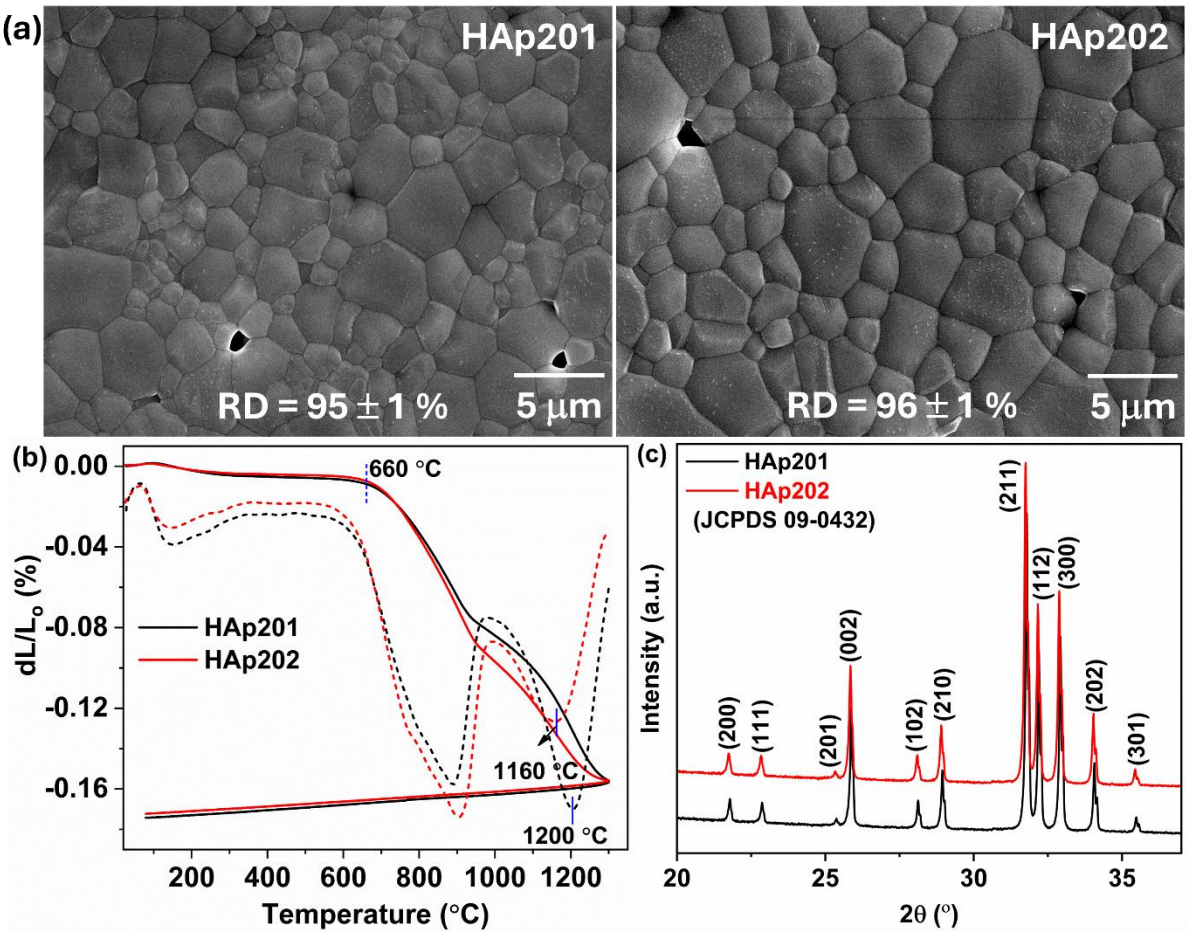

Figure 4.2 *(a) Microstructure from SEM, (b) dilatometry curve (dashed lines represent the first order temperature derivative of the corresponding linear shrinkage curve), and (c) X-ray diffraction patterns of conventionally sintered commercial hydroxyapatite powders (HAp201 & HAp202).*

The dilatometry sintering curve in Fig. 4.2(b) exhibits the onset of shrinkage at ~660 °C, remarking the start of initial sintering and necking between particles. The gradual

shrinkage beyond 660 °C indicates the progressive pore elimination and densification, driven by the thermal-induced diffusion mechanisms (discussed in section 2.3.1). The shrinkage rate decreases progressively, and the curve levels off near ~1295 °C, signifying that most of the open porosity has been eliminated and densification is nearly complete. The first derivative of the corresponding dilatometry curve (dashed line in Fig. 4.2(b)) reveals two distinct peak sintering rates at ~890-900 °C, and ~1160-1200 °C. The former is associated with the initial/intermediate stages of sintering, corresponding to the onset of grain-boundary diffusion and interparticle pore removal. The latter corresponds to the peak densification rate of the final sintering stage, where rapid densification occurs, dominated by grain growth and the closure of open/interconnected porosity within the compact. Based on these observations, a temperature of 1200 °C is chosen as the optimal, above which excessive grain growth may occur.

Accordingly, the conventional sintering of HA powders was performed at 1200 °C for 2 h, and the entire sintering process lasted around 8 h, including heating-cooling cycles. Driving through the conventional sintering mechanism (discussed in section 2.3.1), both the samples HAp201 & HAp202 achieved a relative density of around 95 % & 96 % respectively. The calculated relative density values reveal that the particle aggregate size has a negligible influence on densification. The sintered HAp201 sample exhibited a total porosity of 4.7 $\pm$ 0.2 % (3.1 $\pm$ 0.4 % isolated), while HAp202 showed 4.0 $\pm$ 0.3 % total porosity (2.2 $\pm$ 0.3 % isolated).

SEM micrographs in Fig. 4.2(a) confirm that both samples have reached a high level of densification, exhibit some residual porosity, and well-diffused micron-sized grains with clear grain boundaries. As witnessed in Fig. 4.2(a), the application of high sintering temperature promoted significant grain growth, with the microstructure evolving from nano-to-micro-sized grains. The HAp201 sample displays grain sizes ranging from 0.3-2.3 µm, while the HAp202 samples exhibit grain sizes of 0.4-2.8 µm.

Both sintered HA samples exhibit sharp and well-defined XRD patterns (Fig. 4.2(c)) corresponding to the highly crystalline HA phase, which indicates that the sintering temperature of 1200 °C helps improve the crystallinity of the HA compared to the corresponding HA powders (Fig. 4.5(a)). Mechanical properties obtained via

instrumented micro-indentation further support the microstructural and XRD observations. The HAp201 sample exhibits a reduced elastic modulus E_r = 122 ± 5 GPa and a Vickers hardness of 562 ± 6 HV20; HAp202 sample shows E_r = 126 ± 6 GPa and hardness of 576 ± 8 HV20. These values represent the contribution of highly crystalline, micron-sized dense grains to the mechanical performance of sintered HA. The measured values are in good agreement with those reported in the literature for HA ceramics sintered at 1200 °C [29, 30, 115-118].

While the sintering at 1200 °C produced phase-pure and mechanically robust HA ceramics, it is important to recognize that conventional sintering methods inherently suffer from grain coarsening, long processing time, and more energy consumption. These limitations highlight the need to explore low-temperature sintering strategies capable of achieving effective densification while preserving nanoscale grain structures.

4.4 HA Cold Sintering Process

4.4.1 Density Evolution vs Liquid Phase Chemistry

To assess the influence of liquid phase chemistry on the CSP of Hap202 powder, 10 wt.% of transient liquid phases such as water, aqueous solutions of H_3PO_4, and AcOH (acetic acid) of three different ionic concentrations, as well as without using any liquids, were tested. Figure 4.3 (a) presents the calculated relative densities of the HA samples after cold sintering, while Fig. 4.3(b-d) shows the volumetric shrinkage profile (displacement vs time) recorded during CSP at 360 MPa pressure.

The CSP of HA without the use of any liquids exhibited a relative density of approximately 66 %, whereas the CSP of HA with transient liquids exhibited a significant improvement in relative density. Within each acid type, the relative density values increased with ionic concentration, demonstrating the role of acid concentration in CSP of HA. However, the concentration [0.5, 1.0 M] of both acids yielded densities comparable to those obtained with water. Moreover, only a marginal improvement in density was observed with 2 M acetic acid compared to water. In contrast, the 2 M phosphoric acid solution yielded a maximum densification of 90 %. These density differences indirectly demonstrate the role of liquid phase chemistry in activating pressure-solution creep (dissolution-precipitation) during CSP.

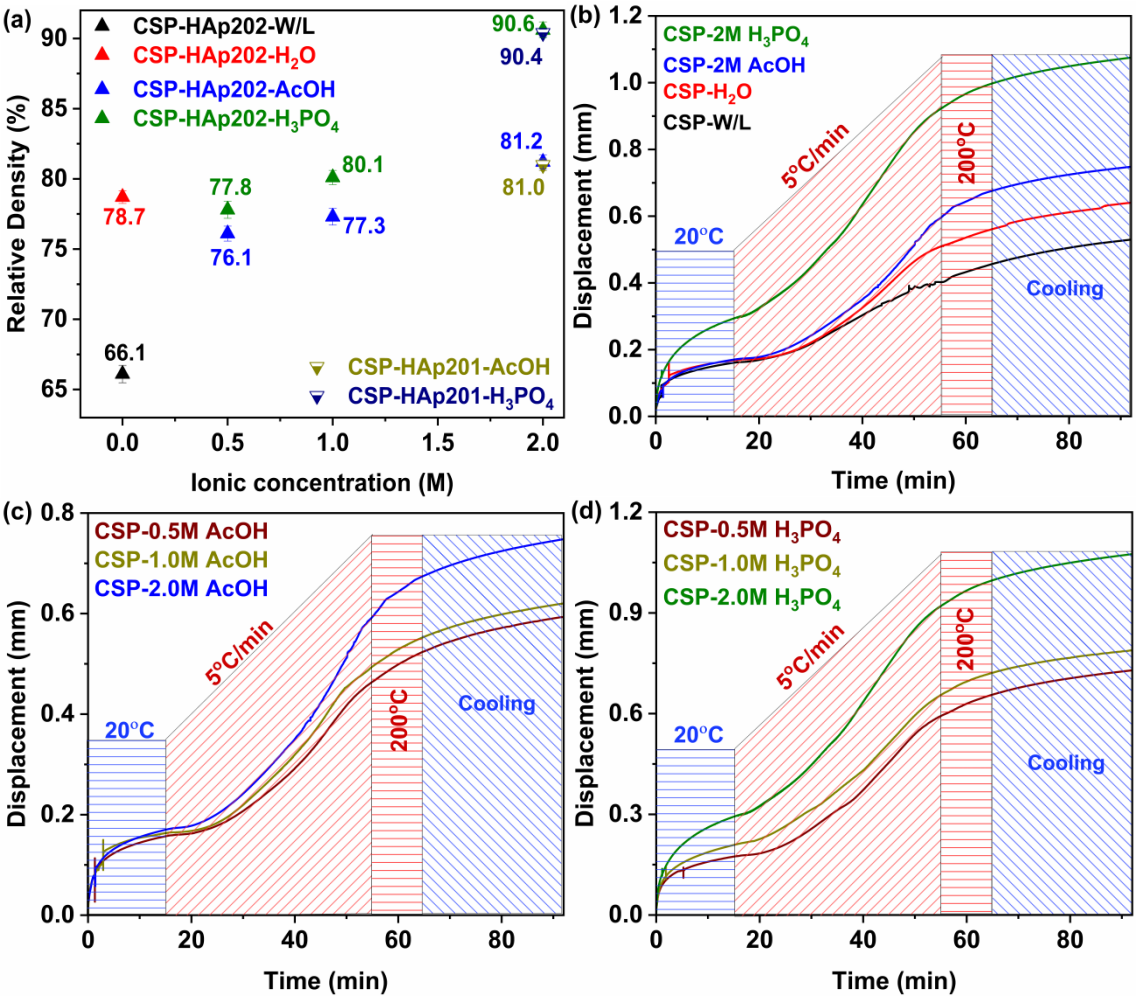

Figure 4.3 *(a) Relative density values obtained for densified HA corresponding to liquid solutions and their concentrations in CSP. Comparison of linear shrinkage profile obtained during the CSP under 360 MPa at 200 °C (b) without liquids, with water, 2 M AcOH, and H_3PO_4 solution, (c&d) with different concentrations of AcOH & H_3PO_4 solutions, respectively. The measured volumetric shrinkage profile represents the total displacement, not corrected for the thermal expansion of the die.*

Within the CSP framework, the process begins with particle rearrangement: applied pressure induces plastic deformation of HA grains, creating more grain contact points. Comparing volumetric shrinkage profiles of the CSP without using liquids, water, 2 M AcOH, and H_3PO_4 solution (Fig. 4.3(b)), the initial volume shrinkage during the 15 min hold time under 360 MPa was observed more with 2 M phosphoric acid, indicating its higher reactivity. Moreover, the acid concentration-dependent differences in the initial shrinkage (Fig. 4.3(c & d)) were only observed across phosphoric acid solution than acetic acid solution of different concentrations. This observation can be correlated to the

strength of the acids; the phosphoric acid (pK_{a1} = 2.14, pK_{a2} = 7.21, pK_{a3} = 12.35) is inherently stronger than acetic acid (pK_a = 4.76). Since higher molarity results in lower pH, the 2 M H_3PO_4 is more acidic than the lower-concentration variants, leading to increased surface reactivity with HA particles. This may cause early dissolution at the HA surface, as shown in equation 4.1, contributing to greater plastic deformation, as indicated by the volume shrinkage profile in Fig. 4.3(b). Following the particle rearrangement, the dissolution-precipitation, recrystallization-liquid evaporation (stages II & III of CSP) occurs only during the heating ramp. This step particularly contributes to mass transport via ionic diffusion due to pressure and chemical gradients [201]. Although the volume shrinkage curve is not relevant to pinpointing the exact temperature range or the kinetics of dissolution or precipitation, or recrystallization, the comparable differences in Fig. 4.3 (b-d) during heating rationally support that both the liquid type (chemistry) and the ionic concentration of acid solutions strongly govern the kinetics of these latter CSP stages.

Given the observed effectiveness of 2 M acid solutions in promoting densification, the CSP of HAp201 and HAp202 powder was compared to determine the influence of particle size distribution. The HAp201 powder was cold sintered with 2 M acetic and phosphoric acid solutions, and the average relative density values (Fig. 4.3(a)) are essentially identical to those of HAp202. Although both HA powders have identical physical properties except for particle aggregate size distribution and tap density, which are expected to affect grain packing density and, consequently, final densification. But the average relative densities of both cold-sintered powders indicate that these differences have no significant impact on densification. Shen et al., previously reported that the particle size of HA powder (20 nm, <100 nm, and 30 µm) has no significant effect on cold sintering of commercial HA powder, even when using different transient liquids (H_2O, acetic acid, NH_4OH) at 500 MPa/150 °C, yielding relative densities ≤72 % [52]. Likewise, cold sintering studies on freshly precipitated HA powder, without transient liquids or using H_2O, at 500-600 MPa and 150-200 °C have reported densification levels of 90-97 % [51-55]. Correlating the literature results with the present study strongly emphasizes that, regardless of particle aggregate sizes, only the transient liquid chemistry primarily governs the densification over other cold sintering parameters such as pressure or temperature.

4.4.2 Microstructure and Mechanical Property

Fig. 4.4 illustrates the microstructural features of the HAp202 samples cold sintered without liquids, and with H_2O, 2 M AcOH & H_3PO_4 transient liquids.

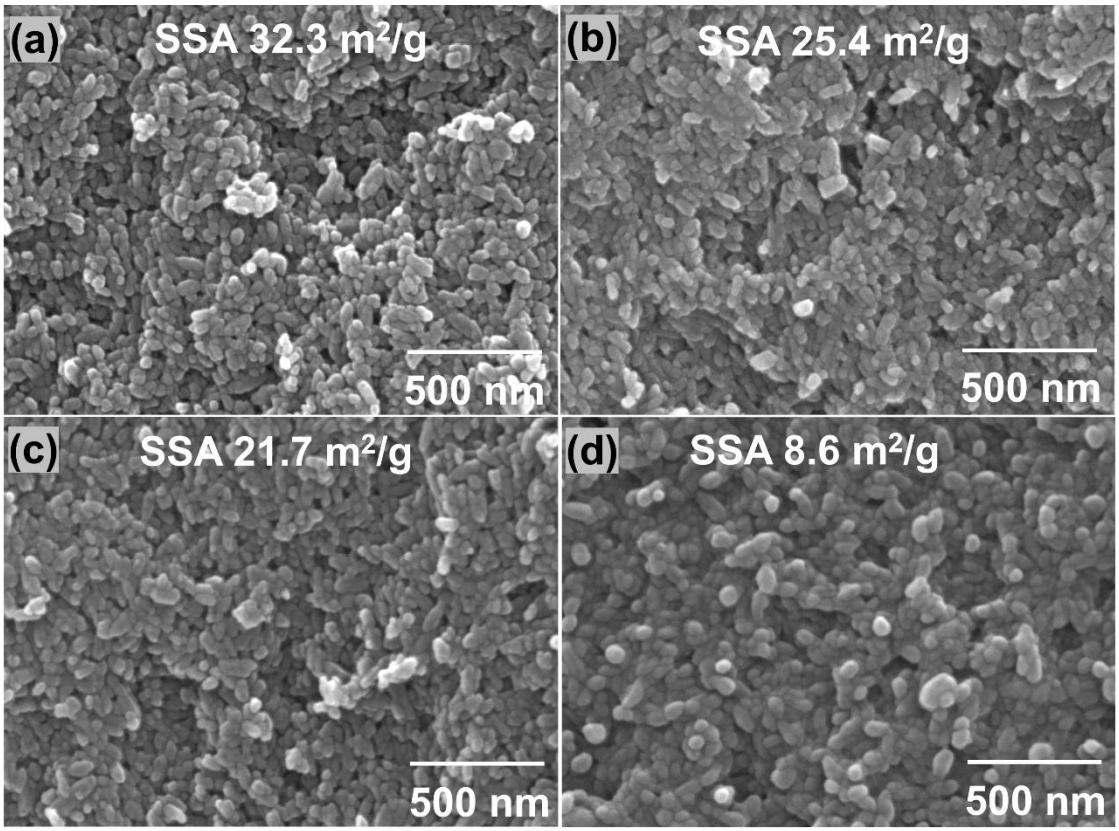

Figure 4.4 *SEM microstructure images (fractured surface) of HAp202 powder cold sintered at 200 °C (a) without using liquids, (b) with H_2O, (c) with 2 M AcOH solution, and (d) with 2 M H_3PO_4 solution.*

SEM images provide clear evidence that the microstructure of cold sintered samples is primarily composed of densely packed nano-grains, but the degree of particle packing and the prevalence of interparticle necks (bonding) vary depending on the efficacy of dissolution-reprecipitation phenomena driven by each transient liquid. Additionally, the differences in the BET specific SSA (inset values in image Fig. 4.4) demonstrate that the dissolution–reprecipitation kinetics increase in the order H_2O < AcOH < H_3PO_4, consistent with the observed differences in microstructural grains consolidation.

The microstructure of HA cold sintered with 2 M H_3PO_4 (Fig. 4.4 (d)) exhibited well-diffused, blunt-edged grains with SSA value <10 m^2/g, whereas the HA cold sintered with

2 M AcOH or water or without liquids exhibits coalesced lamellar grains with irregular edges, and high SSA between 20 to 30 m^2/g. In conventional high-temperature sintering, the reduction in SSA is due to the thermally activated grain growth, which fuses particles. In contrast, cold sintering relies on a dissolution-precipitation-recrystallisation mechanism, which governs the densification, and hence, negligible grain growth is observed. Under the applied pressure of 360 MPa, the agglomerates are broken down, rearranged into stacked lamellar grains. Then, applying heat must accelerate the reactivity of the transient liquid, dissolute ions at interparticle contacts, and pressure/chemical gradients drive ion transport along grain boundaries. This sequence is most effective with 2 M H_3PO_4, which accelerates surface dissolution, enhances intergranular diffusion, and enables plastic rearrangement, thereby closing pores without significant grain growth. The blunt-grain edges observed in the phosphoric-acid sample indicate that an intensified dissolution must occur at the grain surface, and then the precipitated transient phase must recrystallize at intergranular grain boundary regions [233]. In other cold sintered samples, the dissolution-precipitation pathway is only weakly activated, and especially in the CSP without liquid, this pathway is quite uncertain.

Table 4.2 compares the average reduced elastic modulus and Vickers hardness of cold-sintered versus conventionally sintered HAp202 samples. The HA cold sintered with H_3PO_4 exhibited superior mechanical properties compared to HA cold sintered with H_2O or AcOH, or without liquids, yet ~50-55 % lower than those of conventionally sintered HA. These differences could be attributed to the grain size and grain-boundary effects. Conventional high-temperature sintering promotes excess grain growth to several microns, which lowers the total grain-boundary area and produces fully crystalline, stiff contacts between grains. In contrast, cold sintering with H_3PO_4, despite achieving 90 % densification, retains the nano-sized grains, dramatically increasing grain-boundary density. These nano-grain boundaries often contain residual amorphous or poorly crystalline intergranular phases (resulting from dissolution-precipitation-recrystallization mechanism) and sub-micron voids at triple junctions, both of which make softer grain boundaries, which concentrate stress under indentation, thereby reducing apparent modulus and hardness [201-203].

Literature lacks an in-depth understanding of the lower mechanical properties of cold sintered vs conventionally sintered HA. However, Jabr et al. provided insights into the differences in the strength of cold sintered ZnO, which was approximately 50 % lower than that of conventionally sintered ZnO. This reduction was attributed to the lower fracture toughness (0.57 $MPa \cdot m^{1/2}$ compared to 1.15 $MPa \cdot m^{1/2}$), associated with a grain-size effect that promotes low-energy intergranular fracture paths along nanometric grains. Interestingly, the highest hardness measured in cold-sintered ZnO reflected the typical mechanical behavior of nanoceramics, that is, increased hardness but reduced fracture toughness [200-203].

Table 4.2 *Comparison of mechanical properties of conventionally-sintered and cold sintered HAp202 samples.*

HAp202 Samples	Elastic modulus (Er in GPa)	Vickers Hardness (HV20)
Conventionally sintered (1200 °C)	126 ± 6	576 ± 8
CSP WL (200 °C)	20 ± 4	70 ± 5
CSP H_2O (200 °C)	29 ± 4	114 ± 8
CSP 2 M AcOH (200 °C)	33 ± 5	162 ± 8
CSP 2 M H_3PO_4 (200 °C)	63 ± 7	270 ± 9

4.4.3 Phase and Chemical Characteristics

The influence of transient liquids after the CSP of HA was systematically assessed using XRD, FTIR, and TGA analysis; the results are presented in Fig. 4.5. Relative density measurements and SEM microstructural observations indicate that higher concentration acidic solutions significantly enhanced the densification of HA compared to their lower concentration counterparts and pure water. Therefore, to compare, the HA cold sintered with water, 2 M AcOH, and H_3PO_4 solutions, as well as their low-concentration counterparts, 0.5 M, were considered for XRD analysis.

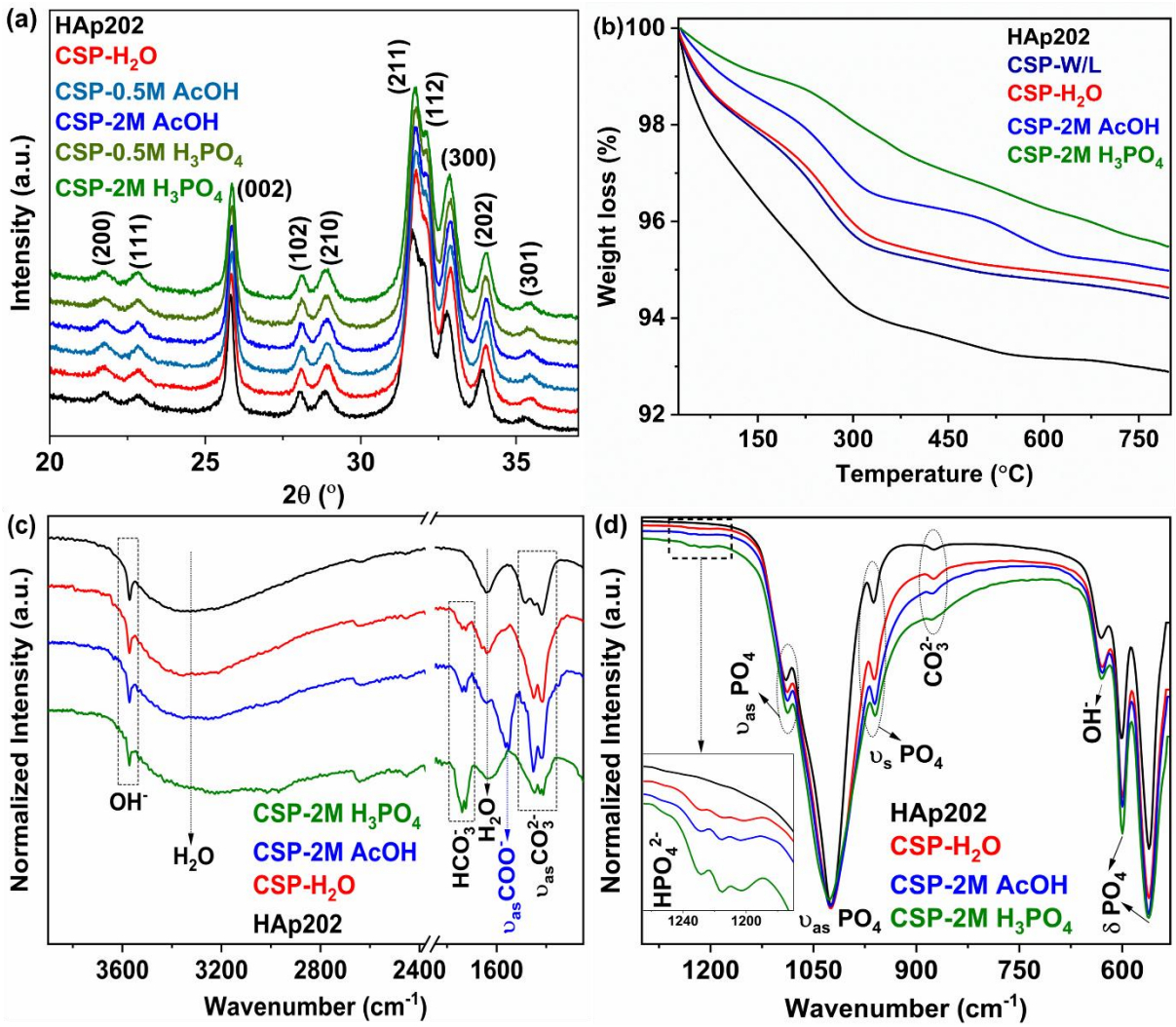

Figure 4.5 *(a) X-ray diffraction patterns of cold sintered HAp202 powder with H_2O, ([0.5 & 2 M]) AcOH & H_3PO_4 solution, (b) Thermogram of cold sintered HAp202 powder using without liquid, H_2O, [2 M] AcOH & H_3PO_4 solutions. FTIR patterns plotted (c) between wavenumber range 4000 to 1250 cm^{-1}, and (d) between 1250 to 530 cm^{-1}.*

The XRD patterns in Fig. 4.5(a) confirmed that the HA phase in HAp 202 powders (consistent with JCPDS 09-0432) remains unchanged after CSP regardless of acid concentration or type. This substantially supports the hypothesis proposed earlier (section 4.1), that the metastable ACP-type Posner's cluster forms as a transient phase and recrystallizes to the HA phase [229-231]. However, the dissolution of PO_4^{3-}/Ca^{2+} ions is crucial to initiate the precipitation of the ACP phase (mimicking the dissolution-precipitation in CSP driving force), and this will alter the HA crystal lattice. This is confirmed by the changes in the lattice parameters a & c values of the cold sintered samples compared to HA powders, which are presented in Fig. 4.6(a) [234, 235]. These

changes are indicative of perturbation in the HA hexagonal crystal lattice due to the dissolution of PO_4^{3-} ions along the c-axis and ionic substitution (H-bonding) along the a-axis, caused by the dissolution-precipitation-recrystallization phenomena [52].

The ionic substitutions in the HA crystal lattice were further complemented by the FTIR spectrum of cold sintered samples given in Fig. 4.5(c & d). The observation of vibrational bands corresponding to HCO_3^- (1700-1770 cm^{-1}) and HPO_4^{2-} (1200-1250 cm^{-1}) in the cold sintered samples ascribed to the ionic substitutions within the HA lattice [234-235]. In particular, the HA densified with 2 M AcOH shows chemisorption of acetate ions on particle surfaces after CSP, indicating that the temperature of 200 °C of CSP is insufficient to decompose the organic residue. Compared to HA powder, CSP samples exhibit notable intensity changes and broadening in symmetric and asymmetric vibrational peaks of PO_4^{3-} groups, along with the presence of a vibration peak for non-apatite groups (inset image in Fig. 4.5(d)) consistent with the substitution of non-apatitic groups ($HPO4^{2-}$) into the HA lattice [231, 236, 237]. These changes were more pronounced in the CSP-2 M H_3PO_4 samples. The peak for lattice water (1640 cm^{-1}) in the H_3PO_4 sample appears broader, possibly due to the formation of H-bonding with the dissolved PO_4^{3-} ions. Another possibility is that the HPO_4^{2-} ions from the H_3PO_4 solution might occupy the site where PO_4^{3-} ions dissolved from the HA lattice along the c-axis, forming hydrogen bonds with hydroxyl groups in HA [52].

Additionally, the deviation in the Ca/P ratio for the CSP-2 M H_3PO_4 sample (Fig. 4.6(b)) from the stoichiometric 1.679 of HAp202 powders further confirms the incorporation of non-apatitic phosphate groups from the phosphoric acid solution after CSP. This non-apatitic phase likely recrystallized within grain boundaries in trace quantities insufficient for detection via XRD. In contrast, the Ca/P ratio for samples cold sintered with water and 2 M AcOH closely matches the HA powder ratio, suggesting these transient liquids lack the reactivity observed with phosphoric acid necessary to promote substantial dissolution-precipitation-driven densification. However, the comparable density values between low-concentration phosphoric acid samples and water can be attributed to the limited availability of reactive ions (HPO_4^{2-}) in dilute phosphoric acid solutions.

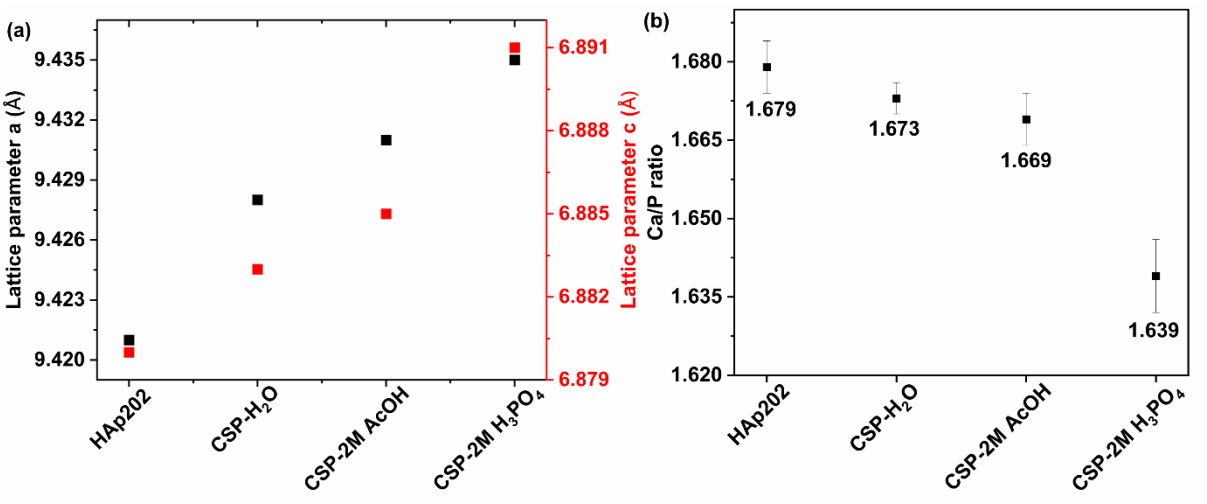

Figure 4.6 *(a) Lattice parameters along the a and c-axis, and (b) Ca/P ratio values for the HAp202 powder and its cold sintered samples with H_2O, 2 M AcOH, and 2 M H_3PO_4.*

TGA data (Fig. 4.5(b)) reveal the mass losses up to 200 °C for cold sintered samples, without liquid, with H_2O, 2 M AcOH, & H_3PO_4 solutions, were around 2.7, 2.5, 1.8, and 1.1 % respectively. These losses are notably lower than the 4.3 % observed for HAp202 powder, despite the addition of 10 wt.% liquids. This suggests that the adsorbed water molecules possibly evaporated during the CSP or are involved in a dissolution reaction. Thus, the coalescence of grains after CSP without liquid should be due to the capillary action from adsorbed moisture to promote H-bonding between the HA lattice, as revealed by Shen et al. Furthermore, TGA results confirm additional mass loss beyond 350 °C for HA cold sintered with 2 M H_3PO_4, due to lattice water release and decomposition of non-apatitic groups [239]. These findings support the proposed ionic substitutions within the HA lattice, as evidenced by changes in lattice parameters and the Ca/P ratio. For samples cold sintered with 2 M AcOH, TGA analysis validates the decomposition of chemisorbed acetate ions in HA crystals at temperatures above 400 °C.

4.4.4 Influence of Physical Properties in CSP

The null effect of the particle aggregate size of HA powders on the CSP has been demonstrated in section 4.4.1, followed by sections 4.4.2 & 4.4.3 argue that 2 M phosphoric acid effectively contributes to the densification of HA than other liquids tested. Since the dissolution-precipitation reaction occurs at the HA surface, both its crystallinity and SSA influence the reactivity [196]. To verify this, the HAp202 powder

underwent calcination at 600 °C and 900 °C, aimed at removing the nanoporosity within the aggregated particles and water molecules. Following calcination at these temperatures for 1 h at a ramp rate of 5 °C/min, a weight loss of ~3.96 and 6.27 % was observed at 600 °C and 900 °C, respectively; the calcined HAp202 powder was then named HAp202_600 and HAp202_900 according to the calcination temperatures. The calcination temperatures have been selected based on the onset and offset shrinkage points illustrated in the dilatometric linear shrinkage profile (Fig. 4.2(b)).

Table 4.3 shows that higher calcination temperatures reduce SSA while increasing both particle-aggregate and crystallite sizes, confirming nanopore removal and particle shrinkage due to pre-sintering effect [240]. The Hap202 powder is somewhat not fully crystalline, as confirmed by the XRD pattern (Fig. 4.5(a)) compared to those calcined powders. The HAp202_900 powder is completely crystalline compared to HAp202_600 powder, as confirmed by the sharp XRD patterns given in Fig. 4.8(a & b).

Table 4.3. *Physical properties of the calcined HAp202 powders (at 600 & 900 °C).*

Calcined HAp202 powders	**BET SSA (m^2/g)**	**True density (g/cm^3)**	**Particle aggregate size distribution (µm)**			**Crystallite size (nm)**
			D_{10}	D_{50}	D_{90}	
HAp202_600	39.08	3.09	1.69	5.42	15.96	36 ± 2
HAp202_900	8.20	3.14	1.40	4.98	15.20	63 ± 2

Eventually, these powders were cold sintered under the previously optimized conditions using 2 M H_3PO_4 as the transient liquid. The cold sintered samples were then named as CSP-HAp202_600 and CSP-HAp202_900, and differences in density evolution trends during CSP are illustrated by the volume shrinkage profile given in Fig. 4.7. The volume shrinkage profile of CSP-HAp202_900 exhibits limited volume shrinkage during heating with a burst-relaxation signature, implying that the early dissolution of its coarser HA grains is inactive, which in turn restricts particle rearrangement compared with CSP-HAp202 _600 [239]. As a result, the CSP-HAp202_600 sample achieved a relative density of around 82 %, while the CSP-HAp202_900 sample reached around 68 %. Importantly, the cold sintered pellet CSP-HAp202_900 sample remains structurally stable, like other

cold sintered samples, during the density measurements conducted via hydrostatic weighing. This further implies the possibility of consolidation, not simply compaction.

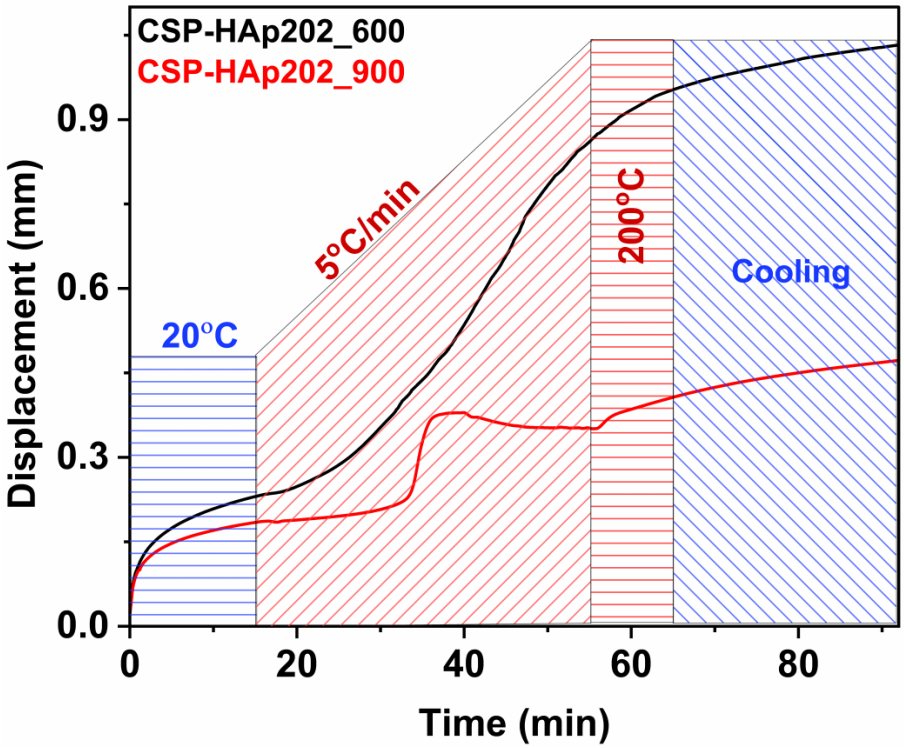

Figure 4.7 *Volumetric shrinkage profile of cold-sintered HAp202_600 and HAp202_900 powders under 360 MPa at 200 °C using 2 M H_3PO_4. The measured volumetric shrinkage profile represents the total displacement, not corrected for the thermal expansion of the die.*

The XRD pattern (Fig. 4.7(a & b)) for the densified samples revealed the presence of secondary peaks corresponding to dicalcium phosphate ($CaHPO_4$, DCPA). These peaks were relatively less intense in the CSP-HAp202_600 sample than in the CSP-HAp202_900 sample. The extent of DCPA formation after cold sintering of calcined HA was governed by the powder's SSA and crystallinity [242]. The HA powder with low crystallinity and high SSA undergoes uniform dissolution (Ca^{2+}/PO_4^{2-} ions), offering more nucleation sites for HA recrystallization; in contrast, lower SSA and higher crystallinity favor localized surface dissolution with limited nucleation sites, promoting reprecipitation of DCPA phase [216, 240]. Therefore, in the HAp202_900 sample, due to fewer nucleation sites driving Ca^{2+} ions released by localized dissolution, to react with HPO_4^{2-} ions from the H_3PO_4 solution, subsequently recrystallizing as amorphous $CaHPO_4$ during CSP. This reaction must be

partially suppressed in CSP-HAp202_600 because its higher SSA favors direct HA recrystallisation, with limited DCPA formation, and consequently improves densification.

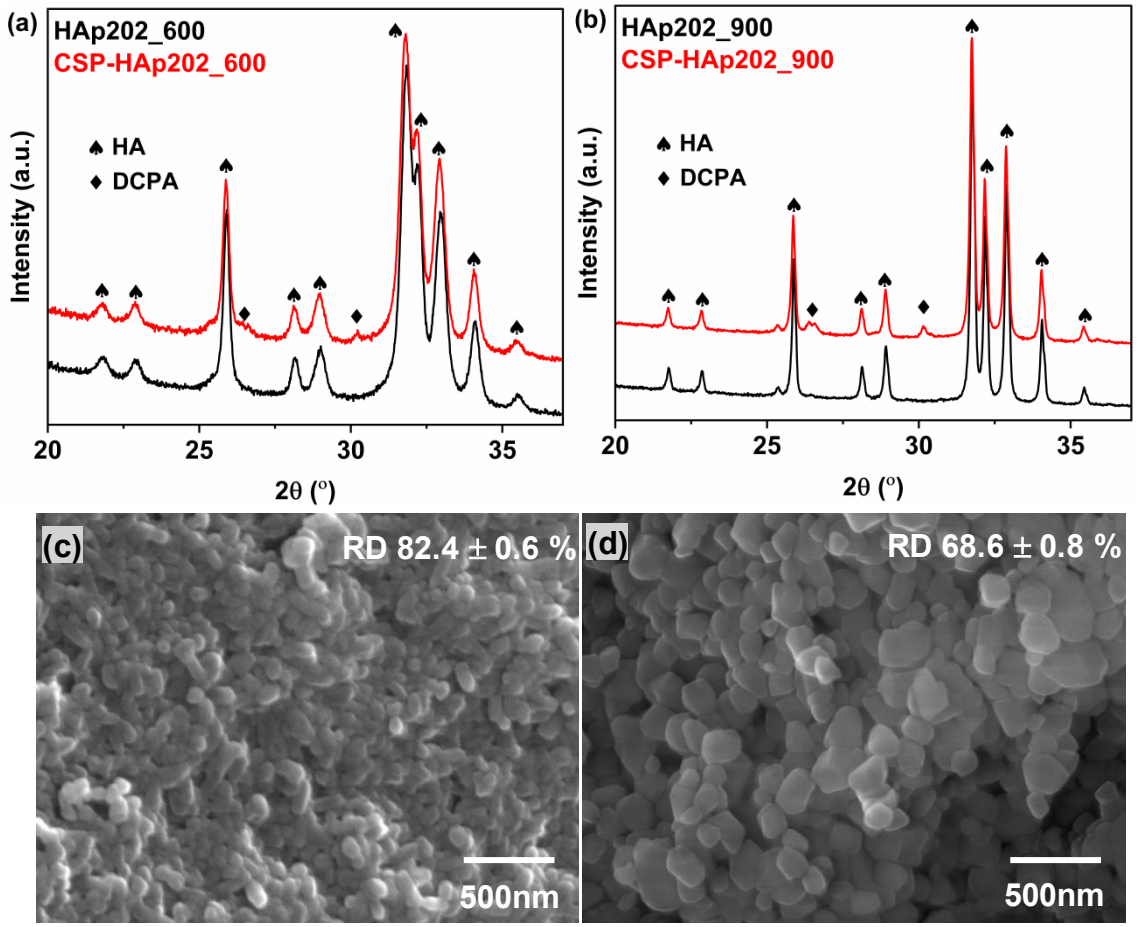

Figure 4.8 *(a & b) Comparative XRD patterns for the HAp202 calcined powders (600 & 900 °C) and cold sintered calcined HA powders at 200 °C using 2 M H_3PO_4 solution, respectively. Microstructure of cold sintered (c) HAp202_600 powder and (d) HAp202_900 powder.*

The SEM microstructure of cold sintered sample, given in Fig. 4.8(c & d), further supports the above argument. The grain sizes of the CSP-HAp202_900 sample are larger than CSP-HAp202_600 sample, which is due to the differences in calcination temperatures. The high-temperature calcination (900 °C) promoted the fusion of fine nano grains into larger nano grains. After cold sintering, the larger grains of the CSP-HAp202_900 sample appear loosely packed, coalesced grains with visible grain boundaries, evidence of the limited pressure-solution creep due to localized dissolution. By contrast, the fine nano-grain of CSP-HAp202_600 sample exhibits well-diffused, densely packed grain microstructure

resembling that of HAp202 powder cold sintered with 2 M H_3PO_4 (Fig. 4.4(d)). Overall, these results confirm that HA powders with high SSA and low crystallinity can be successfully densified with a suitable liquid phase without generating secondary phases, whereas fully crystalline, low-SSA HA powders are much harder to densify under the same cold-sintering conditions.

4.5 HA In-Situ CSP Investigation

HAp202 powder was cold-sintered under 250 MPa pressure (200 °C / 10 min isothermal holding) using the transparent capillary miniature CSP setup with 2 M H_3PO_4, H_2O, and without any liquid. During CSP, changes in sample length were recorded continuously with a digital camera, and the measured relative linear shrinkage (vs time), along with representative in-situ images at selected temperature intervals (inset in Fig. 4.9), were presented in Fig. 4.9. The relative linear shrinkage as a function of temperature, measured during the CSP of HA, is shown in Fig. S1 (Appendin A).

The linear shrinkage profile provides insight into descriptive HA densification kinetics across the three CSP stages: (I) room-temperature uniaxial compaction, (II and III) heating, isothermal holding, and cooling. For CSP, without liquid Stage I, contributes to achieving roughly 89 % of the total densification, whereas Stages II and III proceed with reduced densification kinetics and together contribute ~11 % to the overall densification. This is consistent with the increased interparticle friction after grain interlocking and/or transient thermal expansion associated with slow evaporation of surface-adsorbed water molecules [216]. When H_2O is used for CSP of HA, Stage I accounts for approximately 82 % of the overall densification, while Stages II and III contribute about 18 %. The shrinkage observed during Stages II and III (up to 140 °C, corresponding to ~12 %) must be driven by hydroplastic deformation-assisted rearrangement, which reduces intragranular friction, followed by the consolidation of intergranular necks during water evaporation [243]. The CSP of HA with H_3PO_4: Stage I contributes ~71 %, and Stages II–III ~29 % of the total densification. The accelerated shrinkage during Stages II and III (up to 140-150 °C, corresponding to ~24 %) is driven by H_3PO_4-promoted incongruent dissolution-precipitation (pressure-solution creep) at the HA grain contacts, surface, which supports grain consolidation.

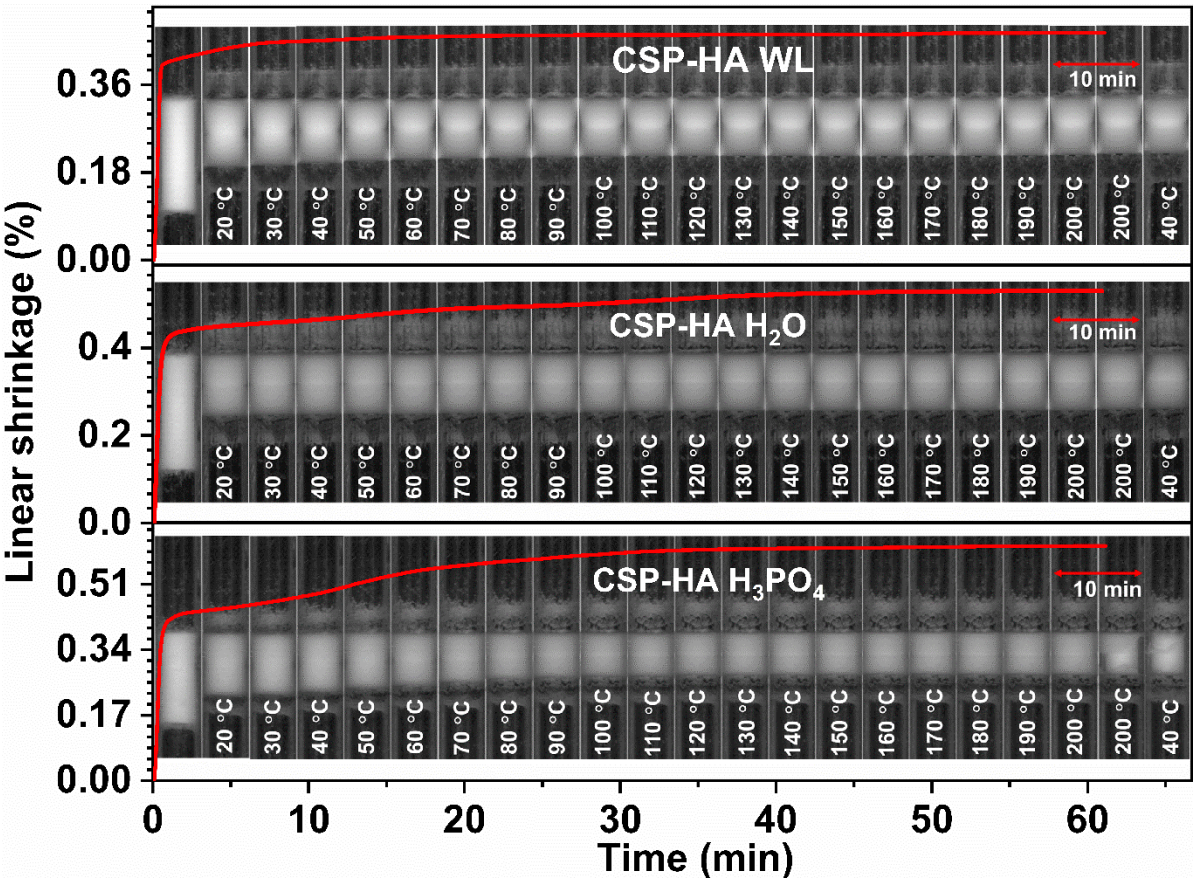

Figure 4.9 *Relative linear shrinkage profile (vs time) measured from the relative changes in the sample length during the CSP of HA (HAp202 powder) without liquid, with H_2O, and with 2 M H_3PO_4. (Inset) Corresponding* in-situ *sample image frames of particular temperature intervals.*

The dynamics of the dissolution-precipitation-recrystallization process driven by the H_3PO_4 during the II and III stages of CSP were monitored based on in-situ Raman analysis, and the spectral data are illustrated in Fig. 4.10. The in-situ Raman spectra of HA powder (Fig. 4.10(b)) show characteristic bending/stretching of PO_4^{3-} modes at 962 cm^{-1} (ν_1 symmetric P-O stretching), 590 & 608 cm^{-1} (ν_4 O-P-O bending), and 1049 & 1073 cm^{-1} (ν_4 asymmetric O-P-O stretching). The HA powder after mixing with H_3PO_4, two new bands appear at ~879 cm^{-1} (weak shoulder) and 986 cm^{-1} (sharp), attributable to HPO_4^{2-} modes [242-244]. This reveals the early precipitation of calcium hydrogen phosphate dihydrate (DCPD, $CaHPO_4{\cdot}2H_2O$) on HA surfaces via protonation of surface PO_4^{3-} groups and subsequent binding of HPO_4^{2-} to exposed Ca^{2+} sites. XRD collected immediately after mixing HA with H_3PO_4 (Fig. 4.10(b)) confirms the presence of DCPD. During subsequent heating (Stages II and III), the intensities of the HPO_4^{2-} related bands (normalized to 962

cm^{-1}) decrease progressively from 25 °C to ~90 °C; beyond ~90 °C and through isothermal holding and cooling, no further intensity changes were noticed (Fig. 4.10(c)). Concomitantly, after 90 °C, the ~879 cm^{-1} band shifts to ~897 cm^{-1}, and the 986 cm^{-1} band broadens into a halo, indicating structural reorganization of the intergranular phase (DCPD) [244-246].

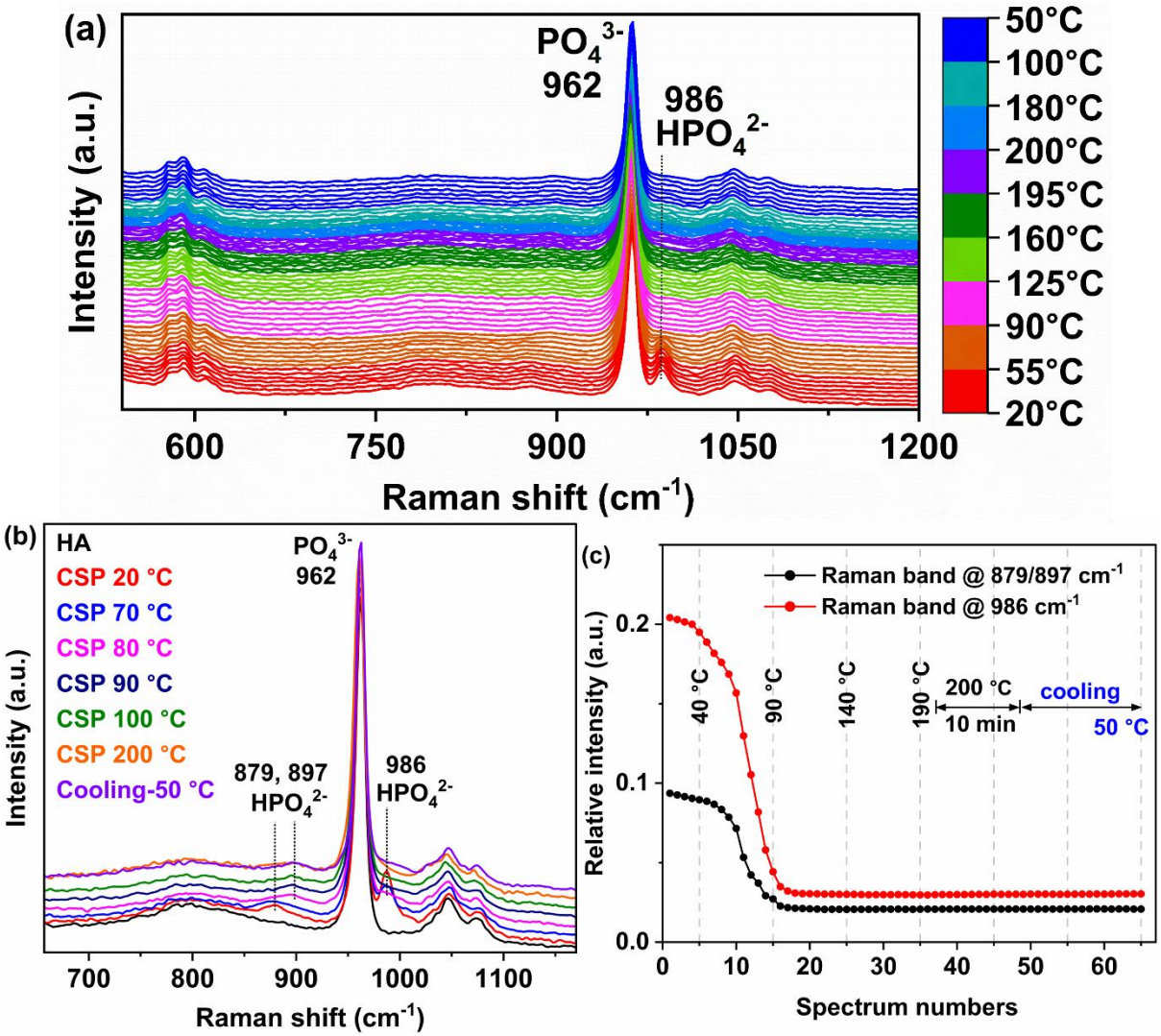

Figure 4.10 *(a) Overall* in-situ *Raman spectra acquired every 60 s during CSP of HA with 2 M H_3PO_4 (T = 200 °C). At this acquisition rate, each spectrum during the heating ramp corresponds to ~5 °C; spectra were also recorded during the isothermal holding (10 min) and cooling cycle (to 50 °C). (b) Selected spectra at specific temperatures spanning the heating and cooling stages. (c) Relative intensity of the HPO_4^{2-} bands normalized to the main PO_4^{3-} band (962 cm^{-1}). The dashed line in the inset indicates the temperature segments; each data point corresponds to a spectrum shown in panel (a).*

The operative Stages II–III begin with dissolution at stressed grain contacts driven by the protonation of surface PO_4^{3-} group of HA ((HA surface) PO_4^{3-} + $H^+ \rightleftharpoons$ (HA surface) HPO_4^{2-}). This weakens Ca-O-P linkages, and the conjugate base in aqueous medium (HPO_4^{2-} of H_3PO_4), attaches to exposed surface Ca^{2+} sites, thus forming a thin acid-phosphate interphase (as hydrated $Ca_{10-x}(PO_4)_{6-x}(HPO_4)_x(OH)_{2-x}$ layers, referred to as DCPD) [231, 246]. Under uniaxial load, this transient interphase acts as a necking bridge between neighboring grains, sustaining continued pressure-solution/precipitation mediated by the aqueous environment and chemical/pressure gradients until a saturation regime is reached near 90-100 °C. Above ~100 °C, the dehydration process initiated: gradual evaporation of water from the HA compact, dehydration of the DCPD layer, and recrystallization into anhydrous form (DCPA-$CaHPO_4$). This sequence of dissolution → precipitation → recrystallization events drives substantial shrinkage during Stages II–III.

Further, the ex-situ control experiments highlight the role of pressure on the above-discussed transformations. HAp202 powder was mixed with 2 M H_3PO_4 and heated without compaction (free powder form) in an oven (5 °C min^{-1} to 200 °C, 10 min hold). XRD patterns recorded before and after heating are given in Fig. 4.11, indicating that the surface precipitated DCPD present before heating transforms to the anhydrous DCPA (Fig. 4.11(b & c) after heating. In contrast, the XRD reflections for DCPA are absent in cold-sintered HA compacts (Fig. 4.5(a)). However, changes in the lattice parameter values (a & c), the Ca/P ratio (given in Fig. 4.6(a & b)), and the corresponding FTIR spectral changes (Fig. 4.5(c & d)) support the incorporation of HPO_4^{2-} into the apatite lattice. Correlating these observations with the persistence of HPO_4^{2-} signatures in the in-situ Raman spectra supports that the HPO_4^{2-} group is chemically incorporated into the HA lattice at Ca^{2+} sites -i.e., formation of HPO_4^{2-} substituted HA ($Ca_{10-x}(PO_4)_{6-x}(HPO_4)_x(OH)_{2-x}$) rather than discrete DCPD/DCPA precipitated phases. Thus, applied pressure is pivotal in steering reaction pathways and recrystallization dynamics during CSP of HA.

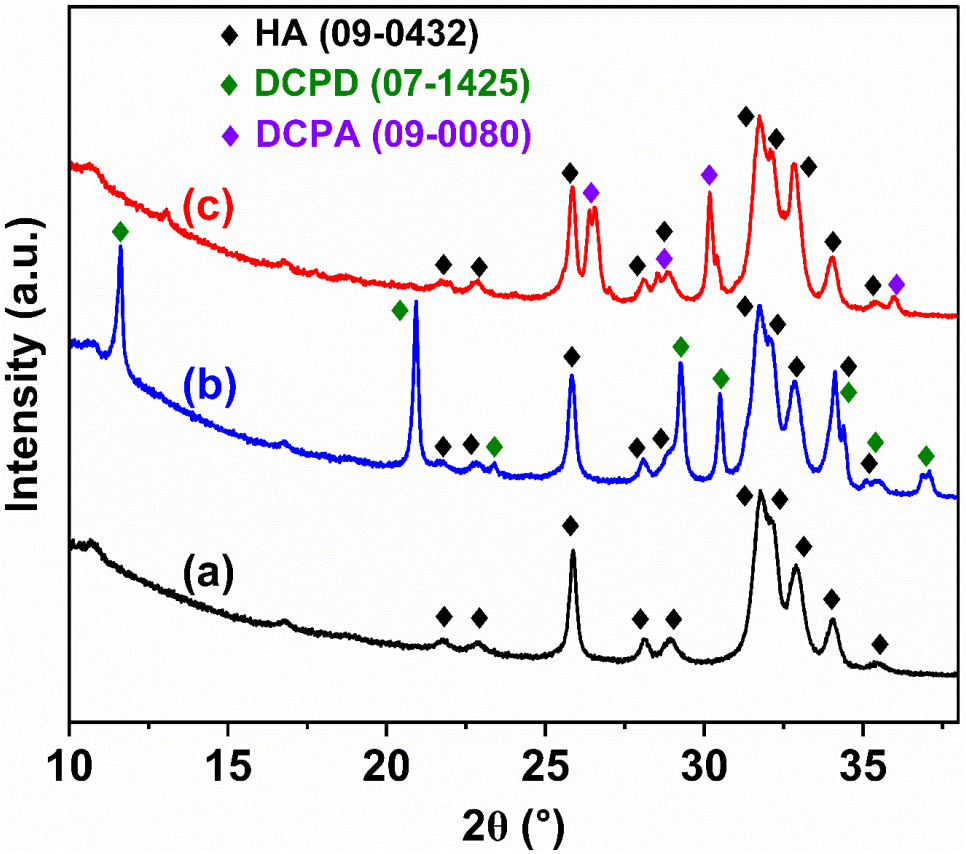

Figure 4.11 XRD patterns of (a) HA powder (HAp202), (b and c) HA powder mixed with 2 M H_3PO_4 solution before and after heating treatment, respectively. The heat treatment was carried out in powder form at 200 °C (5 °C/min, 10 min isothermal holding).

4.6 CSP mechanism of HA densification

In line with the ex-situ, in-situ data presented in Sections 4.4 and 4.5, Fig. 4.12 presents a generalized schematic of the mechanisms governing HA densification during CSP.

In all cases of cold sintering, the initial application of pressure (CSP Stage I) promotes particle rearranging and contact flattening through plastic deformation, producing a densely packed assembly of HA grains. Stage I is intensified when a transient liquid phase is present, due to viscous-flow-assisted plastic deformation, and establishes a pressure gradient across grain contacts and intergranular pores [243]. CSP stages II and III then facilitate mass transfer via dissolution, diffusion, precipitation, recrystallization, and solvent evaporation processes collectively referred to as pressure-solution creep.

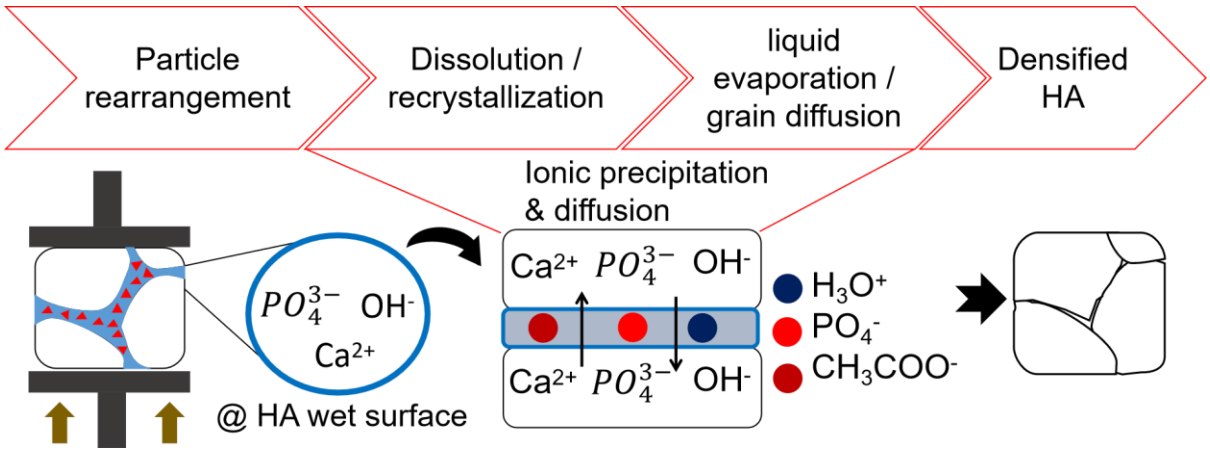

Figure 4.12 *Schematic illustration of the densification mechanism that occurs during the cold sintering of HA.*

When the cold sintering is performed without liquids, pressure-solution creep is no longer the primary densification mechanism; densification proceeds mainly through stress-induced plastic deformation and grain-boundary sliding. Adsorbed water on the HA surface can still promote intergranular hydrogen bonding, as proposed by Shen et al. [52] (Fig. 4.13(c)). Although the HAp202 powder holds 5.6 wt.% (indicated by TGA (Fig. 4.5(b)) adsorbed water, the resulting densification remains modest.

When the cold sintering is performed with transient liquid, pressure-solution creep dominates, but its efficacy depends on the specific HA-liquid chemistry. In case of H_2O, which auto-ionizes to produce H_3O^+ ions, incongruent dissolution of HA (as described in Reaction 4.1) cannot proceed under neutral to mildly basic pH conditions. Instead, mass transfer is primarily promoted by partial ionic substitution and hydrogen bonding, as illustrated by Shen et al. (Fig. 4.13(c)) [52]. Here, hydronium ions solvate PO_4^{3-} groups of HA and facilitate their partial substitution with HPO_4^{2-} within the HA lattice [239]. This mechanism is supported by the slight yet measurable shifts in lattice parameters (Fig. 4.6 (a)) and the corresponding FTIR spectral changes (Fig. 4.5(c & d)). Additionally, the formation of H_3O^+ allows for hydrogen bonding to type B carbonate sites ($CO_3^{2-} \rightarrow HCO_3^-$) in the crystal lattice, which further contributes to the observed lattice-parameter variations [52].

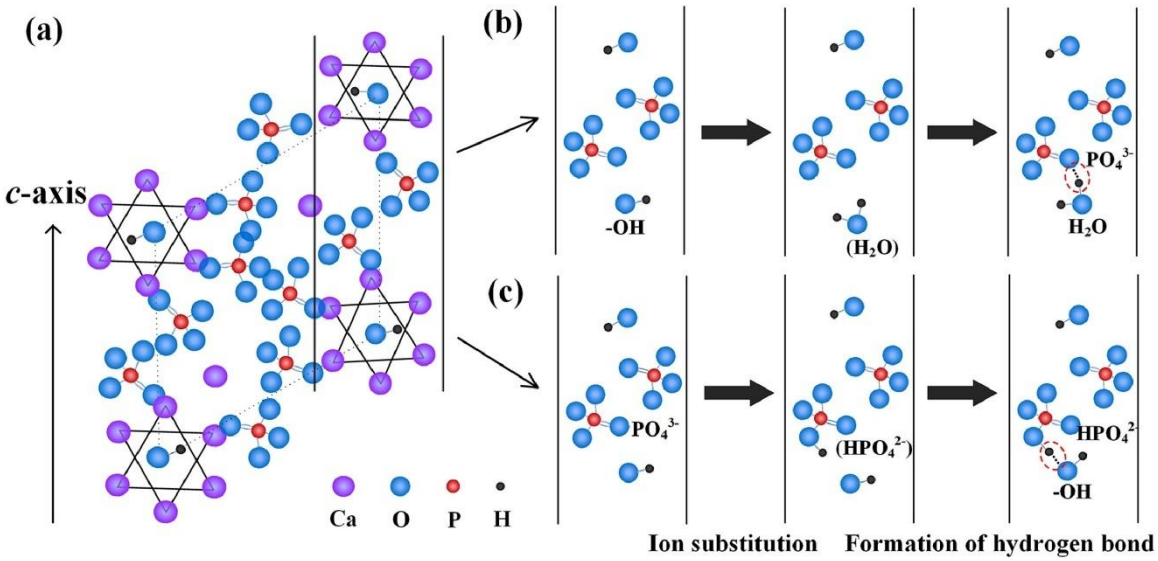

Figure 4.13 *Schematic illustrations of (a) HA crystal structure and (b-c) two models of ion substitution and formation of H-bonding in HA during CSP (since Ca^{2+} ions are not involved in ion substitution and formation of H-bonding, they are not shown in diagrams (b) and (c)) [52].*

Cold sintering with acid solutions, AcOH and H_3PO_4, can initiate incongruent dissolution at the HA surface and drive the formation of transient thin $Ca_{10-x}(PO_4)_{6-x}(HPO_4)_x(OH)_{2-x}$ layers [230, 231, 245]. With AcOH, its weak ionizable nature (pK_a = 4.76) produces low $[H_3O^+]$, leading to mild surface protonation, and precipitate hydrated acetate anion in the HA crystal lattice (at Ca^{2+} sites), which is then recrystallized to the dehydrated form. These surface reactions are analogous to CSP of ZnO with acetic acid, but are not efficient in HA. In contrast, H_3PO_4 solution generates a much higher proton activity, promoting extensive incongruent dissolution of HA, nucleation of $Ca_{10-x}(PO_4)_{6-x}(HPO_4)_x(OH)_{2-x}$ layers, at grain boundaries, and recrystallizes as HPO_4^{2-}-substituted HA, as detailed in section 4.5 [219, 229]. This pressure-solution creep sequence, yielding superior grain consolidation (see microstructure in Fig. 4.4(d)). Overall, H_3PO_4 solutions are the right transient liquid for effective densification of HA at low temperature.

4.7 Conclusions

This work highlights the pivotal role of transient liquid phase chemistry in the cold sintering process framework of HA. The commercial HA powders were successfully cold sintered under 360 MPa and 200 °C, using transient liquids such as water, aqueous

solutions of acetic and phosphoric acid. The densification was found to be increased concerning the chemistry of the transient liquid as well as the ionic strength of the corresponding acid-liquids, which strongly demonstrated their influence in dictating the HA densification. Notably, the 2 M H_3PO_4 was identified as a suitable transient liquid for cold sintering HA with a maximum densification of up to 90 %. Furthermore, the XRD measurements and SEM observations confirmed the ability of the cold sintering process to preserve the original phase and grain size of hydroxyapatite even when a 2 M ionic concentration of acid liquids was utilized. However, the use of 2 M H_3PO_4 slightly changes the lattice parameters and stoichiometry of HA, owing to the ionic substitution resulting from the dissolution-recrystallization process.

Further, the influence of physical parameters such as surface area and crystallinity of HA on densification during CSP was demonstrated using cold sintering of calcined HA powders (600 & 900 °C) with 2 M H_3PO_4. The HA Powder calcined at 600 °C (high SSA, lower crystallinity) achieved ~82 % relative density, undergoes uniform dissolution with minimal reprecipitation of secondary dicalcium phosphate (DCPA) formation, and a dense microstructure. In contrast, the 900 °C powder (low SSA, higher crystallinity) showed localized surface dissolution with excessive DCPA reprecipitation, limited particle rearrangement, and a loosely packed grain microstructure. The extent of DCPA formation thus indirectly reflects phosphoric acid's reactivity at the HA surface, driving the chemo-mechanical mechanisms that govern densification.

Further, the underlying pressure-solution creep event and its dynamics during CSP of HA with H_3PO_4 were successfully resolved by combining a miniature transparent-die CSP setup and in-situ Raman analysis. The Raman reveals the dissolution-precipitation drives formation of acid-phosphate interphase (DCPD; ~879 and 986 cm^{-1}) at grain contacts, which saturates near 90-100 °C, subsequently recrystallizes/dehydrates above ~100 °C. Correlating in-situ Raman with ex-situ controls establishes the central role of pressure: it not only increases grain contact and particle rearrangement, but it also redirects reaction pathways. Under pressure, the surface precipitated DCPD recrystallizes to substituted HA form ($Ca_{10-x}(PO_4)_{6-x}(HPO_4)_x(OH)_{2-x}$). Without pressure, DCPD transforms to DCPA rather than HA.

Overall, this study offers new, valuable insights into the significance of liquid phase chemistry and physical properties of HA powders in the cold sintering process, particularly for achieving nano-level densification of bio-active ceramics. Given the pressure-solution creep framework of CSP, HA densification is effective only with reactive transient liquids such as H_3PO_4. Mechanistically, CSP of HA with water and without liquid routes is dominated by pressure-assisted rearrangement and hydroplastic flow, with limited diffusional contribution.

Future study directions must focus on a comprehensive understanding of the biological and mechanical properties (compressive strength/fracture toughness before and after bioactivity tests) of cold sintered HA to accelerate its translation as dense implants for bone-regeneration applications.

Chapter 5: Cold Sintering Process Framework for Ternary Bioglass

5.1 Context

Since the introduction of Bioglass (45S5 - 46.1 mol% SiO_2, 24.4 mol% Na_2O, 26.9 mol% CaO, 2.6 mol% P_2O_5) by Hench et al. in 1969, recent decades have witnessed the development of variants of bioglass compositions, including silicate-based, borate-based, and phosphate-based systems [92, 24, 108-112]. Among the silicate-based bioglasses, sol-gel-derived ternary glass systems (SiO_2-CaO-P_2O_5) developed by Li et al. in 1991 have received significant interest for their distinctive characteristics, such as processing flexibility, improved thermal stability, and broader compositional tunability for specific clinical needs [25-28]. Unlike 45S5, ternary systems typically exclude alkali oxides, resulting in higher network connectivity and greater resistance to devitrification. Importantly, the sol-gel method provides several advantages over the conventional melt-quenching method of glass preparation. It includes lower processing temperatures, high chemical purity, a broad alkali-free compositional range, and reduced processing steps and time [25, 26].

As highlighted by Li et al., ternary bioglass with an optimized composition of ~50-55 mol% SiO_2, 40-45 mol% CaO, 4-5 mol% P_2O_5 has balanced glass-forming ability and bioactivity [25]. However, these ternary glasses still undergo crystallization at elevated sintering temperatures (> 700 °C), which influences the bioactivity [31-33, 247-249]. For instance, Ma et al showed that the 58S sol-gel derived ternary bioglass (58 mol% SiO_2, 38 mol% CaO, 4 mol% P_2O_5) begins crystallization during sintering above 700 °C and transforms into a glass-ceramic containing wollastonite, pseudo wollastonite, β-tricalcium phosphate, and other calcium phosphate phases at temperatures exceeding 1000 °C [31]. A similar observation was also reported by Román et al. in a 55S sol-gel derived ternary glass system (55 mol% SiO_2, 41 mol% CaO, 4 mol% P_2O_5) [248]. Both these studies emphasize that the high temperature-induced amorphous-to-crystalline transition markedly reduces their bioactivity tested in simulated body fluid [31, 247, 248].

Although many studies on ternary bioglass sintering focus primarily on phase evolution and bioactivity, the mechanical performance depends critically on both densification and phase composition. Amorphous glasses generally exhibit lower stiffness than their glass-ceramic counterparts. Dehagani et al. investigated a 58S sol-gel derived nano bioglass powder (58.3 mol% SiO_2, 37.3 mol% CaO, 3.2 mol% P_2O_5) and reported that samples sintered at 600 °C remained fully amorphous with an elastic modulus of ~17 GPa, whereas those sintered at 1000 °C developed crystalline phases (tricalcium phosphate and wollastonite) and attained an elastic modulus of ~47 GPa [28]. Thus, conventional high-temperature sintering poses a great challenge for producing ternary bioglass-based synthetic grafts without crystallization, while maintaining bioactivity with optimal mechanical properties [28, 29].

The cold sintering process, as a low-temperature non-conventional sintering method, provides a promising solution to overcome the drawbacks of high-temperature sintering. To date, the CSP framework for ternary bioglass systems has not been thoroughly explored, and only a few bioglass types have been researched within the concept of low-temperature and high-pressure consolidation techniques.

Degraeve et al. utilized hydrothermal hot pressing (HyHP) to fabricate a porous monolith of sol-gel derived 50S ternary bioglass (50 mol% SiO_2, 40 mol% CaO, and 5 mol% P_2O_5, wt.%), using water or a 2 M NaOH solution, without observing crystallization [250]. Olivera et al. demonstrated the cold sintering of a TCP-bioglass composite, achieving 85 % density for the composite containing 60 % S53P4 bioglass (53 mol% SiO_2, 20 mol% CaO, 23 mol% Na_2O, and 4 mol% P_2O_5, wt.%) at 166 MPa and 200 °C using water as a transient liquid [219]. Andrews et al. reported achieving ~95 % relative density for cold sintered 45S5 bioglass (200 MPa/ 100 °C) using 80 wt.% water as a transient liquid, without crystallization [220]. Taveri et al. documented the consolidation of 45S5 bioglass without crystallization to densities exceeding 97 % using water or 1 M NaOH solution by cold isostatic pressing at 400 MPa [251]. Nawaz et al. studied 45S5 bioglass consolidated by cold hydrostatic pressing with water, reaching approximately 75 % density without crystallization [252].

Although all of these approaches couple high pressure with a transient liquid phase, the underlying sintering mechanisms were poorly understood. Moreover, CSP is

conceptually and experimentally distinct from cold-isostatic pressing (CIP) and HyHP. In the previous chapter, it was found that the HA densification is strongly governed by the chemistry of the transient liquid, and a 2 M H_3PO_4 solution enabled achieving 90 % densification driven by pressure-solution creep phenomena. In the case of bioglass materials, the key sintering parameters, especially the effect of transient liquids and the dominant densification mechanisms, remain largely unexplored within the CSP framework.

This chapter investigates the role of liquid chemistry and its influence on the densification of sol-gel derived 50S ternary nano bioglass powder (50 mol% SiO_2, 40 mol% CaO, and 5 mol% P_2O_5, wt.%). A systematic study has been conducted to elucidate the densification mechanism, concerning the transient liquids viz., H_2O, NaOH & H_3PO_4, as well as their effect on microstructure evolution, phase, physical, and mechanical properties. The use of NaOH is chosen based on the study reported by Taveri et al., and also, the literature claims that the cold sintering of silica is effective with NaOH [211, 212, 251]. So it is decided to compare the 2 M concentration as optimized in Chapter 4. The cold sintering of the BG was performed using previously optimized CSP parameters (360 MPa pressure, 200 °C, 10 min holding time, and a 5 °C/min heating ramp) established for HA densification. Finally, the progress of densification and the dynamics of dissolution-precipitation-recrystallization (pressure-solution creep) events were investigated by deploying a custom-built transparent CSP setup and in-situ time-gated Raman analysis to describe the underlying CSP mechanism.

5.2 BG Powder Characteristics

Fig. 5.1 illustrates the physicochemical characterization of the as-received 50S BG powder. The XRD pattern in Fig. 5.1(b) confirms the sol-derived 50S BG is completely amorphous (SiO_2-rich network), indicated by the appearance of two broad halos centered around 2θ, ~20-23°, and ~28-31°. This observation is consistent with related ternary bioglasses of near-similar compositions [248-253]. The SEM micrograph in Fig. 5.1(a) reveals that the 50S BG powder consists of fine nanoscale particles aggregated into micron-sized, angular, or blocky cluster morphologies. The particle aggregate size distribution curve (Fig. 5.1(c)) further confirmed that the BG powder has micron-sized

particles of different size distribution range from 2-100 μm (the percentile size distribution is indicated in the inset of Fig. 5.1(c)). The TGA result presented in Fig. 5.1(d) indicates a mass loss of ~ 2.8% up to 200 °C (temperature corresponding to CSP). This weight loss is attributed to the removal of absorbed water, suggesting the BG powder contains ~2.8% moisture.

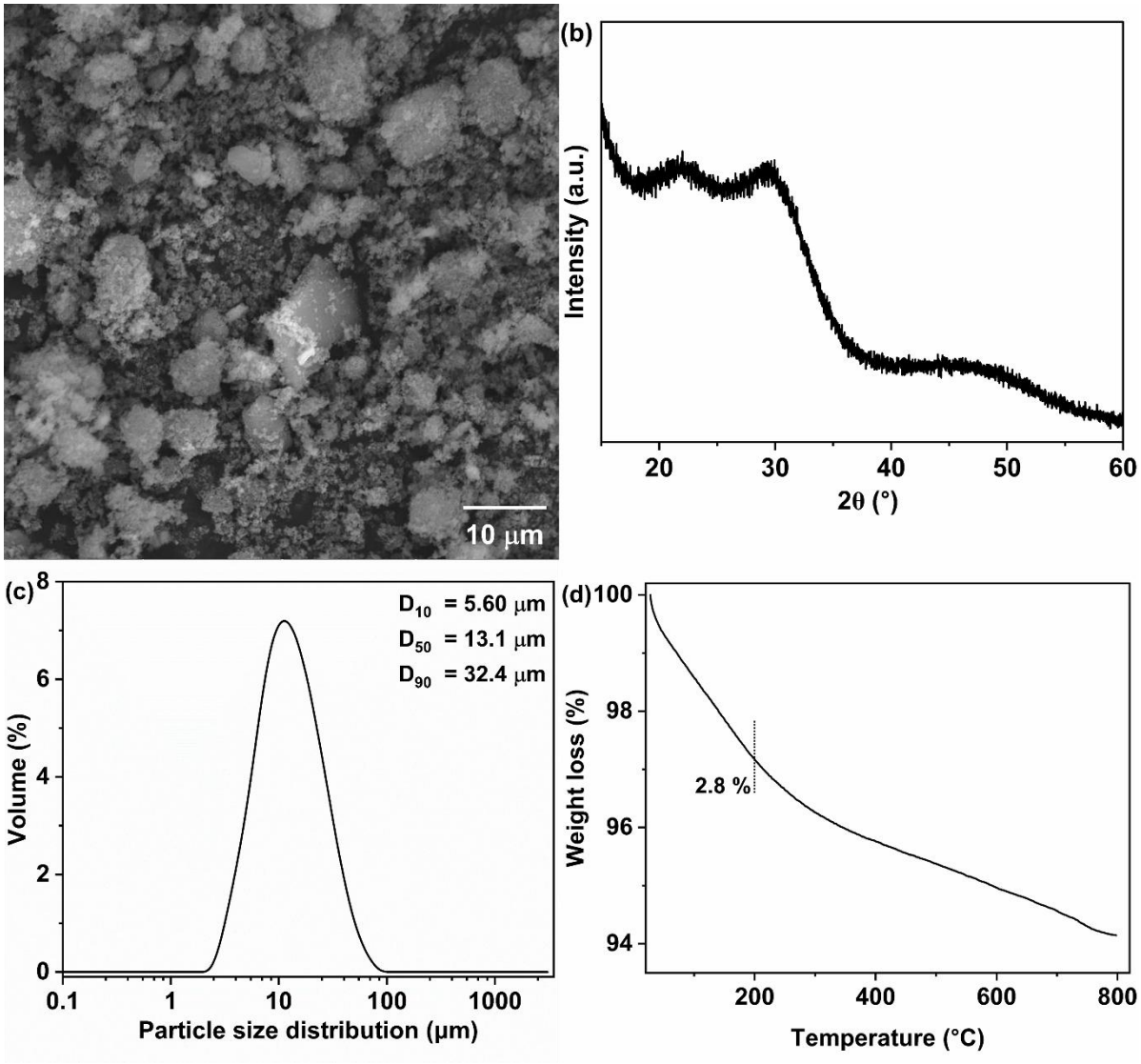

Figure 5.1 (a) SEM morphology, (b) XRD pattern, (c) particle aggregate size distribution, and (d) thermogram of the sol-gel derived 50S BG powder.

5.3 BG Conventional Sintering

The 50S BG powders were sintered conventionally to evaluate the impact of high-temperature application. The sintering temperature was chosen based on the differential thermal analysis (DTA) results reported by Degraeve et al., given in Fig. S2 (Appendix A)

[250]. As this BG powder has three crystallization points, T_{c1}, T_{c2}, and T_{c3} at temperatures 893, 879, and 1228 °C, respectively, which correspond to crystallization of different silicates and calcium silicate phases. Thus, an optimal temperature of 1000 °C was chosen as the sintering temperature for effective densification with limited crystallization [250]. The entire sintering process lasted around 8 h, including heating-cooling cycles. After sintering, the BG samples achieved an average relative density of around 98.0 ± 0.2 % with open and total porosity accounting for 1.8 ± 0.4 % and 5.1 ± 0.2 % respectively.

The SEM micrograph in Fig. 5.2(left) reveals a dense microstructure of fine-grained crystals embedded in a glassy-like matrix with visible interconnected/open pores. The relatively smooth, glassy-like surface indicates that the densification occurs via viscous flow accompanied by crystallization during high-temperature treatment [254, 255]. This interpretation is consistent with the XRD patterns given in Fig. 5.2(right), which display a broad halo in the low-angle region, roughly between 15-25° 2θ, superimposed with numerous sharp reflections characteristic of a crystalline phase. The major crystalline phases identified are wollastonite (β-$CaSiO_3$) (ICDD 43-1460), HA (ICDD 09-0432), and β-TCP (ICDD 09-0169). The high-temperature sintering transforms the 50S BG into a glass-ceramic composite; a similar kind of observation was reported in 58S and 60S bioglass systems sintered above 1000 °C [28, 253-252].

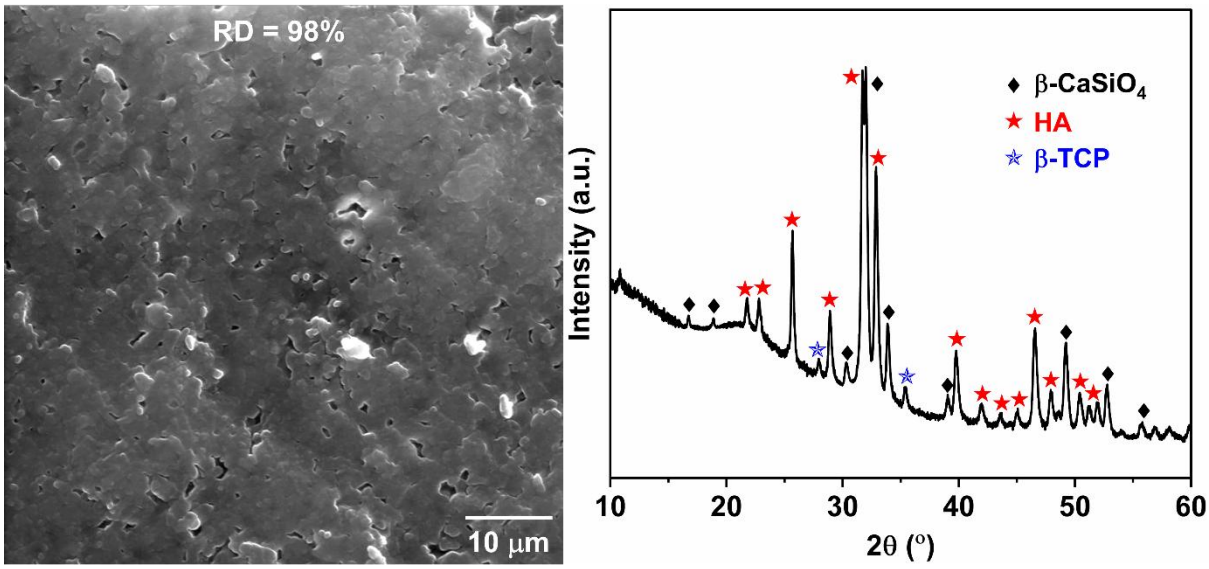

Figure 5.2 *(left) SEM microstructure image (fractured surface) and (right) X-ray diffraction patterns of conventionally sintered 50S BG at 1000 °C.*

As the sintering temperature is 1000 °C, which is beyond the exothermic crystallization (T_{c1} and T_{c2}) reported by Degraeve et al., it is expected that the initial densification is expected to be facilitated by viscous flow [250, 255]. Subsequently, the diffusion-controlled solid-state reactions occur among the constituents of BG; CaO-rich domains react with the SiO_2 network to form wollastonite (β-$CaSiO_3$), while CaO and P_2O_5 combine to yield HA and β-TCP. These crystalline precipitates locally control the viscous flow, and they then recrystallize in the residual glassy matrix [254, 255].

Microindentation analysis on the sintered BG deduced an average reduced elastic modulus $E_r = 62 \pm 4$ GPa and a Vickers hardness value 486 ± 6 (HV20). In comparison, the measured elastic modulus and hardness values are higher than reported for 58S BG sintered at 1100 °C (Elastic modulus 47.9 GPa and Vickers Hardness 159.7), reflecting the composition of a major crystalline phase (HA, TCP) than the glassy phase after sintering at 1000 °C [28]. Also, the measured hardness value of BG is not far from the hardness value (571 HV20) of pure HA sintered at 1200 °C (RD 95-96 %) reported in section 4.3 (Chapter 4), further witnessing that the co-existence of more crystalline HA, $CaSiO_4$, and TCP phases endows the BG (glass-ceramics) with good mechanical properties.

5.4 BG Cold Sintering Process

5.4.1 Density Evolution vs Liquid Phase Chemistry

Fig. 5.3(a) shows the volumetric shrinkage profile (displacement vs time) recorded during CSP of BG at 360 MPa using different transient liquids. During the first stage of CSP under pressure application, consolidation is dominated by particle rearrangement and plastic deformation flattening [243]. This initial stage of CSP is influenced by the type of transient liquid used, as indicated by the difference in volumetric shrinkage observed during the 15 min hold time at 360 MPa. The use of transient liquid reduces the interparticle friction and enables hydroplastic flow, so their lubrication ability influences the initial consolidation in stage I of CSP [243]. Among the transient liquids tested, 2 M NaOH enables the largest volume shrinkage, indicating the greater consolidation of BG particles, which can be rationalized by its higher viscosity nature (lubrication effect) compared with 2 M H_3PO_4 or water at room temperature.

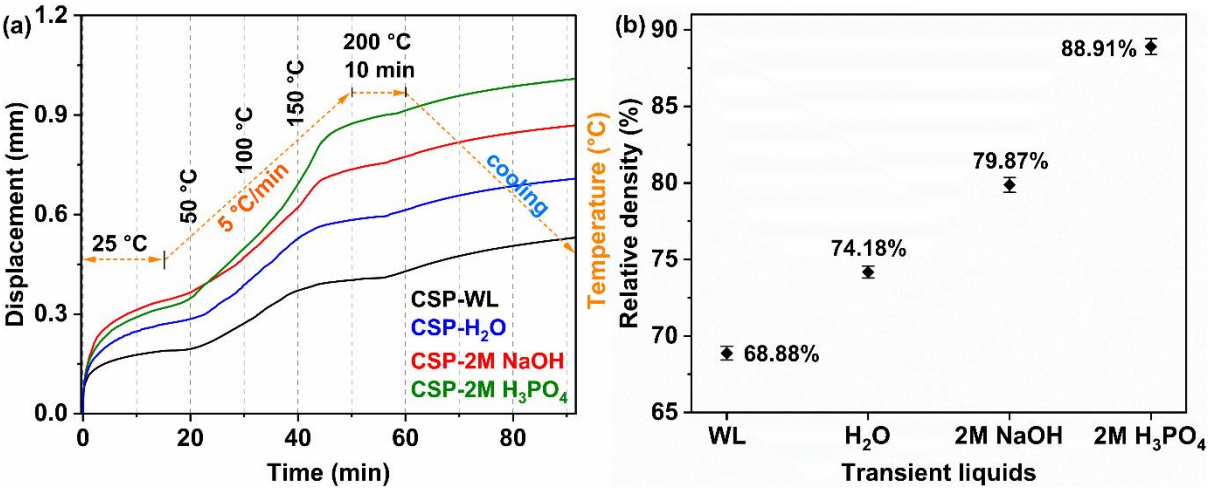

Figure 5.3 *(a) Comparison of total volume shrinkage profile (displacement vs time) obtained during the CSP of BG under 360MPa at 200 °C using different transient liquids and (b) the calculated average relative density values of the densified 50S BG corresponding to transient liquids. The measured volumetric shrinkage profile represents the total displacement, not corrected for the thermal expansion of the die.*

Following the initial stage of CSP (particle rearrangement), the dissolution-precipitation-recrystallization-liquid evaporation (stages 2 & 3 of CSP) occur only during the heating ramp. These chemo-mechanical mechanisms contribute additional volume shrinkage and enable mass transport via ionic diffusion under combined pressure and chemical gradients. Although the volume shrinkage curve is not relevant to pinpoint, the observed comparable differences in Fig. 5.3(a) during heating rationally support that the dissolution-precipitation mechanism seems more vigorous with 2 M H_3PO_4 than 2 M NaOH or H_2O. The exact dynamics associated with dissolution-precipitation-recrystallization during CSP of BG with H_3PO_4 are detailed in section 5.6.

The calculated relative density values were illustrated in Fig. 5.3(b). The CSP of BG without liquid only enabled ~68 % densification. The use of transient liquids significantly improved densification, reaching up to ~89 % with 2 M H_3PO_4. These data demonstrate that phosphoric acid is more effective than NaOH or water in activating pressure-solution creep and accelerating densification during cold sintering of 50S BG.

5.4.2 Phase and Chemical Characteristics

The calculated relative density values and the volume shrinkage profile (Fig. 5.3) illustrated the dependency of the transient liquid phase on BG densification. The underlying effects of transient liquid on the phase and chemical structure are presented in Fig. 5.4.

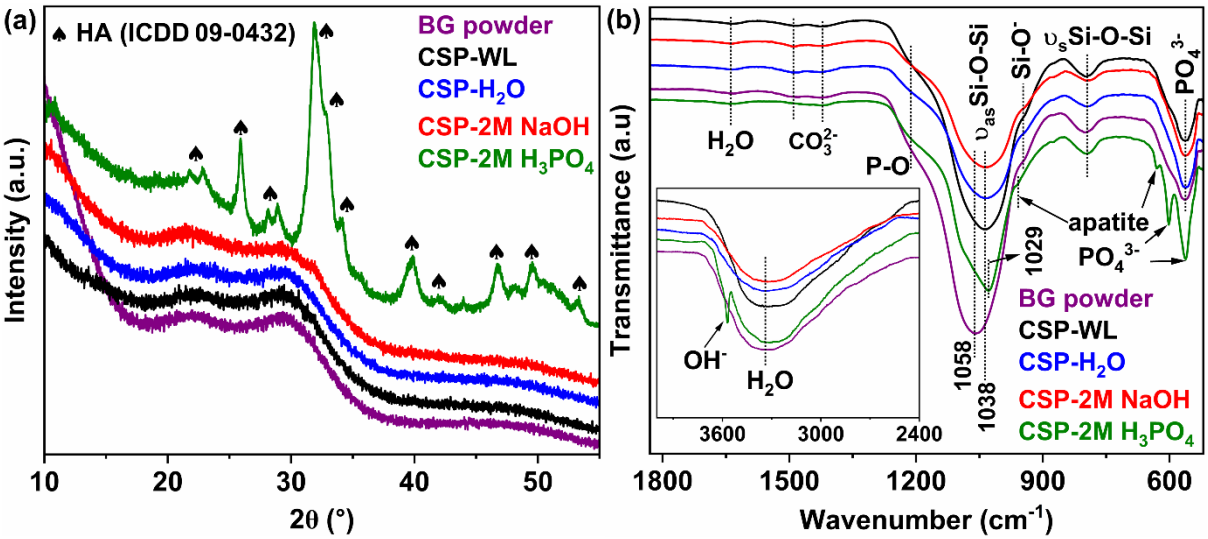

Figure 5.4 *(a) XRD patterns and (b) FTIR spectrum (wavenumber 1830-520 cm^{-1} with inset image (wavenumber 4000-2400 cm^{-1})) of the 50S BG after CSP with different transient liquids.*

The XRD patterns of cold sintered 50S BG without liquid, with H_2O, or with 2 M NaOH retain the two broad halos (centered around 2θ, ~20-23°, and ~28-31°) characteristic of amorphous BG powder, indicating that no significant crystallization occurs after cold sintering. In the case of CSP of BG with 2 M H_3PO_4, the XRD pattern shows a overlapped broad halo along with sharp/broad crystalline XRD peaks corresponding to the HA phase (ICDD 09-0432), indicating that H_3PO_4 promoted the partial crystallization of BG. This partial crystallization reflects that the phosphoric acid's localized pH-driven chemical reactivity (dissolution-precipitation) with BG constituents (CaO/P_2O_5) and re-precipitation into secondary phases (HA) at the glass network during the CSP. These XRD results highlight that, phosphoric acid produces glass-ceramic after CSP due to in-situ HA formation, whereas water and NaOH retained the glassy phases.

The chemical structure and probable chemical reaction pathways during the CSP of BG with different transient liquids can be argued based on the qualitative observation from the FTIR spectrum given in Fig. 5.4(b). The amorphous 50S BG powder exhibits the vibration bands associated to the silicate network centered at 796, 950 (shoulder) and 1058 $cm^{-1,}$ which are assigned respectively to Si–O–Si symmetric stretching (SiO_4 tetrahedra network), Si–O– stretching (non-bridging oxygen), and Si–O–Si asymmetric stretching mode (SiO_4 tetrahedra network) respectively. The vibration bands around 563 (broad single peak) and 1210 cm^{-1} (broad shoulder) are characteristic of the amorphous PO_4^{3-} group (orthophosphate) [247, 250].

After cold sintering without liquid, with H_2O or 2 M NaOH, the main Si–O–Si asymmetric stretching peaks shift to 1038 cm^{-1}, signifying increased formation of non-bridging oxygen caused by dissolution-precipitation reactions [250, 252]. In aqueous medium, the silicate network undergoes depolymerization (hydrolysis reaction) according to relations 5.1 & 5.2, and the silanol can repolymerize (during dehydration above the boiling point of water) into a silicate network along with partially cation modifiers (Na^+ or H^+, or Ca^{2+}), capped silanol network, creating more non-bridging oxygen [250, 252]. These congruent dissolution pathways are more aggressive in alkaline NaOH (pH >10) than in H_2O (pH <8), which justifies the superior densification observed with NaOH compared to H_2O. By contrast, in CSP without liquid, the limited absorbed water is insufficient to drive substantial dissolution–precipitation, yielding lower densification. Furthermore, the peaks for the apatite phosphate group were not observed, confirming that the water or NaOH reacted solely with the silicate network, not with the PO_4^{3-} group (hydrolysis and reprecipitation of calcium phosphates) of BG.

$$\equiv Si–O–Si\equiv + H^+OH^- \rightarrow \equiv Si–O–H + \equiv Si–OH \qquad (5.1)$$

$$\equiv Si–O–Si\equiv + Na^+OH^- \rightarrow \equiv Si–O–Na + \equiv Si–OH \qquad (5.2)$$

The FTIR spectrum of cold sintered BG with H_3PO_4 exhibits new vibrational peaks corresponding to apatite phosphate groups (HA) (960(shoulder), 628, 600 & 560 cm^{-1}. This observation strongly supports that the phosphoric acid promotes an incongruent dissolution-precipitation mechanism; HPO_4^{2-} ions from H_3PO_4 react with the CaO/P_2O_5 components of the glass (after hydrolysis) to form a metastable brushite ($CaHPO_4 \cdot 2H_2O$)

intermediate, which subsequently recrystallizes into HA. Such a brushite-to-HA transformation during cold sintering has been reported earlier [188, 221]. Concurrently, the observed redshift of the Si–O–Si asymmetric stretching peak to 1029 cm^{-1} with skewed overlapped shoulders between 1140-1030 cm^{-1} reflects the acidic-catalyzed depolymerization of silicate network (congruent dissolution), creating non-bridging oxygen (Si–O–P linkages) [250-252]. Consequently, in-situ formation of HA at the glass particle interfaces is the primary driver for enhanced densification compared to H_2O or NaOH.

Therefore, under identical processing parameters (200 °C, 360 MPa), the chemistry of transient liquid dictates distinct dissolution-reprecipitation routes: neutral or basic media drive silicate hydrolysis-condensation and densify the glass without crystallization, while acidic media drive incongruent dissolution and densify BG along with HA crystallization, yielding the highest densification.

5.4.3 Microstructure and Mechanical Property

The SEM images in Fig. 5.5 depict how the transient liquid influences interparticle bonding that contributes to microstructural evolution. The SEM microstructure of BG cold sintered without liquid (Fig. 5.5(a)) exhibits rough, plastically deformed BG particles with randomly bonded necks, indicating poor dissolution-reprecipitation, and minimal densification. The BG compact after cold sintering without liquid exhibited reduced surface area as well as pore volume compared to the BG powder, which indicates that the residual water molecules only contribute minimal chemical interactions at the BG particle surface, primarily promoting intergranular bonding under applied pressure and heat. These microstructural features exhibited lower average reduced elastic modulus and hardness values (given in Table 5.1) compared to other samples, which can be attributed to the amorphous phase as well as limited densification achieved.

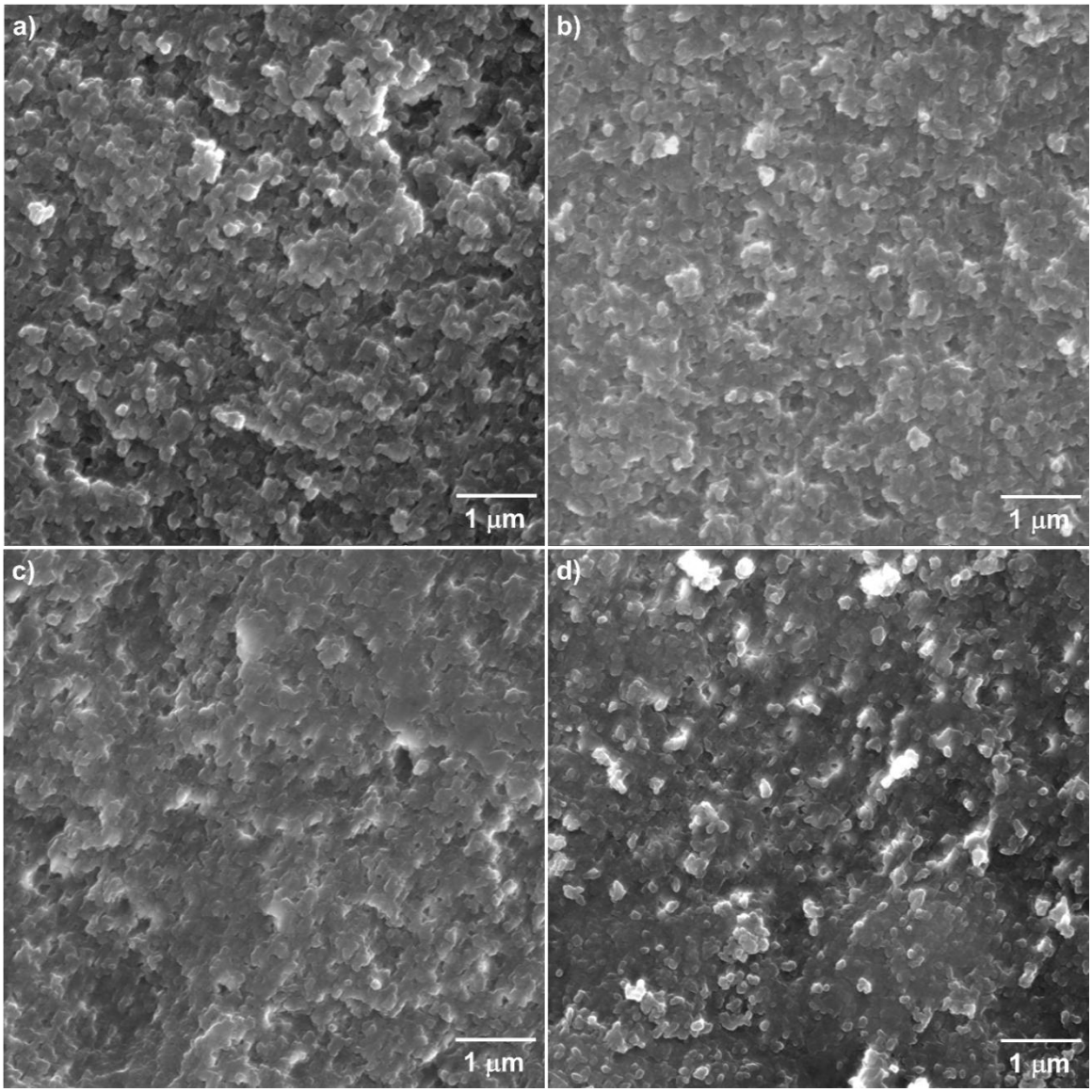

Figure 5.5 *SEM microstructure images (fractured surface) of the cold sintered 50S BG at 200 °C/ 360 MPa (a) without liquid, (b) with H_2O, (c) with 2 M NaOH solution, and (d) with 2 M H_3PO_4 solution.*

Introducing liquids for BG cold sintering yielded a smooth microstructure compared to Fig. 5.5(a). Both the microstructure of BG cold sintered with H_2O and 2 M NaOH (Fig. 5.5(b & c)) exhibits well-bonded BG particles with smooth necks or bridges, interspersed with residual pores. These microstructural features reflect the congruent dissolution-precipitation of the silicate network (discussed in section 5.4.2) at the intergranular particle contact. The BG cold sintered with NaOH exhibits reduced SSA and pore volume with superior mechanical properties (Table 5.1) compared to the BG cold sintered with H_2O. Still, both samples retain the amorphous nature after cold sintering; however,

comparatively, the BG cold sintered with NaOH has a glassy surface with more faded grain boundaries into a continuous matrix than the BG cold sintered with H_2O. Moreover, the increased mechanical properties for BG cold sintered with NaOH are attributed to increased intergranular particle diffusion, aided by the accelerated congruent dissolution-precipitation (section 5.4.2) with 2 M NaOH (pH >10), which promoted more densification than H_2O, as evidenced by the microstructure (Fig. 5.5(b & c)).

The microstructure of BG cold sintered with 2 M H_3PO_4 produces a distinctive dual-phase microstructure: a smooth, glassy-like matrix decorated with HA crystallites (rough faceted particles). This distinct microstructure and XRD patterns (Fig. 5.4(a)), along with SSA/pore volume values compared to other cold sintered BG samples (Table 5.1), confirm that incongruent dissolution-precipitation and in-situ HA crystallization create a densified BG compact. This phase transformation underlies its superior mechanical properties (Table 5.1) than other cold sintered samples. However, the measured average reduced elastic modulus E_r = 40 $\pm$ 6 GPa for the CSP-2 M H_3PO_4 sample is ~16 & 35 % lower than for the conventionally sintered 50S BG at 1200 °C (62 $\pm$ 4 GPa) reported in section 5.3, and 58S sol-gel derived BG sintered at 1100 °C (47.9 GPa) [28].

Table 5.1 *Comparison of physical/mechanical properties of BG samples after CSP.*

Sample	BET specific surface area (m^2/g)	Pore volume (cm^3/g)	Open porosity (%)	Elastic modulus, E_r (GPa)	Vickers Hardness, HV20
BG powder	170	0.751	-	-	-
CSP-WL	97	0.225	29.2 $\pm$ 0.6	14 $\pm$ 4	60 $\pm$ 5
CSP-H_2O	85	0.199	24.0 $\pm$ 0.4	19 $\pm$ 5	89 $\pm$ 4
CSP- 2 M NaOH	77	0.126	19.3 $\pm$ 0.8	29 $\pm$ 4	136 $\pm$ 6
CSP- 2 M H_3PO_4	68	0.091	10.0 $\pm$ 0.5	40 $\pm$ 6	190 $\pm$ 8

5.5 CSP of HA-BG composite

In Chapter 4, HA powders achieved up to 90 % densification when cold sintered with 2 M H_3PO_4. Because BG is more soluble than HA, we hypothesized that incorporating BG as an additive would accelerate dissolution–precipitation, promote HA densification, and yield a ceramic–glass composite microstructure. In line with this, Oliveira et al. reported

that S53P4 bioactive glass (53 % SiO_2, 20 % CaO, 23 % Na_2O, and 4 % PO_4, wt.%) acts as a sintering aid for β-TCP during CSP with 10 wt.% H_2O, with density increasing proportionally to BG content [219].

Accordingly, 50S BG powders were evaluated as a densification aid for CSP of HA. BG was incorporated at 10 wt.% into the HA matrix and cold sintered using 2 M H_3PO_4 without any added liquid for comparison. A higher BG loading (20 wt.%) was also examined using 2 M H_3PO_4. The resulting physical and mechnical properties of the cold sintered HA-BG composite are summarized in Table 5.2. For convenience, the cold sintered composites were named as HA+10BG, and HA+20BG represent the 10 and 20 wt.% BG addition.

Table 5.2 *Comparison of physical/mechanical properties of cold sintered HA-BG and HA samples*

Sample	Relative density	BET SSA (m^2/g)	Pore volume (cm^3/g)	Mechanical properties
CSP-HA WL	66.10 %	32.3	-	$E_r = 20 \pm 4$ GPa $HV20 = 70 \pm 5$
CSP-HA 2 M H_3PO_4	90.60 %	8.6	0.009	$E_r = 63 \pm 7$ GPa $HV20 = 270 \pm 9$
CSP-HA+10BG W/L	68.65 %	66.7	0.174	$E_r = 17 \pm 3$ GPa $HV20 = 62 \pm 6$
CSP-HA+10BG 2 M H_3PO_4	90.06 %	27.37	0.058	$E_r = 49.2 \pm 4$ GPa $HV20 = 220 \pm 6$
CSP-HA+20BG 2 M H_3PO_4	88.75 %	33.71	0.032	$E_r = 45.60 \pm 2$ GPa $HV20 = 202 \pm 5$

All the tested HA-BG compositions were densified successfully; BG addition enhances the physical properties, such as pore volume and SSA, relative to HA cold-sintered with 2 M H_3PO_4 (Table 5.2). Without a transient liquid, HA+10BG relative density reached up to 68 % comparable to its pure HA counterpart. With 2 M H_3PO_4, pure HA reached ~90 % relative density; HA+10BG attained a similar value, and HA+20BG reached ~88 %. Under a rule-of-mixtures assumption, the densification of the HA fraction in HA-BG is similar to that of CSP of HA, indicating that BG has no significant effect on the densification of HA. This could be attributed to the differences in the particle morphology, size/shape: BG powder (Fig. 5.1(a)) consists of coarser irregular aggregates (D_{50} ~13.1 μm), whereas HA

powders (Fig. 4.1) consist of smoother fine spherical aggregates (D_{50} ~5.7 µm), which can alter fragmentation, interparticle locking, and rearrangement. Additionally, the 10 wt.% liquid addition may be insufficient, as both HA and BG need an adequate reactive medium for driving dissolution-precipitation events.

The microstructure images given in Fig. 5.6 support the above statement. Microstructurally speaking, HA+10BG cold sintered without liquid (Fig. 5.6(a_1-a_3)) appears rougher than cold sintered with H_3PO_4 (Fig. 5.6(b_1-b_3)). This is consistent with the H_3PO_4 solution reducing friction, promoting plastic flow-assisted deformation during compaction. In both cases, a good interfacial integration between the BG aggregate and HA grains is observed, and the HA grain morphology in HA-BG composite resembles that of pure HA counterparts (Fig. 4.4 (a&d)). This strongly indicates the 2 M H_3PO_4 drives solution-precipitation phenomena within HA and well as BG.

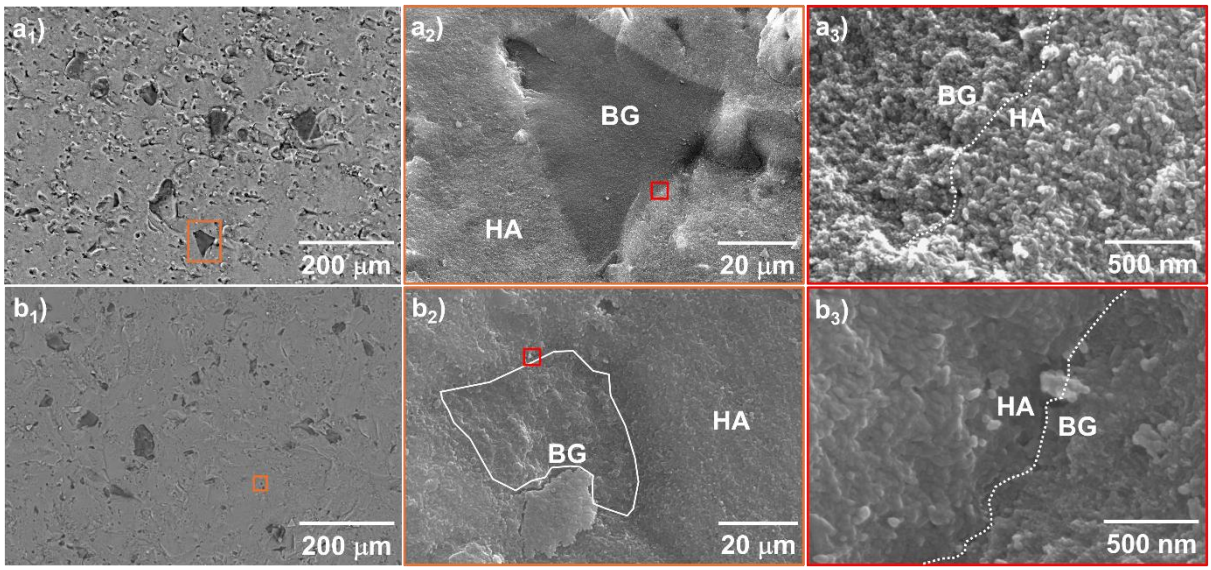

Figure 5.6 *SEM microstructure images (fractured surface)* of the HA+10BG sample cold sintered (a_{1-3}) without transient liquid and (b_{1-3}) with 2 M H_3PO_4 solution.

The XRD patterns in Fig. 5.7 support the above interpretations. For HA+10BG cold-sintered with H_3PO_4, peaks corresponding to calcium dihydrogen phosphate (DCPA) were detected along with changes in HA peak intensity at 2θ = 28.9° (indicated by an arrow in Fig. 5.7). In, BG cold sintered with H_3PO_4 only shows HA peaks (Fig. 5.4(a)) where the dissolution-precipitation is uniform (uniform wetting by H_3PO_4 solution). In HA-BG composite, there is a chance for localized wetting due to pressure gradient and particle

shape/size differences. This rationally supports that the DCPA formation must stem from the localized incongruent dissolution reaction between HPO_4^{2-} from phosphoric acid and Ca^{2+} (from CaO in BG), precipitates calcium dihydrogen phosphate dihydrate (DCPD), which recrystallizes to DCPA. The HA matrix grain morphology resembles its pure CSP HA counterpart (Fig. 4.4(d)), indirectly supporting a similar incongruent dissolution-precipitation-recrystallization occurring in HA grains, as discussed in sections 4.4.4 & 4.4.5. However, the formation of crystallite DCPA phase in HA-BG, either at the interphase between HA and BG, or within the BG particles or HA grains, is quite complex to visualize with SEM. For cold-sintered HA+10BG without liquid, DCPA peaks were absent; nevertheless, the intensity change of the HA peak at 2θ = 28.9° (indicated by an arrow in Fig. 5.7) implies that adsorbed H_2O (in both HA and BG) may promote hydrogen bonding through PO_4^{3-} groups between HA and BG grains, as proposed by Shen et al. (Fig. 4.8(c)) [52].

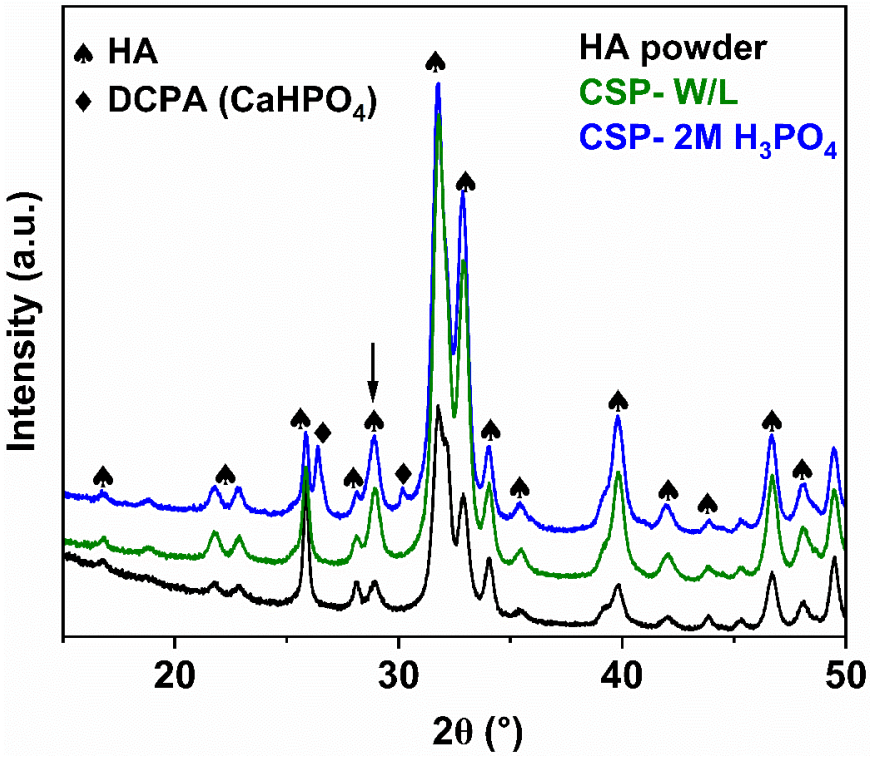

Figure 5.7 *XRD patterns of the cold sintered HA+10BG composite samples without transient liquid and with 2 M H_2PO_4 solution.*

Despite successful densification, introducing BG reduces mechanical performance relative to pure HA counterparts (compared in Table 5.2). CSP without liquid, the elastic

modulus and Vickers hardness of HA+10BG are comparable to those of the pure HA counterpart. In HA-BG composite cold sintered with H_3PO_4, increasing the BG addition from 10 to 20 wt.% reduces both the elastic modulus and Vickers hardness compared to the pure HA counterpart. This could likely be due to the amorphous nature of BG and/or the presence of secondary DCPA phase. However, XRD peaks have no strong evidence for the existence of an amorphous glassy matrix of BG, as HA remains the dominant crystalline phase in the HA-BG composites. Overall, it brings a preliminary idea of developing bioactive ceramic composites by CSP.

5.6 BG In-Situ CSP Investigation

In-Situ observations during the CSP of BG were carried out under 250 MPa pressure (200 °C / 10 min isothermal holding), and the measured relative linear shrinkage, along with representative in-situ images at selected temperature intervals (inset in Fig. 5.8), is shown in Fig. 5.8. The relative linear shrinkage as a function of temperature, measured during the CSP of HA, is shown in Fig. S3 (Appendix A).

For CSP without liquid, Stage I accounts for ~93 %, whereas Stages II and III together contribute ~11 % of the overall densification. When H_2O is used for CSP of BG, Stage I accounts for ~90 %, while the subsequent Stages II and III contribute ~10 % to the overall densification. Thus, cold sintering without liquid or using H_2O, the densification largely relies on the pressure-assisted particle compaction, which aids the consolidation of intergranular necks via hydrogen bonding under stress concentration [52]. In contrast, CSP of BG with H_3PO_4, Stage I contributes ~70 %, and Stages II–III ~30 % of the total densification. In this case, the dissolution-precipitation process differs completely from that observed for CSP of HA with 2 M H_3PO_4.

The in-situ Raman data illustrated in Fig. 5.9 outline the dynamics of the underlying dissolution-precipitation-recrystallization process during CSP of BG with 2 M H_3PO_4. The BG being an amorphous powder, the in-situ Raman spectra (Fig. 5.9(b)) show a characteristic PO_4^{3-} band at 953 cm^{-1}, assigned to ν_1 symmetric P-O stretching of the Q^o orthophosphate unit [242-244, 253, 254]. The BG powder after mixing with H_3PO_4, two new bands appear at ~879 cm^{-1} (weak shoulder) and 986 cm^{-1} (sharp), attributable to HPO_4^{2-} modes [242-244, 253, 254]. These features indicate early precipitation of DCPD

on the silicate network (glass surface), as H_3PO_4 dissolves Ca^{2+} from the glass network by protonation (equation 5.3), and precipitates as DCPD.

$$\equiv Si–O–Ca^{2+}–O^{-}–Si\equiv + 2\ H^{+} \rightarrow \equiv Si–OH + Ca^{2+}(aq) + \equiv Si–OH \quad (5.3)$$

Ex-situ XRD collected immediately after mixing BG with H_3PO_4 (Fig. 5.10(b)) confirms the presence of DCPD. During subsequent heating (Stages II and III), the relative intensities of the HPO_4^{2-} band decrease progressively from 25 °C to ~85 °C (Fig. 5.9(c)). Concurrently, the 953 cm^{-1} band increases in intensity, broadens, and shifts to 957 cm^{-1} near 80-85 °C, becoming sharp and intense in intensity above 90 °C (Fig. 5.9(c)) [253]. These spectral changes are signatures of the dissolution-precipitation-recrystallization events characteristic of Stages II and III of CSP.

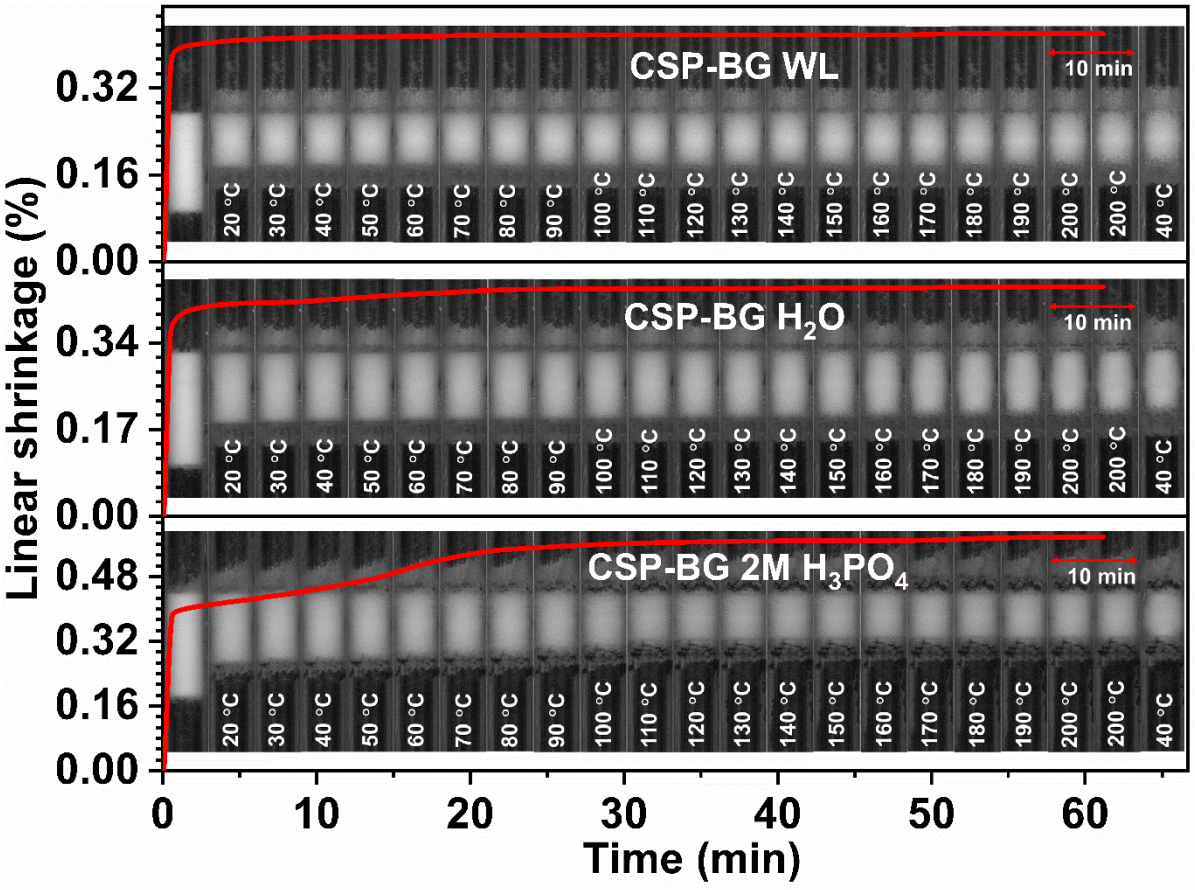

Figure 5.8 *Relative linear shrinkage profile measured from the relative changes in the sample length during the CSP of BG without liquid, with H_2O, and with 2 M H_3PO_4. (Inset) Corresponding* in-situ *sample image frames of particular temperature intervals.*

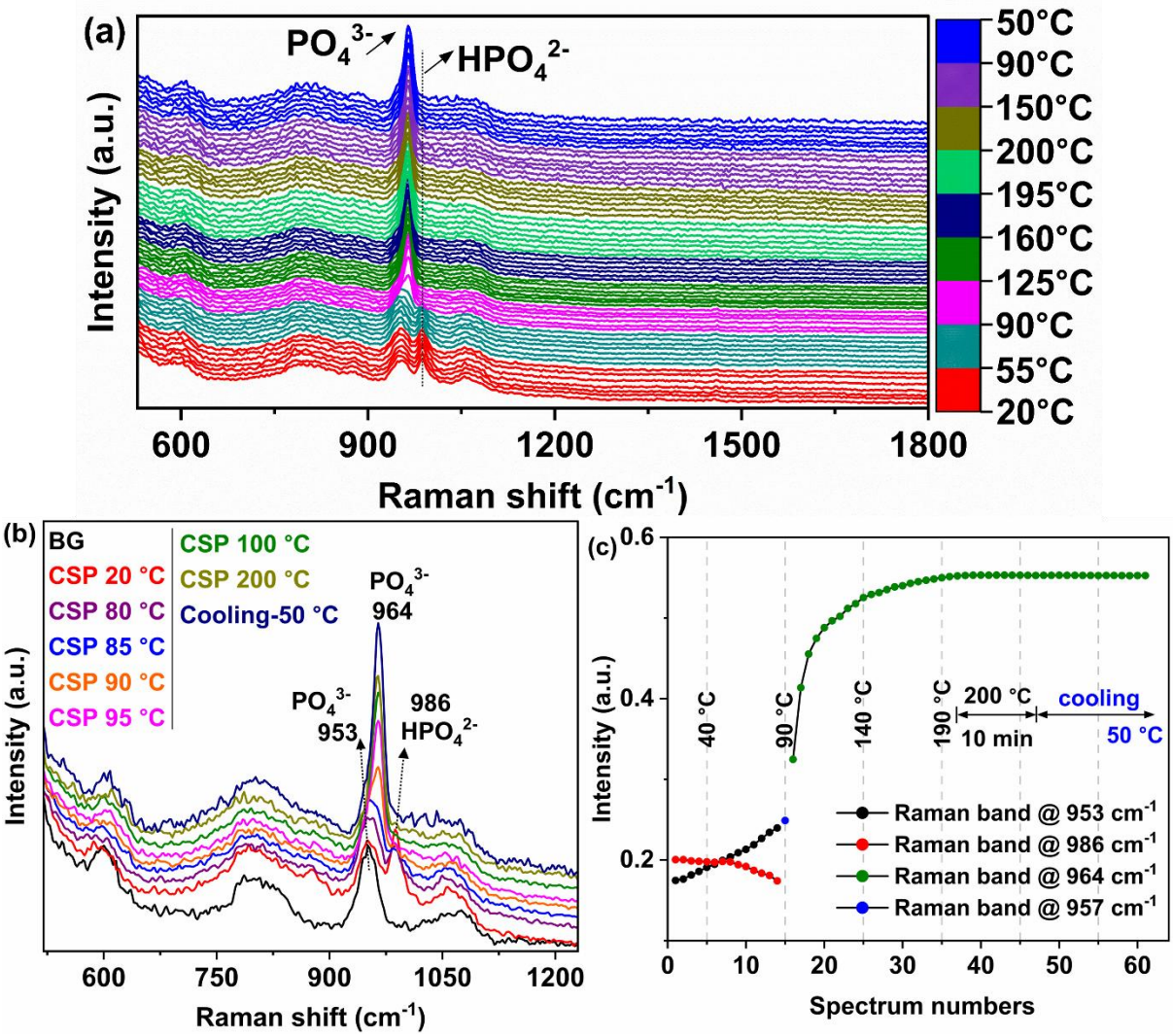

Figure 5.9 *(a) Overall* in-situ *Raman spectra acquired every 60 s during CSP of BG with 2 M H_3PO_4 (200 °C/250 MPa). At this acquisition rate, each spectrum during the heating ramp corresponds to ~5 °C; spectra were also recorded during the isothermal holding (10 min) and cooling cycle (to 50 °C). (b) Selected spectra at specific temperatures spanning the heating and cooling stages. (c) Temperature-dependent relative intensity of the HPO_4^{2-}), and PO_4^{3-} bands. The dashed line in the inset indicates the temperature intervals; each data point corresponds to a spectrum shown in panel (a).*

The rising intensity and broadening of the 953 cm^{-1} band reflect continued DCPD precipitation driven by pressure/chemical gradients. Saturation of this dissolution-precipitation reached between 80-90 °C, marked by the shift of the v_1 PO_4^{3-} band from 953 cm^{-1} to 957 cm^{-1}. Simultaneously, the 986 cm^{-1} band intensity diminishes and disappears after 90 °C, indicating the dehydration and transformation to DCPA. Above 90 °C, the

recrystallization of DCPA to HA occurs, evidenced by the appearance of an intense 964 cm^{-1} band (ν_1 PO_4^{3-}) alongside the gradual dehydration of H_2O from the BG compact. The band at 964 cm^{-1} (ν_1 symmetric P-O stretching) is consistent with calcium-deficient or carbonated apatite [253,254]. Overall, the sequence of dissolution → precipitation → recrystallization events drives substantial shrinkage during Stages II–III.

The ex-situ results highlighted in sections 5.4.2 and 5.4.3 are consistent with the above arguments. Furthermore, ex-situ control experiments differentiate the role of pressure on the transition of intermediate phases. The BG powder was mixed with 2 M H_3PO_4 and heated without compaction (free powder form) in an oven (5 °C min^{-1} to 200 °C, 10 min hold). XRD patterns recorded before and after heating are given in Fig. 5.10, revealing that the precipitated DCPD (after H_3PO_4 mixing) transforms to the anhydrous DCPA, rather than into HA. By contrast, cold-sintered BG compacts show reflections only from HA (Fig. 5.4(a)), indicating that applied pressure drives the recrystallization of DCPD → HA during CSP with H_3PO_4.

However, the in-situ Raman spectra for CSP of HA (Fig. 4.9(b)), the ν_1 PO_4^{3-} band appears at 962 cm^{-1}, whereas for BG it appears at 964 cm^{-1}, supporting the assignment to Ca-deficient or carbonate-substituted HA [256, 257]. The FTIR data (Fig. 5.4(b)) is consistent with the presence of type-b carbonate peaks along with PO_4^{3-} stretching/bending vibrations, supporting the above observation.

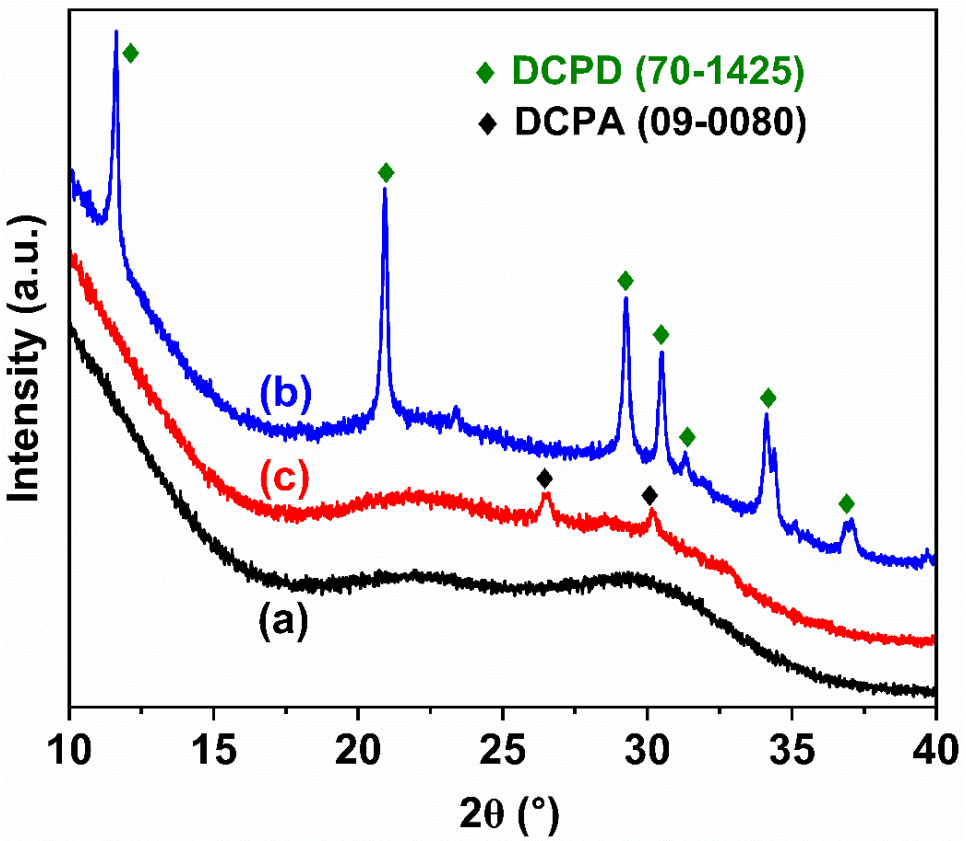

Figure 5.10 *XRD patterns of (a) HA powder (HAp202), (b and c) HA powder mixed with 2 M H_3PO_4 solution before and after heating treatment, respectively. The heat treatment was carried out in powder form at 200 °C (5 °C/min, 10 min isothermal holding).*

5.7 Conclusions

The present study underscores the fundamental densification framework of sol-gel-derived 50S ternary bioglass powder at low temperature (200 °C) by the cold sintering process. By applying 360 MPa at 200 °C, CSP of BG using 2 M H_3PO_4 transient liquid achieved up to 89 % densification in under 2 h, a dramatic reduction in both temperature and processing time compared to conventional sintering (1200 °C lasts 8 h), which attains 98 % densification with extensive crystallization.

Under identical pressure and temperature conditions, the transient-liquid chemistry was shown to dictate the dominant sintering mechanism, microstructural evolution, and resulting mechanical performance. As highlighted by the XRD, FTIR, and SEM results, CSP with water or NaOH, the dissolution-precipitation proceeds via a congruent chemical pathway: hydrolysis and condensation of the silicate network facilitate

interparticle ionic diffusion and glass-network repolymerization, yielding densified yet amorphous compacts. In contrast, CSP with H_3PO_4, the dissolution-precipitation follows an incongruent dissolution pathway, aiding ionic diffusion as well as recrystallization of in-situ HA crystallites. This leads to the highest densification, lowest residual porosity, and superior mechanical performance (Er = 40 ± 6 GPa).

The densification of HA-BG was also demonstrated using 2 M H_3PO_4. Incorporating 10 wt.% BG into the HA matrix achieved 90 % densification and improved physical properties such as specific surface area (SSA) and pore volume compared with CSP of pure HA under the same conditions. However, mechanical indentation analysis indicated that increasing BG content reduced the mechanical properties of the composite. Despite this, BG, as an amorphous reactive additive, had no significant effect on enhancing HA densification. XRD results revealed that localized dissolution-precipitation-recrystallization in BG promotes the formation of dicalcium phosphate anhydrous (DCPA) phases, though it remains unclear whether these phases are present within the HA matrix or BG particles, or at the intergranular interface between HA and BG.

Further, the underlying pressure-solution creep event and its dynamics during CSP of BG with H_3PO_4 were successfully resolved by combining a miniature transparent-die CSP setup and in-situ Raman analysis. The Raman reveals dissolution-precipitation drives formation of transient DCPD intermediate (indicated by bands at ~879 and 986 cm^{-1}), which saturates near 90-100 °C, subsequently dehydrates/recrystallizes to HA above ~100 °C. Correlating in-situ Raman with ex-situ controls establishes the central role of pressure: it not only increases grain contact and particle rearrangement, but it also redirects reaction pathways. Under pressure, the surface precipitated DCPD recrystallizes to the substituted HA form. Without pressure, DCPD transforms to DCPA rather than HA.

Overall, this preliminary study demonstrates the feasibility of cold sintering bioactive ceramic components and BG-based systems and proposes an approach for developing composites with tunable physical properties, enabling control over both mechanical and biological performance. Collectively, these findings establish a fundamental CSP framework for densifying sol–gel-derived ternary 50S BG and identify phosphoric acid as

an effective transient liquid, except in cases where excessive HA crystallization is undesirable. Future work must focus on a comprehensive understanding of how different transient liquids and CSP parameters (pressure, temperature, liquid volume, etc.) influence both biological and mechanical behavior. Such studies could expand CSP's applicability to other ternary bioglass compositions, bioglass systems, and composite materials, ultimately enabling the production of dense, bioactive structures optimized for uncompromised bone regeneration.

Chapter 6: Cold Sintering Process Framework for HA-PLA composite

6.1 Context

From the perspective of bone biology and composition, certain bone defects, such as critically sized damage, require graft materials in large quantities with suitable biological and mechanical properties, emphasizing the use of synthetic bone substitutes. Unlike traditional gold standard autogenous bone grafts, whose safely harvestable volume is limited, synthetic bone substitutes enable scalable production with adjustable properties [7-15]. Since bone is a composite mineralized matrix mainly made up of collagen (organic phase) and apatite crystals (inorganic phase), ceramic-polymer composite grafts are especially suitable for use in such challenging bone defects [6-10]. Additionally, these grafts not only provide structural support but can be functionalized with instructive biomaterials, such as cells and growth factors, for treating critically sized bone defects, particularly in patients with limited regenerative capacity or infections [12-14].

HA, due to its structural and chemical similarity to the inorganic mineral, has been extensively investigated as the ceramic component in developing polymer-ceramic composites [20-23]. PLA, a biodegradable and biocompatible polyester, serves as an ideal polymer counterpart owing to its tailorable degradation rate, high stiffness, and wide processing temperature window [35-39]. PLA rich in L-lactide isomeric composition holds T_m close to 180°C and a T_g close to 60°C, which allows tailorability by copolymerization, offering additional advantage in terms of processing, and controlling the *in vivo* degradation profiles [34, 35, 129]. Despite their advantageous features, HA and PLA possess inherent limitations; HA presents an elevated brittleness, and PLA lacks bioactivity with low strength [34, 35]. Consequently, integrating the beneficial properties of both HA and PLA has garnered significant interest, as their combination overcomes individual limitations, supports bone ingrowth, and facilitates the gradual replacement of implants with new bone tissue [121-123].

HA-PLA polymer-ceramic composites developed with techniques such as additive manufacturing, solvent casting, or injection molding typically utilize a lower fraction of HA (up to 50 %). Consequently, only modest improvements regarding the mechanical properties have been achieved with those techniques, particularly higher ceramic loading, negatively influencing the interfacial bonding, dispersion, as well as the overall processability of the composite, leading to suboptimal mechanical performance as discussed in section 2.2.5 [37-41]. Moreover, a lack of HA densification within the PLA matrix is another reason for the poor mechanical performance of the composites. Consolidation of HA is usually done at high temperatures, which densifies the HA particles and improves the mechanical properties. Notably, the temperature disparity between HA and PLA restricts the co-sintering.

The CSP, due to its low-temperature processing window, allows co-sintering ceramic-polymer systems [44-50]. Within the framework of CSP, only a few studies demonstrating the co-sintering of HA-polymer-based composites, briefly discussed in section 2.5. Previous studies, however, leave open questions about the key drivers of co-sintering. Hu et al reported the cold sintering of *in-situ* drug-loaded HA-PLA composites at various temperatures (60-120 °C) and pressures (100-700 MPa) [219]. Specifically, for the HA-PLA 80/20 wt.% composite proportion, they observed that the relative density did not exceed 87 %, even with increasing temperature and pressure [219]. This leaves uncertainty regarding whether the co-sintering was primarily dependent on temperature, pressure, or their interplay. Alternatively, Pietrzykowska et al., consolidated the 80/20 wt.% HA/PLA composite using various protocols [149]. They found that cold pressing at a pressure of 1 GPa achieved a relative density of up to 85 %. Moreover, a two-step process involving cold axial pressing at 1 GPa followed by hot isostatic pressing at 75 MPa and 165 °C resulted in a relative density of 99 % [149]. Notably, the reported CSP studies of HA-PLA were achieved without any liquids, since aqueous liquids induce the hydrolytic degradation of the aliphatic polyester chains of PLA [258].

In chapter 4, we demonstrated the densification of HA at 200 °C using CSP, particularly CSP of HA without liquid, which does not promote densification, instead consolidating the nano-grain with 67 % relative density. Thus, co-sintering of PLA with HA at 200 °C is feasible only via the consolidation mechanism. However, it is still uncertain how the

consolidation between HA and PLA, as well as HA consolidation within the PLA matrix, occurs, especially with varied ratios of HA to PLA. We hypothesized that the temperature-dependent PLA fluidity, along with pressure application, might influence both the consolidation between HA-PLA as well as HA within the PLA.

This chapter explores the consolidation behavior of HA/PLA composites under 360 MPa pressure at 200 °C. The composites were prepared with varied HA-to-PLA ratios. Further, the plasticization effect of PLA in the CSP of composites has been tested, as plasticizers are known to enhance the fluidity, flexibility, and ductility of PLA [154-158]. Tributyl citrate (TBC), a plasticizer with low molecular weight, was selected for its miscibility, biocompatibility, and proven effectiveness in improving PLA fluidity and compatibility with HA [156, 158]. Systematic investigations have been made to examine the interfacial bonding between HA and PLA, the effects of varying HA-to-PLA ratios, and the impact of PLA plasticization, to understand the fundamental consolidation mechanism in HA-PLA composites processed by CSP. Finally, employing the in-situ CSP monitoring setup and in-situ Raman analysis, the progression of consolidation and the underlying mechanism were studied and validated.

6.2 Consolidation vs HA-to-PLA ratio

6.2.1 Density Evolution

The influence of HA-to-PLA ratio on consolidation and density evolution during CSP is illustrated by the compact volume shrinkage profile shown in Fig. 6.1(b). The inset dotted lines of Fig. 6.1(b) indicate the heating program during the CSP at 360 MPa. As shown by the displacement vs time profile (Fig. 6.1(b)), the total volumetric reduction follows the order: HA:PLA 80:20 > 70:30 > 60:40 > 50:50. However, the relative density exhibits an opposite trend (Fig. 6.1(a)), suggesting differences in the consolidation pattern between HA and PLA.

During the initial compaction phase at room temperature for 15 minutes, HA particles deform elastically, while PLA particles experience viscous deformation. This synergistic rearrangement causes a dense, compact arrangement between HA and PLA, thereby reducing porosity. This allows achieving a relative density of more than 80 % (Fig. 6.1(a)).

However, the extent of elastic deformation of HA particles within the compact varies depending on the HA-to-PLA ratio [38, 39, 256].

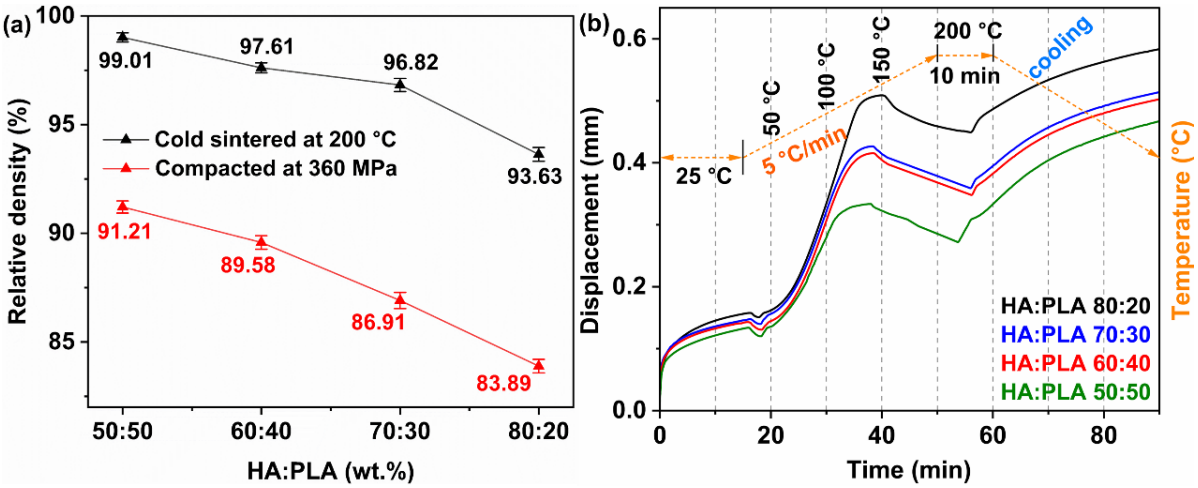

Figure 6.1 *(a) Relative density values of the compacted and cold sintered samples, and (b) volume shrinkage profile recorded in terms of total displacement versus time during the cold sintering of the composite under 360 MPa. The measured volumetric shrinkage profile represents the total displacement, not corrected for the thermal expansion of the die.*

During the heating ramp up to 200 °C at a 5 °C/min ramp rate, two instances of negative volume shrinkage were observed between 30-50 °C and above 140 °C due to the thermal expansion of PLA. The first negative shrinkage (30-50 °C) arises from the release of internal stress as the rigid PLA chains transition into a less dense, flexible form [260, 261]. Between 140 °C and 200 °C, the softened PLA gradually transitions into a flowable state, accompanied by volume relaxation of the polymer chains, which contributes to the second negative volume shrinkage (Fig. 6.1(a)) [260, 261]. This process may induce strong repulsion at the interphase, likely due to polarity differences or thermal expansion mismatches between HA and PLA [260]. During the 10-minute isothermal holding, PLA remains in a flowable state, allowing for viscoelastic deformation during the subsequent cooling stage. This facilitates further binding with HA particles and fills any interparticle voids, thereby enhancing composite consolidation. However, the flowability of PLA may vary with HA content, resulting in different consolidation patterns between HA and PLA. Additionally, the composite's consolidation mechanism is considerably more complex compared to the consolidation of pure HA powders under similar conditions.

6.2.2 Microstructure

The differences in the observed relative density trends and consolidation pattern can be commented on relating to the microstructure of the composite samples illustrated in Fig. 6.2. As seen in Fig. 6.2(b_1-d_1), the mechanical interlocking between PLA and the HA aggregates becomes more pronounced with an increasing PLA content [30, 31]. Additionally, Fig. 6.2(b_2-d_2) shows evidence of PLA infiltration into the interparticle gaps of the HA aggregates. Thus, as the PLA ratio increases in the composite, it hinders the breakdown of HA aggregates and affects their packing density within the PLA matrix (Fig. 6.2(b_1-d_1)), yielding a microstructure with discrete HA clusters embedded in a continuous PLA phase. In these cases, co-sintering is primarily facilitated only by the consolidation between HA aggregates and PLA, where PLA forms a uniform matrix that binds the HA aggregates, likely contributing to higher relative densities.

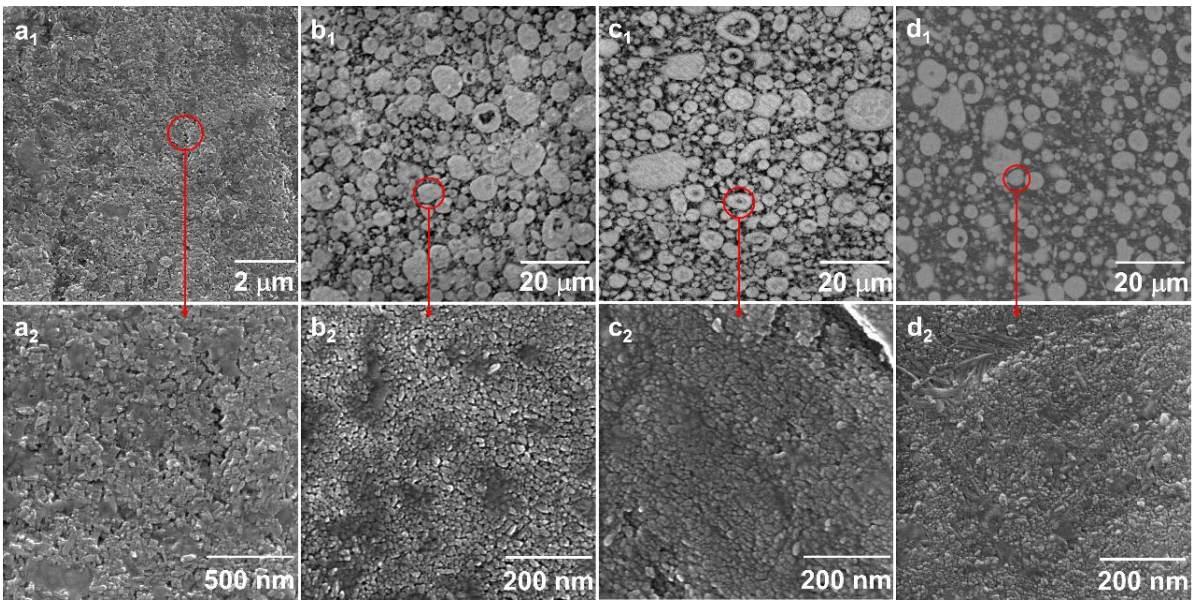

Figure 6.2 *Cold sintered composites microstructure (polished surface); (a_1&a_2) 80:20 fraction captured in SE mode at magnification 110Kx / 150Kx, (b_1-d_1) and (b_2-d_2) correspond to 70:30, 60:40, and 50:50 fractions captured in BSE mode at magnification 2Kx and in SE mode at 150Kx magnification, respectively.*

In contrast, the microstructure of HA:PLA 80:20 sample (Fig. 6.2(a_1 & a_2)) consists of well-consolidated nano HA grains with PLA homogeneously binding the inter-particle matrix grains. The packing of HA grains in the microstructure of the HA:PLA 80:20 sample is comparable to that of cold sintered HA (Fig. 4.3(a) in Chapter 4). This indicates that low

PLA fractions facilitate the de-aggregation of HA into fine nanograins and promote direct HA-HA interparticle bonding. Further, the PLA hierarchically binds at HA grain boundaries and within residual porosity of the compact, thereby enabling greater volumetric shrinkage during CSP (Fig. 6.1(b)) [146, 259]. Thus, the increased PLA content hinders the breakdown of HA aggregates and affects their dense packing within the PLA matrix (Fig. 6.2(b_1-d_1)). As a result, the consolidation of HA grains becomes less feasible with higher PLA content.

The FIB cross-sectioned SEM images given in Fig. 6.3 support the above arguments. It reveals that cold sintered sample HA:PLA 80:20 has a continuous nano HA grain matrix, while the HA:PLA 70:30 sample shows a densely packed HA aggregate as it is surrounded by more PLA matrix. These microstructural distinctions confirm that the HA-to-PLA ratio governs the consolidation between HA and PLA.

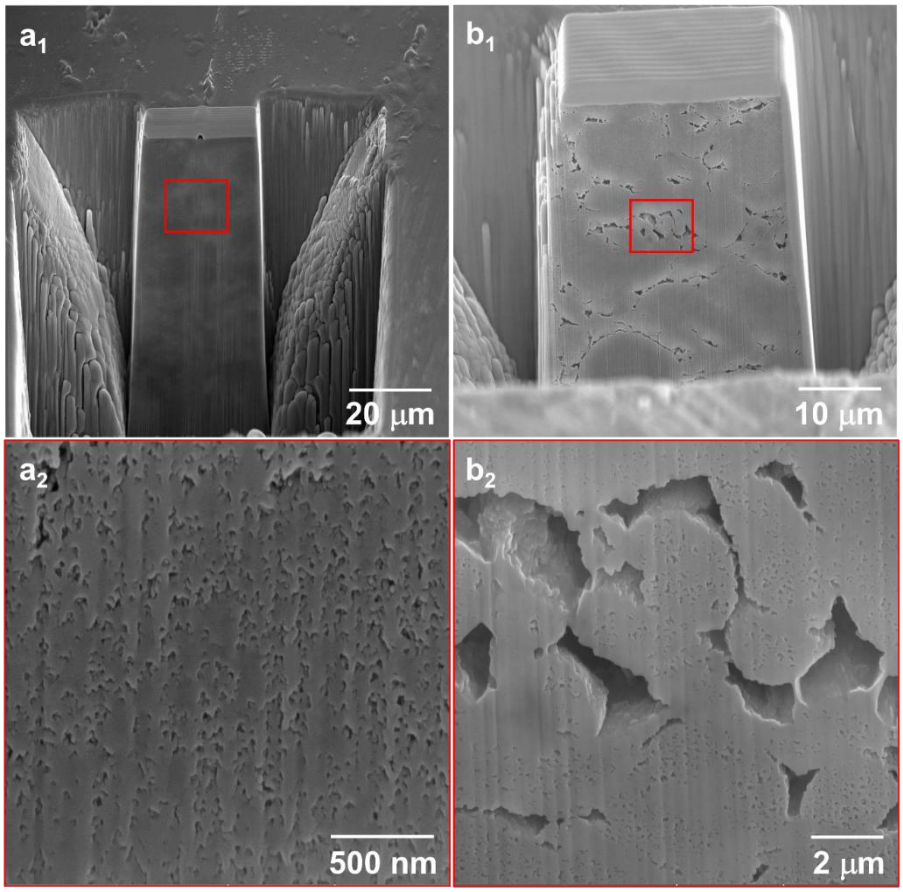

Figure 6.3 *FIB cross-sectioned SEM micrographs of (a_1 & a_2) 80:20 captured at a magnification of 3Kx / 100Kx, and (b_1 & b_2) 70:30 fraction captured at a magnification of 5Kx / 50Kx.*

6.3 Plasticization Effect on Composite Consolidation

Firstly, the effect of PLA plasticization by tributyl citrate (TBC) was assessed by thermal characterization. The DSC curves of PLA plasticized with different TBC concentrations are presented in Fig. 6.4(a), and the summarized values of the thermal properties are given in supporting information Table 6.1.

Table 6.1. *DSC parameters of PLA and TBC plasticized PLA*.

Sample	T_g	T_c	T_m
PLA6201D	62.3	143.4	169.2
5TBC/PLA	52.7	100.4	168.3
10TBC/PLA	39.6	90.2	165.7
20TBC/PLA	27.4	77.9	163.6

The changes in the cold-crystallization T_c, and melting temperature T_m of the plasticized PLA indicate that TBC partially disrupts the crystalline regions of PLA. As the TBC concentration increases, the glass transition T_g shifts to lower temperatures, confirming that plasticization enhances the mobility of PLA chains [156, 158]. Since the PLA used in this study is semi-crystalline, plasticization not only helps enhance the fluidity of PLA but is also expected to facilitate better interaction between HA and PLA [128, 129].

The influence of plasticization on the consolidation behavior during CSP was tested with the 80:20 fraction of HA:PLA, where the HA de-aggregation is significant (Fig. 6.2(a_1 & a_2)). Comparing the volume shrinkage profile shown in Fig. 6.4(b) for the HA:TBC/PLA 80:20 composites and HA:PLA 80:20 composite, the consolidation pattern for composites made with plasticized PLA is the same as that of unplasticized PLA. The elastic deformation at the initial compaction phase, i.e., at room temperature, is similar to that made with unplasticized PLA (HA:PLA 80:20). However, due to the enhanced fluidity of plasticized PLA, a visible difference in the compact volume changes is observed when heating up to 140 °C, likely consistent with improved polymer flow into residual voids. Correspondingly, the relative density values (Fig. 6.4(c)) of the plasticized PLA composites increased TBC concentration and are higher compared to the unplasticized PLA composite.

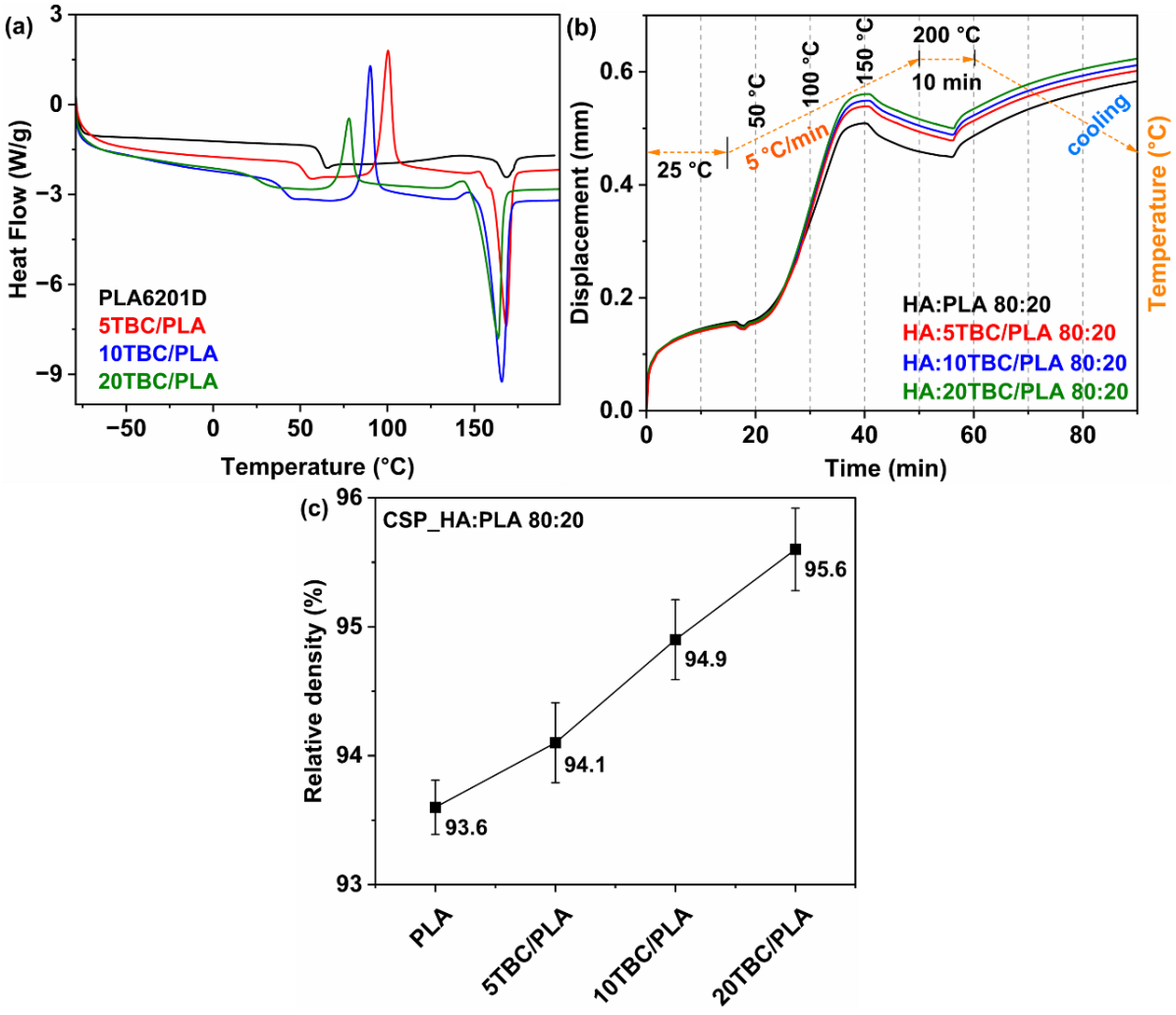

Figure 6.4 *(a) DSC thermograms of the TBC plasticized PLA, (b) volume shrinkage profile of the compact recorded in terms of total displacement versus time during the cold sintering of the composite made with plasticized PLA under 360 MPa, and (c) Relative density values of cold sintered composites made with plasticized PLA.*

Further, the microstructure observation of 80:20 composite made with 20TBC plasticized PLA, shown in Fig. 6.5, reveals a significant improvement in the dense packing of nano HA grains bonded with PLA. Thus, plasticization positively impacts both the overall composite consolidation and the consolidation of HA within the composite matrix. This strongly highlights that the composite consolidation during CSP is significantly influenced by the fluidity of PLA.

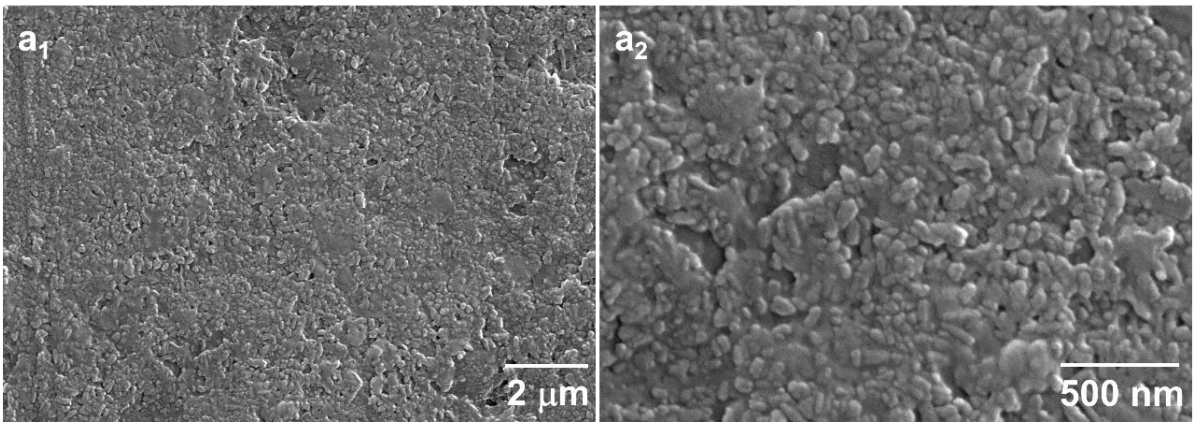

Figure 6.5 *(a_1&a_2) Microstructure of the cold sintered composite (polished surface); HA:20TBC/PLA 80:20 fraction captured in SE mode at magnification of 110Kx & 150Kx.*

6.4 HA Consolidation in the Composite Matrix

The extent of HA consolidation within the composite matrix was evaluated by selectively removing PLA. The cold sintered samples HA:PLA 80:20, 70:30, 60:40, 50:50, and HA:20TBC/PLA were subjected to PLA extraction by the Soxhlet extraction method using chloroform, as it serves as PLA's good solvent. After 24 h of extraction, the HA matrix was retrieved (shown in Fig. S5) only for the samples with an 80:20 proportion. The retrieved porous HA matrix only has handling strength but is not mechanically durable. In both these samples, the complete extraction of PLA was confirmed by a weight change of 19.2 % after drying at 100 °C. In contrast, the other compositions only yielded the HA powders. This implies that the lower PLA ratio in 80:20 samples allows sufficient consolidation of HA grain within the composite, providing structural integrity along with PLA bonding.

Furthermore, SEM analyses, along with specific surface area (SSA) measurements, were carried out for the retrieved HA matrix from both plasticized (20TBC) and unplasticized 80:20 composite samples. From Fig. 6.6, it is confirmed that the HA matrix of both samples constitutes loosely bonded nanograins and has different SSA values (inset value in Fig. 6.6). Comparing the SSA values of these samples, grain consolidation occurs more in the composite made of plasticized PLA. In chapter 4, the cold sintered HA without liquid consists of well-consolidated nanograins (relative density of 66 %) with an SSA reduced to 33 m^2/g, which is lower than for the HA powder (~97 m^2/g). This reduced the SSA attribute to mass transfer across grain boundaries, due to the necking effect and chemical interactions.

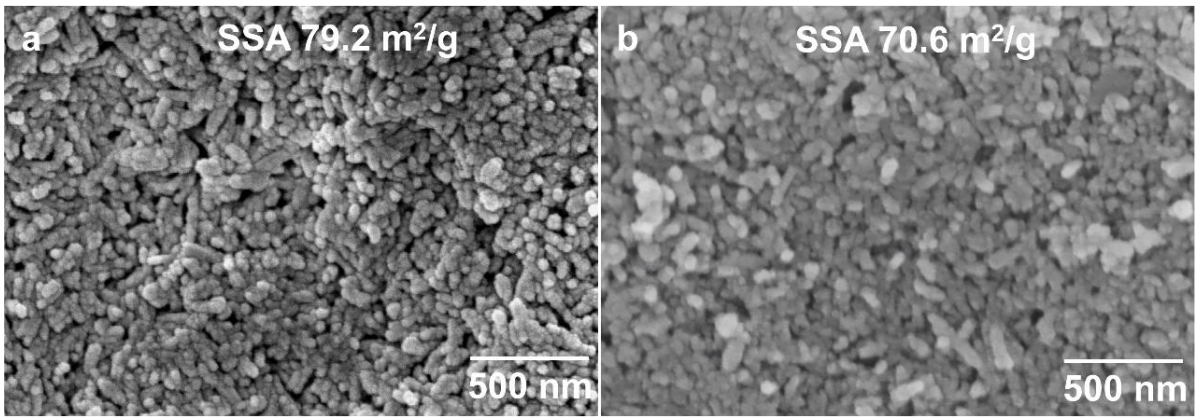

Figure 6.6 *(a) Microstructure of the HA matrix after extracting the PLA from cold sintered HA:PLA 80:20 and (b) HA:20TBC/PLA 80:20 composite. The SEM images were captured in SE mode at a magnification of 150Kx.*

In the case of HA-PLA composite, PLA likely hinders the consolidation dynamics of HA grains in the composite matrix. During CSP, PLA may partially hinder the direct grain-to-grain contact that impedes incomplete mass transfer across HA nanograins. As a result, the HA grains within the composite are cohesively bonded but are not as dense as observed in the cold sintering of pure HA (Fig. 4.4(a) - Chapter 4). Interestingly, the plasticizing effect contributes to a more cohesive consolidation of HA nanograins within the composite matrix due to the increased flexibility of PLA with a high content of TBC.

6.5 Phase Composition and Thermal Behavior

PLA6202D is a semi-crystalline polymer with very low D-isomer content (<2 %) and thus able to crystallize into ordered α and disordered α' polymorphs, depending on the crystallization temperature, as extensively discussed in the literature [262, 263]. However, its crystallization behavior in the composite is influenced by the cold-sintering temperature, integration pattern between the HA and PLA, and plasticization effect.

In section 6.4, it is highlighted that the HA:PLA 80:20 composite made with pure PLA and TBC-plasticized PLA, only has interfacial bonding between HA-HA grains and HA-PLA. Thus, for convenience, the crystallization behavior of PLA within these composite fractions is first discussed, and the composite with increasing PLA fraction is discussed.

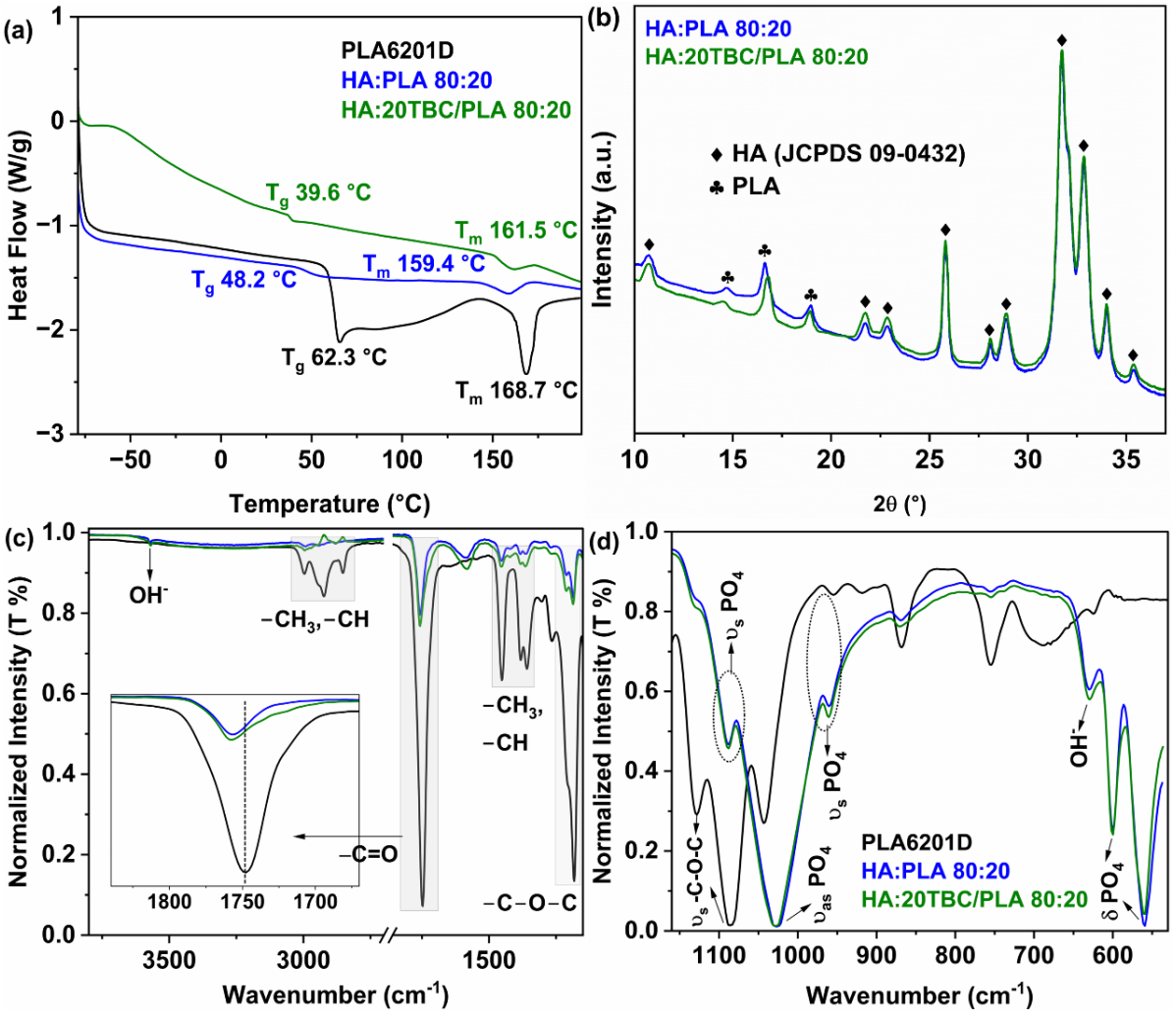

Figure 6.7 (a) DSC thermogram, (b) XRD patterns, and (c and d) FTIR plot of the HA:PLA 80:20 composite made with unplasticized and 20TBC-plasticized PLA.

The DSC thermogram of the cold sintered HA:PLA 80:20 composite fraction made with unplasticized and 20TBC plasticized PLA is shown in Fig. 6.7(a). Compared to the pure PLA, the unplasticized composite exhibited reduced glass transition temperature (T_g = 48.2 °C), whereas the plasticized composite glass transition temperature (T_g = 39.6 °C) was slightly increased that of the pure plasticized PLA (T_g = 27.4 °C). These observations can be attributed to the restricted chain mobility due to improved interactions between HA particles and PLA via either H-bonding or mechanical interlocking [38, 39, 146]. The existence of hydrogen bonding between HA and PLA was evidenced by the red shift of the characteristic C=O stretching vibration peak for PLA (1748 cm^{-1}) as shown in the FTIR spectrum in Fig. 6.7(c) [217, 264].

In the unplasticized composites, the downward shift in T_m, accompanied by a broad endotherm, indicates a disrupted crystalline structure caused by the nucleating effect of HA. In contrast, the plasticized composite showed no significant T_m shifts. Furthermore, the difference in T_m between the plasticized (161.5 °C) and unplasticized (159.4°C) composites suggests that the plasticization enhances the degree of crystallization or improves the molecular arrangement of PLA [262, 263]. These observations are further supported by the XRD patterns as illustrated in Fig. 6.7(a). The XRD results confirm that cold sintered composites present HA and PLA phases. The diffraction peaks corresponding to the HA crystal phase align with the JCPDS 00-009-0432 pattern. Both the composite shows the diffraction peaks at 2θ = 14.7, 16.6, and 18.9° correspond to (010), (110)/(200), and (203) lattice planes of the α/α' crystal forms of PLA [262, 263]. The heterogeneity in the crystal form of PLA, attributed to the nucleation effect of HA, is further evidenced by the FTIR bands at 755 and 867 cm^{-1} (Fig. 6.7(d)) [264, 265]. While comparing the unplasticized composite, the diffraction peak at 16.6° in the plasticized composite slightly shifts to 16.8°, accompanied by a minor increase in intensity. This shift suggests that plasticization enhances the PLA crystallization during the cold sintering process [266].

In the composite samples HA:PLA 50:50 and 60:40, the observation of dual melting peaks at 153 and 160 °C (Fig. 6.8(a)) can be attributed to coexisting α'/α crystals populations (PLA chains) and differing HA-PLA interactions within the composite [263-265]. In contrast, the composite HA:PLA 70:30 has a very broad melting peak (Fig. 6.8(a)). These variations in melting peaks concerning PLA likely arise from variations in HA-aggregate packing: SEM microstructure (Fig. 6(b_1-d_1)) indicates denser HA packing in 70:30 than in 60:40 and 50:50. Such packing constrains PLA crystallization and increases heterogeneity; moreover, as HA content decreases, the number of heterogeneous nucleation sites diminishes, further altering PLA crystallization behavior.

The coexisting α'/α crystals populations in the HA:PLA composites are consistent with the diffraction peaks (Fig. 6.8(b)), at 2θ = 14.7, 16.6, and 18.9° correspond to (010), (110)/(200), and (203) lattice planes of the α/α' crystal forms of PLA [262, 263]. Additionally, irrespective of the difference in HA-PLA consolidation patterns, the existence of hydrogen bonding between HA and PLA is evidenced by the red shift of the

characteristic vibration peak (Fig. 6.8(c)) for C=O stretching vibration of PLA at 1748 cm^{-1} [219, 264].

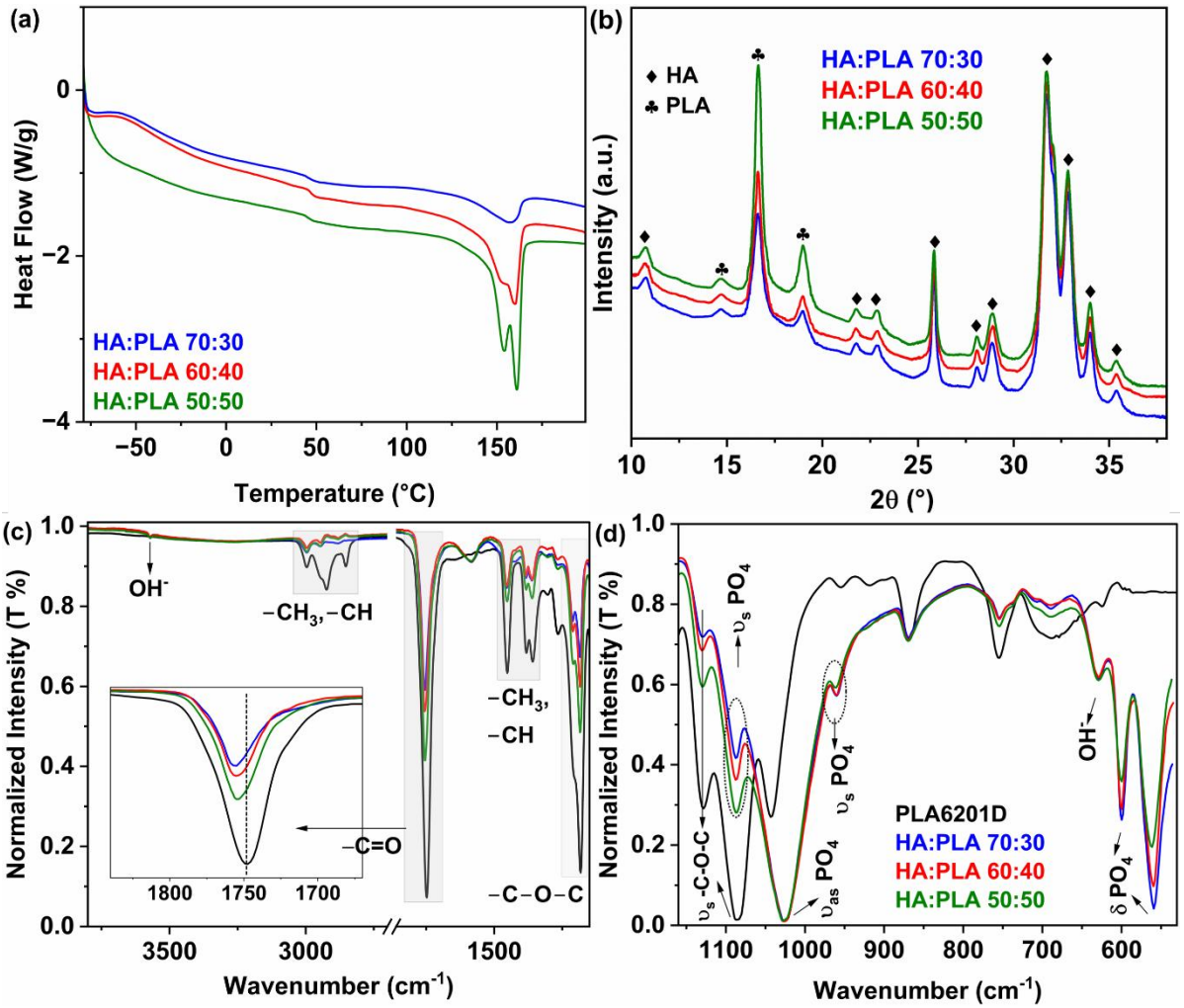

Figure 6.8 (a) DSC thermogram, (b) XRD patterns, and (c and d) FTIR plot of the HA:PLA 70:30, 60:40, 50:50 composites made with unplasticized PLA.

6.6 Composite Mechanical Property

The microindentation analysis reveals significant insights into the mechanical interfacial bonding between HA and PLA in cold sintered composites. As illustrated in Fig. 6.9(a), the 80:20 HA-PLA composite exhibits the highest elastic modulus (E_r = 25 GPa) and superior hardness, outperforming other composite compositions. In comparison, pure HA cold sintered under the same conditions (RD 66 %) shows a slightly lower elastic modulus (E_r = 21 GPa) but a higher hardness (112 HV). This indicates that the PLA addition improves stiffness but reduces hardness due to the integration of a flexible polymer matrix. PLA,

being a soft material with low stiffness and hardness, the increasing proportion of PLA in composites reduces the hardness and E_r values relative to HA. However, the lower PLA content (20 %) provides optimal mechanical performance, due to the cohesive consolidation of HA nanograins (Fig. 6.9(a)) within the matrix facilitated by PLA's binding effect.

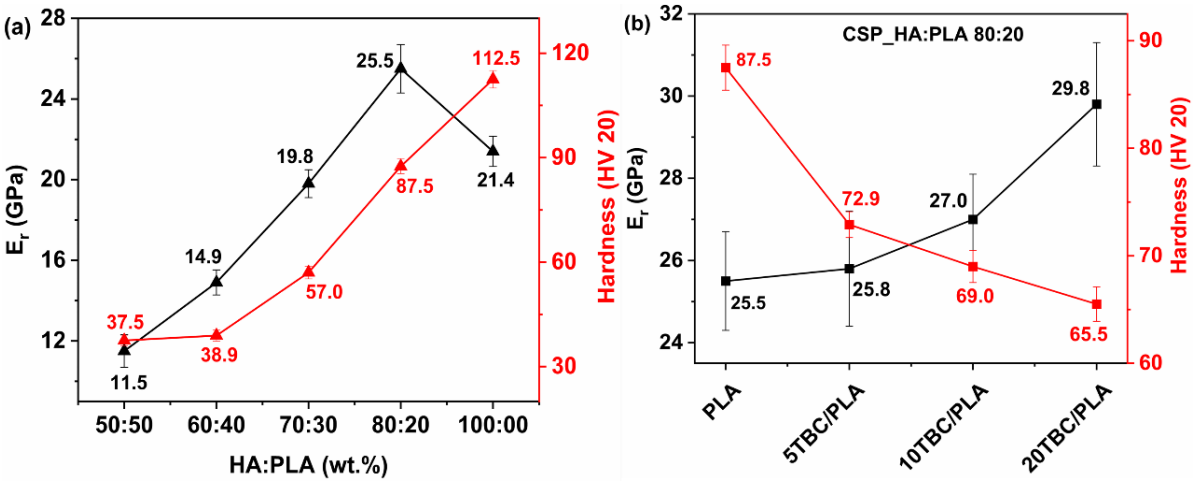

Figure 6.9 *(a) Stiffness/hardness values for cold sintered composites made with unplasticized PLA and (b) 80:20 composite made with TBC-plasticized PLA.*

Similarly, when TBC plasticized PLA was used in 80:20 composites, the stiffness increased with higher TBC content, while hardness decreased (Fig. 6.9(b)). The increase in stiffness is attributed to the plasticization effect. This enhances the cohesive consolidation of HA grains (Fig. 6.9(b)) within the composite matrix. The lowering of hardness values suggests that the plasticization softens the PLA matrix, as indicated by the DSC profile (Fig. 6.4(a)) [35]. As HA primarily provides stiffness, the consolidation of HA in the composite matrix contributes higher stiffness values for HA:PLA 80:20 proportion composites, offering excellent structural integrity through the combined effect of binding between PLA and HA. The microstructural observations and the results in section 6.3 together support this conclusion. Overall, the obtained stiffness values are comparable to the stiffness value (7-30 GPa) of human cortical bone reported in the literature [67-70]. The composite processed through the cold-sintering process is therefore suitable for bone substitutes at load-bearing sites.

6.7 HA-PLA In-Situ CSP Investigation

Fig. 6.10 presents the linear shrinkage profile HA:PLA (80:20 wt.%) composite, along with representative in-situ images captured at selected temperatures (inset in Fig. 6.10), during CSP carried out at 200 °C under 200 MPa. The relative linear shrinkage as a function of temperature is shown in Fig. S6 (Appendix A).

The previous section has no evidence for supporting dissolution-precipitation in HA:PLA composites; CSP Stage I is referred to as room-temperature compaction, Stage II as heating (including isothermal holding), and Stage III as cooling. Accordingly, CSP of HA:PLA without liquid, Stage I contributes ~47 % of the total consolidation, whereas Stages II and III together contribute ~49 % and 4 % respectively.

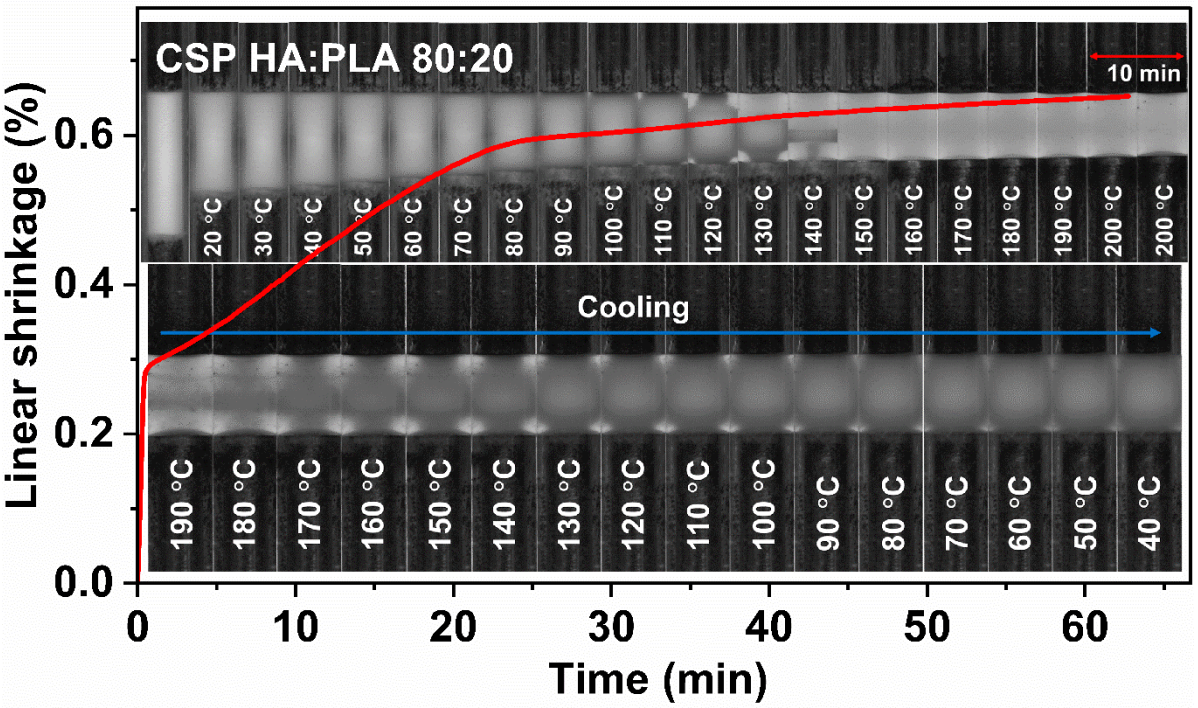

Figure 6.10 *Relative linear shrinkage profile measured from the relative changes in the sample length during the CSP of HA:PLA (80:20 wt.%) composite without liquid. (Inset) Corresponding in-situ sample image frames of particular temperature intervals.*

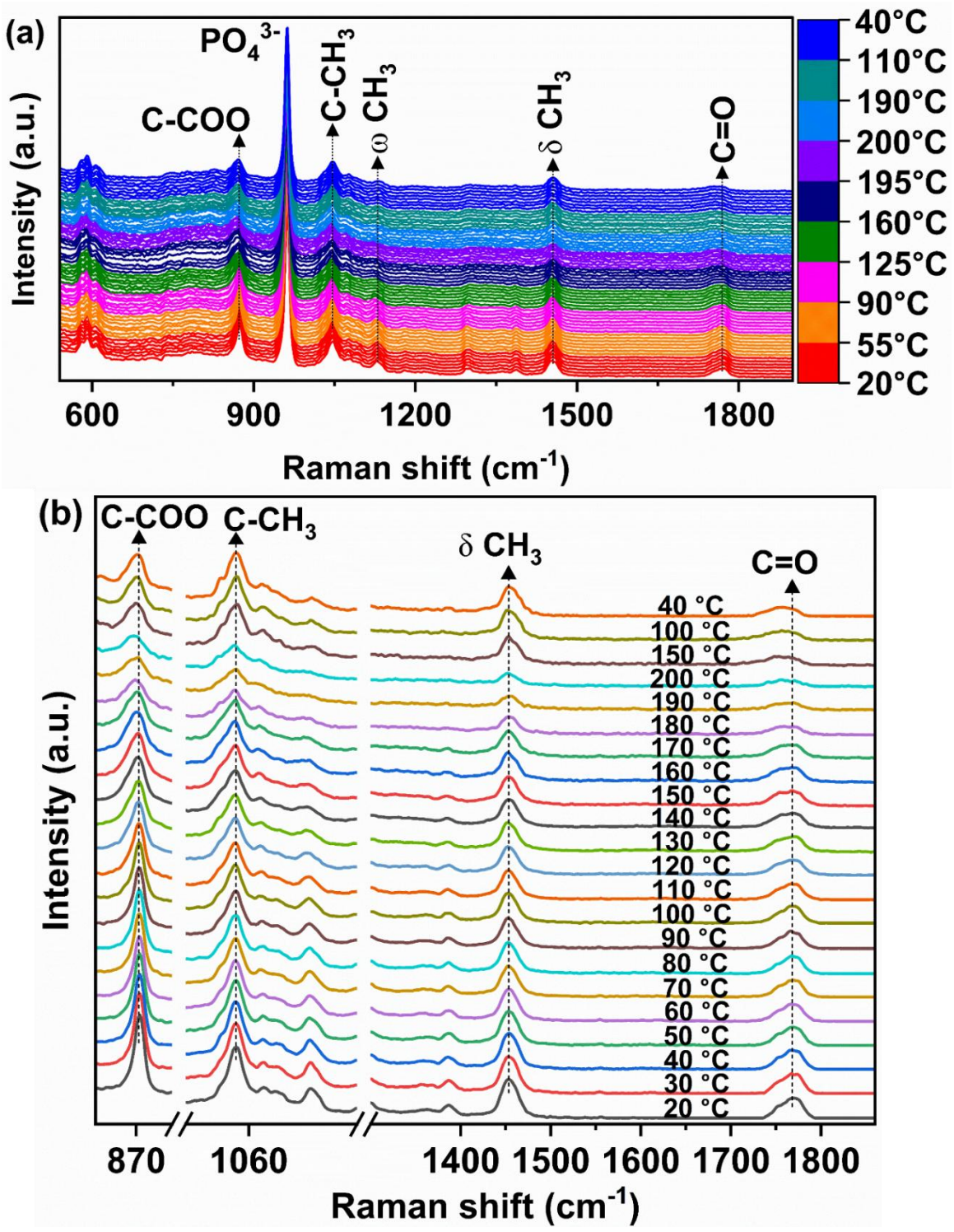

Figure 6.11 *(a) Overall* in-situ *Raman spectra acquired every 60 s during CSP of HAPLA (80:20 wt.%) composite without liquid (T = 200 °C). At this acquisition rate, each spectrum during the heating ramp corresponds to ~5 °C; spectra were also recorded during the isothermal hold (10 min) and cooling cycle (to 40 °C). (b) Selected spectra (only PLA bands) at specific temperatures spanning the heating and cooling stages.*

The in-situ visual images (Fig. 6.10(inset)) strongly correlate the progression of consolidation with the thermal-induced flowability changes of PLA, which is consistent with the observed ~49 % shrinkage during Stage II. DSC (Fig. 6.7(a)) of HA:PLA 80:20 powder indicates an onset glass transition (T_g) temperature ~35 °C, and an onset melting temperature (T_m) near ~140 °C. Above T_g, PLA chains gain mobility; as the temperature approaches T_m, it transitions to a viscous, flowable phase that wets the whole compact, enabling further particle rearrangements and consolidation of the compact. During stage II, the compact becomes glassy and translucent by 110 °C, and fully translucent above 140 °C. This is consistent with PLA melting into a viscous flowable phase. Once PLA becomes flowable, it reduces the interparticulate friction among HA grains, homogeneously wets the HA matrix, and enhances the intergranular cohesion. During stage III (upon cooling), PLA solidifies, bonds to the HA matrix, and fills in the intergranular porosity. These interpretations align with the SEM microstructures in Fig. 6.2(a_1 & a_2) and 6.3(a_1 & a_2).

In-Situ Raman spectra acquired during the CSP of HA:PLA are presented in Fig. 6.11(a&b). The HA bands are observed at 962 cm^{-1} (ν_1 symmetric P-O stretching of PO_4^{3-} group), and at 590 & 608 cm^{-1} (ν_4 O-P-O bending of PO_4^{3-} group). The PLA bands are observed at 874 cm^{-1} (C-COO stretching), 1046 cm^{-1} (C-CH_3 stretching), 1126 & 1453 cm^{-1} (CH_3 rocking & bending), and 1769 cm^{-1} (C=O stretching) [264]. During heating, the PLA bands at 874, 1046, 1453, 1769 cm^{-1} characteristic of PLA broaden (Fig. 6.11(b)) and decrease in intensity (Fig. 6.12) due to thermal-induced chain disordering or pressure-induced thermal degradation [267]. During cooling, the intensity of those bands rises gradually as the PLA chain mobility decreases and crystallization proceeds.

Notably, the carbonyl-related stretching bands exhibit downshifts after consolidation: the C=O mode moves from 1769 cm^{-1} to 1758 cm^{-1}, and the C-COO mode from 874 cm^{-1} to 870 cm^{-1}. This plausibly indicated the H-bonding interfacial interaction between PLA carbonyls and HA surface hydroxyl/phosphate groups. A pronounced drop in overall relative Raman intensity (Fig. 6.12) occurs above ~155 °C and persists until the isothermal holding at 200 °C, which is coincident with the HA:PLA compact becoming translucent. This optical effect likely alters the effective sampling probed volume (laser–sample overlap), producing an apparent intensity loss during heating and recovered upon

cooling [268, 269]. Despite such optical effects, the characteristic PLA bands recover their intensities during cooling. A residual ~13-15 % intensity decrease in the C-CH_3 band remains after CSP, which could be due to the thermal-induced degradation (chain scission) known to occur near T_m. In contrast, the C=O and C–COO stretching bands show respective reductions in relative intensity of ~50 % and ~30-35 % after CSP, consistent with diminished PLA crystallinity and/or increased morphological heterogeneity (detailed in Section 6.5) [265].

Collectively, the in-situ observations indicate that consolidation of the HA:PLA composite is driven primarily by thermally controlled changes in PLA fluidity and interfacial wetting, with no spectroscopic evidence for pressure-solution creep in HA.

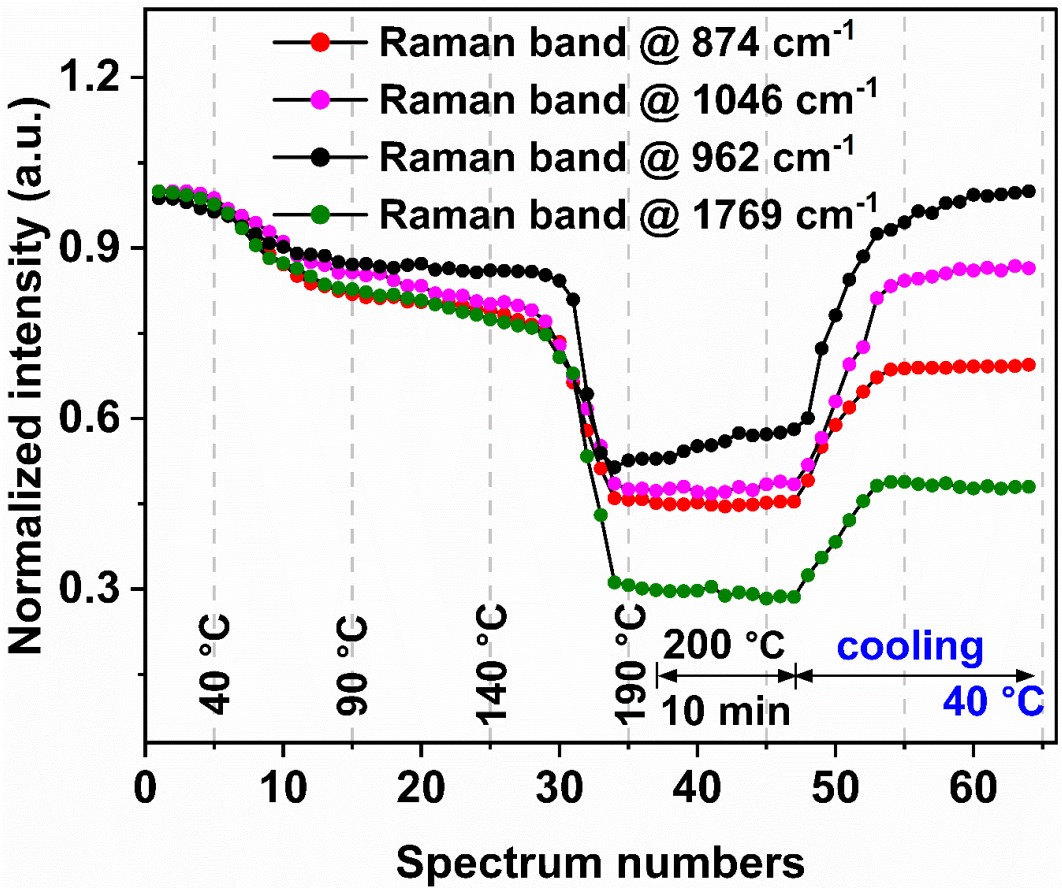

Figure 6.12 *Temperature-dependent relative intensity changes of PLA and HA bands. The dashed line in the inset indicates the temperature intervals; each data point corresponds to a spectrum shown in Fig. 6.10 (a).*

6.8 Conclusions

This study offers new insights into the consolidation behavior during the cold sintering of HA-PLA composites at 200 °C under 360 MPa pressure. CSP facilitates the creation of high-strength, dense composites with a relative density exceeding 90 %, effectively combining HA's stiffness with PLA's flexibility.

The consolidation pattern between HA and PLA, as well as the consolidation of HA grains within the composite matrix, depends significantly on the HA-to-PLA ratio and the temperature-dependent flowability of PLA. Higher PLA content increases the overall density of the composite, as consolidation primarily occurs between HA aggregates and PLA. In contrast, lower PLA content promotes the consolidation of HA grains within the matrix, as well as between HA grains and PLA. In particular, the HA:PLA ratio of 80:20 delivers superior mechanical performance, attributed to robust HA-HA cohesive bonding coupled with mechanical interlocking at HA-PLA interfaces.

Additionally, the key role of the plasticization effect in enhancing the consolidation as well as the crystallization of PLA during cold sintering was also established with 80:20 HA:PLA fraction. Plasticization effects were found to improve the HA-HA grain consolidation and strengthen the interaction between the well-crystallized PLA and HA. This produces a stiff composite structure, although the plasticizer introduces some flexibility, resulting in reduced hardness compared to the unplasticized composite.

Furthermore, in-situ CSP experiments on the HA:PLA 80:20 fraction (unplasticized) establish that consolidation is governed by the thermally controlled PLA fluidity, with no spectroscopic evidence for pressure-solution processes. Stage II (heating under pressure) primarily controls the consolidation, proceeding via melt-mediated interfacial wetting of HA by PLA, reduction of HA intergranular friction, and enables cohesive HA-HA bonding; upon cooling, PLA solidifies to lock in the compact (PLA binding effect). These events control the density and microstructure in the composites prepared with varied HA:PLA ratios. In-situ Raman and FTIR results support the interfacial H-bonding between HA and PLA.

Collectively, CSP enables the cohesive consolidation of HA nanograins, and the formation of a strong mechanical/chemical interfacial bond provides ultimate strength

equivalent to dense cortical bone. The HA-HA bonding remains critical for providing the necessary stiffness in the composite structure. To deepen understanding and improve performance, the composites' dynamic mechanical behavior, mesoporosity, and surface hydrophilicity should be optimized and directly correlated with biological outcomes. A comprehensive evaluation integrating mechanical characterization with in vitro and in vivo testing is essential to ensure that cold-sintered composite grafts provide structural support, promote tissue regeneration, and undergo controlled resorption, potentially eliminating the need for secondary surgeries.

Chapter 7: General Conclusions and Future Work

Over the past few decades, advances in sintering technology have shifted emphasis from conventional high-temperature methods to non-conventional, low-temperature approaches. In this context, the cold sintering process, a pressure-assisted, low-temperature technique introduced in 2016 by Randall and co-workers. It has opened significant opportunities for processing functional ceramics and ceramic–polymer composites that are constrained by high-temperature exposure. Since its introduction, multiple research directions have sought to strengthen CSP's mechanistic foundations and to map parameter–processing–property relationships, thereby advancing its technology readiness level. To date, ZnO and $BaTiO_3$ have been the most extensively studied systems, providing key insights into the pressure–solution creep mechanisms operative in CSP.

This thesis establishes a fundamental CSP framework for bioactive materials, including hydroxyapatite (HA), a ternary sol-gel-derived bioactive glass (BG; SiO_2–CaO–P_2O_5), and HA-polylactic acid (HA-PLA) composites. Collectively, the results identify suitable transient liquid phases and the underlying chemical mechanistic pathways that enable effective low-temperature densification of HA and BG. Also, elucidated the consolidation of HA-PLA as a function of ceramic-polymer ratio and polymer flowability, and clarified the associated consolidation mechanisms. Finally, complementing the ex-situ findings, in-situ monitoring coupled with in-situ Raman spectroscopy established the operative dissolution-precipitation pathways in HA and BG, as well as the consolidation mechanisms in HA-PLA.

In CSP, the transient liquid plays a central role in driving dissolution-precipitation, and this study shows a decisive dependence on transient-liquid chemistry and ionic strength, particularly under acidic conditions, for densifying HA and BG. Using phosphoric acid (2 M H_3PO_4), CSP of HA achieved ~90 % relative density at 360 MPa and 200 °C while

preserving nanometric grains and HA phase purity; the same conditions yielded ~89 % density for BG and induced partial in-situ recrystallization of HA within the glass matrix.

Because dissolution-precipitation is surface-mediated, the powders' physicochemical properties strongly influence outcomes: HA with higher specific surface area and lower crystallinity (600 °C calcined HA) promoted uniform dissolution with minimal secondary phosphate formation, whereas lower-SSA, more crystalline HA (900 °C calcined HA) exhibited localized dissolution, reprecipitation of dicalcium phosphate anhydrous (DCPA), and reduced densification (~68 %). However, in BG, the sequence of dissolution–precipitation–recrystallization depended on the transient liquid: water or NaOH favored largely congruent hydrolysis/condensation of the silicate network, producing densified yet amorphous compacts without HA formation, while H_3PO_4 drove incongruent dissolution, precipitation of DCPA, nucleation, and recrystallization of HA. This particularly improved the mechanical properties of the BG relative to BG cold sintered with NaOH.

To date, a concise consolidation mechanism for ceramic-polymer composites has not been established. In systems containing hydrophobic polymers, aqueous transient liquids are generally incompatible because they can degrade the polymer and hinder compaction. Central to this, this thesis demonstrated consolidation of HA-PLA without liquid, at 200 °C / 360 MPa. Consolidation is governed by the flowability of PLA and by the HA-to-PLA ratio, which sets the balance between HA-HA bonding and HA-PLA interfacial bonding. This provided the best mechanical response due to cohesive HA-HA bonding with strong interfacial interlocking of HA-PLA. Plasticizing PLA with tributyl citrate increased polymer flowability, enhanced consolidation, and promoted PLA crystallization, but reduced hardness because the plasticized polymer is softer than neat PLA.

Finally, in-situ CSP monitoring coupled with in-situ Raman spectroscopy provided a transferable framework for tuning liquid chemistry and thermal holds across ceramics, glasses, and ceramic-polymer systems. In-situ Raman revealed early precipitation of transient phases in HA and BG upon mixing with H_3PO_4, continued pressure-assisted dissolution-precipitation up to ~90 °C, followed by recrystallization as the added aqueous phase evaporated and consolidating the grains. In HA-PLA, in-situ CSP setup

furnished direct evidence of melt-mediated interfacial wetting and bonding, wherein consolidation occurs during heating under compaction, then PLA locks in upon solidification.

The bioactive materials investigated in this thesis are ideal for bone-regenerative applications as synthetic structural grafts. When considering these bioactive materials as dense synthetic grafts for addressing critical-sized bone defects, requires stronger emphasis on translational research. This thesis work primarily focused on understanding the fundamentals of CSP of bioactive materials: ceramics and composite systems. Results validated that the CSP allows fabricating dense nano-grained HA or composite with high ceramic fraction; however, the critical parameters, such as surface porosity/wettability of the cold sintered samples, remain an active area of exploration. Moreover, in-depth mechanical assessment, such as dynamic mechanical analysis (before and after bioactivity tests), fatigue behavior, or fracture toughness of cold-sintered HA, BG, or HA-PLA composites, is also important. Hence, future research aimed to focus on establishing correlations between the mechanical performance and porosity features of cold-sintered samples interrelated to the influence of transient liquids (for ceramics) or polymer types (for composites).

Porosity distribution (nano-to-meso scale size) plays a crucial role in the biological responses, including ion-release profiles, cell adhesion, and in-vitro/in-vivo resorption or degradation. Future studies should therefore investigate the pore architecture of cold-sintered samples using advanced characterization techniques like micro-CT or FIB-SEM. Further, the outcomes of porosity features would help to correlate the ion release and cell-adhesion behaviour of the cold sintered samples. Additionally, a combined analysis of pore characteristics and biological performance will help clarify whether cold-sintering effects, such as residual non-apatitic phosphate in HA, variations in HA crystallinity, HA crystal phase in BG, or composite surface hydrophilicity, impact the bioactivity or resorption/degradation behavior of dense samples.

Bioactive glasses encompass silicate-, phosphate-, and borate-based families, each is available in varied chemical compositions. Although BG is known for faster bioactivity than HA, CSP studies remain limited: to date, only the 45S5 and S53P4 compositions have been examined. The present results on cold sintering of 50S ternary silicate bioglass

with different transient liquids should therefore be extended to additional BG variants. Moreover, CSP offers a route to integrate HA and BG into composites. While this study demonstrated adding BG to an HA matrix, future work could invert the architecture by cold-sintering HA within a BG matrix. This may help control crystallization, particularly when phosphoric acid is used as the transient liquid, and enhance the mechanical performance of BG.

In the case of polymer-ceramic composites, this thesis focused solely on the HA-PLA system. Because PLA is a hydrophobic polymer, it is incompatible with transient liquids, making activation of the pressure-solution creep mechanism during CSP unfeasible. We hypothesize that this mechanism could be activated by employing a hydrophilic polymer system, such as chitosan, which is compatible with acetic acid, a transient liquid used in the CSP of HA (Chapter 4). Comparative studies on cold-sintering HA with hydrophilic polymers are therefore needed to determine whether specific transient liquids promote pressure-solution creep and to elucidate how CSP mechanisms vary with polymer chemistry.

Developing simple yet hierarchical porous complex structures would be highly beneficial for addressing complex-shaped bone defects. A promising strategy could involve combining screw-based 3D printing to create composite-based architectures, followed by CSP consolidation through activation of plastic-deformation mechanisms using hot-isostatic pressing or high-pressure injection molding. It is purely a hypothesis; no such research has been reported in the literature. If it becomes feasible, it could represent a significant advancement in the manufacturing of synthetic bone grafts using the CSP framework, paving the way toward commercial translation.

Appendix

Appendix A: Supplementary Material

Linear shrinkage profile from In-situ CSP monitoring

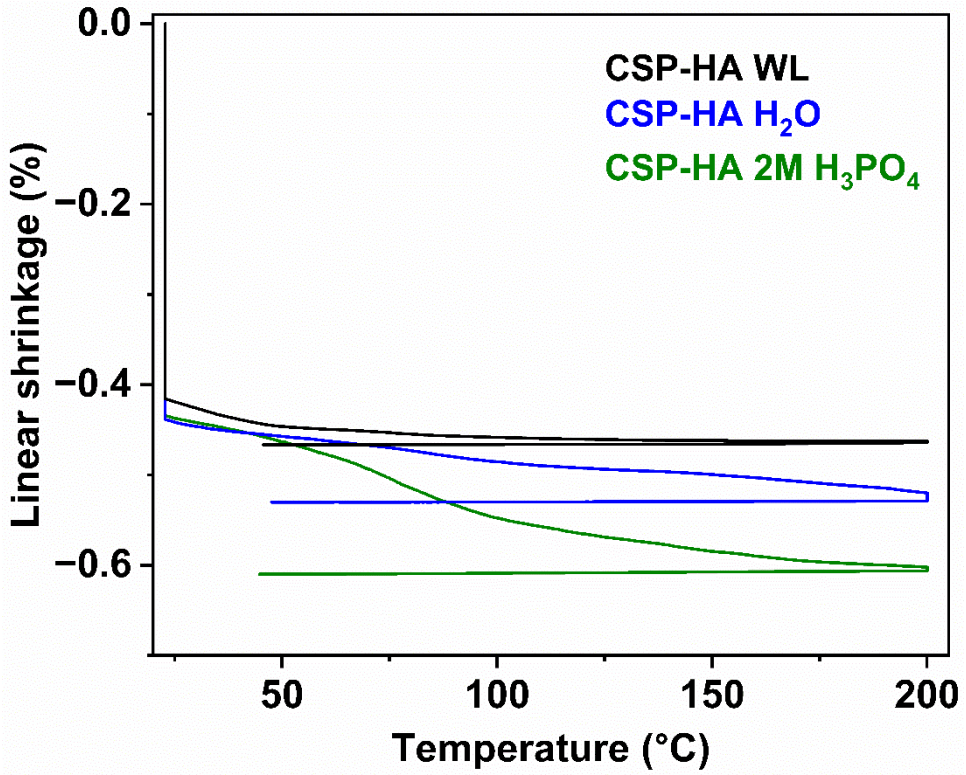

Figure S1 *Relative linear shrinkage profile (vs temperature) measured from the relative changes in the sample length during the CSP of HA (HAp202 powder) without liquid, with H_2O, and with 2 M H_3PO_4.*

Differential thermal analysis of BG powder

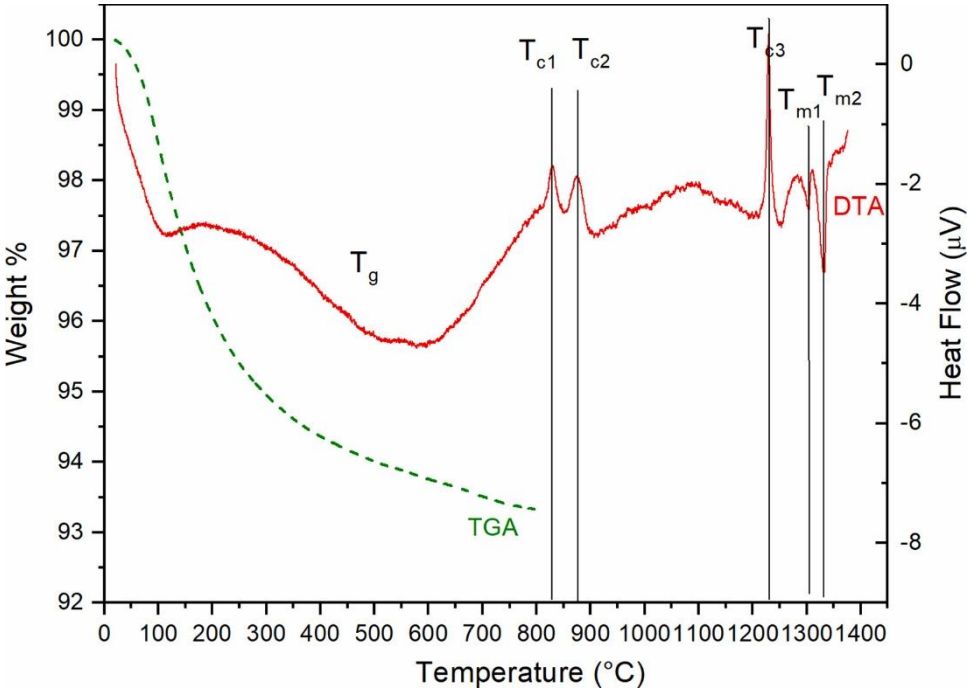

Figure S2 *DTA-TGA curve of sol-gel derived 50S bioglass powder taken from [225].*

Linear shrinkage profile from In-situ CSP monitoring

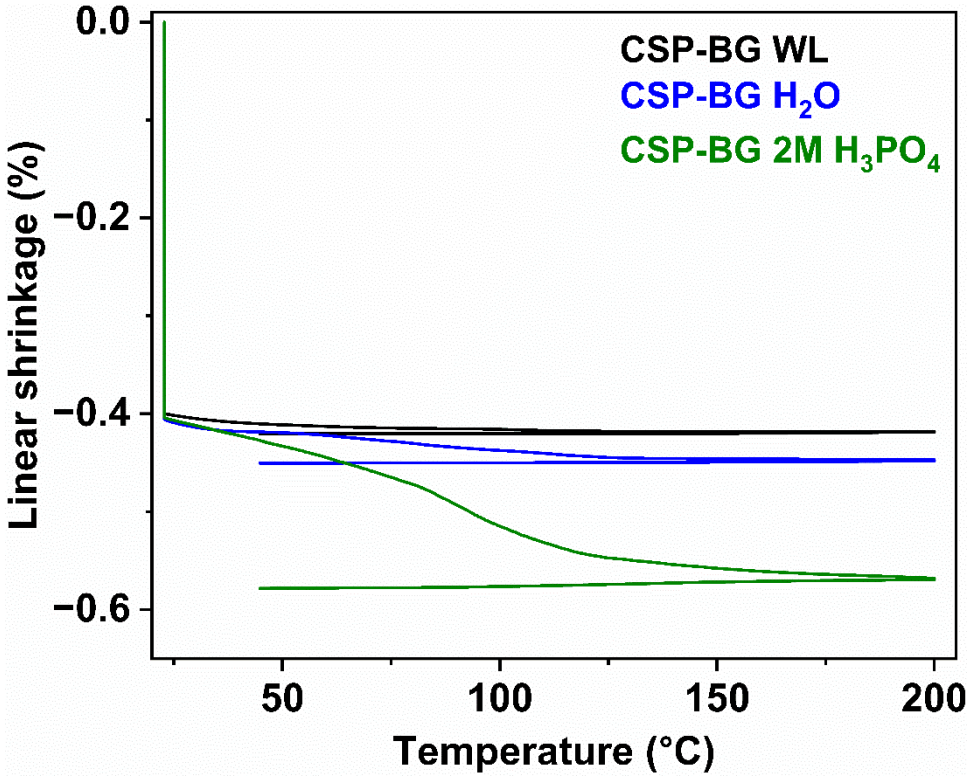

Figure S3 *Relative linear shrinkage profile (vs temperature) measured from the relative changes in the sample length during the CSP of BG without liquid, with H_2O, and with 2 M H_3PO_4.*

HA:PLA composite powder characteristics

The HA powder consists of spherical aggregates of nano-sized HA particles (Fig. S4(a_1&a_2)). In the HA:PLA (80:20) composite, these aggregates are retained, with PLA adsorbed (coated) over the HA aggregate particle surfaces (Fig. S4b). This surface adsorption accounts for the composite's free-flowing, soft texture after chloroform evaporation. As the PLA content increases, however, PLA-encapsulated HA aggregates coalesce during solvent removal, forming hard lumps. Consistent with this trend, the HA:PLA (70:30) powder (Fig. S4(c)) exhibits irregular, submicron particles after cryo-milling, indicating that higher PLA loadings disrupt powder uniformity. The 70:30, 60:40, and 50:50 composite lumps were cryo-milled; however, the resulting powders' physical texture was not as free-flowing as the 80:20 powder.

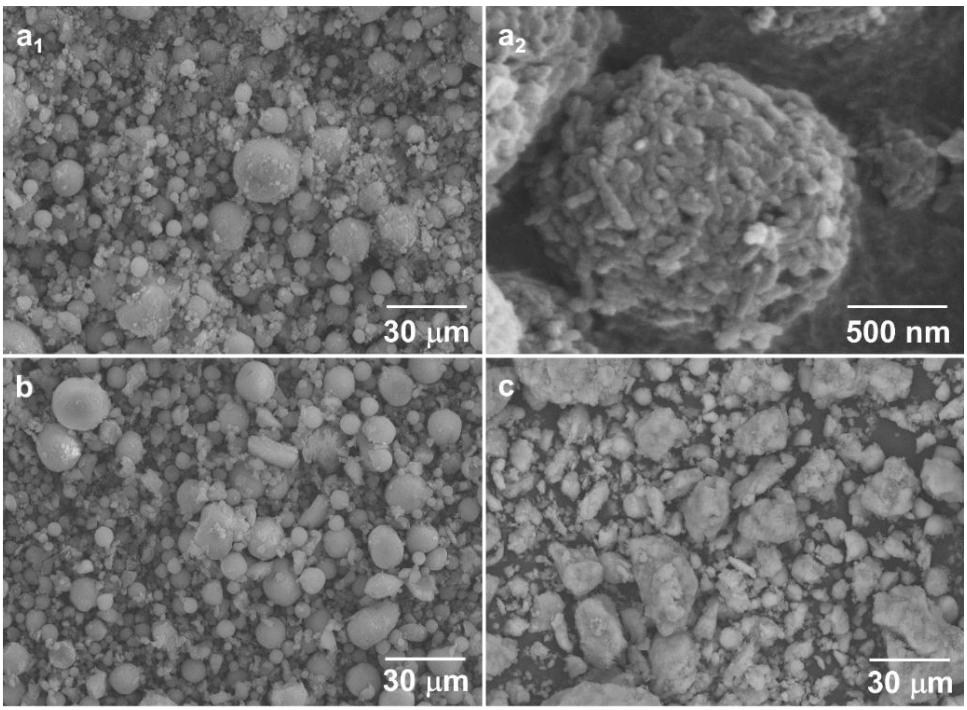

Figure S4 *(a_1,a_2) SEM images of Hap202 powder, (b) HA:PLA 80:20, and (c) HA:PLA 70:30 composite powders.*

Consolidated HA matrix from HA:PLA composite

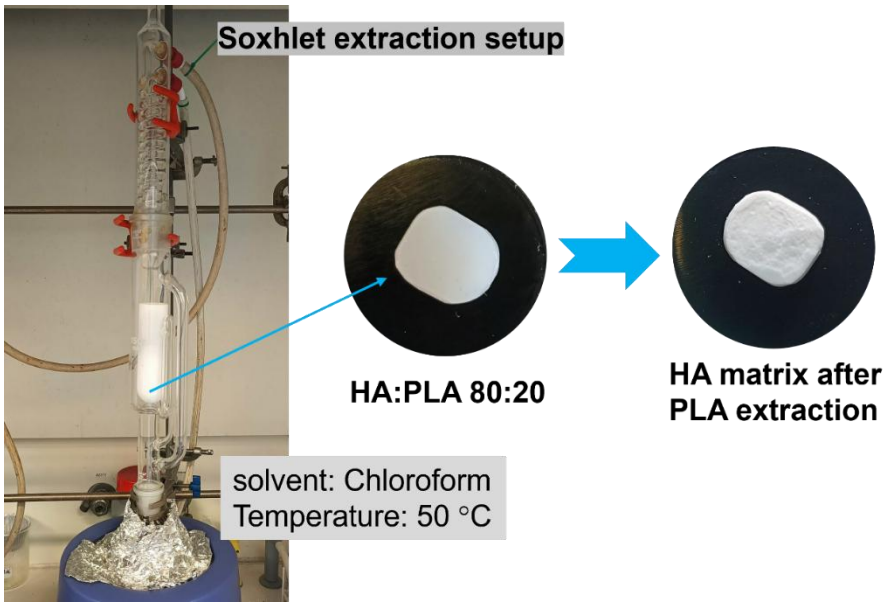

Figure S5 Illustration of the Soxhlet extraction setup and the HA matrix extracted after PLA *extraction*.

Linear shrinkage profile from In-situ CSP monitoring

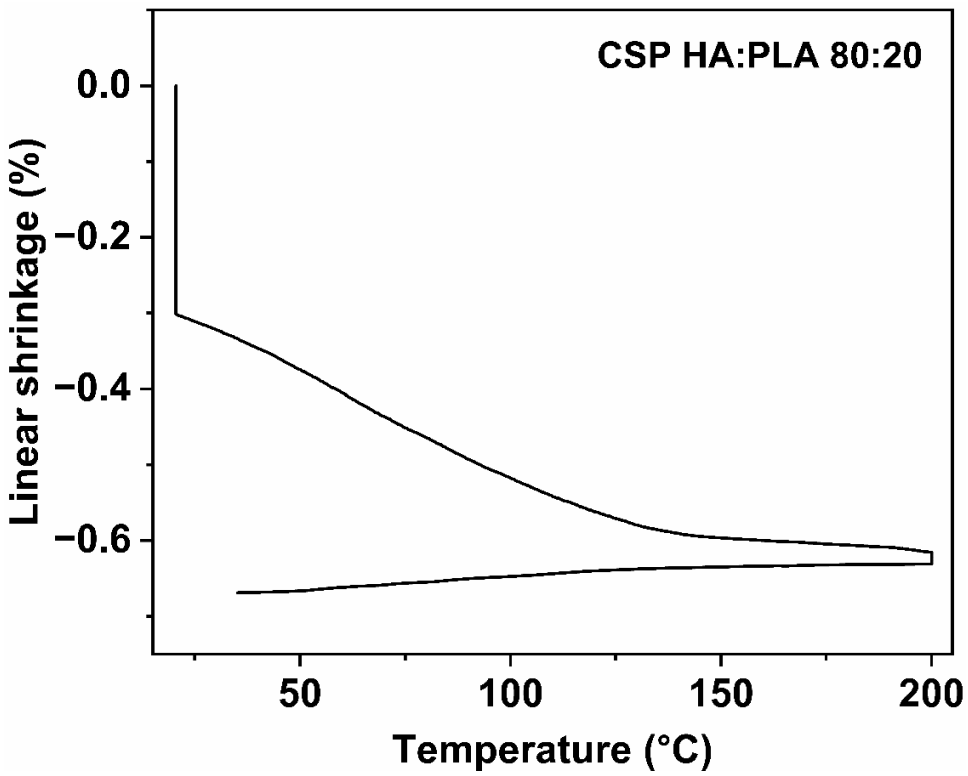

Figure S6 *Relative linear shrinkage profile (vs temperature) measured from the relative changes in the sample length during the CSP of HA:PLA 80:20 without liquid.*

Appendix B: Scientific Dissemination

Peer-reviewed Journal Articles

1. **Kumar, M.**, Achour, M.A.B., Lasgorceix, M., Quadros, P., Mincheva, R., Raquez, J.M. and Leriche, A., **2024**. Densification of hydroxyapatite through cold sintering process: role of liquid phase chemistry and physical characteristic of HA powder. *Open Ceramics*, *17*, 100566. https://doi.org/10.1016/j.oceram.2024.100566
2. **Kumar, M.**, Achour, M.A.B., Ölmez, V., Lasgorceix, M., Mincheva, R., Leriche, A. and Raquez, J.M., **2025**. Consolidation behavior of HA-PLA nanocomposites during cold sintering process: Influence of HA-to-PLA ratio and the plasticizing effect of PLA. *Materials Today Communications*, *45*, 112322. https://doi.org/10.1016/j.mtcomm.2025.112322

Conference Presentations

1. Oral Presentation – 2025, 19th ECerS Conference and Exhibition, Dresden, Germany.
2. Oral Presentation – 2025, Belgium Ceramic Society Annual Meeting, Ghent, Belgium.
3. Oral Presentation – 2024, Belgium Ceramic Society Annual Meeting, Liege, Belgium.
4. Oral Presentation – 2024, 15th ECerS Conference for Young Scientists in Ceramics, Novi Sad, Serbia.
5. Oral Presentation – 2024, 1st Student Speech Contest, Bioceramics Network, Online.
6. Poster Presentation – 2024, Mardi des Chercheurs (Researchers' Tuesday), Mons, Belgium.
7. Oral Presentation – 2023, BioCAM workshop, Mons, Belgium.
8. Oral Presentation – 2023, International Conference on Advanced Materials and Their Applications, Thoothukudi, India.
9. Poster Presentation – 2023, 18th ECerS Conference and Exhibition, Lyon, France.
10. Poster Presentation – 2023, Summer School on Non-Conventional Sintering: Science and Technology, Trento, Italy.
11. Oral Presentation – 2023, 3rd Young Ceramists Network Workshop, Aveiro, Portugal.
12. Poster Presentation – 2023, Mardi des Chercheurs (Researchers' Tuesday), Valenciennes, France.

Bibliography

[1] Ratner, B. D., Hoffman, A. S., Schoen, F. J., & Lemons, J. E. (2004). Biomaterials science: an introduction to materials in medicine, Elsevier.

[2] Williams, D. F. (2009). On the nature of biomaterials. *Biomaterials*, *30*(30), 5897-5909.

[3] Yu, X., Tang, X., Gohil, S. V., & Laurencin, C. T. (2015). Biomaterials for bone regenerative engineering. *Adv. Healthc. Mater.*, *4*(9), 1268-1285.

[4] Ramachandran, M. (Ed.). (2018). *Basic orthopaedic sciences*. CRC Press.

[5] Dimitriou, R., Jones, E., McGonagle, D., & Giannoudis, P. V. (2011). Bone regeneration: current concepts and future directions. *BMC Medicine*, *9*, 1-10.

[6] Cacchioli, A., Spaggiari, B., Ravanetti, F., Martini, F.M., Borghetti, P. and Gabbi, C., 2006. The critical sized bone defect: morphological study of bone healing.

[7] Verrier, S., Alini, M., Alsberg, E., Buchman, S. R., Kelly, D., Laschke, M. W., ... & Evans, C. (2016). Tissue engineering and regenerative approaches to improving the healing of large bone defects. *Eur. Cell Mater.*, *32*, 87-110.

[8] Bongio, M., Van Den Beucken, J. J., Leeuwenburgh, S. C., & Jansen, J. A. (2010). Development of bone substitute materials: from 'biocompatible' to 'instructive'. *J Mater. Chem.*, *20*(40), 8747-8759.

[9] Basha, R. Y., TS, S. K., & Doble, M. (2015). Design of biocomposite materials for bone tissue regeneration. *Mater. Sci. Eng. C.*, *57*, 452-463.

[10] Tang, G., Liu, Z., Liu, Y., Yu, J., Wang, X., Tan, Z., & Ye, X. (2021). Recent trends in the development of bone regenerative biomaterials. *Front. Cell Dev. Biol.*, *9*, 665813.

[11] Wang, W., & Yeung, K. W. (2017). Bone grafts and biomaterials substitutes for bone defect repair: A review. Bioact. Mater., 2(4), 224-247.

[12] Lasanianos, N.G., Kanakaris, N.K. and Giannoudis, P.V., 2010. Current management of long bone large segmental defects. *Orthopaedics and Trauma*, *24*(2), 149-163.

[13] Roddy, E., DeBaun, M.R., Daoud-Gray, A., Yang, Y.P. and Gardner, M.J., 2018. Treatment of critical-sized bone defects: clinical and tissue engineering perspectives. *European Journal of Orthopaedic Surgery & Traumatology*, *28*, 351-362.

[14] Gugala, Z., Lindsey, R.W. and Gogolewski, S., 2007, August. New approaches in the treatment of critical-size segmental defects in long bones. In *Macromolecular symposia* (Vol. 253, No. 1, 147-161). Weinheim: WILEY-VCH Verlag.

[15] Gómez-Barrena, E. and Ehrnthaller, C., 2024. Long bone uninfected non-union: Grafting techniques. *EFORT open reviews*, *9*(5), 329-338.

[16] Albrektsson, T., & Johansson, C. (2001). Osteoinduction, osteoconduction and osseointegration. *Eur. Spine J.*, *10*, S96-S101.

[17] Georgeanu, V. A., Gingu, O., Antoniac, I. V., & Manolea, H. O. (2023). Current options and future perspectives on bone graft and biomaterials substitutes for bone repair, from clinical needs to advanced biomaterials research. *Appl. Sci.*, *13*(14), 8471.

[18] Hutmacher, D. W., Schantz, J. T., Lam, C. X. F., Tan, K. C., & Lim, T. C. (2007). State of the art and future directions of scaffold-based bone engineering from a biomaterials perspective. *J Tissue Eng. Regen. Med.*, *1*(4), 245-260.

[19] Babis, G. C., & Soucacos, P. N. (2005). Bone scaffolds: The role of mechanical stability and instrumentation. *Injury*, *36*(4), S38-S44.

[20] Dorozhkin, S. V. (2010). Bioceramics of calcium orthophosphates. *Biomater.*, *31*(7), 1465-1485.

[21] Fiume, E., Magnaterra, G., Rahdar, A., Verné, E., & Baino, F. (2021). Hydroxyapatite for biomedical applications: A short overview. *Ceram.*, *4*(4), 542-563.

[22] Zhou, H., & Lee, J. (2011). Nanoscale hydroxyapatite particles for bone tissue engineering. *Acta Biomater.*, *7*(7), 2769-2781.

[23] Du, M., Chen, J., Liu, K., Xing, H., & Song, C. (2021). Recent advances in biomedical engineering of nano-hydroxyapatite including dentistry, cancer treatment and bone repair. *Compos. B: Eng.*, *215*, 108790.

[24] Hench, L.L., 2006. The story of Bioglass®. *Journal of materials science: materials in medicine*, *17*(11), 967-978.

[25] Li, R., Clark, A.E. and Hench, L.L., 1991. An investigation of bioactive glass powders by sol-gel processing. *J. Appl. Biomater.*, *2*(4), 231-239.

[26] Sepulveda, P., Jones, J.R. and Hench, L.L. (2001), Characterization of melt-derived 45S5 and sol-gel–derived 58S bioactive glasses. J. Biomed. Mater. Res., 58: 734-740.

[27] Balamurugan, A., Balossier, G., Kannan, S., Michel, J., Rebelo, A.H. and Ferreira, J.M., 2007. Development and in vitro characterization of sol–gel derived CaO–P2O5–SiO2–ZnO bioglass. *Acta Biomater.*, *3*(2), 255-262.

[28] Taghian Dehaghani, M., Ahmadian, M. and Fathi, M., 2015. Synthesis, characterization, and bioactivity evaluation of amorphous and crystallized 58S bioglass nanopowders. *Int. J. Appl. Ceram. Technol.*, *12*(4), 867-874.

[29] Trzaskowska, M., Vivcharenko, V., & Przekora, A. (2023). The impact of hydroxyapatite sintering temperature on its microstructural, mechanical, and biological properties. *Int. J. Molecular Sciences*, *24*(6), 5083.

[30] Youness, R. A., Taha, M. A., & Ibrahim, M. A. (2017). Effect of sintering temperatures on the in vitro bioactivity, molecular structure and mechanical properties of titanium/carbonated hydroxyapatite nanobiocomposites. *Journal of Molecular Structure*, *1150*, 188-195.

[31] Ma, J., Chen, C.Z., Wang, D.G., Meng, X.G. and Shi, J.Z., 2010. Influence of the sintering temperature on the structural feature and bioactivity of sol–gel derived SiO2–CaO–P2O5 bioglass. *Ceram. Int.*, *36*(6), 1911-1916.

[32] Stiller, A., Engblom, M., Vainio, E. and Hupa, L., 2024. Understanding the crystallization behavior of bioactive glass S53P4 powder compacts under various heating conditions. *Journal of Non-Crystalline Solids*, *644*, 123178.

[33] Mecca, F.G., Bellucci, D. and Cannillo, V., 2023. Effect of thermal treatments and ion substitution on sintering and crystallization of bioactive glasses: A review. *Materials*, *16*(13), 4651.

[34] Raquez, J. M., Habibi, Y., Murariu, M., & Dubois, P. (2013). Polylactide (PLA)-based nanocomposites. *Progress in Polymer Science*, *38*(10-11), 1504-1542.

[35] Sha, L., Chen, Z., Chen, Z., Zhang, A., & Yang, Z. (2016). Polylactic acid based nanocomposites: Promising safe and biodegradable materials in biomedical field. *International Journal of Polymer Science*, *2016*(1), 6869154.

[36] Danoux, C.B., Barbieri, D., Yuan, H., de Bruijn, J.D., van Blitterswijk, C.A. and Habibovic, P., 2014. In vitro and in vivo bioactivity assessment of a polylactic acid/hydroxyapatite composite for bone regeneration. *Biomatter*, *4*(1), e27664.

[37] Odabaş, E., Öztürk, O., & Akarsu, E. (2024). Modulation of mechanical and thermal properties of poly(lactic acid)/hydroxyapatite composites by interface crosslinking. *Polymer Composites*, 45(18): 17280-17293.

[38] Russias, J., Saiz, E., Nalla, R. K., Gryn, K., Ritchie, R. O., & Tomsia, A. P. (2006). Fabrication and mechanical properties of PLA/HA composites: A study of in vitro degradation. *Materials Science and Engineering: C*, *26*(8), 1289-1295.

[39] Konopka, K., Boczkowska, A., Batorski, K., Szafran, M., & Kurzydłowski, K. J. (2004). Microstructure and properties of novel ceramic–polymer composites. *Materials Letters*, *58*(30), 3857-3862.

[40] Fallon, J. J., McKnight, S. H., & Bortner, M. J. (2019). Highly loaded fiber filled polymers for material extrusion: A review of current understanding. *Additive Manufacturing*, *30*, 100810.

[41] Šupová, M. (2009). Problem of hydroxyapatite dispersion in polymer matrices: a review. *Journal of Materials Science: Materials in Medicine*, *20*, 1201-1213.

[42] Carette, X., Dhond, L., Hemberg, A., Thiry, D., Mincheva, R., Cailloux, J., ... & Raquez, J. M. (2021). Innovative one-shot paradigm to tune filler–polymer matrix interface properties by plasma polymer coating in osteosynthesis applications. *ACS Applied Bio Materials*, *4*(4), 3067-3078.

[43] Guo, H., Guo, J., Baker, A., & Randall, C. A. (2016). Hydrothermal-assisted cold sintering process: a new guidance for low-temperature ceramic sintering. *ACS applied materials & interfaces*, *8*(32), 20909-20915.

[44] Guo, H., Baker, A., Guo, J., & Randall, C. A. (2016). Protocol for ultralow-temperature ceramic sintering: an integration of nanotechnology and the cold sintering process. *ACS nano*, *10*(11), 10606-10614.

[45] Yu, T., Cheng, J., Li, L., Sun, B., Bao, X. and Zhang, H., 2019. Current understanding and applications of the cold sintering process. *Frontiers of Chemical Science and Engineering*, *13*(4), 654-664.

[46] Guo, J., Floyd, R., Lowum, S., Maria, J.P., Herisson de Beauvoir, T., Seo, J.H. and Randall, C.A., 2019. Cold sintering: progress, challenges, and future opportunities. *Annual Review of Materials Research*, *49*(1), 275-295.

[47] Grasso, S., Biesuz, M., Zoli, L., Taveri, G., Duff, A.I., Ke, D., Jiang, A. and Reece, M.J., 2020. A review of cold sintering processes. *Advances in Applied Ceramics*, *119*(3), 115-143.

[48] Guo, J., Zhao, X., Herisson De Beauvoir, T., Seo, J. H., Berbano, S. S., Baker, A. L., ... & Randall, C. A. (2018). Recent progress in applications of the cold sintering process for ceramic–polymer composites. *Advanced Functional Materials*, *28*(39), 1801724.

[49] Guo, J., Berbano, S. S., Guo, H., Baker, A. L., Lanagan, M. T., & Randall, C. A. (2016). Cold sintering process of composites: bridging the processing temperature gap of ceramic and polymer materials. *Advanced Functional Materials*, *26*(39), 7115-7121.

[50] Dursun, S., Tsuji, K., Bang, S.H., Ndayishimiye, A. and Randall, C.A., 2020. A route towards fabrication of functional ceramic/polymer nanocomposite devices using the cold sintering process. *ACS Applied Electronic Materials*, *2*(7), 1917-1924.

[51] ul Hassan, M., & Ryu, H. J. (2019). Cold sintering and durability of iodate-substituted calcium hydroxyapatite (IO-HAp) for the immobilization of radioiodine. *Journal of Nuclear Materials*, *514*, 84-89.

[52] Shen, H. Z., Guo, N., Zhao, L., & Shen, P. (2020). Role of ion substitution and lattice water in the densification of cold-sintered hydroxyapatite. *Scripta Materialia*, *177*, 141-145.

[53] ul Hassan, M., Akmal, M., & Ryu, H. J. (2021). Cold sintering of as-dried nanostructured calcium hydroxyapatite without using additives. *Journal of Materials Research and Technology*, *11*, 811-822.

[54] Galotta, A., Agostinacchio, F., Motta, A., Dire, S., & Sglavo, V. M. (2023). Mechanochemical synthesis and cold sintering of mussel shell-derived hydroxyapatite nano-powders for bone tissue regeneration. *Journal of the European Ceramic Society*, *43*(2), 639-647.

[55] Shen, H. Z., Guo, N., Liang, Y. H., & Shen, P. (2021). Synthesis and densification of hydroxyapatite by mechanochemically-activated reactive cold sintering. *Scripta Materialia*, *194*, 113717.

[56] Kumar, M., Achour, M. A. B., Lasgorceix, M., Quadros, P., Mincheva, R., Raquez, J. M., & Leriche, A. (2024). Densification of hydroxyapatite through cold sintering process: Role of liquid phase chemistry and physical characteristic of HA powder. *Open Ceramics*, *17*, 100566.

[57] Guo, H., Baker, A., Guo, J., & Randall, C. A. (2016). Cold sintering process: a novel technique for low-temperature ceramic processing of ferroelectrics. *Journal of the American Ceramic Society*, *99*(11), 3489-3507.

[58] Ding, J., Guo, J., Yan, R., Li, W., Ma, S., Fu, Y., Xie, W., Riedel, R. and Weidenkaffa, A., 2024. Cold sintering process: A green route to fabricate thermoelectrics. Journal of Advanced Ceramics.

[59] Liu, Y., Sun, Q., Wang, D., Adair, K., Liang, J. and Sun, X., 2018. Development of the cold sintering process and its application in solid-state lithium batteries. *Journal of Power Sources*, *393*, 193-203.

[60] Wang, D., Li, L., Jiang, J., Lu, Z., Wang, G., Song, K., Zhou, D. and Reaney, I.M., 2021. Cold sintering of microwave dielectric ceramics and devices. *Journal of Materials Research*, *36*(2), 333-349.

[61] Lopes, D., Martins-Cruz, C., Oliveira, M.B. and Mano, J.F., 2018. Bone physiology as inspiration for tissue regenerative therapies. *Biomaterials*, *185*, 240-275.

[62] Florencio-Silva, R., Sasso, G.R.D.S., Sasso-Cerri, E., Simões, M.J. and Cerri, P.S., 2015. Biology of bone tissue: structure, function, and factors that influence bone cells. *BioMed Research International*, *2015*(1), 421746.

[63] Gao, C., Peng, S., Feng, P. and Shuai, C., 2017. Bone biomaterials and interactions with stem cells. *Bone research*, *5*(1), 1-33.

[64] Wopenka, B. and Pasteris, J.D., 2005. A mineralogical perspective on the apatite in bone. *Materials Science and Engineering: C*, *25*(2), 131-143.

[65] Von Euw, S., Wang, Y., Laurent, G., Drouet, C., Babonneau, F., Nassif, N. and Azaïs, T., 2019. Bone mineral: new insights into its chemical composition. *Scientific reports*, *9*(1),8456.

[66] Ressler, A., Žužić, A., Ivanišević, I., Kamboj, N. and Ivanković, H., 2021. Ionic substituted hydroxyapatite for bone regeneration applications: A review. *Open Ceramics*, *6*, 100122.

[67] Morgan, E.F., Unnikrisnan, G.U. and Hussein, A.I., 2018. Bone mechanical properties in healthy and diseased states. *Annual review of biomedical engineering*, *20*(1), 119-143.

[68] Reilly, D.T. and Burstein, A.H., 1975. The elastic and ultimate properties of compact bone tissue. *Journal of biomechanics*, *8*(6), 393-405.

[69] Mirzaali, M.J., Schwiedrzik, J.J., Thaiwichai, S., Best, J.P., Michler, J., Zysset, P.K. and Wolfram, U., 2016. Mechanical properties of cortical bone and their relationships with age, gender, composition and microindentation properties in the elderly. *Bone*, *93*, 196-211.

[70] Rho, J.Y., Tsui, T.Y. and Pharr, G.M., 1997. Elastic properties of human cortical and trabecular lamellar bone measured by nanoindentation. *Biomaterials*, *18*(20), 1325-1330.

[71] Rho, J.Y., Ashman, R.B. and Turner, C.H., 1993. Young's modulus of trabecular and cortical bone material: ultrasonic and microtensile measurements. *Journal of biomechanics*, *26*(2), 111-119.

[72] Turner, C.H., Rho, J., Takano, Y., Tsui, T.Y. and Pharr, G.M., 1999. The elastic properties of trabecular and cortical bone tissues are similar: results from two microscopic measurement techniques. *Journal of biomechanics*, *32*(4), 437-441.

[73] Hamed, E., Jasiuk, I., Yoo, A., Lee, Y. and Liszka, T., 2012. Multi-scale modelling of elastic moduli of trabecular bone. *Journal of The Royal Society Interface*, *9*(72), 1654-1673.

[74] Rho, J.Y., Kuhn-Spearing, L. and Zioupos, P., 1998. Mechanical properties and the hierarchical structure of bone. *Medical engineering & physics*, *20*(2), 92-102.

[75] Nair, A.K., Gautieri, A., Chang, S.W. and Buehler, M.J., 2013. Molecular mechanics of mineralized collagen fibrils in bone. *Nature communications*, *4*(1), 1724.

[76] Buckwalter, J.A., Glimcher, M.J., Cooper, R.R. and Recker, R., 1995. Bone biology. *JBJS*, *77*(8), 1276-1289.
[77] Šromová, V., Sobola, D. and Kaspar, P., 2023. A brief review of bone cell function and importance. *Cells*, *12*(21), 2576.
[78] Einhorn, T.A. and Gerstenfeld, L.C., 2015. Fracture healing: mechanisms and interventions. *Nature Reviews Rheumatology*, *11*(1), 45-54.
[79] Einhorn, T.A., 1998. The cell and molecular biology of fracture healing. *Clinical Orthopaedics and Related Research®*, *355*, S7-S21.
[80] Sela, J.J. and Bab, I.A., 2012. Healing of bone fracture: General concepts. In *Principles of Bone Regeneration*, Boston, MA: Springer US.
[81] DeLacure, M.D., 1994. Physiology of bone healing and bone grafts. *Otolaryngologic Clinics of North America*, *27*(5), 859-874.
[82] Claes, L., Eckert-Hübner, K. and Augat, P., 2003. The fracture gap size influences the local vascularization and tissue differentiation in callus healing. *Langenbeck's archives of surgery*, *388*, 316-322.
[83] Reichert, J.C., Saifzadeh, S., Wullschleger, M.E., Epari, D.R., Schütz, M.A., Duda, G.N., Schell, H., van Griensven, M., Redl, H. and Hutmacher, D.W., 2009. The challenge of establishing preclinical models for segmental bone defect research. *Biomaterials*, *30*(12), 2149-2163.
[84] Baldwin, P., Li, D.J., Auston, D.A., Mir, H.S., Yoon, R.S. and Koval, K.J., 2019. Autograft, allograft, and bone graft substitutes: clinical evidence and indications for use in the setting of orthopaedic trauma surgery. *Journal of orthopaedic trauma*, *33*(4), 203-213.
[85] Kim, D.H., Rhim, R., Li, L., Martha, J., Swaim, B.H., Banco, R.J., Jenis, L.G. and Tromanhauser, S.G., 2009. Prospective study of iliac crest bone graft harvest site pain and morbidity. *The Spine Journal*, *9*(11), 886-892.
[86] Delloye, C., Cornu, O., Druez, V. and Barbier, O., 2007. Bone allografts: what they can offer and what they cannot. *The Journal of Bone & Joint Surgery British Volume*, *89*(5), 574-580.
[87] Amid, R., Kheiri, A., Kheiri, L., Kadkhodazadeh, M. and Ekhlasmandkermani, M., 2021. Structural and chemical features of xenograft bone substitutes: A systematic review of in vitro studies. *Biotechnology and Applied Biochemistry*, *68*(6), 1432-1452.
[88] Kaiser, M., 2004. Xenotransplantation–ethical considerations based on human and societal perspectives. *Acta Veterinaria Scandinavica*, *45*(1), S65.
[89] Hughes, J., 1998. Xenografting: ethical issues. *Journal of Medical Ethics*, *24*(1), 18-24.
[90] Williams, D.F., 1987. Tissue-biomaterial interactions. *Journal of Materials science*, *22*, 3421-3445.
[91] Williams, D.F., 2009. On the nature of biomaterials. *Biomaterials*, *30*(30), 5897-5909.
[92] Cao, W. and Hench, L.L., 1996. Bioactive materials. *Ceramics International*, *22*(6), 493-507.

[93] Barrère, F., Mahmood, T.A., De Groot, K. and Van Blitterswijk, C.A., 2008. Advanced biomaterials for skeletal tissue regeneration: Instructive and smart functions. *Materials Science and Engineering: R: Reports*, *59*(1-6), 38-71.
[94] Navarro, M., Michiardi, A., Castano, O. and Planell, J.A., 2008. Biomaterials in orthopaedics. *Journal of the Royal Society Interface*, *5*(27), 1137-1158.
[95] Babis, G.C. and Soucacos, P.N., 2005. Bone scaffolds: the role of mechanical stability and instrumentation. *Injury*, *36*(4), S38-S44.
[96] Towards health care - Bone Grafts and Substitutes Market. https://www.towardshealthcare.com/insights/bone-grafts-and-substitutes-market-sizing
[97] Gautam, G., Kumar, S. and Kumar, K., 2022. Processing of biomaterials for bone tissue engineering: State of the art. *Materials today: proceedings*, *50*, 2206-2217.
[98] Hench, L.L. and Polak, J.M., 2002. Third-generation biomedical materials. *Science*, *295*(5557), 1014-1017.
[99] Farjaminejad, S., Farjaminejad, R., Hasani, M., Garcia-Godoy, F., Abdouss, M., Marya, A., Harsoputranto, A. and Jamilian, A., 2024. Advances and Challenges in Polymer-Based Scaffolds for Bone Tissue Engineering: A Path Towards Personalized Regenerative Medicine. *Polymers*, *16*(23), 3303.
[100] Wang, M., 2003. Developing bioactive composite materials for tissue replacement. *Biomaterials*, *24*(13), 2133-2151.
[101] Alkaron, W., Almansoori, A., Balázsi, C. and Balázsi, K., 2024. A Critical Review of Natural and Synthetic Polymer-Based Biological Apatite Composites for Bone Tissue Engineering. *Journal of Composites Science*, *8*(12), 523.
[102] Hou, X., Zhang, L., Zhou, Z., Luo, X., Wang, T., Zhao, X., Lu, B., Chen, F. and Zheng, L., 2022. Calcium phosphate-based biomaterials for bone repair. *Journal of functional biomaterials*, *13*(4), 187.
[103] Jeong, J., Kim, J.H., Shim, J.H., Hwang, N.S. and Heo, C.Y., 2019. Bioactive calcium phosphate materials and applications in bone regeneration. *Biomaterials research*, *23*(1), 4.
[104] Zhao, J., Liu, Y., Sun, W.B. and Zhang, H., 2011. Amorphous calcium phosphate and its application in dentistry. *Chemistry Central Journal*, *5*, 1-7.
[105] Lobo, S.E. and Arinzeh, T.L., 2010. Biphasic calcium phosphate ceramics for bone regeneration and tissue engineering applications. *Materials*, *3*(2), 815-826.
[106] Kim, S.E. and Park, K., 2020. Recent advances of biphasic calcium phosphate bioceramics for bone tissue regeneration. *Biomimicked Biomaterials: Advances in Tissue Engineering and Regenerative Medicine*, 177-188.
[107] Fakher, S. and Westenberg, D., 2024. Borate-based bioactive glasses properties: clinical and biomedical applications. *Ceramics International*. 50(24), 52190-52204.
[108] Hench, L.L., 2006. The story of Bioglass®. *Journal of materials science: materials in medicine*, *17*(11), 967-978.
[109] Jones, J. and Clare, A. eds., 2012. *Bio-glasses: an introduction*. John Wiley & Sons.
[110] Abodunrin, O.D., El Mabrouk, K. and Bricha, M., 2023. A review on borate bioactive glasses (BBG): effect of doping elements, degradation, and applications. *Journal of Materials Chemistry B*, *11*(5), 955-973.

[111] Abou Neel, E.A., Pickup, D.M., Valappil, S.P., Newport, R.J. and Knowles, J.C., 2009. Bioactive functional materials: a perspective on phosphate-based glasses. *Journal of Materials Chemistry*, *19*(6), 690-701.
[112] Yeo, T., Ko, Y.G., Kim, E.J., Kwon, O.K., Chung, H.Y. and Kwon, O.H., 2021. Promoting bone regeneration by 3D-printed poly (glycolic acid)/hydroxyapatite composite scaffolds. *Journal of Industrial and Engineering Chemistry*, *94*, 343-351.
[113] Gentile, P., Chiono, V., Carmagnola, I. and Hatton, P.V., 2014. An overview of poly (lactic-co-glycolic) acid (PLGA)-based biomaterials for bone tissue engineering. *International journal of molecular sciences*, *15*(3), 3640-3659.
[114] Hou, Y., Wang, W. and Bartolo, P., 2022. Investigation of polycaprolactone for bone tissue engineering scaffolds: In vitro degradation and biological studies. *Materials & Design*, *216*, 110582.
[115] Fritsch, A., Dormieux, L., Hellmich, C. and Sanahuja, J. (2009), Mechanical behavior of hydroxyapatite biomaterials: An experimentally validated micromechanical model for elasticity and strength. J. Biomed. Mater. Res., 88A: 149-161.
[116] Cinici, B., Yaba, S., Kurt, M., Yalcin, H.C., Duta, L. and Gunduz, O., 2024. Fabrication strategies for bioceramic scaffolds in bone tissue engineering with generative design applications. *Biomimetics*, *9*(7), 409.
[117] Muralithran, G. and Ramesh, S.J.C.I., 2000. The effects of sintering temperature on the properties of hydroxyapatite. *Ceramics International*, *26*(2), 221-230.
[118] Mondal, S., Hoang, G., Manivasagan, P., Moorthy, M.S., Nguyen, T.P., Phan, T.T.V., Kim, H.H., Kim, M.H., Nam, S.Y. and Oh, J., 2018. Nano-hydroxyapatite bioactive glass composite scaffold with enhanced mechanical and biological performance for tissue engineering application. *Ceramics International*, *44*(13), 15735-15746.
[119] Andersson, Ö.H., Liu, G., Karlsson, K.H., Niemi, L., Miettinen, J. and Juhanoja, J., 1990. In vivo behaviour of glasses in the SiO2-Na2O-CaO-P2O5-Al2O3-B2O3 system. *Journal of Materials Science: Materials in Medicine*, *1*, 219-227.
[120] Jones, J.R., Brauer, D.S., Hupa, L. and Greenspan, D.C., 2016. Bioglass and bioactive glasses and their impact on healthcare. *International Journal of Applied Glass Science*, *7*(4), 423-434.
[121] Culla, A.C., Vater, C., Tian, X., Bolte, J., Ahlfeld, T., Bretschneider, H., Pape, A., Goodman, S.B., Gelinsky, M. and Zwingenberger, S., 2022. Treatment of critical size femoral bone defects with biomimetic hybrid scaffolds of 3D plotted calcium phosphate cement and mineralized collagen matrix. *International Journal of Molecular Sciences*, *23*(6), 3400.
[122] Zhang, H., Mao, X., Du, Z., Jiang, W., Han, X., Zhao, D., Han, D. and Li, Q., 2016. Three dimensional printed macroporous polylactic acid/hydroxyapatite composite scaffolds for promoting bone formation in a critical-size rat calvarial defect model. *Science and Technology of Advanced materials*, *17*(1), 136-148.
[123] Fernandes, G.V.O., Castro, F., Pereira, R.M., Teixeira, W., Gehrke, S., Joly, J.C., Blanco Carrion, J. and Fernandes, J.C.H., 2024. Critical-size defects reconstruction with four different bone grafts associated with e-PTFE membrane: A histomorphometric experimental in vivo study. *Clinical Oral Implants Research*, *35*(2), 167-178.
[124] Ramesh, N., Moratti, S.C. and Dias, G.J., 2018. Hydroxyapatite–polymer biocomposites for bone regeneration: A review of current trends. *Journal of Biomedical Materials Research Part B: Applied Biomaterials*, *106*(5), 2046-2057.

[125] Radulescu, D.E., Neacsu, I.A., Grumezescu, A.M. and Andronescu, E., 2022. Novel trends into the development of natural hydroxyapatite-based polymeric composites for bone tissue engineering. *Polymers*, *14*(5), 899.
[126] Durucan, C. and Brown, P.W., 2001. Biodegradable hydroxyapatite–polymer composites. *Advanced Engineering Materials*, *3*(4), 227-231.
[127] Satchanska, G., Davidova, S. and Petrov, P.D., 2024. Natural and synthetic polymers for biomedical and environmental applications. *Polymers*, *16*(8), 1159.
[128] Reddy, M.S.B., Ponnamma, D., Choudhary, R. and Sadasivuni, K.K., 2021. A comparative review of natural and synthetic biopolymer composite scaffolds. *Polymers*, *13*(7), 1105.
[129] Magoń, A. and Pyda, M., 2009. Study of crystalline and amorphous phases of biodegradable poly (lactic acid) by advanced thermal analysis. *Polymer*, *50*(16), 3967-3973.
[130] Jariyavidyanont, K., Yu, Q., Petzold, A., Thurn-Albrecht, T., Glüge, R., Altenbach, H. and Androsch, R., 2023. Young's modulus of the different crystalline phases of poly (l-lactic acid). *Journal of the Mechanical Behavior of Biomedical Materials*, *137*, 105546.
[131] Ma, B., Wang, X., He, Y., Dong, Z., Zhang, X., Chen, X. and Liu, T., 2021. Effect of poly (lactic acid) crystallization on its mechanical and heat resistance performances. *Polymer*, *212*, 123280.
[132] Da Silva, D., Kaduri, M., Poley, M., Adir, O., Krinsky, N., Shainsky-Roitman, J. and Schroeder, A., 2018. Biocompatibility, biodegradation and excretion of polylactic acid (PLA) in medical implants and theranostic systems. *Chemical Engineering Journal*, *340*, 9-14.
[133] Polak-Kraśna, K., Abaei, A.R., Shirazi, R.N., Parle, E., Carroll, O., Ronan, W. and Vaughan, T.J., 2021. Physical and mechanical degradation behaviour of semi-crystalline PLLA for bioresorbable stent applications. *Journal of the mechanical behavior of biomedical materials*, *118*, 104409.
[134] Tsuji, H., Mizuno, A. and Ikada, Y., 2000. Properties and morphology of poly (L-lactide). III. Effects of initial crystallinity on long-term in vitro hydrolysis of high molecular weight poly (L-lactide) film in phosphate-buffered solution. *Journal of Applied Polymer Science*, *77*(7), 1452-1464.
[135] Hickey, D.J., Ercan, B., Sun, L. and Webster, T.J., 2015. Adding MgO nanoparticles to hydroxyapatite–PLLA nanocomposites for improved bone tissue engineering applications. *Acta biomaterialia*, *14*, 175-184.
[136] Çelik, T., Saraçoğlu, B., Özkan, A. and İlhan, Y., 2023. Biodegradable Pla/Ha Composite Material Production and Mechanical Characterization for Temporary Implant Applications. *International Journal of Pioneering Technology and Engineering*, *2*(02), 188-192.
[137] Rocha, C.R., Chávez-Flores, D., Zuverza-Mena, N., Duarte, A., Rocha-Gutiérrez, B.A., Zaragoza-Contreras, E.A. and Flores-Gallardo, S., 2020. Surface organo-modification of hydroxyapatites to improve PLA/HA compatibility. *Journal of Applied Polymer Science*, *137*(42), 49293.
[138] Xiong, Y., Li, L. and Tan, P., 2025. Preparation and Properties of the Hydroxyapatite/polylactic Acid (HA/PLA) Nanocomposites. *Journal of Wuhan University of Technology-Mater. Sci. Ed.*, *40*(3), 668-673.

[139] Tao, Y., Zhang, Y., Xia, T. and Lin, N., 2024. Melt Compounding of Poly (lactic acid)-Based Composites: Blending Strategies, Process Conditions, and Mechanical Properties. *Macromolecular Rapid Communications*, *45*(20), 2400380.
[140] Rakmae, S., Ruksakulpiwat, Y., Sutapun, W. and Suppakarn, N., 2011. Physical properties and cytotoxicity of surface-modified bovine bone-based hydroxyapatite/poly (lactic acid) composites. *Journal of composite materials*, *45*(12), 1259-1269.
[141] Akindoyo, J.O., Beg, M.D., Ghazali, S., Heim, H.P. and Feldmann, M., 2018. Impact modified PLA-hydroxyapatite composites–Thermo-mechanical properties. *Composites Part A: Applied Science and Manufacturing*, *107*, 326-333.
[142] Kryszak, B., Biernat, M., Tymowicz-Grzyb, P., Junka, A., Brożyna, M., Worek, M., Dzienny, P., Antończak, A. and Szustakiewicz, K., 2023. The effect of extrusion and injection molding on physical, chemical, and biological properties of PLLA/HAp whiskers composites. *Polymer*, *287*, 126428.
[143] Marzuki, A.P., Mohd Salleh, F., Rosli, M.N.S., Tharazi, I., Abdullah, A.H. and Abdul Halim, N.H., 2022. Rheological, mechanical and physical properties of poly-lactic acid (PLA)/hydroxyapatites (HA) composites prepared by an injection moulding process. *Journal of Mechanical Engineering (JMechE)*, *19*(2), 17-40.
[144] Narayanan P, L. and A, S., 2024. Study on distribution of hydroxyapatite (HA) in twin screw extruded cum injection moulded polylactic acid (PLA) composites and their effect on mechanical property. *Advanced Composite Materials*, 1-26.
[145] Ferri, J.M., Jordá, J., Montanes, N., Fenollar, O. and Balart, R., 2018. Manufacturing and characterization of poly (lactic acid) composites with hydroxyapatite. *Journal of thermoplastic composite Materials*, *31*(7), 865-881.
[146] Ignjatovic, N. and Uskokovic, D., 2004. Synthesis and application of hydroxyapatite/polylactide composite biomaterial. *Applied Surface Science*, *238*(1-4), 314-319.
[147] Kasuga, T., Ota, Y., Nogami, M. and Abe, Y., 2000. Preparation and mechanical properties of polylactic acid composites containing hydroxyapatite fibers. *Biomaterials*, *22*(1), 19-23.
[148] Ignjatovic, N., Suljovrujic, E., Budinski-Simendic, J., Krakovsky, I. and Uskokovic, D., 2004. Evaluation of hot-pressed hydroxyapatite/poly-L-lactide composite biomaterial characteristics. *Journal of Biomedical Materials Research Part B: Applied Biomaterials*, *71*(2), 284-294.
[149] Pietrzykowska, E., Romelczyk-Baishya, B., Wojnarowicz, J., Sokolova, M., Szlazak, K., Swieszkowski, W., Locs, J. and Lojkowski, W., 2020. Preparation of a ceramic matrix composite made of hydroxyapatite nanoparticles and polylactic acid by consolidation of composite granules. *Nanomaterials*, *10*(6), 1060.
[150] Winarso, R., Anggoro, P.W., Ismail, R., Jamari, J. and Bayuseno, A.P., 2022. Application of fused deposition modeling (FDM) on bone scaffold manufacturing process: a review. *Heliyon*, *8*(11).
[151] Sardar, M.Z., Gide, K.M., Stuart, A., Rostobaya, V., Zarrabinia, K., Beheshti, A. and Bagheri, S., 2025. Evaluating mixing methods for FFF-printed PLA-HA composites: Towards high-performance composites and advancements in additive manufacturing. *The International Journal of Advanced Manufacturing Technology*, *136*(3), 1267-1280.

[152] Ojo, S.A., Abere, D.V., Adejo, H.O., Robert, R.A. and Oluwasegun, K.M., 2023. Additive manufacturing of hydroxyapatite-based composites for bioengineering applications. *Bioprinting*, *32*, e00278.
[153] Takayama, T., Uchiumi, K., Ito, H., Kawai, T. and Todo, M., 2013. Particle size distribution effects on physical properties of injection molded HA/PLA composites. *Advanced Composite Materials*, *22*(5), 327-337.
[154] Jacobsen, S. and Fritz, H.G., 1999. Plasticizing polylactide—the effect of different plasticizers on the mechanical properties. *Polymer Engineering & Science*, *39*(7), 1303-1310.
[155] Martin, O. and Avérous, L., 2001. Poly (lactic acid): plasticization and properties of biodegradable multiphase systems. *Polymer*, *42*(14), 6209-6219.
[156] Ljungberg, N. and Wesslen, B., 2003. Tributyl citrate oligomers as plasticizers for poly (lactic acid): thermo-mechanical film properties and aging. *Polymer*, *44*(25), 7679-7688.
[157] Kulinski, Z., Piorkowska, E., Gadzinowska, K. and Stasiak, M., 2006. Plasticization of poly (L-lactide) with poly (propylene glycol). *Biomacromolecules*, *7*(7), 2128-2135.
[158] Murariu, M., Da Silva Ferreira, A., Alexandre, M. and Dubois, P., 2008. Polylactide (PLA) designed with desired end-use properties: 1. PLA compositions with low molecular weight ester-like plasticizers and related performances. *Polymers for Advanced Technologies*, *19*(6), 636-646.
[159] Kang, S.J.L., 2005, January. Sintering processes. In *Sintering* (3-8). Oxford, UK: Butterworth-Heinemann.
[160] German, R.M., 2017. The emergence of quantitative sintering theory from 1945 to 1955. *JOM*, *69*(4), 630-634.
[161] German,R. Sintering. In Encyclopedia of Materials: Science and Technology; Elsevier: Oxford, UK, 2001; 8641–8643.
[162] Rahaman, M.N., 2017. *Ceramic processing and sintering*. CRC press.
[163] Kong, L.B., Huang, Y., Que, W., Zhang, T., Li, S., Zhang, J., Dong, Z. and Tang, D., 2015. Sintering and densification (I)—conventional sintering technologies. In *Transparent Ceramics*, 291-394, Cham: Springer International Publishing.
[164] Leriche, A., Hampshire, S. and Cambier, F., 2017. Sintering of ceramics. *Reference Module in Materials Science and Materials Engineering*.
[165] Lee, W.E. and Rainforth, M., 1994. *Ceramic microstructures: property control by processing*. Springer Science & Business Media.
[166] De Jonghe, L.C. and Rahaman, M.N., 2003. Sintering of ceramics. In *Handbook of advanced ceramics: materials, applications, processing and properties*.
[167] Biesuz, M., Grasso, S. and Sglavo, V.M., 2020. What's new in ceramics sintering? A short report on the latest trends and future prospects. *Current Opinion in Solid State and Materials Science*, *24*(5), 100868.
[168] Tokita, M., 2006. Development of advanced spark plasma sintering (SPS) systems and its industrial applications. *Pulse Electric Current Synthesis and Processing of Materials*, 51-59.
[169] Tokita, M., 2021. Progress of spark plasma sintering (SPS) method, systems, ceramics applications and industrialization. *Ceramics*, *4*(2), 160-198.
[170] Chaffee, J.G., Bell Telephone Laboratories Inc, 1939. *Method and apparatus for heating dielectric materials*. U.S. Patent 2,147,689.

[171] Agrawal, D.K., 1998. Microwave processing of ceramics. *Current Opinion in Solid State and Materials Science*, *3*(5), 480-485.
[172] Cologna, M., Rashkova, B. and Raj, R., 2010. Flash sintering of nanograin zirconia in< 5 s at 850 C. *Journal of the American Ceramic Society*, *93*(11), 3556-3559.
[173] Sglavo, V.M., De Bona, E. and Mazo, I., 2024. Flash sintering of metal-like ceramics: a short overview. *Ceramics International*, *50*(19), 37356-37365.
[174] Bajpai, I., Han, Y.H., Yun, J., Francis, J., Kim, S. and Raj, R., 2016. Preliminary investigation of hydroxyapatite microstructures prepared by flash sintering. *Advances in Applied Ceramics*, *115*(5), 276-281.
[175] Hwang, C. and Yun, J., 2021. Flash sintering of hydroxyapatite ceramics. *Journal of Asian Ceramic Societies*, *9*(1), 304-311.
[176] Fang, Y., Agrawal, D.K., Roy, D.M. and Roy, R., 1994. Microwave sintering of hydroxyapatite ceramics. *Journal of materials research*, *9*(1), 180-187.
[177] Yang, Y., Ong, J.L. and Tian, J., 2002. Rapid sintering of hydroxyapatite by microwave processing. *Journal of materials science letters*, *21*(1), 67-69.
[178] Quan, V.M., Dang-Ngoc, T.N., Nguyen, T.H. and Van Quang, D., 2024. Rapid fabrication of mechanical-improved hydroxyapatite scaffolds from the microwave sintering with homogenous incorporated nanosilver particles. *Materials Letters*, *367*, 136555.
[179] Gu, Y.W., Loh, N.H., Khor, K.A., Tor, S.B. and Cheang, P., 2002. Spark plasma sintering of hydroxyapatite powders. *Biomaterials*, *23*(1), 37-43.
[180] Guo, X., Xiao, P., Liu, J. and Shen, Z., 2005. Fabrication of nanostructured hydroxyapatite via hydrothermal synthesis and spark plasma sintering. *Journal of the american ceramic society*, *88*(4), 1026-1029.
[181] Nakahira, A., Tamai, M., Eguchi, K., Nakamura, S. and Yamashita, K., 2002. Preparation and evaluation of dense hydroxyapatite by PECS method. *Key Engineering Materials*, *240*, 551-554.
[182] Eriksson, M., Liu, Y., Hu, J., Gao, L., Nygren, M. and Shen, Z., 2011. Transparent hydroxyapatite ceramics with nanograin structure prepared by high pressure spark plasma sintering at the minimized sintering temperature. *Journal of the European Ceramic Society*, *31*(9), 1533-1540.
[183] Ortali, C., Julien, I., Vandenhende, M., Drouet, C. and Champion, E., 2018. Consolidation of bone-like apatite bioceramics by spark plasma sintering of amorphous carbonated calcium phosphate at very low temperature. *Journal of the European Ceramic Society*, *38*(4), 2098-2109.
[184] Ortali, C., Julien, I., Drouet, C. and Champion, E., 2020. Influence of carbonation on the low-temperature consolidation by Spark Plasma Sintering of carbonated calcium phosphate bioceramics. Ceramics International, 46(5), 5799-5810.
[185] Li, J.G. and Hashida, T., 2006. In situ formation of hydroxyapatite-whisker ceramics by hydrothermal hot-pressing method. *Journal of the American Ceramic Society*, *89*(11), 3544-3546.
[186] Li, J. and Hashida, T., 2007. Preparation of hydroxyapatite ceramics by hydrothermal hot-pressing method at 300 C. *Journal of materials science*, *42*(13), 5013-5019.
[187] Montoya-Cisneros, K.L., Rendón-Angeles, J.C., Matamoros-Veloza, Z., Matamoros-Veloza, A. and Yanagisawa, K., 2017. Low-temperature densification of Mg-doped hydroxyapatite fine powders under hydrothermal hot processing conditions. *Ceramics International*, *43*(15), 11907-11919.

[188] Guo, N., Shen, H.Z., Jin, Q. and Shen, P., 2021. Hydrated precursor-assisted densification of hydroxyapatite and its composites by cold sintering. *Ceramics International*, *47*(10), 14348-14353.
[189] Iqbal, S., ul Hassan, M., Ryu, H.J. and Yun, J.I., 2019. Efficient immobilization of ionic corrosion products by a silica-hydroxyapatite composite via a cold sintering route. *RSC advances*, *9*(60), 34872-34879.
[190] Huang, Z., Zuo, Y., Zheng, J., Deng, M., Chen, R. and Wang, H., 2025. Utilizing the cold sintering process for the SiO2-HA glass-ceramics. *Ceramics International*, *51*(8), 10650-10659.
[191] Seo, Y., Goto, T., Cho, S. and Sekino, T., 2024. Densification of transparent hydroxyapatite ceramics via cold sintering process combined with biomineralization. *Journal of the European Ceramic Society*, *44*(6), 4285-4293.
[192] Rubenis, K., Zemjane, S., Vecstaudza, J., Bitenieks, J. and Locs, J., 2021. Densification of amorphous calcium phosphate using principles of the cold sintering process. *Journal of the European Ceramic Society*, *41*(1), 912-919.
[193] Ndayishimiye, A., Sengul, M.Y., Sada, T., Dursun, S., Bang, S.H., Grady, Z.A., Tsuji, K., Funahashi, S., van Duin, A.C. and Randall, C.A., 2020. Roadmap for densification in cold sintering: Chemical pathways. *Open Ceramics*, *2*, 100019.
[194] Biesuz, M., Taveri, G., Duff, A.I., Olevsky, E., Zhu, D., Hu, C. and Grasso, S., 2020. A theoretical analysis of cold sintering. *Advances in Applied Ceramics*, *119*(2), 75-89.
[195] Ndayishimiye, A., Bang, S.H., Spiers, C.J. and Randall, C.A., 2023. Reassessing cold sintering in the framework of pressure solution theory. *Journal of the European Ceramic Society*, *43*(1), 1-13.
[196] Galotta, A. and Sglavo, V.M., 2021. The cold sintering process: A review on processing features, densification mechanisms and perspectives. *Journal of the European Ceramic Society*, *41*(16), 1-17.
[197] Bang, S.H., Sengul, M.Y., Fan, Z., Ndayishimiye, A., van Duin, A.C.T. and Randall, C.A., 2022. Morphological and chemical evolution of transient interfaces during zinc oxide cold sintering process. *Materials Today Chemistry*, *24*, 100925.
[198] Ndayishimiye, A., Sengul, M.Y., Bang, S.H., Tsuji, K., Takashima, K., de Beauvoir, T.H., Denux, D., Thibaud, J.M., van Duin, A.C., Elissalde, C. and Goglio, G., 2020. Comparing hydrothermal sintering and cold sintering process: Mechanisms, microstructure, kinetics and chemistry. *Journal of the European Ceramic Society*, *40*(4), 1312-1324.
[199] Gonzalez-Julian, J., Neuhaus, K., Bernemann, M., Da Silva, J.P., Laptev, A., Bram, M. and Guillon, O., 2018. Unveiling the mechanisms of cold sintering of ZnO at 250 C by varying applied stress and characterizing grain boundaries by Kelvin Probe Force Microscopy. *Acta Materialia*, *144*, 116-128.
[200] Jabr, A., Fanghanel, J., Fan, Z., Bermejo, R. and Randall, C., 2023. The effect of liquid phase chemistry on the densification and strength of cold sintered ZnO. *Journal of the European Ceramic Society*, *43*(4), 1531-1541.
[201] Jabr, A., Jones, H.N., Argüelles, A.P., Trolier-McKinstry, S., Randall, C. and Bermejo, R., 2023. Scaling up the cold sintering process of ceramics. *Journal of the European Ceramic Society*, *43*(12), 5319-5329.
[202] Jabr, A., Ribul, E., Salamon, D. and Bermejo, R., 2025. Understanding the lower fracture resistance of cold sintered ceramics. *Journal of the European Ceramic Society*, *45*(2), 116968.

[203] Jabr, A., 2025. Understanding the effect of processing conditions on the properties of cold sintered ceramics. (PhD thesis, Montanuniversität Leoben).
[204] Gratier, J.P., Dysthe, D.K. and Renard, F., 2013. The role of pressure solution creep in the ductility of the Earth's upper crust. *Advances in Geophysics*, *54*, 47-179.
[205] Hellmann, R.O.L.A.N.D., Renders, P.J., Gratier, J.P. and Guiguet, R.O.B.E.R.T., 2002. Experimental pressure solution compaction of chalk in aqueous solutions. Part 1. Deformation behavior and chemistry. *Water-rock interactions, ore deposits, and environmental geochemistry: A tribute to David A. Crerar*, *7*(7), 153-178.
[206] Rutter, E.H., 1983. Pressure solution in nature, theory and experiment. *Journal of the Geological Society*, *140*(5), 725-740.
[207] Lee, B.K., Chung, S.Y. and Kang, S.J.L., 2000. Grain boundary faceting and abnormal grain growth in BaTiO3. *Acta materialia*, *48*(7), 1575-1580.
[208] Ndayishimiye, A., Sengul, M.Y., Akbarian, D., Fan, Z., Tsuji, K., Bang, S.H., Van Duin, A.C. and Randall, C.A., 2021. Dynamics of the chemically driven densification of barium titanate using molten hydroxides. *Nano letters*, *21*(8), 3451-3457.
[209] Tsuji, K., Ndayishimiye, A., Lowum, S., Floyd, R., Wang, K., Wetherington, M., Maria, J.P. and Randall, C.A., 2020. Single step densification of high permittivity BaTiO3 ceramics at 300 ºC. Journal of the European Ceramic Society, 40(4), 1280-1284.
[210] Guo, H., Bayer, T.J., Guo, J., Baker, A. and Randall, C.A., 2017. Current progress and perspectives of applying cold sintering process to ZrO2-based ceramics. *Scripta Materialia*, *136*, 141-148.
[211] Galotta, A., Giust, E., Bortolotti, M., Sorarù, G.D., Sglavo, V.M. and Biesuz, M., 2021. Cold sintering of diatomaceous earth. *Journal of the American Ceramic Society*, *104*(9), 4329-4340.
[212] Santhosh, B., Galotta, A., Soraru, G.D., Sglavo, V.M. and Biesuz, M., 2022. Cold sintering of colloidal silica particles using different alkali solutions. *Ceramics International*, *48*(23), 35627-35632.
[213] Rosenberger, A., Blair, V., Hlubb, L. and Golt, M., 2022. *Cold Sintering of Zinc Oxide (ZnO) and Silica (SiO2)* (No. ARLTR9557). Technical report.
[214] de Beauvoir, T.H., Taberna, P.L., Simon, P. and Estournès, C., 2022. Cold Sintering Process characterization by in operando electrochemical impedance spectroscopy. *Journal of the European Ceramic Society*, *42*(13), 5747-5755.
[215] Allen, A.J., Levin, I., Maier, R.A., Witt, S.E., Zhang, F. and Kuzmenko, I., 2021. In situ characterization of ceramic cold sintering by small-angle scattering. *Journal of the American Ceramic Society*, *104*(6), 2442-2448.
[216] Allen, A.J., Maier, R.A., Zhang, F., Kuzmenko, I. and Ilavsky, J., 2022. In situ microstructure characterization of potassium di-phosphate (KDP) densification during cold sintering. *Applied Sciences*, *12*(20), 10493.
[217] Zhang, F., Maier, R.A., Levin, I., Allen, A.J., Park, J.S., Kenesei, P., Kuzmenko, I., Jemian, P. and Ilavsky, J., 2023. In situ probing of interfacial roughness and transient phases during ceramic cold sintering process. *Acta Materialia*, *259*, 119283.
[218] Maier, R.A., 2024. In situ observation of the multistep process of cold sintering. *Journal of the American Ceramic Society*, *107*(10), 6544-6553.
[219] Oliveira, R.L.M.S., Antonelli, E., Montufar, E.B. and de Sousa Trichês, E., 2024. Cold sintering of β-tricalcium phosphate/bioactive glass composites. *Ceramics International*, *50*(11), 18138-18145.

[220] Andrews, J., Bullock, G., Miller, C.A., Booth, J., Ren, H., Kelly, N.L., Hanna, J.V. and Reaney, I.M., 2023. Cold sintering of bioglass and bioglass/polymer composites. *Journal of the American Ceramic Society*, *106*(6), 3396-3409.
[221] Wang, X., Zhang, H., Yu, X., Mo, X., Gao, J., Hu, Y., Min, J., Ding, Q., Fan, Y. and Jiang, W., 2024. Effects of water on cold-sintered highly dense dicalcium phosphate anhydrous bioceramic using its hydrate. *Journal of the American Ceramic Society*, *107*(7), 4631-4640.
[222] Galotta, A., Rubenis, K., Locs, J. and Sglavo, V.M., 2023. Dissolution-precipitation synthesis and cold sintering of mussel shells-derived hydroxyapatite and hydroxyapatite/chitosan composites for bone tissue engineering. *Open Ceramics*, *15*, 100418.
[223] Guo, N., Shen, H.Z. and Shen, P., 2022. Cold sintering of chitosan/hydroxyapatite composites. *Materialia*, *21*, 101294.
[224] Hu, Y., Xia, D., Shen, H., Nan, J., Ma, N., Guo, Z., Wang, X. and Jin, Q., 2023. Cold sintering constructed in situ drug-loaded high strength HA-PLA composites: Potential bone substitution material. *Ceramics International*, *49*(7), 11655-11663.
[225] Galotta, A., Demir, Ö., Marsan, O., Sglavo, V.M., Loca, D., Combes, C. and Locs, J., 2024. Apatite/chitosan composites formed by cold sintering for drug delivery and bone tissue engineering applications. *Nanomaterials*, *14*(5), 441.
[226] Abbas, H.O., Smeig, H.A. and Ameer, Z.J.A., 2023. Utilising cold sintering process for sintering hydroxyapatite-polyetheretherketone nanocomposite. *Archives of Materials Science and Engineering*, *124*(1).
[227] Rocton, N., 2019. *Élaboration de bioverres et de nano-bioverres ostéoinducteurs associés à des molécules à usage thérapeutique* (Doctoral thesis, Université de Rennes).
[228] Pharr, G.M., Oliver, W.C. and Brotzen, F.R., 1992. On the generality of the relationship among contact stiffness, contact area, and elastic modulus during indentation. *Journal of materials research*, *7*(3), 613-617.
[229] Dorozhkin, S.V., 1999. Inorganic chemistry of the dissolution phenomenon: The dissolution mechanism of calcium apatites at the atomic (ionic) level. *Comments on Inorganic Chemistry*, *20*(4-6), 285-299.
[230] Dorozhkin, S.V., 2012. Dissolution mechanism of calcium apatites in acids: A review of literature. *World journal of methodology*, *2*(1), 1.
[231] Smith, A.N., Posner, A.M. and Quirk, J.P., 1974. Incongruent dissolution and surface complexes of hydroxyapatite. *Journal of Colloid and Interface Science*, *48*(3), 442-449.
[232] Silva, V.M., Quadros, P.A., Laranjeira, P.E., Dias, M.M. and Lopes, J.C., 2008. A novel continuous industrial process for producing hydroxyapatite nanoparticles. *Journal of Dispersion Science and Technology*, *29*(4), 542-547.
[233] Jongebloed, W.L., Molenaar, I. and Arends, J., 1973. Orientation-dependent etchpit penetration and dissolution of fluoroapatite. *Caries Research*, *7*(2), 154-165.
[234] Hills, J.E. and Sullivan, H.R., 1958. Studies on the acid decalcification of human dental enamel. I. *Australian Dental Journal*, *3*(1), 6-18.
[235] Pearce, E.I.F., 1988. On the dissolution of hydroxyapatite in acid solutions. *Journal of dental research*, *67*(7), 1056-1058.
[236] Johnson, N.W., 1966. Differences in the shape of human enamel crystallites after partial destruction by caries, EDTA and various acids. *Archives of Oral Biology*, *11*(12), 1421-IN49.

[237] Hossain, M.S. and Ahmed, S., 2023. FTIR spectrum analysis to predict the crystalline and amorphous phases of hydroxyapatite: a comparison of vibrational motion to reflection. *RSC advances*, *13*(21), 14625-14630.
[238] Diallo-Garcia, S., Osman, M.B., Krafft, J.M., Casale, S., Thomas, C., Kubo, J. and Costentin, G., 2014. Identification of surface basic sites and acid–base pairs of hydroxyapatite. *The Journal of Physical Chemistry C*, *118*(24), 12744-12757.
[239] Joris, S.J. and Amberg, C.H., 1971. Nature of deficiency in nonstoichiometric hydroxyapatites. II. Spectroscopic studies of calcium and strontium hydroxyapatites. *The Journal of Physical Chemistry*, *75*(20), 3172-3178.
[240] Ma, J. and Lim, L.C., 2002. Effect of particle size distribution on sintering of agglomerate-free submicron alumina powder compacts. *Journal of the European Ceramic Society*, *22*(13), 2197-2208.
[241] Brujić, J., Wang, P., Song, C., Johnson, D.L., Sindt, O. and Makse, H.A., 2005. Granular dynamics in compaction and stress relaxation. *Physical review letters*, *95*(12), 128001.
[242] Ballardini, A., 2017. Development of novel multi-substituted apatite nanophases with advanced functionalities for bone regeneration. (Doctoral thesis, Università di Bologna)
[243] Kingery, W.D., 1959. Densification during sintering in the presence of a liquid phase. I. Theory. *Journal of Applied Physics*, *30*(3), 301-306.
[244] Stammeier, J.A., Purgstaller, B., Hippler, D., Mavromatis, V. and Dietzel, M., 2018. In-situ Raman spectroscopy of amorphous calcium phosphate to crystalline hydroxyapatite transformation. *MethodsX*, *5*, 1241-1250.
[245] Montes-Hernandez, G. and Renard, F., 2020. Nucleation of brushite and hydroxyapatite from amorphous calcium phosphate phases revealed by dynamic in situ Raman spectroscopy. *The Journal of Physical Chemistry C*, *124*(28), 15302-15311.
[246] Karampas, I.A. and Kontoyannis, C.G., 2013. Characterization of calcium phosphates mixtures. *Vibrational Spectroscopy*, *64*, 126-133.
[247] Panah, N.G., Atkin, R. and Sercombe, T.B., 2022. Bioactivity and biodegradability of high-temperature sintered 58S ceramics. *Journal of the European Ceramic Society*, *42*(8), 3614-3623.
[248] Roman, J., Padilla, S. and Vallet-Regi, M., 2003. Sol–gel glasses as precursors of bioactive glass ceramics. *Chemistry of materials*, *15*(3), 798-806.
[249] Catauro, M., Bollino, F., Renella, R. and Papale, F., 2015. Sol–gel synthesis of SiO2–CaO–P2O5 glasses: Influence of the heat treatment on their bioactivity and biocompatibility. *Ceramics International*, *41*(10), 12578-12588.
[250] Degraeve, B., Lefeuvre, B., Rocton, N., Herbert, N., Hamrouni, N., Hauss, G., Largeteau, A., Prakasam, M., Oudadesse, H. and Merdrignac-Conanec, O., 2022. Processing of highly porous bioglass monoliths by hydrothermal hot pressing. *Ceramics International*, *48*(13), 18190-18198.
[251] Taveri, G., Hanzel, O., Sedláček, J., Toušek, J., Neščaková, Z., Michálek, M., Dlouhý, I. and Hnatko, M., 2021. Consolidation of Bioglass® 45S5 suspension through cold isostatic pressing. *Ceramics International*, *47*(3), 4090-4096.

[252] Nawaz, Q., Pantulap, U., Hurle, K., Luo, N., Grasso, S. and Boccaccini, A.R., 2023. Cold hydrostatic sintering of 45S5 bioactive glass. *European Journal of Materials*, *3*(1), 1-10.

[253] Braem, A., Neirinck, B., Schrooten, J., Van der Biest, O. and Vleugels, J., 2012. Biofunctionalization of porous titanium coatings through sol–gel impregnation with a bioactive glass–ceramic. *Materials Science and Engineering: C*, *32*(8), 2292-2298.

[254] Blaeß, C., Müller, R., Poologasundarampillai, G. and Brauer, D.S., 2019. Sintering and concomitant crystallization of bioactive glasses. *International Journal of Applied Glass Science*, *10*(4), 449-462.

[255] Bretcanu, O., Chatzistavrou, X., Paraskevopoulos, K., Conradt, R., Thompson, I. and Boccaccini, A.R., 2009. Sintering and crystallisation of 45S5 Bioglass® powder. *Journal of the European Ceramic Society*, *29*(16), 3299-3306.

[256] Bonino, F., Damin, A., Aina, V., Miola, M., Verne, E., Bretcanu, O., Bordiga, S., Zecchina, A. and Morterra, C., 2008. In situ Raman study to monitor bioactive glasses reactivity. *Journal of Raman Spectroscopy*, *39*(2), 260-264.

[257] Bellucci, D., Bolelli, G., Cannillo, V., Cattini, A. and Sola, A., 2011. In situ Raman spectroscopy investigation of bioactive glass reactivity: Simulated body fluid solution vs TRIS-buffered solution. *Materials characterization*, *62*(10), 1021-1028.

[258] Elsawy, M.A., Kim, K.H., Park, J.W. and Deep, A., 2017. Hydrolytic degradation of polylactic acid (PLA) and its composites. *Renewable and Sustainable Energy Reviews*, *79*, 1346-1352.

[259] Muhanna, A.H. and Blazynski, T.Z., 1988. Implosive consolidation of polymer ceramic powder composites. *Composites science and technology*, *33*(2), 121-133.

[260] Cristea, M., Ionita, D. and Iftime, M.M., 2020. Dynamic mechanical analysis investigations of PLA-based renewable materials: how are they useful?. *Materials*, *13*(22), 5302.

[261] Avegnon, K.L.M., Bedke, A.M., Minyard, J.D., Garda, M.R., Delbreilh, L., Vieille, B., Negahban, M. and Sealy, M.P., 2024. Use of negative thermal expansion to design scaffolds for cultured meat. *Materials & Design*, *242*, 112992.

[262] Puchalski, M., Kwolek, S., Szparaga, G., Chrzanowski, M. and Krucińska, I., 2017. Investigation of the influence of PLA molecular structure on the crystalline forms (α'and α) and mechanical properties of wet spinning fibres. *Polymers*, *9*(1), 18.

[263] Tábi, T., Hajba, S. and Kovács, J.G., 2016. Effect of crystalline forms (α' and α) of poly (lactic acid) on its mechanical, thermo-mechanical, heat deflection temperature and creep properties. *European Polymer Journal*, *82*, 232-243.

[264] Zhou, S., Zheng, X., Yu, X., Wang, J., Weng, J., Li, X., Feng, B. and Yin, M., 2007. Hydrogen bonding interaction of poly (D, L-lactide)/hydroxyapatite nanocomposites. *Chemistry of materials*, *19*(2), 247-253.

[265] Lee, H.W., Insyani, R., Prasetyo, D., Prajitno, H. and Sitompul, J., 2015. Molecular Weight and Structural Properties of Biodegradable PLA Synthesized with Different

Catalysts by Direct Melt Polycondensation. *Journal of Engineering & Technological Sciences*, *47*(4), 364-373.

[266] Muller, J., Jiménez, A., González-Martínez, C. and Chiralt, A., 2016. Influence of plasticizers on thermal properties and crystallization behaviour of poly (lactic acid) films obtained by compression moulding. *Polymer International*, *65*(8), 970-978.

[267] Lin, Z., Guo, X., He, Z., Liang, X., Wang, M. and Jin, G., 2021. Thermal degradation kinetics study of molten polylactide based on Raman spectroscopy. *Polymer Engineering & Science*, *61*(1), 201-210.

[268] Everall, N., 2008. The influence of out-of-focus sample regions on the surface specificity of confocal Raman microscopy. *Applied spectroscopy*, *62*(6), 591-598.

[269] Koh, M., Kitt, J.P., Pendergast, A.D., Harris, J.M., Minteer, S.D. and Korzeniewski, C., 2025. Confocal Raman Microscopy for Measuring In Situ Temperature-Dependent Structural Changes in Poly (Ethylene Oxide) Thin Films. *Applied Spectroscopy*.